UNIVERSITY OF IOANNINA
SCHOOL OF SCIENCES
DEPARTMENT OF MATERIALS SCIENCE AND ENGINEERING

DEVELOPMENT AND STUDY OF NOVEL NANO-STRUCTURED HYBRID MATERIALS BASED ON CARBON

ANDREAS ROSSOS

Doctoral Dissertation

Ioannina, 2014

UNIVERSITY OF IOANNINA
SCHOOL OF SCIENCES
DEPARTMENT OF MATERIALS SCIENCE AND ENGINEERING

DEVELOPMENT AND STUDY OF NOVEL NANO-STRUCTURED HYBRID MATERIALS BASED ON CARBON

ANDREAS ROSSOS

Doctoral Dissertation

Ioannina, 2014

«Η έγκριση της διδακτορικής διατριβής από το Τμήμα Μηχανικών Επιστήμης Υλικών της Σχολής Θετικών Επιστημών του Πανεπιστημίου Ιωαννίνων δεν υποδηλώνει αποδοχή των γνωμών του συγγραφέα Ν. 5343/32, άρθρο 202, παράγραφος 2».

Ημερομηνία αίτησης του κου Ανδρέα Ρώσσου: 15/03/2011.

Ημερομηνία ορισμού Τριμελούς Συμβουλευτικής Επιτροπής: 16/03/2011

Μέλη Τριμελούς Συμβουλευτικής Επιτροπής:

Επιβλέπων

Δημήτριος Γουρνής, Καθηγητής του Τμήματος Μηχανικών Επιστήμης Υλικών της Σχολής Θετικών Επιστημών του Πανεπιστημίου Ιωαννίνων

Μέλη

Κωνσταντίνος Κορδάτος, Αναπληρωτής Καθηγητής της Σχολής Χημικών Μηχανικών του Εθνικού Μετσόβιου Πολυτεχνείου, Αθήνα

Απόστολος Αυγερόπουλος, Καθηγητής του Τμήματος Μηχανικών Επιστήμης Υλικών της Σχολής Θετικών Επιστημών του Πανεπιστημίου Ιωαννίνων

Ημερομηνία ορισμού θέματος: 16/03/2011

Ανάπτυξη και μελέτη καινοτόμων νανοδομημένων υβριδικών υλικών με βάση τον άνθρακα

(Development and study of novel nano-structured hybrid materials based on carbon)

ΔΙΟΡΙΣΜΟΣ ΕΠΤΑΜΕΛΟΥΣ ΕΞΕΤΑΣΤΙΚΗΣ ΕΠΙΤΡΟΠΗΣ : 29/10/2014

ΓΟΥΡΝΗΣ	ΔΗΜΗΤΡΙΟΣ
ΚΟΡΔΑΤΟΣ	ΚΩΝΣΤΑΝΤΙΝΟΣ
ΑΥΓΕΡΟΠΟΥΛΟΣ	ΑΠΟΣΤΟΛΟΣ
ΚΑΡΑΚΑΣΙΔΗΣ	ΜΙΧΑΗΛ
ΜΠΑΚΑΣ	ΘΩΜΑΣ
ΔΟΥΒΑΛΗΣ	ΑΛΕΞΙΟΣ
ΜΠΟΥΡΛΙΝΟΣ	ΑΘΑΝΑΣΙΟΣ

Έγκριση Διδακτορικής Διατριβής με βαθμό **«ΑΡΙΣΤΑ»** στις **08/12/2014**

Ο Πρόεδρος του Τμήματος	**Η Γραμματέας του Τμήματος**
Καρακασίδης Μιχαήλ	**Ξανθή Τουτουνζόγλου**
Καθηγητής	

ΠΑΝΕΠΙΣΤΗΜΙΟ ΙΩΑΝΝΙΝΩΝ
Τμήμα Μηχανικών Επιστήμης Υλικών
Κτίριο Διοίκησης – Πανεπιστημιούπολη - 45110 ΙΩΑΝΝΙΝΑ

ΕΞΕΤΑΣΤΙΚΗ ΕΠΙΤΡΟΠΗ
ΔΙΔΑΚΤΟΡΙΚΗΣ ΔΙΑΤΡΙΒΗΣ
Αποφ.Γ.Σ.Ε.Σ.
αριθμ. συνεδρ. **266/29-10-2014**

Ιωάννινα, 8 Δεκεμβρίου 2014

ΘΕΜΑ: «**Διαβίβαση πρακτικού απόφασης της Επιτροπής**».

Προς
Το Τμήμα Μηχανικών Επιστήμης Υλικών του Παν/μίου Ιωαννίνων

Σας διαβιβάζουμε συνημμένο το από 8 Δεκεμβρίου 2014 πρακτικό της επταμελούς εξεταστικής επιτροπής σχετικά με την αξιολόγηση και κρίση της διατριβής του υποψήφιου διδάκτορα κ. Ανδρέα Ρώσσου με θέμα: **«Ανάπτυξη και Μελέτη Νέων Νανοδομημένων Υβριδικών Υλικών με βάση τον άνθρακα»** και παρακαλούμε για τη συνέχιση της διαδικασίας που αφορά την αναγόρευση του υποψηφίου σε διδάκτορα από τη Γ.Σ.Ε.Σ.

Με τιμή
Ο Πρόεδρος
της Εξεταστικής Επιτροπής

Δημήτριος Γουρνής
Καθηγητής

ΠΡΑΚΤΙΚΟ

της Επταμελούς Εξεταστικής Επιτροπής για την αναγόρευση σε διδάκτορα του Τμήματος Μηχανικών Επιστήμης Υλικών του Πανεπιστημίου Ιωαννίνων του κ. **Ανδρέα Ρώσσου.**

Η Γενική Συνέλευση Ειδικής Σύνθεσης (Γ.Σ.Ε.Σ) του Τμήματος Μηχανικών Επιστήμης Υλικών του Πανεπιστημίου Ιωαννίνων στη συνεδρίαση της αριθμ. **266/29-10-2014** ύστερα από την κρίση της Τριμελούς Συμβουλευτικής Επιτροπής ότι η ερευνητική εργασία του υποψηφίου διδάκτορα κ. **Ανδρέα Ρώσσου** έχει ολοκληρωθεί και έχει κατατεθεί στο Τμήμα, όρισε σύμφωνα με το άρθρο 12 παρ.5 εδ. Β του Ν.2083/92, και το άρθ. 9 παρ.4 εδ. α του Ν. 3685/2008 Επταμελή Εξεταστική Επιτροπή που αποτελείται από τους κ.κ. **Δημήτριο Γουρνή** Καθηγητή του ΤΜΕΥ του Πανεπιστημίου Ιωαννίνων, **Μιχαήλ Καρακασίδη** Καθηγητή και Πρόεδρο του ΤΜΕΥ του Πανεπιστημίου Ιωαννίνων, **Κωνσταντίνο Κορδάτο** Αναπληρωτή Καθηγητή της Σχολής Χημικών Μηχανικών του Εθνικού Μετσόβιου Πολυτεχνείου, **Απόστολο Αυγερόπουλο** Καθηγητή του ΤΜΕΥ του Πανεπιστημίου Ιωαννίνων, **Θωμά Μπάκα** Καθηγητή του Τμήματος Φυσικής και Αναπληρωτή Πρύτανη του Πανεπιστημίου Ιωαννίνων, **Αλέξιο Δούβαλη** Επίκουρο Καθηγητή του Φυσικής του Πανεπιστημίου Ιωαννίνων, και **Αθανάσιο Μπουρλίνο** Επίκουρο Καθηγητή του Φυσικής του Πανεπιστημίου Ιωαννίνων, για να αναπτύξει ενώπιον της ο υποψήφιος διδάκτορας κ. **Ανδρέα Ρώσσος** τη διατριβή του με θέμα: **«Ανάπτυξη και Μελέτη Νέων Νανοδομημένων Υβριδικών Υλικών με βάση τον άνθρακα».**

Η Επταμελής Εξεταστική Επιτροπή, συνήλθε **σήμερα 8 Δεκεμβρίου 2014 ημέρα Δευτέρα και ώρα 12:00 μ.μ. στο χώρο του Νέου Κτιρίου του ΤΜΕΥ του Πανεπιστημίου Ιωαννίνων** για να εξετάσει την διδακτορική διατριβή του υποψηφίου διδάκτορα κ. **Ανδρέα Ρώσσου**. Ο Αναπλ. Καθ. κ. Κ. Κορδάτος συμμετείχε στην διαδικασία μέσω τηλεδιάσκεψης όπως είχε ενημερώσει με έγγραφό του (στον Πρόεδρο της Εξεταστικής Επιτροπής κ. Δ. Γουρνή).

Χρέη προέδρου της Εξεταστικής Επιτροπής ανέθεσαν τα μέλη της στον κ. **Δημήτριο Γουρνή,** Καθηγητή του Τμήματος Μηχανικών Επιστήμης Υλικών του Πανεπιστημίου Ιωαννίνων.

Στο σημείο αυτό, τίθεται υπόψη της 7μελούς Εξεταστικής Επιτροπής το αρθ. 36 του Ν.1268/82, τα άρθ. 12 και 13 του Ν. 2083/92 και το άρθ. 9 παρ.4 εδ. α του Ν. 3685/2008 και τα αρθ. 40 και 41 του Εσωτερικού Κανονισμού Λειτουργίας του Πανεπιστημίου Ιωαννίνων (ΦΕΚ 310/10.03.05 τ. 2^{ο}). Τα μέλη της Επιτροπής έλαβαν εγκαίρως (01 Νοεμβρίου 2014) και μελέτησαν τη διατριβή του υποψηφίου.

Ο υποψήφιος κ. **Ανδρέας Ρώσσος** ανέπτυξε ενώπιον της Επιτροπής τη διατριβή του με θέμα: **«Ανάπτυξη και Μελέτη Νέων Νανοδομημένων Υβριδικών Υλικών με βάση τον άνθρακα»** τονίζοντας τα σημεία, στα οποία κατά τη γνώμη του η διατριβή είναι πρωτότυπη και αποτελεί συμβολή στην επιστήμη.

Τα μέλη της Εξεταστικής Επιτροπής απηύθυναν ερωτήσεις στον υποψήφιο, μετά την προφορική ανάπτυξη απ' αυτόν του θέματος. Η ανάπτυξη και οι ερωτήσεις έγιναν σε δημόσια συνεδρίαση.

Στη συνέχεια το ακροατήριο και ο υποψήφιος αποχώρησαν και τα μέλη της Εξεταστικής Επιτροπής συσκέφθηκαν και ψήφισαν, υπέρ της παραδοχής της διατριβής, **με ψήφους επτά (7) και κατά μηδέν (0).**

Πρότειναν, δε, με ψήφους έξι (7) έναντι μηδενός (0) το βαθμό **Άριστα** εφαρμόζοντας την παρ. 6 του αρθ. 40 του Εσωτερικού Κανονισμού Λειτουργίας του Πανεπιστημίου Ιωαννίνων (ΦΕΚ 310/10.03.05 τ. 2^{ο}).

Το παρόν πρακτικό μετά την υπογραφή του από τα υπόλοιπα μέλη της Επταμελούς Εξεταστικής Επιτροπής αποσταλεί ταχυδρομικώς στον Αναπλ. Καθ. Κ. Κορδάτο για ην έγκριση και τη σύμφωνη γνώμη του.

Ιωάννινα, 8 Δεκεμβρίου 2014

Η Εξεταστική Επιτροπή

1. **Δημήτριος Γουρνής**, Καθ. του ΤΜΕΥ του Παν/μίου Ιωαννίνων.....
2. **Μιχαήλ Καρακασίδης**, Καθ. του ΤΜΕΥ του Παν/μίου Ιωαννίνων.....
3. **Κων/νος Κορδάτος**, Αναπλ. Καθ. της Σχ. Χημ. Μηχ. του ΕΜΠ.....
4. **Θωμάς Μπάκας**, Καθ. του Τμ. Φυσικής του Παν/μίου Ιωαννίνων.....
5. **Απόστολος Αυγερόπουλος**, Καθ. του του ΤΜΕΥ του Παν/μίου Ιωαννίνων .....
6. **Αλέξιος Δούβαλης**, Επικ. Καθ. του Τμ. Φυσικής του Παν/μίου Ιωαννίνων .....
7. **Αθανάσιος Μπουρλίνος**, Επικ. Καθ. του Τμ. Φυσικής του Παν/μίου Ιωαννίνων .....

Preface

First of all, I would like to thank my supervisor, Professor Dimitrios Gournis for all the help and guidance during the whole procedure of my Doctoral Dissertation. Furthermore, I would like to thank the other two members of the three-member committee, Associate Professor Konstantinos Kordatos and Professor Apostolos Avgeropoulos, as well as the remaining members of the seven-member committee, Thomas Bakas, Alexios Douvalis, Michail Karakasidis and Athanassios Bourlinos (University of Ioannina).

Additionally, I would like to thank Pantelis Trikalitis (University of Crete), Ricky Reidy and Peyman Samimi (Univiversity of North Texas, USA), Xiaoxing Ke and Gustaaf van Tendeloo (University of Antwerp, Belgium) for the TEM measurements. Also, Alexios Douvalis and Thomas Bakas (University of Ioannina) for the Mössbauer data, Dimitra Giasafaki and Theodore Steriotis (DEMOKRITOS, Athens) for the SEM images, Oleksiy Ivashenko, Regis Gengler and Petra Rudolf (University of Groningen) for the XPS data, as well as Konstantinos Dimos and Lubos Jankovic (University of Ioannina). For the SQUID measurements I would like to thank Radek Zboril and Jiří Tucek (University of Palacky, Olomouc, Czech). For the XRD data, I would like to thank Christina Papachristodoulou (University of Ioannina) and Maria Baikousi for the Raman spectra (University of Ioannina). Special thanks to Angeliki Lekatou and Alexandros Karatzalis (University of Ioannina) for providing the tin-lead alloy as well as all members of the Ceramics and Composites Laboratory (University of Ioannina).

I would like to thank Professor R.J. Dwayne Miller of the Center for Free Electron Laser Science (CFEL) of Deutsches Elektronen Synchrotron (DESY), Max Plank Institute of Hamburg for giving me the opportunity to work with his research group. I also owe many thanks to Daniel Badali, Gaston Corthey, Khalid Siddiqui, Stuart Hayes and Wesley Robertson for helping me with receiving and evaluating the TEM data, with spelling corrections and for the scientific advice during my Dissertation.

Finally, I would especially like to thank my beautiful wife Elli for being always there for me, my mother Maria, my father Kostas, my brothers Fontas and Giorgos, Ioannis, Victoria, Marina, Orfeas, Pakita and Hara for their love, constant support, inspiration and faith in me.

Andreas K. Rossos

Dedicated to my wife Elli,

my parents and my brothers

CONTENTS

A. INTRODUCTION.....18

Introduction.....18

Motivation-Scope.....21

B. THEORETICAL PART.....25

B1. Carbon.....27

B1.1 Allotropic carbon forms.....27

B1.2 Fullerenes.....28

B2. Carbon Nanotubes.....29

B2.1 Introduction - History.....29

B2.2 Structure – types of carbon nanotubes.....29

B2.3 Single Wall Carbon Nanotubes (SWNTs).....30

B2.4 Multi Wall Carbon Nanotubes (MWNTs).....32

B2.5 Synthetic methods.....32

B2.6 Cleaning-methods.....35

B2.7 Properties of Carbon Nanotubes.....35

B2.8 Applications.....38

B2.9 Chemical modification of Carbon Nanotubes.....41

B3. Nanowires.....44

B3.1 General.....44

B3.2 Synthetic methods.....45

B3.3 Properties.....46

B3.4 Applications of Nanowires.....48

B4. Carbon nanotubes encapsulating nanowires and nanorods.....51

B4.1 Carbon nanotubes encapsulating superconducting Tin-nanowires.....52

B4.2 Carbon nanotubes encapsulating Sn-Pb nanowires……53

B5. Nanostructured magnetic materials……54

B6. Introduction-Physical properties of the Mn-Bi alloy……59

B7. Graphene oxide (GO)……61

B8. Prussian-Blue Analogues……67

B9. Langmuir–Blodgett Technique……71

B9.1 Context……71

B9.2 Theory……71

B10. Characterization Techniques……83

B10.1 X-Ray Diffraction (XRD)……83

B10.2 Raman Spectroscopy……84

B10.3 Thermal Analysis……87

B10.4 Scanning Electron Microscopy (SEM)……89

B10.5 Transmission Electron Microscopy (TEM)……90

B10.6 Mössbauer Spectroscopy……92

B10.7 Superconducting quantum interference device (SQUID)……96

B10.8 Vibrating Sample Magnetometer (VSM)……97

B10.9 Infrared Spectroscopy (IR)……99

B10.10 Ultraviolet Spectroscopy (UV-Vis)……101

B10.11 X-ray photoelectron spectroscopy (XPS)……103

C. EXPERIMENTAL PART……107

C1. Synthesis of carbon nanotubes encapsulating super-conducting tin nanowires (Sn@CNTs) using the CCVD method……109

C1.1 Chemical Reagents and apparatus……109

C1.2 Experimental procedure……109

C1.3 Purification of Sn@CNTs samples……110

C2. Synthesis of carbon nanotubes encapsulating Tin-Lead nanowires (SnPb@CNTs) using the CCVD method.....111

C2.1 Chemical reagents and apparatus.....111

C2.2 Experimental procedure.....111

C2.3 Sodium Chloride (NaCl) removal and purification of SnPb@CNTs.....112

C3. Synthesis of carbon nanotubes encapsulating Manganese- Bismuth (Mn-Bi) nanorods (MnBi@CNTs) using the CCVD method.....113

C3.1 Chemical reagents and apparatus.....113

C3.2 Synthesis of Mn-Bi alloy.....113

C3.3 Experimental procedure.....114

C3.4 Sodium Chloride (NaCl) removal and purification of MnBi@CNTs.....115

C4. Synthesis of 'Kish' Graphene Oxide monolayers using the Langmuir-Blodgett (LB) technique.....116

C4.1 Chemical reagents and apparatus.....116

C4.2 Pristine 'Kish' graphite.....116

C4.3 Preparation of 'Kish' Graphene Oxide.....117

C4.4 Deposition and formation of 'Kish' GO monolayers using the LB.....118

C4.5 Evaluation of the LB isotherms.....119

C5. Development of low-dimensional Prussian-Blue Analogues using the 'inverted' LB method.....120

C5.1 Chemical reagents and apparatus.....120

C5.2 Experimental procedure.....120

C5.3 Evaluation of the LB isotherms.....121

C6. Experimental setup of the characterization techniques-specimen preparation.....122

D. RESULTS AND DISCUSSION.....126

D1. Carbon nanotubes encapsulating superconducting tin nanowires (Sn@CNTs).....128

D2. Carbon nanotubes encapsulating Tin-Lead nanowires (SnPb@CNTs).....138

D3. Synthesis of carbon nanotubes encapsulating Manganese- Bismuth (Mn-Bi) nanorods (MnBi@CNTs).....153

D4. Development of 'Kish' Graphene Oxide monolayers using the Langmuir-Blodgett (LB) technique.....164

D5. Development of low-dimensional Prussian-Blue Analogues using the 'inverted' LB method.....177

E. APPENDIX.....185

F. CONCLUSIONS-FUTURE PLANS.....193

G. BIBLIOGRAPHY.....199

H. ABSTRACT.....218

Introduction

The constantly increasing need for novel materials and systems possessing new intriguing properties has led the scientific community worldwide to design and develop new low-dimensional materials based on metals, oxides, nano-carbons and other nano-materials. In this way, new hybrid materials have been formed which offer interesting properties and applications. Towards this direction, Dr. Sumio Iijima's research group discovered carbon nanotubes while they were conducting experiments on fullerenes. This discovery was one of the most significant discoveries in the field of nano-materials.

Carbon nanotubes state one allotropic form of carbon, along with diamond and graphite. They exhibit unique properties which derive from the combination of their structural, geometric and topological characteristics. Some of them are their fine electric properties, their excellent mechanical durability, high bending tension, elasticity, low density, high thermal conductivity and the relative inert chemical behavior which they show. These interesting properties render them to be suitable and ideal materials in a variety of applications such as light sources, in polymers of high durability and low weight, as nano-electrodes and as hydrogen storage tanks.

Another fascinating category of materials is nanowires. They are nanostructures with diameter of the order of a nanometer (10^{-9}m) and since the length/diameter ratio is 1000 or more they are usually referred as 1-D materials. Because of this, they offer some important properties, such as lower conductivity as compared to the bulk material, decreased magnetic resistance, remarkable thermal stability and optical properties leading to a variety of potential applications such as electronics, optical-electronic devices, nano-electronic devices, as additives in advanced composite materials, as magnetic information storage media, in energy storage devices, in lithium batteries and as nanowires sensors.

One of the most significant applications of carbon nanotubes is their use as a matrix to form nanowires. This can be accomplished by inserting metals inside carbon nanotubes, thus allowing them to improve their conductive, magnetic, electronic and mechanical properties, while the formation of novel hybrid nanostructured systems is also possible. Therefore, by the use of Catalytic Chemical Vapor Deposition method and depending on the catalytic substrate which is used every time, metallic, semi-conductive, insulating, super-conductive or magnetic nanowires can be formed inside carbon nanotubes. The major advantage of carbon nanotubes encapsulating nanowires is that the latter are being protected from corrosion.

Another also very intriguing field of science is a popular derivative of the newly discovered graphene, the so-called *graphene (or graphite) oxide*, which is formed after chemical treatment of graphite with strong acids. Graphene oxide's structure is composed by the same hexagonal graphitic lattice as in the case of graphene and contains mainly hydroxyl-, epoxy- and carboxyl-groups which attribute in turn a strong hydrophilic behavior.

Therefore, graphene oxide has the potential to form homogeneous aqueous suspensions and take part in a variety of reactions so as to be further chemically modified to form novel hybrid materials.

Additionally, one of the aspects of modern materials science that has been captivating scientific interest in the last decade are low-dimensionality systems, mostly because of their physical, chemical and biological properties which are widely different from their bulk material. Also, the lower dimensionality – e.g. thin film - form offers a convenient platform for device application. Towards the direction of forming 2D materials, the properties of Prussian Blue analogues (mixed valence poly-cyanides, PBA) of low dimensionality are so far unexplored. The incorporation of Prussian Blue Analogues into tangible real life applications relies on a control of their crystal size, shape and morphology.

The main subject of this dissertation was the design, development, characterization and study of novel low-dimensional hybrid materials based on carbon. Towards this aim, carbon nanotubes encapsulating Tin and Tin-Lead nanowires and Manganese-Bismuth nanorods were formed using a conventional Catalytic Chemical Vapor Deposition method. The products were examined by the use of a combination of analytical techniques such as XRD, Raman spectroscopy, DTA/TG, TEM, SEM etc. Additionally, a new graphene oxide form was prepared using for the first time as pristine material *Kish graphite* using the Staudenmaier method and monolayers were formed using the Langmuir-Blodgett technique. The produced graphene oxide was examined by the use of XRD, Raman and FT-IR spectroscopies while the produced thin films were examined by TEM microscopy. Finally a new low-dimensional PBA was produced using a Langmuir-Blodgett trough during a controllable on-surface reaction and studied using the Langmuir-Blodgett technique and TEM. The success of the reaction was identified by XPS spectroscopy and HRTEM/EDX/SAED results.

The first part of the dissertation is the theoretical part, where basic information concerning carbon and its derivatives, carbon nanotubes, nanowires (properties and applications), graphene oxide and Prussian Blue Analogues are presented. At the end of this part a detailed background of all the analytical techniques that were used to characterize and study the produced materials is exhibited.

The next chapter is the experimental part. In this part, all the reagents, the experimental procedures and the experimental set-ups for each series of experiments are mentioned in details and explained.

The main part of the dissertation is the results and the discussion section. The first three parts refer to the hybrid nanowires/nanorods and mainly in their detailed structural, morphological and physicochemical characterization. Much attention was given in the part of Tin and Tin-Lead nanowires due to the fact that they constitute a new category of hybrid 1D materials that were for the first time constructed. Following this, a detailed 'Kish graphene oxide' study on the deposited with the LB technique monomolecular films was performed while the characterization of the produced pristine graphene oxide form (using a

modified Staudenmaier method) can also be found. Finally, Prussian Blue Analogues part begins with the XPS data that confirm the successful on-surface reaction and is followed by a detailed study of the L-B isotherms and is completed with a TEM and electron diffraction study as well as with a comprehensive stability examination.

Finally, the dissertation is concluded by stating the basic results and conclusions of the whole study along with prospects and suggestions for potential future work.

Motivation-Scope

The major aim of this dissertation was the design and the production of novel nano-structured hybrid materials based on carbon. The term 'nanoscale' usually refers to structures with a length scale that is applicable to nanotechnology, usually 1–100 nanometers. The nanoscale is the point below which the properties of a material depend on the geometry of it (thickness, width) and that in these low dimensions, can have a drastic effect on quantized states, and therefore, on the properties of a material. In this concept, carbon nanotubes have a wide range of uses, from composites to use in vehicles and sports equipment to integrated circuits for electronic components and energy storage devices. Additionally, nanowires form strong candidates towards the direction of incorporating them into nanotubes, allowing their reinforcement with some of the unique properties that they exhibit, such as magnetic, thermal and optical properties. By the use of bottom-up synthetic methods, the control of the products in nanoscale is possible, aiming at the same time at producing novel hybrid nano-materials.

Furthermore, graphene oxide states another intriguing carbon-based material which due to its hydrophilic character can be combined with other compounds and materials to form novel hybrid products. Another goal of this dissertation was to study a new GO form that was created using for the first time 'Kish' graphite as pristine matrix and subsequent the formation of monolayer films using a modified Langmuir-Blodgett technique. Finally, the formation of 2D Prussian Blue Analogues was also attempted using a controllable on-surface reaction with the help of the Langmuir-Blodgett apparatus. For the time being, 2D materials remain from a morphological point of view bulky powders or crystals. Although they possess intriguing properties, Prussian Blue analogues (mixed valence poly-cyanides) of low dimensionality are so far unstudied. The incorporation of Prussian Blue Analogues into tangible real life applications relies on a control and tailoring of properties like crystal size, shape and morphology, rendering them at the same time interesting materials for electron diffraction studies.

The role of pure metals and their corresponding compounds as both catalyst and source for in-situ growth of filled carbon nanotubes is explored in this dissertation. What has been done so far was extended, presenting a simple method which yields carbon nanotubes encapsulating single crystalline metallic tin nanowires by employing the conventional method of Catalytic Chemical Vapor Deposition (CCVD) over different tin catalysts. These protected tin-nanowires are intended to provide an ideal system in order to study and investigate their physical and chemical properties that are significant apart from their implementation as nano-building blocks in nano-scale devices. Acetylene gas was chosen as a carbon source due to its high reactivity as compared to other hydrocarbon gases (methane, ethane and ethylene). As catalysts for the growth of carbon nanotubes we employed metallic tin (Sn) and its two common oxides namely SnO and SnO_2. The corresponding materials are mentioned as Sn@CNTs. The effects of acetylene flow time on the final products, as well as that of different temperatures of catalytic chemical deposition,

were investigated. Various analytical techniques including Transmission Electron Microscopy (TEM), X-Ray Diffraction (XRD), Raman and Mössbauer spectroscopy were used to characterize the final composite materials.

As mentioned before, the idea of *in-situ* growth of filled carbon nanotubes is a field of great significance and has been a case of extended study over the past decades. The simple method of Catalytic Chemical Vapor Deposition (CCVD) is also applied to yield carbon nanotubes encapsulating single crystalline metallic tin nanowires over SnPb/NaCl catalysts. In the second part of the dissertation, an alloy tin-lead was used as a catalyst, mixed with NaCl, in order to grow carbon nanotubes inside of which SnPb nanowires would have been encapsulated, and study their fundamental properties. The method which was used to produce tin-lead carbon nanotubes was CCVD, a procedure performed for the first time for this kind of products. It is noteworthy that only Tin acts as a catalyst, while lead is inactive. Sodium chloride was used as substrate for the immobilization (impregnation) of the SnPb alloy, since it is also inactive and can be easily removed with water. Lead was chosen due to its higher critical temperature (Tc) compared to tin, since it is expected to increase the critical temperature of the alloy. The critical temperature of lead is 7.05 K and that of tin 3.7 K. It should be reminded that critical temperature is the temperature below which a material acts as a super-conductor. To achieve critical temperature of tin, pumping over liquid Helium atmosphere is required, while, in order to realize that for lead only dipping in liquid Helium is required. The final SnPb@CNTs products that were produced using the CCVD method on SnPb as a catalytic substrate and for different growth times they were characterized using various characterization techniques, such as X-Ray Diffraction (XRD), Thermal Analysis (DTA/TGA), Raman Spectroscopy, Mössbauer Spectroscopy, Transmission Electron Microscopy (TEM), Scanning Electron Microscopy (SEM) and Superconducting Quantum Interference Device (SQUID).

In the third part of the dissertation an alloy MnBi was for the first time incorporated in carbon nanotubes using the CCVD method at different temperatures and for various acetylene flow times. This manganese alloy was chosen because it exhibits interesting magnetic properties (it is paramagnetic but while applying external magnetic field it exhibits macroscopically magnetism) and because of the fact that its melting point is lower than the used nanotube growth temperatures (700°C or 800°C). Therefore, bismuth (Bi) was used, having Tm= 271.5^{o}C, as the second metal in the alloy, allowing in this way the lowering of its melting point, due to the fact that the melting point of Manganese is relatively high (1246°C). Furthermore, during the CCVD process and apart from the desired products, Bismuth forms oxides during the formation of carbon nanotubes, which can be easily removed with mild acid treatment. The final products, which were produced by the CCVD method, using MnBi alloy as catalyst, in different growth times were characterized using various characterization techniques, such as X-Ray Diffraction (XRD), Thermal Analysis (DTA/TGA), Raman Spectroscopy, Scanning Electron Microscopy (SEM) and Transmission Electron Microscopy (TEM).

The fourth part of the dissertation was a study on a new graphene oxide form. Graphite oxide possesses a rich pallet of properties due to the hydrophilic character that it exhibits and which allows it to form stable and homogeneous aqueous solutions that can be easily chemically modified to give hybrid materials. Here for the first time, graphene oxide was prepared using 'Kish' graphite. Beginning from 'Kish' graphite flakes and using the Staudenmaier synthetic method graphene oxide was produced at high yield. A complete Langmuir-Blodgett study was performed, using a trough provided by NIMA technologies for different concentrations and volumes of graphene oxide which would be gently injected on the water surface to form a mono-layer. Afterwards, depositions on copper grids were accomplished allowing us to obtain the formed thin film and examine it using a TEM microscope.

In the final part of the dissertation, a new low-dimensional system based on Prussian Blue Analogues (PBAs) was formed using a modified Langmuir-Schaefer technique where PBA is synthesized from precursors through an on-surface reaction which takes place on a metal chloride sub-phase. In this study, a new low-dimensional system was formed by combining an air-water interface reaction and a Langmuir-Schaefer technique. Atomically thin 2D Prussian blue analogues were synthesized from tetracyanide building blocks precursors by reacting with a metal chloride sub-phase in a self-limited reaction. Here, for the first time a number of tests were performed by the use of the so called "inverted" LB technique. As a precursor, potassium tetra-cyano platinate(II) hydrate was used while copper chloride was filled the Langmuir-Blodgett trough as an aqueous solution. The idea was the following: the tetra-cyanide would be 'softly injected' on the surface of the sub-phase ($CuCl_2$) leading to a superficial ion-substitution reaction which in turn would finally give the PBA as a thin monolayer on the surface of the LB-trough. A detailed study of the L-B isotherms was performed while XPS, TEM and electron diffraction studies shed light to the structural characteristics of the produced low-dimensional PBAs.

Part B: Theoretical

B1. Carbon

Carbon, either as free element or in chemical compounds, is one of the most common elements in nature. Carbon is so unique compared to other elements because of its inner electronic structure allowing it to form many different compounds. Having four valence electrons (the electronic structure is $1s^2$, $2s^2$, $2p^2$), allows carbon to unite with either other atoms of elements such as H, O, N, S, P or with other carbon atoms to form carbon chains the length of which can reach billions of carbon atoms (e.g. DNA). Due to its small atomic radius, carbon forms stable covalent bonds (simple, double, triple) which with combination of other elements' atoms leads to the formation of organic molecules with large number of moieties[2].

B1.1 Allotropic carbon forms

Carbon has the ability to unite in different ways with other carbon atoms to form structures with different properties. Till the 80's the two allotropic structures of carbon were graphite and diamond, two entirely different structures due to carbon's different hybridization. When the four valence electrons are equally shared (sp^3 hybridization) the powerfully isotropic diamond is formed (Figure 1a) a crystalline, transparent, and hard material which is a bad electricity conductor and the unusual carbon form. But when only three electrons are equally shared (sp^2 hybridization) and the fourth is delocalized we have the formation of graphite (Figure B1.1) which is the most common carbon form. Graphite is soft, black and is a fine conductor of electricity.

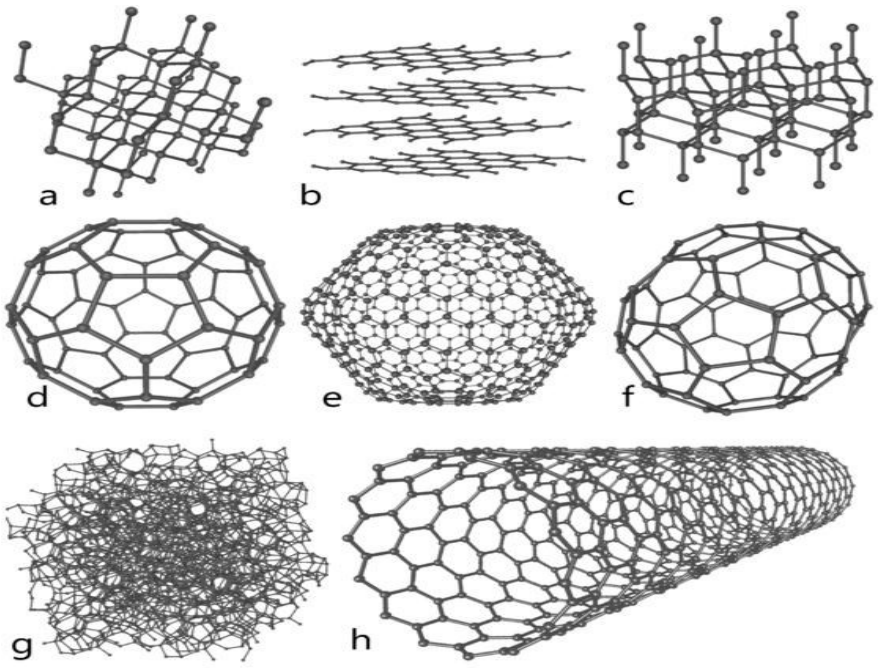

a) Diamond, b) Graphite, c) Lonsdaleite, d) C60 (Fullerene), e) C540 (Fullerene), f) C70 (Fullerene), g) Amorphous carbon, h) single-walled carbon nanotube

Figure B1.1: *Allotropic forms of carbon*[1]

B1.2 Fullerenes

Fullerenes are allotropic carbon structures (such as graphite and diamond) having symmetric spheroidal structure and molecular formulas C_{28},C_{32}, C_{50}, C_{60}, C_{70}, C_{240} and C_{540} with C_{60} being the most common one. The first fullerene to have been ever discovered was Buckminster fullerene (C_{60}), which was formed in 1985 by Richard Smalley, Robert Curl, James Heath, Sean O'Brien, and Harold Kroto in Rice University (Chemistry Nobel Price 1996) and was based on a laser pulse evaporating graphite shapes[1].

In general, they are stable molecules and demand high temperatures (1000°C) so as for the carbon bonds to be disrupted. Their surface consists of five- or six-membered carbon rings placed in each corner exactly like a football ball. The name Fullerenes derives from the name of the architect Buckminster Fuller who would be used to construct buildings with these shapes[1].

The chemical properties of the fullerenes are very interesting since they can lead to various derivatives which may contain metal atoms, ions, complexes etc., after their chemical modification. Fullerenes find diverse applications in many areas such as in optical devices, LEDs (light emitting diodes), photovoltaic cells, thermo-tropic liquid crystals, chemical sensors, gas separating devices, insulating materials, batteries, catalysts, polymers, information storage means, medicine carriers inside the human organism, photo-decomposition of DNA, photo-dynamic treatment of cancer, nuclear medicine and many others[5]. The significant disadvantage though would be the fact that fullerenes are still too expensive to produce which prevents them from becoming highly used[1,3,4,5]

B2. Carbon Nanotubes

B2.1 Introduction - History

Carbon nanotubes are molecular tubes made of graphite closed on every edge, consisting of five-membered rings and can be either multi-layer with one central tube surrounded by one or more graphite layers or single layer, where there is only one tube and no additional graphite layers. Carbon nanotubes, with length/diameter ratio up to 132.000.000:1, have been formed[10]. Their discovery was made by Radushkevich and Lukyanovich in 1952 when they published in a Russian scientific magazine, clear images of 50 nano-diametric carbon tubes. Due to the Cold War their discovery was unnoticed.

Carbon nanotubes had been formed using different techniques since the 70's but did not attract much interest as their structures exhibited defects. As a result they did not seem to have interesting properties. In 1991 though, Sumio Iijima while trying to form fullerenes observed that nanotubes were formed, which at least two layers of outer diameter 3-30 mm. Two years later with Bethume they discovered single-wall nanotubes while in 1996 Smalley's group composed for the first time bundles of aligned single-wall nanotubes[11].

B2.2 Structure – types of carbon nanotubes

The structure of carbon nanotubes can be resembled to bent leaves of graphite which form one or more tubes. The diameter ranges between 1 and 3 nm and length 3-50 μm. Therefore, it is considered to be a one-dimensional nanostructure, while the ratio length to diameter might overpass 10000. The C-C bond length is 5.44 Å and their density varies from 0.8-5.2 g/cm^3. There are two basic carbon nanotubes types, Single Wall Carbon Nanotubes (SWNTs) and Multi Wall Carbon Nanotubes (MWNTs) as it is seen in Figures B2.1 and B2.2.

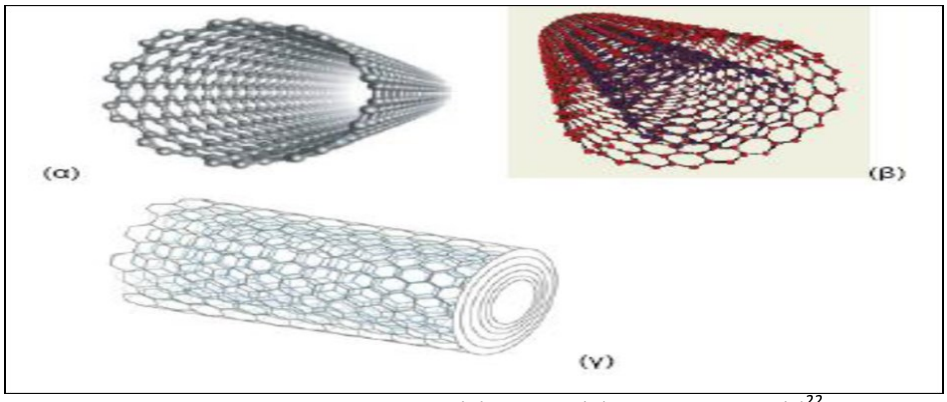

Figure B2.1: *Carbon Nanotube types: Single (a), double (b) and Multi-wall (c)*[22]

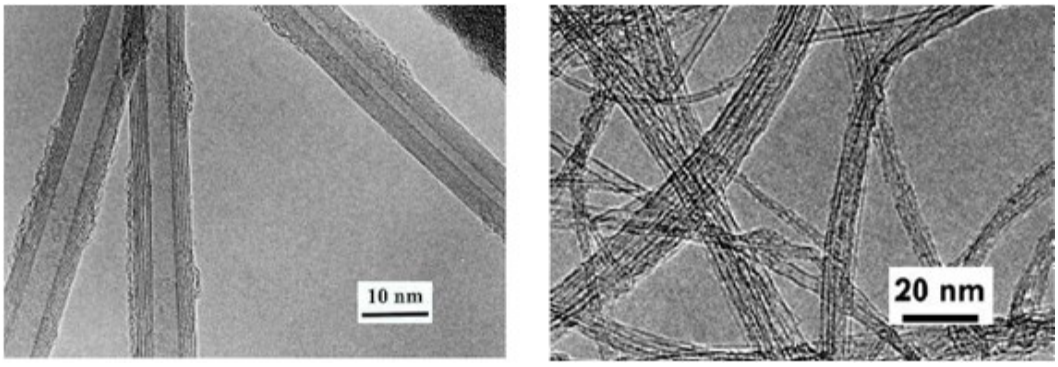

Figure B2.2: *Carbon Nanotube types: Single (a), double (b) and Multi-wall (c), TEM images of single (left) and multi-wall (right) carbon nanotubes*[6]

B2.3 Single Wall Carbon Nanotubes (SWNTs)

The unique properties of SWNTs is a direct result of their structure which consists of C-C bonds resembling the ones of graphite rather than the ones of diamond since they exhibit sp^2 hybridization but their structure is different than that of graphite due to their high curvature. The endogenous durability of the carbon – carbon sp^2 bonds as well as the special structure of nanotubes result in high mechanical durability and a large Young coefficient (Young coefficient values close to 1000 GPa have been predicted or estimated for individual nanotubes, which is 50 times larger than the value for steel). Depending on their geometrical structure they can exhibit metallic or semi-conductive behavior, as slight changes in the geometrical formation can lead to significant changes as far as electronic structure is concerned.

Table B1.1. *Comparison of Young modulus of carbon nanotubes and conventional materials*[14]

Material	Young modulus (GPa)
SWNTs	1054
MWNTs	1200
Steel	208
Epoxy glue	3.5
Wood	16

As seen in Figure B2.3, a SWNT is a homogeneous cylinder having diameter in the scale of nanometers, which can be depicted as wrapped grapheme sheet. The structure of each nanotube can be defined by the diameter and the relative orientation of the carbon hexagons in relevance with the axis of the tube.

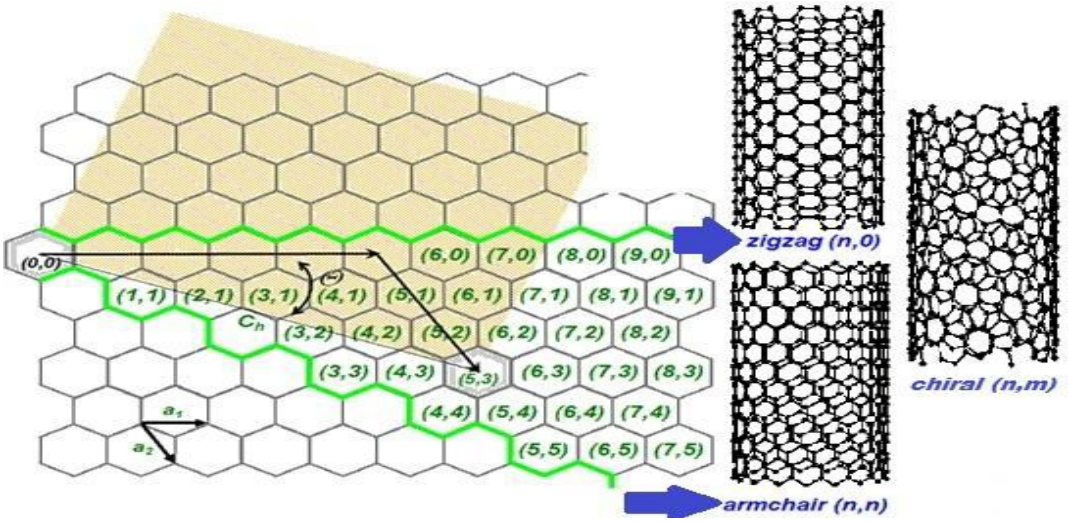

Figure B2.3: *Schematic representation of SWNT's structures*[12]

As a result, every SWNT can be uniquely determined by two indicators n and m, which are two integers that define reticular vector C. The two indicators are connected with the two unit vectors via the function: $\mathbf{C = na_1 + ma_2}$**.** The diameter of the nanotube can be calculated from the indicators n, m according to the following expression: $\mathbf{d = a_0 \bullet (m^2 + mn + n^2)^{1/2}/\pi}$**,** in which a_0 is the atomic lattice constant (=0.246nm). The same way, the Θ angle can be calculated (as seen in Figure 3 using the relation: $\mathbf{\tan \Theta = (n \sqrt{3}) / (2m + m)}$.

Three SWNTs structures can be defined: armchair, zig-zag and chiral. Those symmetries express the orientation of the imaginary initial graphitic lattice to the tube axis.

- The armchair structure of nanotubes which is formed when n=m and $\Theta=30^o$.
- The zig-zag structure of nanotubes which is formed when m=0 and $\Theta=0^o$. These nanotubes are called zig-zag due to the formation created by the carbon atoms.
- The chiral structure of nanotubes which is formed when n≠m and m≠0 and present a winding angle from 0° to 30° to the T vector (which is defined along the SWNT and vertically to C). These nanotubes have such structure so that their reflecting image cannot be anyway identified with the initial one.

The graphitic cylinders for the three kinds of SWNTs result in hemispheric edges. This morphology derives from the pentagon confinement in the hexagonal graphitic lattice during the formation of SWNTs[12,13].

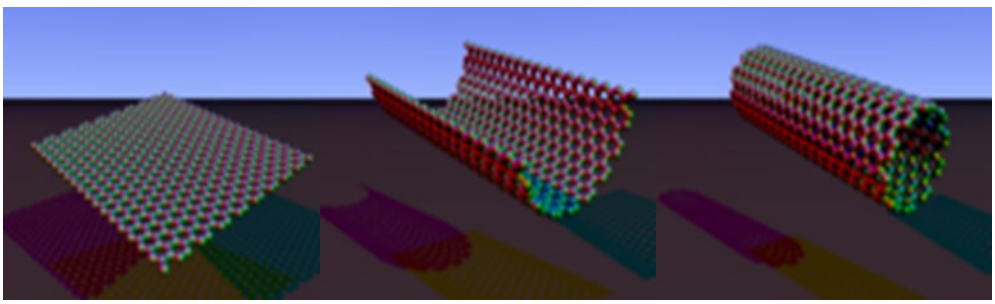

Figure B2.4: *Stage formation of a SWCNT*[13]

B2.4 Multi Wall Carbon Nanotubes (MWNTs)

Multi wall carbon nanotubes (MWNTs) are series of single SWNTs one inside another holding each other with Van der Waals forces (Figure B2.5). There are two models that can describe the structure of MWNTs. The one is "Russian Doll" model where graphite leaves are placed in concentric cylinders. The distance between the levels of these multiple coaxial aligned cylinders ranges from 0.34 nm to 0.39 nm and decreases while the diameter of each tube rises. This distance is slightly larger than the one the graphite levels (0.335 nm). In the other model which is called "Parchment" one single graphite sheet wounds around itself. MWNTs have diameters that range from 2.5 nm to 80 nm and lengths from a few tens of nm to some μm. As in SWNTs, they exhibit a length/diameter ratio from 30 to 3000 approximately. In the edges of the graphite cylinders there are no free bonds, but they are covered by hemispherical structures instead[1,11].

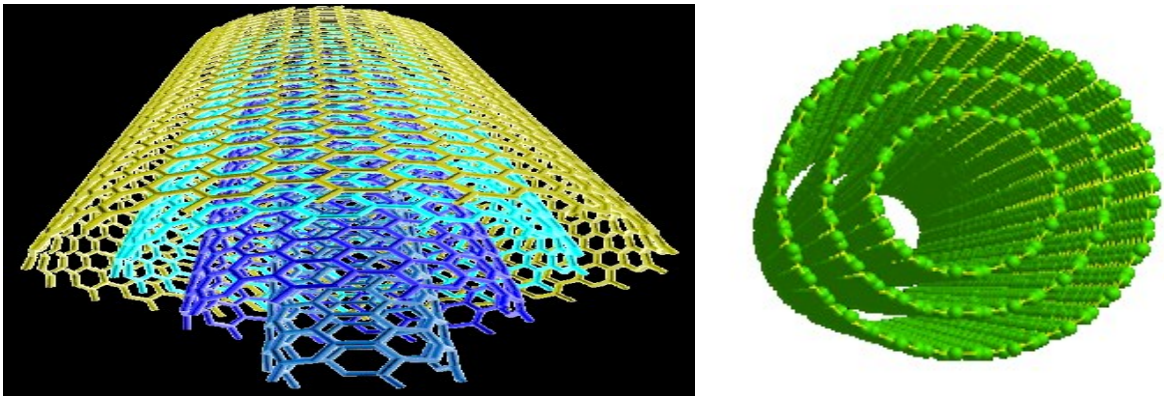

Figure B2.5: *Representation of the MWNT structure*[11]

B2.5 Synthetic methods

The technique that is going to be used to form carbon nanotubes defines completely the characteristics of the product, whether it is going to be single or multi-wall, its dimensions, geometry, chirality, purity, etc. The three most commonly used techniques are: electric arc discharge, laser ablation and chemical vapor deposition[1].

Electric Arc Discharge

The first macroscopic production of carbon nanotubes was made by NEC-company in 1992. The method that was used is called electric arc discharge (Figure B2.6) and produces carbon nanotubes of the highest quality.

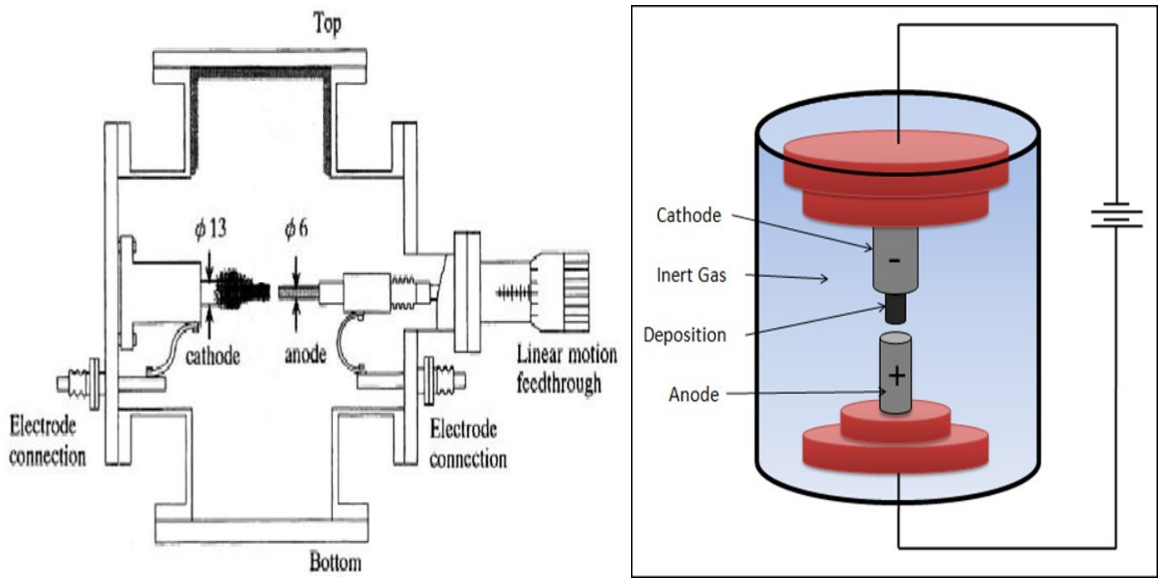

Figure B2.6: *Set-up of the arc discharge*[7]

Arc Discharge method includes the passing of 50 A current through a graphite pin (two graphite electrodes) in Helium or Hydrogen atmosphere. Because of the high temperatures that are caused by the discharge the graphite evaporates, a part of which is condensed on the walls of the reaction beaker or on the cathode. The precipitate on the cathode is responsible for the formation of carbon nanotubes. Single wall carbon nanotubes are produced when cobalt, nickel or other metals are added on the anode. The yield of this method exceeds 30% and produces equally SWNTs and MWNTs (Figure B2.7)[7,11].

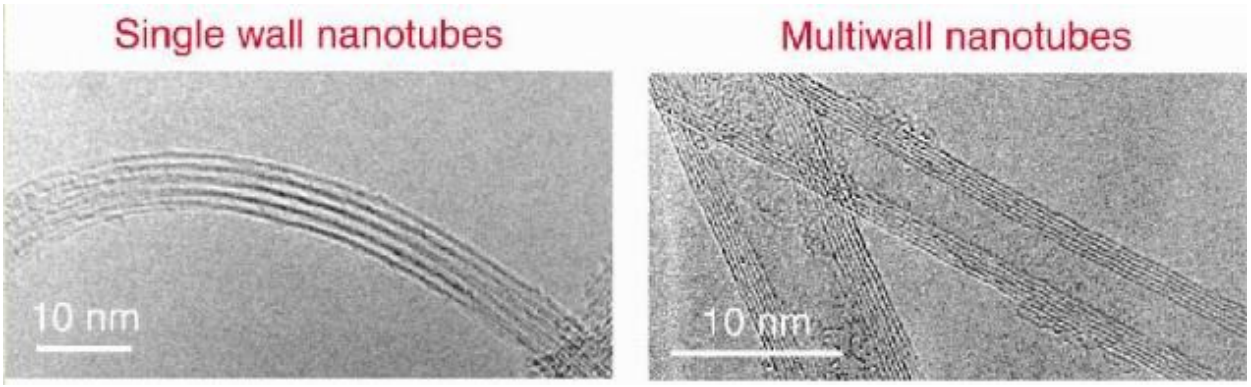

Figure B2.7: *Nanotubes produced by the arc discharge technique*[7]

Laser Ablation

In the laser ablation technique a powerful laser beam is usually used in order to ablate the graphitic target which has usually also some metal addition (Figure B2.8). Continuous or pulse laser is used in order to atomize the graphitic target in an oven at 1200°C. The oven is full of Helium or Argon so that the pressure would be 500 Tor. Atoms leave carbon and the carbon is reconstructed creating various formations such as carbon nanotubes. In order to

produce single wall carbon nanotubes the graphitic target is soaked cobalt and nickel as catalysts. Afterwards, the condensed material is collected on a water-cooled target. This method allows better nanotube control than the arc discharge. With the laser ablation we can produce SWNTs of high quality. Together with the previous technique they can be considered as high temperature (>1000°C) and short reaction time (μs-ms) techniques[1,15].

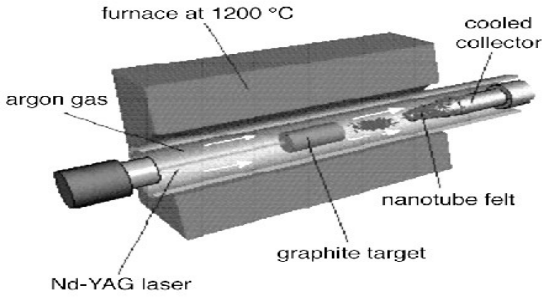

Figure B2.8: *Schematic representation of laser ablation procedure*[7]

Catalytic Chemical Vapor Deposition (CCVD)

The CCVD method (Figure B2.9) includes a substrate of metallic catalysts, usually nickel, cobalt or iron or their combination, which is heated at 500-1000°C, while two different gases are canalized though the reactor, one carrier gas such as ammonia, nitrogen or hydrogen and one organic gas or steams such as ethanol, methanol, ethylene, acetylene etc. The hydrocarbon is disintegrated with the assistance of the catalyst and the carbon atoms are diluted into the catalytic metal. The expulsion of carbon from the blasé in carbon metal particle leads to the formation of a tube-like carbon solid which exhibits sp^2 structure.

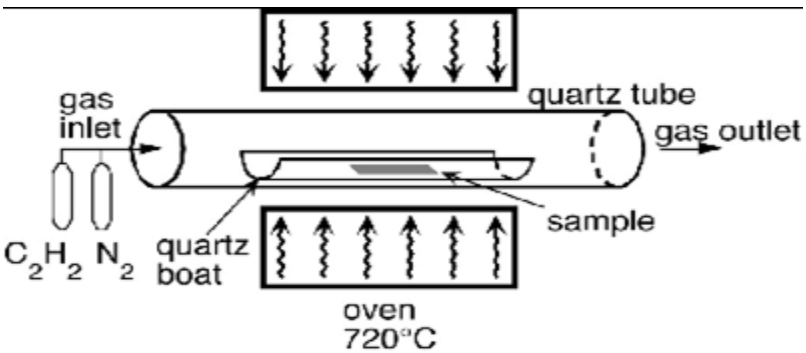

Figure B2.9: *Experimental setup of CCVD*[7]

The quality of the carbon nanotubes produced using this method is poorer than the previous two. Nevertheless, larger scale production is possible. The main parameters that affect the nanotube growth using the CCVD method are the kind of hydrocarbon, the catalyst and the thermal cracking temperature. The products can be SWNTs or MWNTs depending on the method conditions. At low temperatures (500-850°C) and using nickel as catalyst, cobalt or iron, MWNTs are formed while at higher temperatures (990-1200°C)

SWNTs are formed, showing that they exhibit formation energy due to their lower diameter, which leads to high curvature and high distortion energy[1,11].

When the interaction between the catalyst and the substrate is weak (the metal forms acute angle with the substrate), then the substrate lifts while drifted by the growing nanotube and continues to contribute to the nanotube growth from its top. This growth mechanism is known as "tip growth model" (Figure B2.10a). When the interaction between the catalyst and the substrate is strong (the metal forms obtuse angle with the substrate), then carbon nanotubes are formed having the metal particle stabilized on their base. This growth mechanism is called "base growth model" (Figure B2.10b)[16].

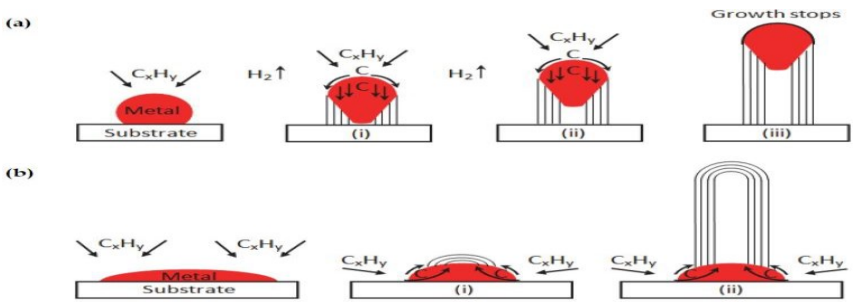

Figure B2.10: *Nanotubes growth mechanisms (a)"tip growth model", (b)"base growth model"*[16]

The rapid development of CCVD methods which has been made since 1998 has led to the production of high quality carbon nanotubes, consisting of single wall, multi wall, aligned, isolated in large volumes, with controlled diameter, controlled length, directly on a substrate or in a massive form[1].

B2.6 Cleaning-methods

The majority of synthetic procedures produce CNTs with various impurities, such as amorphous carbon, graphite-particles, catalyst remains, as well as fullerenes, nano-fibers etc. in the case of using CCVD method, the substrate that was used should be removed. The metallic particles and the fullerenes can be easily removed while graphite and amorphous carbon are more difficult to be removed. For most of the applications, (e.g. electronics) high purity of carbon nanotubes is required. The main issues are, first, the danger of destruction of CNTs by the chemical methods that are used, e.g. geometry change or destruction of the wall crystallinity. The followed procedure is quite complex and usually includes, apart from the physical methods (such as heating, sonication), chemical (strong acid treatment) and physical-chemical procedures such as filtration[19].

B2.7 Properties of Carbon Nanotubes

Electrical Properties

Significant interest is found in the electrical properties of carbon nanotubes due to their many technological applications. The main factor which defines the electrical properties of

are the electrons which are which are space limited. They can move only in the space of the graphite and not in the vertical direction towards the axis of the graphite sheet. Additionally, while its length is much larger than its diameter, the admitted electron states towards the axis direction are many more than the ones at the peripheral.

The finite periphery and the length of the nanotube enter limit conditions which result in distinguished energy levels and the nanotubes present metallic as well as semi-conductive behavior. The relation between n and m is an indicator for whether the nanotube exhibits metallic or semi-conductive behavior. For an (n, m) nanotube, if n-m=3k, where k is an integer, then the nanotube belongs to the metals, when n=m the nanotube is an insulator while in every other case it behaves as a semi-conductor. According to all these, all armchair nanotubes and one third of zig-zag nanotubes are metals. The electrical properties of SWNTs e and MWNTs are similar because the connection of the walls in the MWNTs is very weak. Due to the almost one-dimension electronic structure of metal nanotube the electrons are moving without scattering along its axis, allowing the large current passing with no significant heating. What is more, super-conductivity has been observed only at low temperatures[1,11].

Mechanical Properties

Carbon nanotubes are characterized of high durability because of the sp^2 bonds C-C which are formed between the carbon atoms. A nanotube has a Young modulus 1.2 TPa and maximum durability tension a hundred times larger than the that of steel (250 GPa), while it weighs 6 times less which leads to its heavy weight endurance before it misses. Additionally they are flexible, and can be bent to 90°, while come back to their initial dimensions after mechanical distortion. However, due to their structural disorders those properties are mostly theoretical[1].

Figure B2.11: *Simulation of the initial and final stage of bending a SWNT*[7]

Thermal Properties

Carbon nanotubes exhibit thermal conductivity higher than that of diamond and graphite (2000W/mK). Specifically a MWNT has thermal conductivity higher than 3000 W/mK. Their characteristic would be the high thermal stability that they exhibit and which in air

atmosphere will be 800°C approximately for a SWNT and 650°C approximately for the MWNTs when they are in pure form[1].

Optical Properties

Carbon nanotubes can either absorb or scatter the light but they can also fluorescent depending on their diameter and chirality. Their optical properties can be affected by the length, with increase of which we have amplifying of the ability to absorb light as well as the fluorescence in the nearby infra-red spectrum[17].

Chemical Properties

The chemical inertia that is exhibited by the carbon nanotubes is caused by the dislocated electrons in the graphitic cylinder and by the fact that nanotubes are usually held together in a parallel way in reams, interacting with each other via Van der Waals forces. Therefore, their available surface for several applications is decreasing. Another factor which contributes to the chemical stability of carbon nanotubes would be their extremely smooth surface. The chemical modification of their surface by binding e.g. drastic groups, leads to an increase of reactivity.

The catalytic properties of carbon nanotubes consist of successive mass and heat transfer phenomena between the catalyst particles and the reagents. The small size of the nanotubes helps in minimizing the time needed for completing these transfer phenomena resulting in better catalytic reaction rate control and product selectivity[1].

Table B2.2. *Comparison of carbon nanotubes' properties with other materials*[1]

	Young modulus (GPa)	**Max tension durability σ_{TS}**	**Thermal conductivity (W/mK)**	**Special resistance (μΩ/cm)**
SWNT	**≈1x10^3**	**≈60x10^3**	**1750-5800**	**1**
MWNT	**≈1-1.2x10^3**	**≈3.71±0.5x10^3***	**>3000**	**1**
Diamond	**≈1x10^3**	**≈2.8x10^3****	**895-2300*****	**≈1x10^3**
Plain steel AISI-SAE 1020	**205**	**450**	**52**	**18**
Stainless steel 304	**195**	**550**	**15**	**72**
Titanium (commercial form)	**110**	**330-550**	**180**	**43**

* In epoxy resin

**Depending on tension orientation in relation with the crystal it can reach up to 100 GPa.

***The value depends on the type of diamond (type I: 895, type II: 2300)

B2.8 Applications

Due to their fine properties, carbon nanotubes have a wide range of applications, being therefore used to reinforce composite materials with polymer, ceramic or matrix of other type, to form conductive polymers, absorbing materials for cleaning and separating of gases and also in textiles and overlaps (antistatic, conductive, anti-corrosive). They can also be used in Field Transmission Displays – FEDs, which are based on the creation of a powerful electric field for producing electrons[18]. Another application of carbon nanotubes is in the construction of field-effect molecular transistors - FETs but also of the single electron transistors. Additionally they are used as energy storage devices, as electric energy accumulators and as fuel cell materials (catalyst carriers and Hydrogen storage). At last, they are applied in car industry (coatings, components, plastic parts), in defense (materials for durable uniforms, fighting aircrafts, bullet-proof vests) and in medicine (controlled transfer and release of pharmaceutical substances, bio-sensors)[18].

Carbon nanotubes in the form of aggregates are used for:

- Composite materials as reinforcement phase with advanced mechanical properties
- Electro/mechanical evacuators
- High capacity hydrogen storage media

As individual nanotubes they apply as:

- Field emission sources
- Edges (tips) in the transmission electron microscopy (TEM)
- Nano-valves and
- Chemical sensors

Composite materials

Due to their high tension durability, carbon nanotubes are ideal for structural applications. For example, they could be used to reinforce composite materials of high durability and low weight. The main advantage which is expected to be exhibited by using nanotubes in composite materials of a polymer matrix will be the collision durability increase because they will absorb a large energy percentage due to their fine elastic behavior. Other advantages of these composites will be their low density, the increased electric conductivity and better compression behavior[20]. As far as space applications of carbon nanotubes are concerned, NASA has been using them in space-aircraft technology.

Electronic circuits

The smallest complete circuits lead to largest speeds. Therefore, scientific researches aim at lower dimension circuits. One micro-circuit is seen in Figure B2.12. By posing the semi-conductive nanotubes into non-conductive state and applying the right voltage, only metallic CNTs are destroyed and semi-conductive nanotubes network is formed, which are finally transformed into insulators and reverse[21]. The first transistor made of carbon nanotubes was formed by IBM in 2001[21]. Furthermore, due to their high ratio of length to diameter, their stability at high density current and the low electron emission voltage, carbon nanotubes are ideal candidates to use in electronics microscopes, as well as in liquid crystal screens in order to achieve higher efficiency at lower current usage[21].

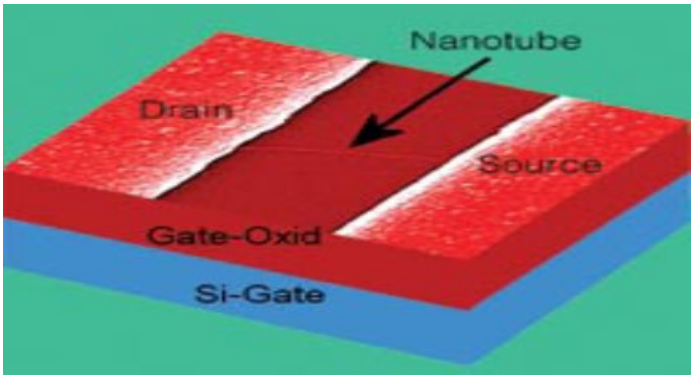

Figure B2.12: *Carbon nanotube transistor*[8]

Medicine and Biology

Since 2002, many researchers have been occupied in uniting carbon nanotubes and DNA molecules as well as nanotube modification with various types of DNA. Specifically, SWCNTs have similar size with DNA, making it possible to hook on the edges of CNTs DNA molecules and other biochemical compounds. The above way enables the nanotubes combined with DNA to be related to DNA decoding, using carbon nanotubes conductivity. Different kinds of DNA have different structures and furthermore different conductivity, so that carbon nanotubes with DNA will repel or attract only specific DNA molecules. Additionally, because of the property above, carbon nanotubes with DNA can be used in advanced therapies with drugs or antibiotics where carbon nanotubes will be the carriers of the pharmaceutical substance and are going to release it only by the time they will have come in contact with the weak cells organism muscles, increasing this way the drug yield and decreasing the healing time[18,22].

Energy Storage

Carbon nanotubes have those characteristics which are desired by a material in order to be used as an electrode in batteries and capacitors, two technologies of constantly increasing significance. Nanotubes exhibit large special are (to the value of $1000m^2/g$),

smooth surface, fine electric conductivity, high chemical stability and most important, their linear geometry makes their surface electrolyte friendly[22,23]. Carbon nanotubes have also found applications in electrodes and fuel cells, where their large thermal conductivity and large special area are used. Furthermore, they are used to store gases and mostly hydrogen. The advantage of hydrogen will be that, as an energy source, water is its burning product. Additionally, hydrogen can be easily re-obtained. So, a system of hydrogen storage is required, satisfying all limitations that deal with its volume and weight. The two most commonly used methods for storage in carbon nanotubes are physical or chemical absorption by them. In the first case, this is done while hydrogen preserves its molecular structure and is attached on the surface via van der Waals interactions. In the second case, atomic hydrogen can form chemical bonds with nanotube carbons. Hydrogen can be stored in nanotubes with several ways: on the inside of theirs, on the surface of the single-fluid or on the external surface of the multi-fluid, between the internal single-fluid surfaces, as well as between nanotubes when they are found in the form of terries. (Figure B2.13)[24]

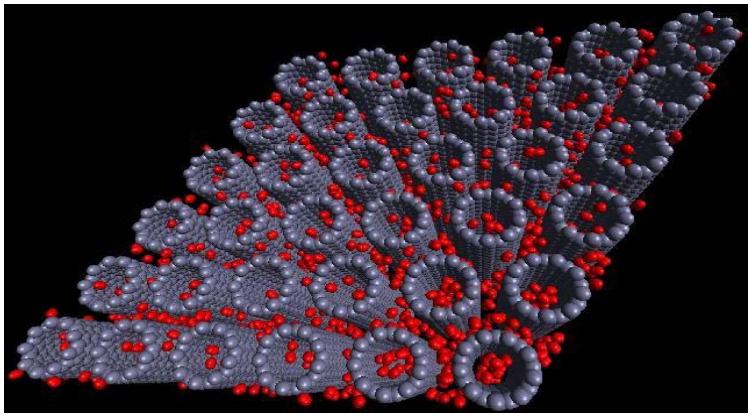

Figure B2.13: *Hydrogen storage in carbon nanotubes*[8]

In the following table some possible applications of carbon nanotubes in the near future are shown, as well as in the following figures (Figure B2.14-B2.15)

Table B2.3. *Future applications of carbon nanotubes*[8]

Future applications of Carbon Nanotubes
Transistors, substitution of Silicon, Nano-capacitors
Quantum computers
Signal reinforcement in cell phones
Artificial muscles
Materials reinforcement in vehicles (spaceships, airplanes, cars), in bullet-proof vests and in tools
Substitution of optical fibers and wires
Space elevators
High sensitivity nano-sensors

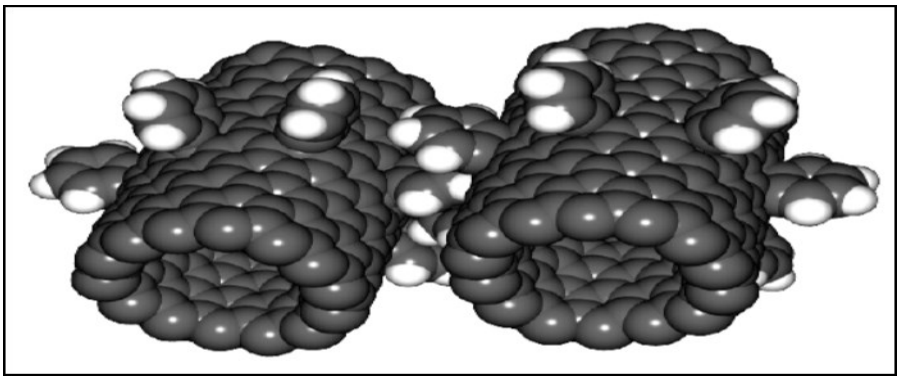

Figure B2.14: *Nanotubes as nano-gears*[20]

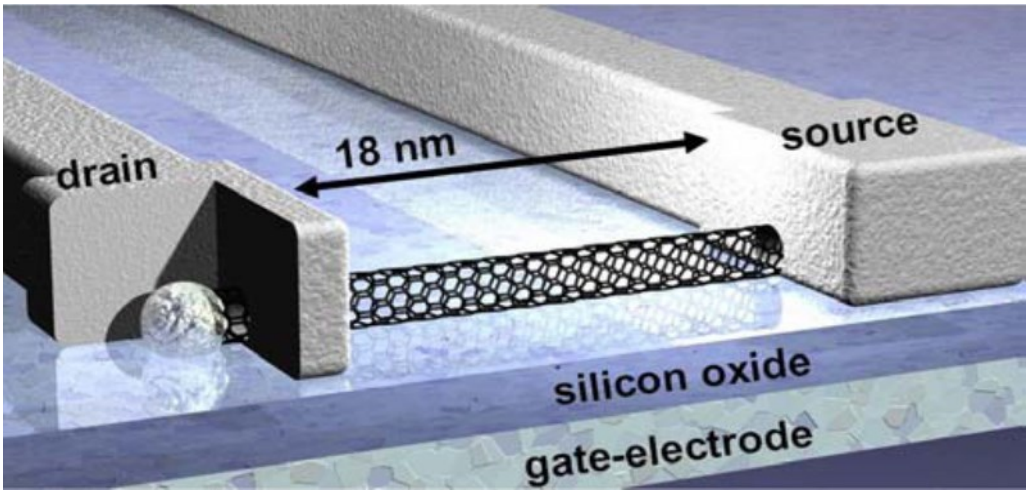

Figure B2.15: *Nanotubes as nanowires in nano-circuits*[20]

B2.9 Chemical modification of Carbon Nanotubes

Some of the characteristics of carbon nanotubes in some occasions form dis-advantages and their chemical modification aims at giving them all those characteristics which are essential for every application, via modifying the open edges, their external walls, their defects as well as their inner cavity. The practical target will be the adjusting of various groups (mostly organic) on carbon nanotubes walls so that they can form the "intermediate link" between them and the application by forming hydrogen bonds or covalent bonds. In order to modify side groups a large number of organic reagents have been used, such as carbenes, nitrenes, aril-roots, aromatic amines, carboxylic acids, phenyl-acetylene etc.

The main procedures that are followed in order to modify carbon nanotubes chemically are summarized in two categories:

- Attachment of chemical groups via formation of covalent bonds on the CNTs surface. Crude carbon nanotubes are treated with acids so that oxygenized groups will be formed, such as parts of carboxylic acids, on the edges or in the side walls of CNTs. Due to these modifications, amines can be attached on CNTs, which are organic

compounds having in their molecule the amine-group and are considered to be alkyl-derivatives of ammonia with general formula RNH_2 for the primary amines, R_2NH for the secondary and R_3N for the tertiary (Figure 17b).

- Non-covalent attachment or winding of a crowd of molecules on the external graphitic surface of the CNTs. Towards that direction, polymers, multi-aromatic derivatives, surfactants and bio-molecules have been used. The above, apart from introducing active chemical groups on the external CNTs surface, they contribute significantly to the bundle cracking so that new isolated CNTs will be formed. Additionally, their non-covalent chemical modification is especially attractive, as it offers the possibility of attaching chemical groups without destructing the electronic lattice of the CNTs, since it is based on the formation of van der Waals bonds or π-π interactions between CNTs and the molecules (Figure B2.16)[25].

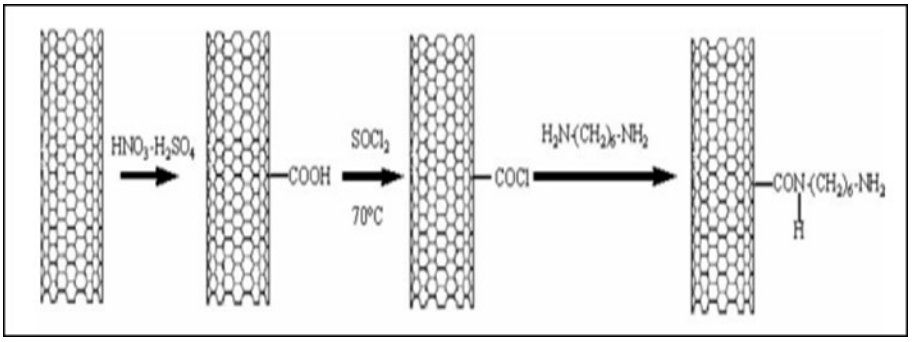

(a)

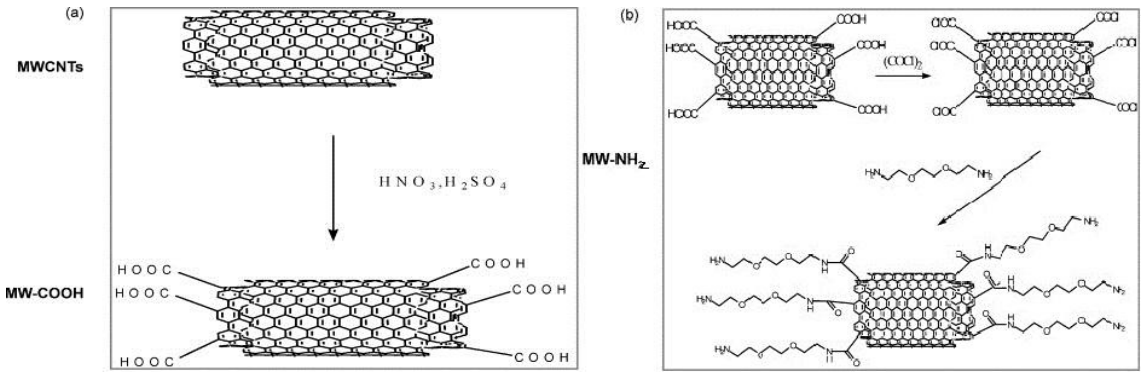

(b)

Figure B2.16: *(a) Schematical representation of chemical modification of CNTs via covalent bonds, (b) Example of chemical modification of MWNTs. Suggested resulting structures: MWNTs, MW-COOH and –NH_2MW, carboxyl- and amino- chemically modified carbon nanotubes respectively*[1]

Characteristic examples of modification of the surface of CNTs is the deposition of metals or other species in order to be applied either in nano-catalysis or in bio-sensors. Other characteristic examples will be the covalent interactions in free carbon atoms on the edges of the nanotube and on defects, the chemistry of covalent interactions of the double bonds

on the walls of a SWNT, the non-covalent interactions π-stacking as well as macro-molecular wrapping (polymer reinforcement).

Considering nanotubes chemical modification there is also the procedure of their subjecting into sonication bath, a way to separate the stacks of the organized carbon nanotubes. This fact allows the increase of their surface, which can contribute to their application as gas dessicants. The most important though is that the use of sonication results in their cutting to smaller lengths. This treatment is performed by using strong acids such as HNO_3-H_2SO_4 in order to oxidize carbon nanotubes[1].

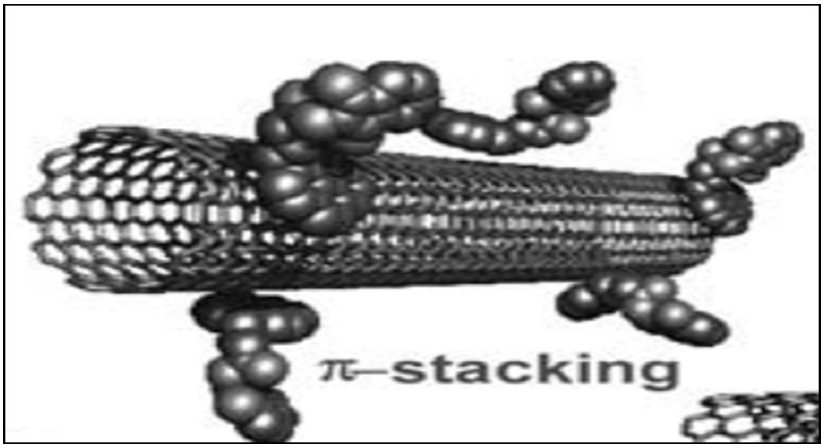

Figure B2.17: *π-π interactions*[26]

B3. Nanowires

A nanowire is a nano-structure, with diameter of the order of a nanometer (10^{-9}m). Nanowires can be defined as the structures with thickness or diameter which is limited in tens of nanometers or less but with unlimited length. In these scales, the quantum-mechanical results are significant so they are called quantum-wires[8]. There are many different types of nanowires such as metallic (e.g. Ni, Pt, Au), semi-conductive (e.g. Si, InP, GaN etc.)[9] and insulating (e.g. SiO_2, TiO_2)[9]. The molecular nanowires consist of a repetition of molecular masses, whether they are organic (e.g. DNA) or inorganic (e.g. $Mo_6S_{9-x}I_x$)[9].

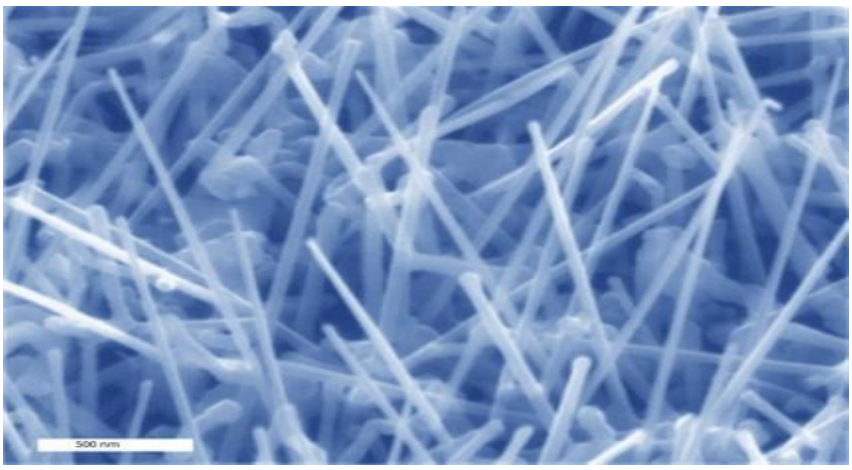

Figure B3.1: *TEM image of InP nanowires*[7]

B3.1 General

Typical nanowires exhibit side ratio (length/width ratio) 1000 or more, which is the reason why they are usually reported as one-dimensional materials. Nanowires have many interesting applications, which are not exhibited in bulk or three-dimensional materials[9]. The electrons inside nanowires are quantum limited on the sides occupying in this way energy fields that are different than the ones of bulk materials. The special characteristics from these quantum limitations result in specific values of electric conductivity. These distinguished values derive from the quantum mechanical limitations concerning the number of electrons which can "travel" through the wire on the scale of nanometers. These values are usually referred as "conductivity quantum" and are integer multiples of $2e^2/h \approx 77.41$ μS[9]. This fraction is the reversed of the well-known resistance unit h/e^2 which will be almost equal to 25812.8 Ω, and is usually referred as von Klitzing constant[9]. Various nanowires such as inorganic molecular nanowires ($Mo_6S_{9-x}I_x$, $Li_2Mo_6Se_6$), semi-conducting (InP, Si, GaN etc.), dielectric (e.g. SiO_2, TiO_2) or metallic (e.g. Ni, Pt) have been synthesized so far with diameter starting from 0.9 nm and length of hundreds of μm[9]. Among others, nanowires find applications in many important fields such as electronics[9], optical-electronic devices[9], nano-electronic devices[9], nano-mechanic devices[9], as well as additives in advanced composite materials[9]. More specifically, they can be used as magnetic information storage media[25], in energy storage devices[25], in Lithium batteries[25] and as nanowires sensors[25].

B3.2 Synthetic methods

There two basic strategies for the synthesis of nanowires namely “top-down” and “bottom-up” approaches. In top-down approach a large piece of the material is decreased into smaller pieces by using various means, such as lithography or electrophoresis. In bottom-up approach the nanowires are composed combining elements of adsorbed atoms[26]. Most of the synthetic techniques in the literature use the bottom-up approach.

Nanowires can be synthesized by common laboratory techniques, such as electrochemical deposition or vapor deposition[9]. A deposited nanowire is a nanowire which is deposited on a surface of different nature (e.g. this can be a single tape of metallic atoms on a non-conductive surface). A nanowire can be also produced by the suspension technique where by chemical insult or by high energy particles bombing (atoms or molecules) a nanowire can be formed[9].

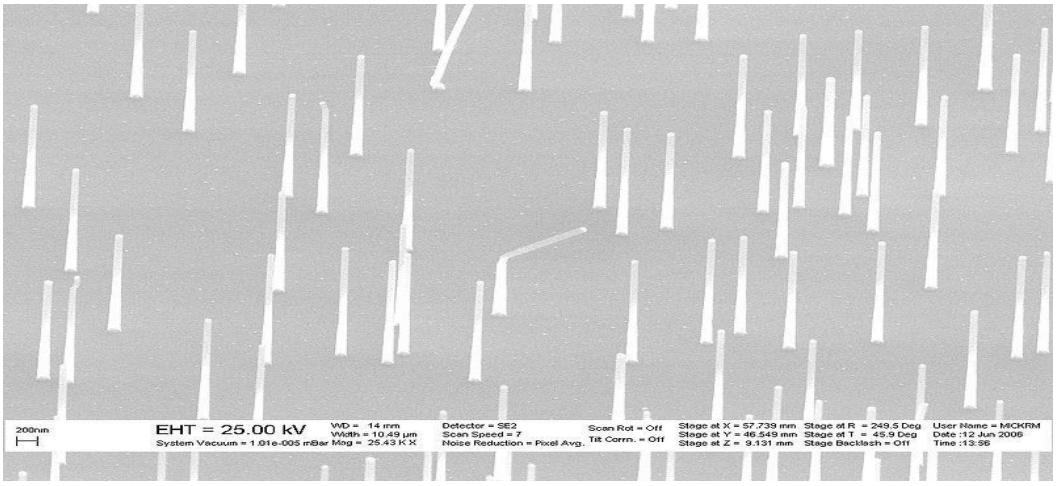

Figure B3.2: *SEM image of the epitaxial nanowire hetero-structure which was developed by the catalytic gold nanoparticles*[9]

Another common technique used to form nanowires is the Vapor-Liquid-Solid (VLS) method[9]. This technique uses as source laser ablated particles, or a feed gas (such as silane). The best catalysts to use for this technique are some complex metals in liquid state (such as gold) which can be bought in colloidal shape and can be deposited either on a substrate or self-assembled from a thin film. This procedure can also produce crystal particles in case of semi-conductive materials. The source inserts the nanoclusters and they are saturated. When super-saturation is achieved the source is stabilized and grows externally of the nanocluster. The final product length can be controlled by simply shutting the source. Composite nanowires made of super-lattices of alternative materials can be formed by source changes when they are still in growth phase[9]. Inorganic nanowires, such as $Mo_6S_{9-x}I_x$ are synthesized by a simple reaction step in gas phase and at high temperature[9].

Furthermore, nanowires have the potential to grow in solution, forming, this way, nanowires of various materials. The method is called Solution-phase synthesis[9] and can lead

to large quantities of products. Additionally, the supercritical fluid-liquid-solid growth method[9] is proposed to be used in order to form semiconducting nanowires such as Si and Ge. Through the use of metal nanoparticles, Si and Ge organometallic precursors are driven into a reactor which is full with a supercritical organic solvent e.g. Toluene. The thermolysis procedure leads to decomposition of the precursor and the Si or Ge are released and diluted into metal nanocrystals. As a result, a nanowire grows from the nanocrystal seed.

Finally, nanowires can be potentially formed in the gas state[9] without the assisting of catalytic components. In order to yield metal oxide nanowires, metals are heated in temperatures that exceed the recrystallization temperature while being in oxidative (oxygen or air) atmosphere.

B3.3 Properties

Conductivity

Nanowire conductivity is expected to be less than the respective bulk materials. This is caused by the fact that there is a ranging of nanowire limits, when nanowire width is smaller than the free electron route of the respective bulk material[9]. For copper for example, the average free route length is 40 nm, so nanowires less than 40 nm wide will decrease the mean free path of the wire.

Moreover, nanowires exhibit some specific electric properties because of their size. Unlike carbon nanotubes, the electron movement of which can be achieved from one electrode to the other, the conductivity of nanowires is influenced strongly by the effects on the edges[9]. The edges consist of atoms which are on the surface of nanowires and are not fully connected to nearby atoms (like the atoms which are on the main part of the nanowire) and thus form a defect source on the nanowire, being able to cause conduction of current smaller than the one of the respective bulk materials[9]. While a nanowire becomes smaller in size, its surface atoms become more compared to the atoms in the internal part of the nanowire, which causes significant electric phenomena on the edges.

Nanowire conductivity is subjected to an energy quantum, which means that the energy of electrons that pass through the wires can receive only specific values, which are integral multiples of Von Klitzing constant $G=2e^2/h$, where h is the Planck constant and e the electron charge[9]. Therefore, the conductivity is described as the aggregate of different quantum energy levels transfer via separate channels. The thinner wire has the smallest number of channels that are available for electron transfer. This quantum has been proven by measurements of one nanowire's conductivity, which swings between two electrodes, while at the same time is being pulled its diameter lowers as well as its conductivity at a stable rate, while the plateau corresponds to multiples of G. The conductivity quantum is tenser in semi-conductors such as Si or GaAs in comparison to other metals, due to its lower electron density and the lower active mass[14,15].

Magnetoresistance

The magnetoresistance is defined as the change in the electric resistance of a material in relation with the externally applied-magnetic field[27]. The measurements of the magnetic resistance (MR) form an important technique for characterizing certain types of nanowires because they can offer much information about the electron scattering and the nanowires' limits, the consequences of enriching and annealing on scattering etc[27]. For example, at low fields the MR data show that there is a square dependence on field B of which estimations about the mobility carrier can be done.

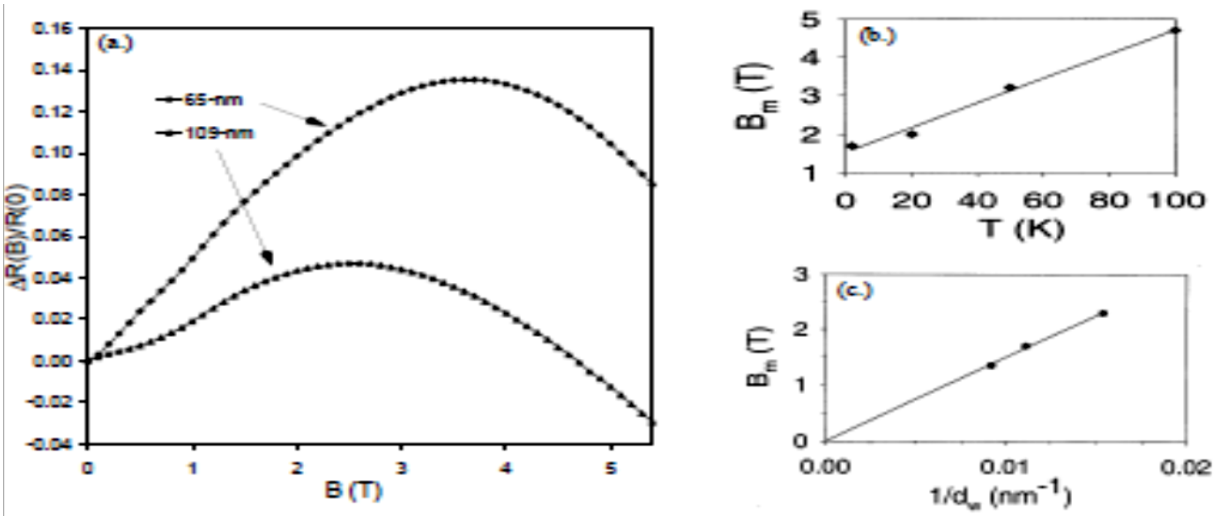

Figure B3.3: *(a) Longitudinal magnetic resistance, ΔR (B)=R (0), at 2 K as a function of B for terries of nanowires of diameter 65 and 109 nm before chemical annealing. (b) The position of top B_m as a function of temperature for the diameter of 109 nm and of the nanowire terry-B_i after thermal annealing. (c) The position of the top B_m of the longitudinal MR (after thermal annealing) at 2 K as a function of $1/d_w$, to reverse of the diameter of the nanowire*[27]

In Figure B3.3 the longitudinal magnetoresistance can be seen (B parallel to nanowire axis) concerning nanowire B_i samples having diameter 65 nm and 109 nm before their thermal annealing at 2 K[27]. The maximum MR in Figure B3.3a derives from the classic impact of size, where the scattering of the nanowire limit reduces as the cyclotron radius becomes smaller than the nanowires diameter on the edge of high field, resulting in a decrease in resistance[27]. This behavior is characteristic for longitudinal MR of nanowires B_i for a diameter range 45 nm to 200 nm. The position of the peak B_m ranges within reduced values of the field B as the diameter of the nanowire increases (Figure B3.3a). B_m changes with the $1/d_w$ in a linear way (Figure B3.3b)[27].

Thermal stability

Another property of nanowires is their remarkable thermal stability[28]. As their size decreases the melting point is reduced. Therefore, one can obtain a much lower annealing temperature for healing. Furthermore, they can be successfully integrated in functional devices and cirquitry (cutting, interconnecting and welding)[28]. Finally, their lowered melting

point allows them to be more sensitive to environmental changes e.g. temperature or stress fluctuation.

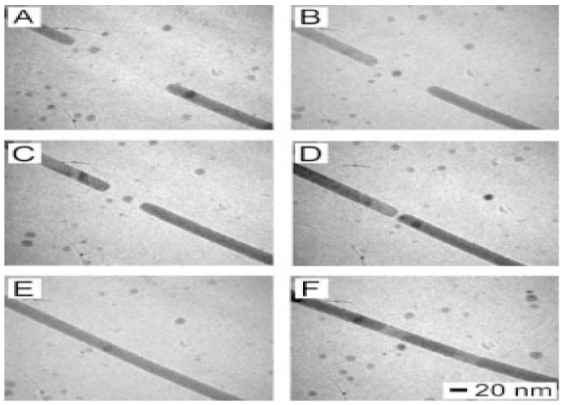

B3.4: *Welding of two Ge nanowires (TEM images, 10-100 nm thickness)*[28]

Optical properties

Nanowires also possess optical properties. When light is emitted from nanowires, it is strongly polarized along their longitudinal axis[28]. As a result, the absorption edge of nanowires is blue-shifted (at higher energies) along with a decreasing diameter. What one also observes is the sharp, discrete features in absorption spectra[28]. One possible explanation for this would include quantum-confined effects in spite of the fact that surface states may contribute additional features[28].

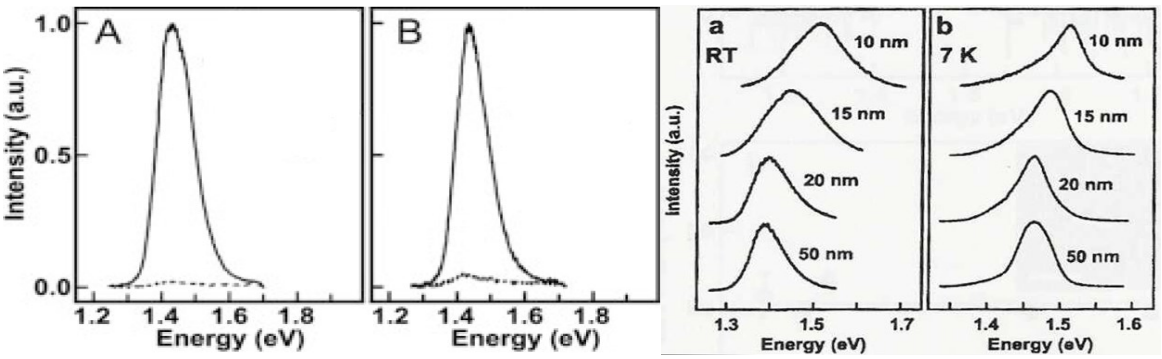

B3.5: *A) Excitation and B) emission spectra from InP nanowire (15nm diameter)(left) and blue-shift (right)*[28]

B3.4 Applications of Nanowires

Nanowires continue to be at an experimental (laboratory) stage, although large steps have been done towards practical applications. They are expected to complete or replace carbon nanotubes in some applications while some early experiments have shown that they can be used to form the next generation computers[9].

To create active electronic elements, the first step would be the doping of single semi-conductive nanowires, which has already been done to form semi-conductors of n and p type. The next step will be to find a way to form a contact p-n, one of the simplest electronic

devices. This was accomplished using two ways; the first will be to place a wire of p-type on a wire of n-type. The second will be to involve a chemical doping of a wire with different dopants along the nanowire. This method produces a p-n contact only using one wire. After the p-n contacts, which were prepared with nanowires, the next step will be to form logical gates and this can be done by connecting several p-n contacts together. In this way, p-n contacts were produced out of semi-conductive nanowires[20].

The most attractive possible applications of nanowires lie on magnetic information storage. Researches have shown that a periodic terry of magnetic nanowires has the ability to store 10^{12} bits/in^2 of infomation[20]. The small diameter of Ni, Co nanowires that are formed inside the pores of the porous anodic aloumina was found to be the most appropriate for this purpose. The large ratio of nanowires' dimensions has as a result their enhanced ability to demagnetize and the suppression of the beginning of the "super-magnetic-limit", which is considered to be very important for preventing the loss of magnetically recorded information among nanowires. Proper separation among nanowires should be followed to prevent overlapping and magnetic bipolar coupling among them. It has been found that nanowires can be used to form[21] a stable magnetic means of terry density $>10^{11}$ wires/cm^2. Furthermore, some other possible future applications of nanowires are mentioned below:

Nanowire sensors

The principle according to which sensors operate is based on the tracking of a macroscopic natural property and its conversion to a countable property of certain characteristics. The advantages of one-dimensional structures compared to the two-dimensional ones are: (i) higher stability due to their high crystallinity, (ii) they exhibit large surface area, while the volume which they occupy is little, (iii) their surface can be modified so that they can be combined with a larger variety of chemical groups and (iv) show reduced percentage of granules limits[25]. Furthermore, the radial dimensions of nanowires play a significant role since nanowires sensitivity is improved.

Nanowire sensors are usually made by a FET assembly[29] (FET assembly is a Field Effect Transistor which uses electric field in order to control the shape and the conductivity of a channel of one type of charge carrier in a semiconducting material) or resistors. One of their applications is the DNA and protein tracking. Additionally, via appropriate modification of the sensor's surface (so that it has high collectability) certain viruses can be tracked[25].

Energy Storage

Recent advances in materials are connected with energy storage and conversion. Progress has also been made in designing of semi-conductive silicon nanowires to enhance their thermal-electric properties while the Seebeck coefficient for the surface roughness has

been improved[25]. These thermal-electrical wires can be applied in cases of regaining heat, cooling and electrical energy as well as in Lithium batteries for electrical power storage[25].

Lithium batteries

A basic concern about the future of energy supply and the usage of alternative energy sources will be the sufficient memory carriers, such as batteries. It is known that, the capacity loss is usually caused by their charging and discharging. Therefore, Lithium batteries form hopeful materials since they offer high conductivity values[25]. In this case, nanowires are used to increase the surface area of one or both of the electrodes of the battery. Silicon and Germanium nanowires have been proposed to be used so as to replace the traditionally used graphite[30]. Silicon has the ability to store ten times more lithium than graphite offering this way improved energy density[30]. The large surface area of the nanowire increases the anode's power density leading to fast charging and higher delivery of the current. On the other hand, the use of a Germanium nanowire as an anode increases the energy density and cycle durability of lithium-ion batteries as well[30]. Like Silicon, Germanium expands while charging is on progress and decomposes after a small number of cycles[30]. Compared to Silicon nanowires, this one seems to reconstruct after certain number of cycles (approx. 100 cycles) to create a mechanically strong continuously porous network, which allows it to loose only 0.01% of its capacity after every cycle since then[30].

B4. Carbon nanotubes encapsulating nanowires and nanorods

The discovery of multi-wall carbon nanotubes in 1991 (MWCNT)[31] has intrigued the imagination of materials scientists and become one of the most active fields of nanoscience and nanotechnology over the last decades. This new form of carbon exhibits unique physical and chemical properties that have been reviewed in many articles[32-42]. In addition to their important electronic and magnetic properties new applications emerged in fields such as catalysis[43-45], catalyst supports[46-48], polymer reinforcements for composites[49-54] and hydrogen storage[55-63] among others[39]. Moreover, the characteristic inner cavity in submicron and nano-dimensions makes them suitable as a host material. Indeed, the inherent pore structure of carbon nanotubes (CNT's) has already been explored as a confined space for encapsulation and stabilization of various elements or compounds[64]. Interestingly, the attempts in early 90's to incorporate pure metals within MWCNT led to the discovery of single-wall carbon nanotubes (SWCNT)[65,66].

The main interest of encapsulating metals within CNT is to stabilize 1D morphologies such as nanorods and nanowires. These nanostructures are expected to exhibit novel electronic and optical properties because of their low dimensionality and the quantum confinement effect. In the composite materials the metallic nanostructures are protected against oxidation or fusion into bulky particles by their graphite-like host. Therefore, these structures present significant opportunities to study their fundamental physical properties (mechanical, optical, electronic, magnetic), as well as their possible applications as catalysts and electronic or magnetic components in devices[67-69].

Up to date several methods have been examined and developed for the encapsulation of metals within carbon nanotubes including arc-discharge method[70], liquid chemical method[71], capillary action[72,73] electrolysis[74] and various catalytic chemical vapor deposition methods[75]. Some of the elements that have been successfully incorporated within CNT are transition metals such as Mn, Fe, Co, and Ni as the most frequently studied because of the prospect to impart novel magnetic properties[78-85]. Main-group metals have also been a subject of attention, especially those with low melting points as for example in the case of Ga and In where the corresponding filled carbon nanotubes have been evaluated as potential nanothermometers[86-88]. Semiconductor Ge nanowires have been synthesized inside CNT employing the arc-discharge method. Remarkably, under the same experimental conditions, metallic tin does not fill CNTs[70]. Also, a simple arc-discharge method for in situ synthesis of Cu-filled CNTs with coal as carbon precursor in an approach which should be further optimized in order to lead to mass production of Cu nanowires with excellent performance, offering more opportunities for studying the physical and electronic properties of Cu nanowires[89]. Additionally, the capillary -effect was used to form double-walled carbon nanotubes (DWCNTs) filled with a-iron and the samples were ferromagnetic in room temperature[90]. It is worth mentioning that multi-metal Co/Pd magnetic and non-magnetic nanowires have also been encapsulated inside multi-walled carbon nanotubes using microwave plasma chemical vapor deposition[91] and thin layers of Co and Pd which were

deposited on Si substrate. Finally, long and continuous silver nanowires were encapsulated inside MWCNTs, after irradiating a suspension of silver nitrate-MWCNTs and while 2-propanol was present[92]. Silver nanowires turned out to be up to 2 μm long exhibiting a well oriented structure.

B4.1 Carbon nanotubes encapsulating superconducting Tin-nanowires

The role of pure metals and their corresponding compounds as both catalysts and source for in-situ growth of filled carbon nanotubes has been a field of major interest during the last decade. The resulting nanostructures are expected to exhibit novel electronic and optical properties because of their low dimensionality and the quantum confinement effect[93]. Recently, Jancovic et al. described a simple method that leads to the yield of carbon nanotubes encapsulating single crystalline metallic tin nanorods by employing the conventional method of Catalytic Chemical Vapor Deposition (CCVD) over different tin catalysts. These protected Sn nanorods are expected to be an ideal system for studying their fundamental physical and chemical properties that are essential apart from their implementation as nano-building blocks in nanoscale devices. Various analytical techniques including Transmission Electron Microscopy, Scanning Electron Microscopy, Transmission Electron Microscopy, X-Ray Diffraction, SQUID and Mössbauer Spectroscopy were used in order to characterize and evaluate the final composite materials.

Lately, a simple and reproducible method was described, with which individual carbon nanotubes of length of micrometers (μm) were produced filled with high purity, single-crystalline superconductive tin nanowires. The breakthrough of this method, as compared to other projects, is that nanowires are fully protected by nanotubes and therefore, are air-inactive. The surrounding nanotubes, which consist of graphitic sheets, are closed in both edges and protect therefore the nanowires. Super-conductive tin nanowires show, because of their reduced dimensions on the scale of nanometers, a critical magnetic field (Hc) more than 30 times higher than the value of metallic tin. This composite nano-structure is symbolized as Sn@CNTs[93].

Furthermore, charge transport properties of single superconducting tin nanowires which are encapsulated inside multi-wall carbon nanotubes have been investigated by multi-probe measurements[94]. The multi-walled carbon nanotubes protect the tin nanowires from getting oxidized allowing in this way the study of their electronic properties. The diameter of the formed tin nanowires is 25 nm approximately and the transparency of the Ti/Au electrode and the nanowire can be tuned by Argon ion etching carbon nanotubes. When one applies a large electrical current local heating occurs at the contact which in turn leads to suppression of superconductivity[94]. Additionally, a molten salt electrolytic method has been suggested to form tin-filled carbon nanotubes[95]. According to this, a melt of LiCl with an addition of $SnCl_2$ is electrolyzed between two graphite electrodes and Li is incorporated into the graphite while tin is deposited on graphite's surface. Li allows the graphitic layers to be released

which surround tin deposits in order to form Sn-filled MWCNTs along with carbon nanoparticles[96]. If one reverses the polarity of the graphite electrodes during the procedure, this can be repeated till the electrodes are totally consumed, offering a larger scale production.

B4.2 Carbon nanotubes encapsulating Sn-Pb nanowires

Walton's group[97] has described a method, according to which Tin-Lead nanowires were encapsulated in carbon nanotubes by using electrolysis of graphite on melted LiCl which contained a quantity of Sn and Pb. Result analysis showed that Sn prevailed on one edge while Pb would prevail on the other edge of the nanowire and that the separate crystals of each metal can be distinctive in the middle part of the nanowire. The substrate where the incorporation takes place plays a significant role in the morphology and in the properties of the nanowire. Therefore, with the above procedure, the 1-D and 2-D morphologies where controlled by maintaining the initial desired super-conductivity that bulk material had. The different melting temperatures of Sn and Pb have as a result the existence of Sn on one edge, Pb on the other, while in the middle a mixture of Sn-Pb in several ratios is observed (Figure B5.1)[97]. In Figure B5.1 a TEM image of Sn-Pb nanowires is observed.

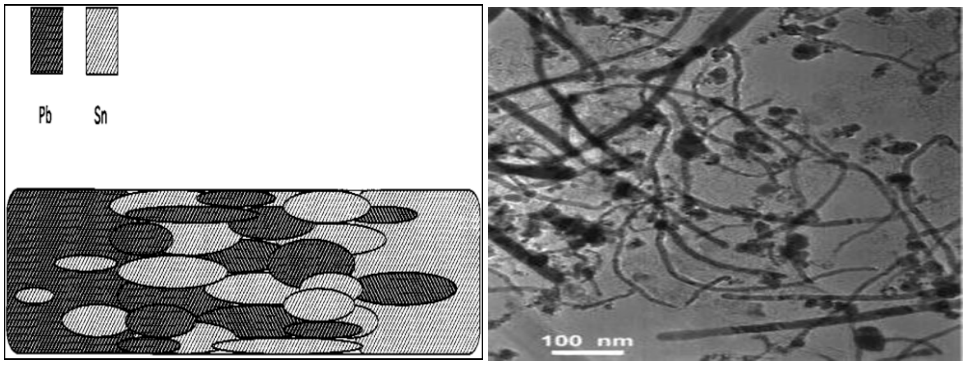

Figure B5.1: *Sn-Pb nanowires structure (left) and TEM image of Sn-Pb nanowire (right)*[97]

Super-conductive nanowires made of Lead (Pb)[98], Tin (Sn)[99,100] and MoGe[101] had been previously composed but they were not appropriate to use since they are corrosion sensitive. If these structures could be protected and stabilized they would be an ideal system of major importance for nano-constructions or nano-devices, such as electron emission sources or super-conductive devices.

B5. Nanostructured Magnetic Materials

Introduction

The magnetic materials are devided to various categories according to the magnetic susceptibility that they exhibit. The periodic table of the elements, as well as the kind of magnetism that is exhibited by the elements is shown below (Figure B5.1)

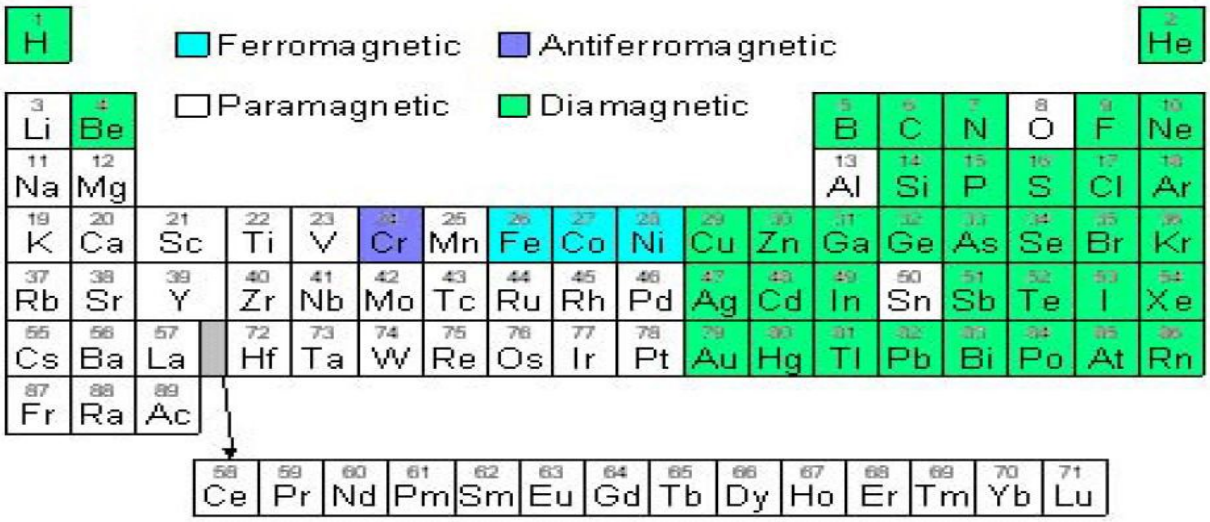

Figure B5.1: *Periodic Table*[102]

According to the theory of Weiss a non-saturated ferromagnet contains a number of small regions called domains, in which the local magnetization is homogeneous and reaches the saturation value. Referring to different domains, the direction of magnetization is not necessarily paralleel[102]. Two domains are separated by domain walls which are regions of approximately 100 nm in bulk materials where the magnetization rotates continuously. They are classified according to the angle of rotation (90° or 180°) and the mode of rotation (Bloch or Neel).

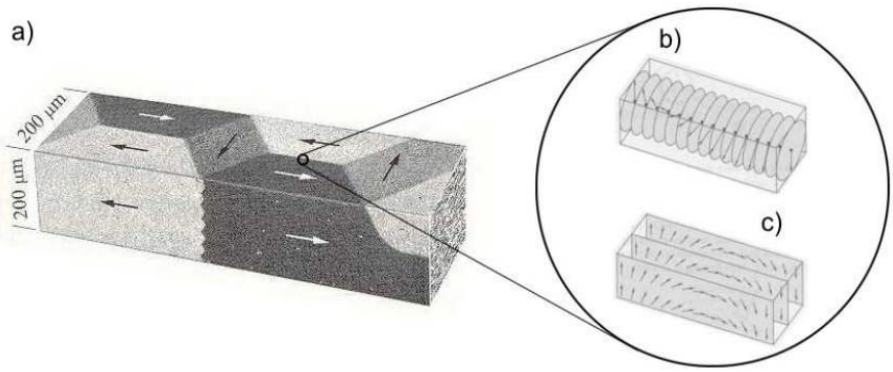

Figure B5.2: *a) Magnetic domain pattern of a Fe whisker b) Bloch wall c) Neel wall*[102]

When one applies an external magnetic field, the domain walls move through the sample which in turn increases the overall magnetization. In magnetically soft materials, domain

walls are broad and therefore, the movement of the walls requires small fields only whereas larger fields are necessary in magnetically hard materials[102]. One second mechanism that increases the magnetization is magnetization rotation within the domains. Certain directions are easier to magnetize than others because of magnetic anisotropies. The spontaneous magnetization lies preferably along one of these easier directions. In case the applied external field is not parallel to such an easy direction, the magnetization rotates and aligns easily along the magnetic flux lines.

Hysteresis

Figure B5.3 shows a typical ferromagnetic hysteresis loop and indicates the predominant, underlying mechanisms for each region. The sample is firstly magnetized to saturation in an applied field (virgin curve). The region of highest permeability is governed by domain wall motion whereas magnetization rotation occurs rather at higher magnetic fields. When the applied field is reduced to zero the remanent magnetization M_r remains. A magnetic field of opposite direction called coercivity field H_c is needed to macroscopically demagnetize the sample. Thus, the hysteresis loop contains important information about the magnetic properties of the sample. Characteristic quantities include the saturation magnetization M_s, the remanent magnetization M_r, the coercivity field H_c, permeability μ and the dissipated energy that is necessary to magnetize the sample in the opposite direction. The dissipated energy can be calculated from the area that is included by the hysteresis loop.

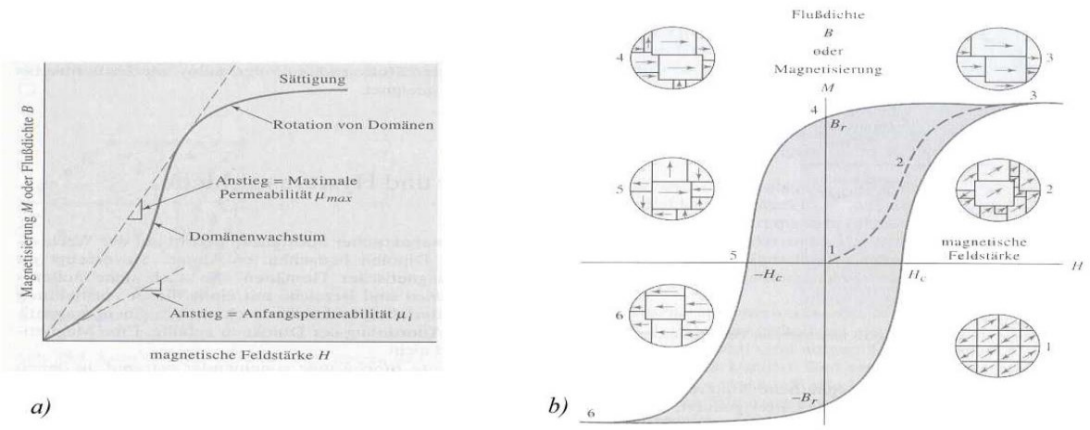

Figure B5.3: *a) Virgin curve b) Hysteresis loop of a ferromagnetic material*[103]

Magnetic Anisotropy

If the magnetic properties of a sample are dependent on directions, it is magnetically anisotropic. Magnetic anisotropy arises from dipole-dipole interactions and spin-orbit coupling. Macroscopic shape anisotropy has its origin in long range dipole interactions arising from free poles at surfaces. It can be represented in terms of the stray fields created external to the sample[104]. In thin films stray field energy is minimized if the magnetization is

in-plane and maximized if the magnetization is out-of-plane. Another form of magnetic anisotropy is the magneto-crystalline anisotropy. When investigating single crystalline Fe, Ni or Co samples, one notices that the magnetization curves along certain crystallographic directions differ from each other. In iron, the magnetization curve along the [100] direction is steeper and reaches saturation at lower external fields than along [110] or [111] and is therefore the easy axis of magnetization. In case of nickel, [111] is the easy axis and [100] the hard axis of magnetization. In absence of an external field, the spontaneous magnetization lies preferably along one of the easy axis. The origin of the magneto-crystalline anisotropy lies both in the coupling of the spin part of the magnetic moment to the electronic orbital shape and orientation (spin-orbit coupling) and the chemical bonding of the orbitals on a given atom with their local environment[104].

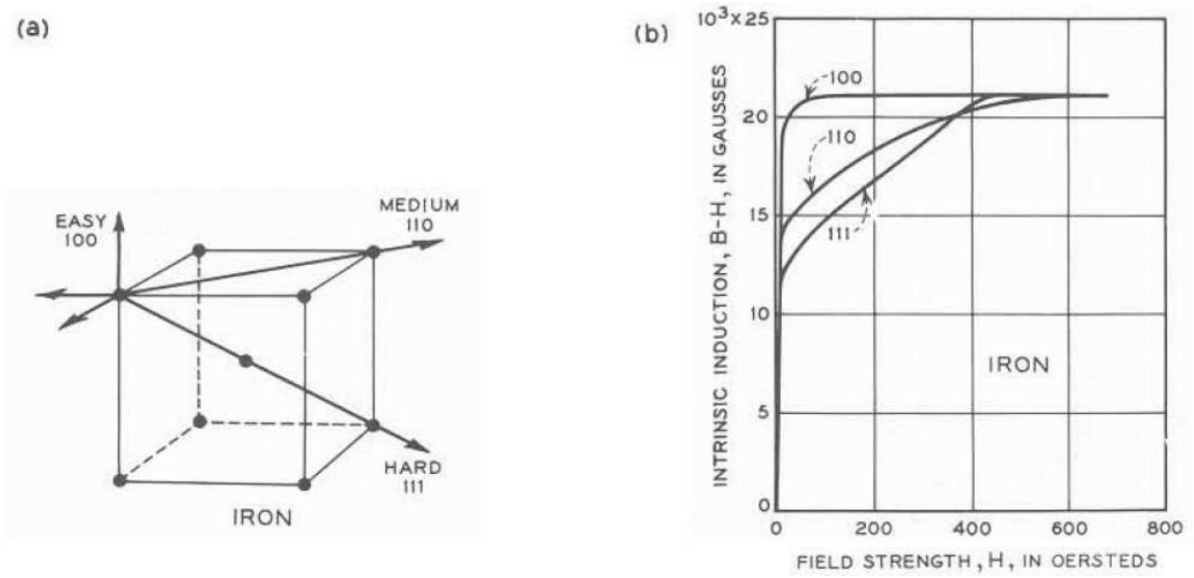

Figure B5.4: *a) Crystal structure of body centered cubic iron, indicated are easy and hard axis of magnetization*

b) Magnetization curves along the corresponding crystallographic axes[104]

Demagnetization

In an external magnetic field, the presence of a magnetic material alters the magnetic induction B. If the sample has a finite length, magnetic poles are generated near the ends of the sample. These poles give rise to a magnetic field that opposes the external field and is therefore called demagnetizing field. The strength of the demagnetizing field depends on the magnetization M and the geometry of the sample. The field inside the magnetic material is now different from the external field and requires correction. The inner field can be calculated by

$$H_{in} = H_{ext} - N_d M$$

where M is the magnetization and N_d the demagnetizing factor which is only determined by the sample shape. For spheres and ellipsoids it is possible to calculate N_d, whereas for other shapes one needs to approximate[105].

Ferromagnetic Materials

Ferromagnetic materials have positive susceptibility, which is much higher than one and depends on the intensity of the magnetic field. They exhibit high remanent magnetization even absent external magnetic field. The relation between the magnetization M and the applied field is generally non-linear. The phenomenon of ferromagnetism appears below a critical temperature which is called Curie temperature Tc, while above that temperature the material becomes paramagnetic.

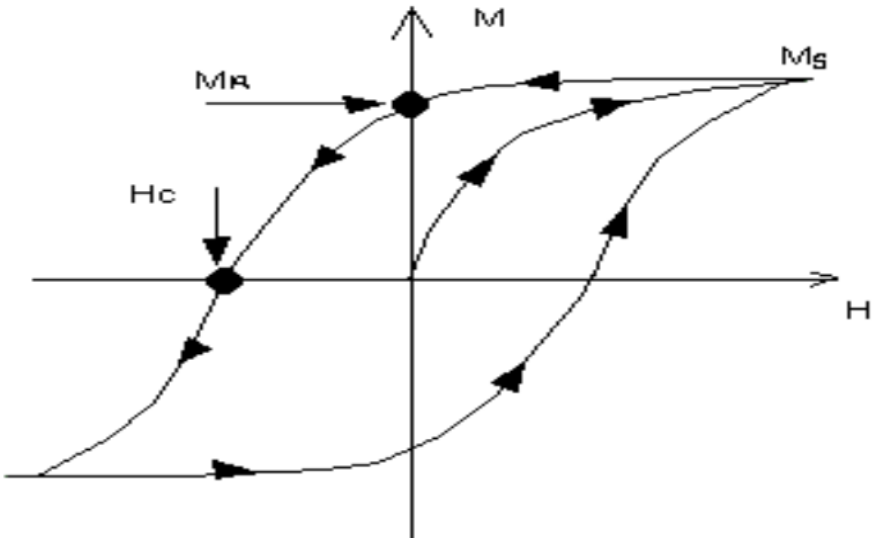

Figure B5.5: *Hysteresis loop curve*[106]

In Figure B6.5 the hysteresis loop can be seen M(H), where beginning from thermally demagnetized sample (H=0, M=0) we get the so-called initial magnetization curve. Beginning from the fully magnetized sample (saturation magnetization Ms in quite high field) and by lowering the magnetic field to zero value, the magnetization is not becoming zero but obtains an MR value which is called remanent magnetization. By reversing the field M it is gradually decreasing and becomes zero at the point HC which is called cohesive magnetic field[106].

Diamagnetic Materials

Diamagnetic materials exhibit weak negative susceptibilities in the class of 10^{-5} and this occurs because they generate parallel magnetic field, but of the opposite (repulsion) to the induced field direction. A substance is also diamagnetic when the atoms of which it consists have filled their layers and sub-layers and, absent applied field, no atom has a permanent magnetic moment. The diamagnetism was for the first time observed by Faraday in Bismuth, which is a known diamagnetic material[106].

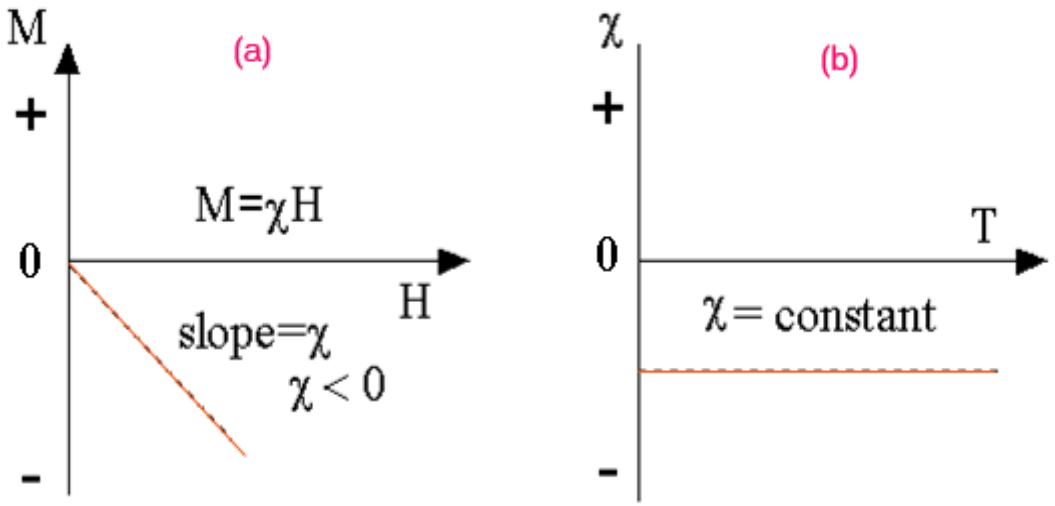

Figure B5.6: *Magnetization of diamagnetic materials: (a) for zero-magnetic field the magnetization is zero and the appearance of negative magnetization in magnetic field exposure leads to negative susceptibility, (b) the susceptibility is temperature independent*[106]

Paramagnetic Materials

Paramagnetic materials in small fields exhibit susceptibility which is conversely analogous to the absolute temperature χ=C/T. They are characterized by small positive susceptibility values in the class of 10^{-4} to 10^{-5} and exhibit therefore no interest as far as applications are concerned. They consist of atoms which have bipolar magnetic moments μ which do not interact with each other being able to turn in space freely and independently one of another. In zero-field, due to the thermal movement, the magnetic atom-moments are being found in random orientations and the magnetization is zero. The application of an external field orientates partly the magnetic torques leading to the appearance of macroscopic magnetic torque[106].

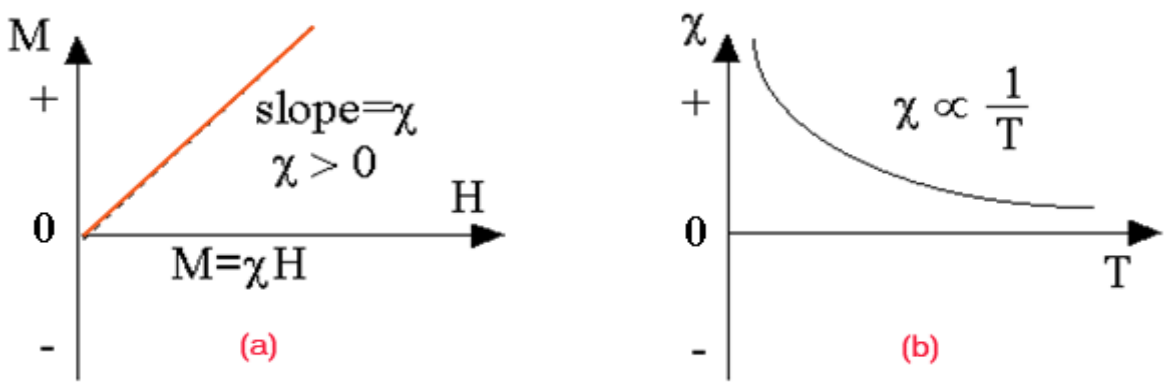

Figure B5.7: *Magnetization of paramagnetic materials: (a) applied field leads to positive magnetization and hence positive susceptibility and (b) susceptibility is analogous to 1/T*[106]

B6. Introduction-Physical Properties of the Mn-Bi alloy

A quite interesting alloy is the case of Mn-Bi, material that exhibits exhiting magnetic properties. In room temperature it is ferromagnetic and is crystallized into a hexagonal structure, exactly as Nickel-Arsenite (Ni-As type), having unit cell of dimensions a=4.29 Å and c=6.12 Å and is called low-temperature-phase (LTP)[107]. At 628 K a first order transition takes part, at which we get a paramagnetic phase called high temperature phase (HTP), and is accompanied by 3% decrease of c axis and 1.5% increase of the a axis. This transition corresponds to a phase cracking:

$$\mathbf{MnBi \rightarrow Mn_{1.08}Bi + Bi}$$

A part of the manganese now occupies the intermediate places of the bi-pyramid NiAs structure. If the HTP phase is dyed rapidly then it can be preserved in lower than 628 K temperature. The high dying temperature phase (QHTP) is also ferromagnetic, with an ordering temperature of 460 K. the crystal structure can be susceptible to some slight changes due to the dying and can be re-adjusted into orthorhombic unit cell.

Although Mn-Bi is a very intriguing alloy there are many difficulties in preparing homogeneous samples. This can be observed by looking at the phase diagram of the Mn-Bi system (Figure 5). In the liquid phase, the Mn-Bi system shows a gap in mixture above the mono-eutectic temperature of 1528 K[107]. At 719 K the inter-metallic ferromagnetic compound Mn1-xBi (with x≈0.08) is formed re-eutectic. By applying more cooling, the HTP phase cracks and the LTP phase is stoichiometrically formed at 613 K, according to the reaction:

$$\mathbf{MnBi \rightarrow Mn_{1.08}Bi + Bi}$$

Attention is required as far as the thermal hysteresis in the LTP – HTP transition is concerned.

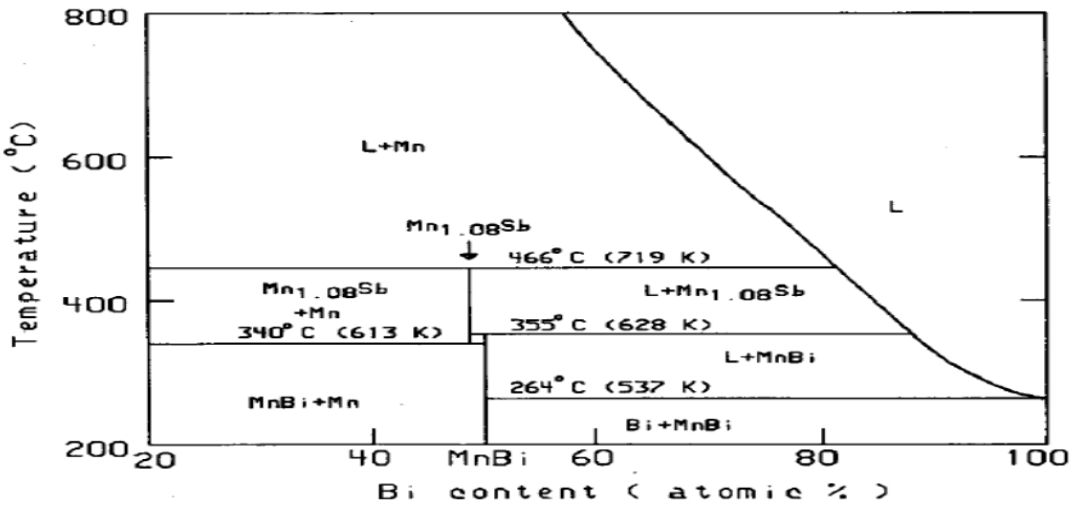

Figure B6.8: *Phase diagram of the MnBi system*[107]

When the Manganese-Bismuth alloys are melt and solidified by the gravity, the different densities of the alloy ingredients cause the separation of the larger manganese part as a primary ingredient as well as its ascendance inside the melt so that it will no longer be available for the re-eutectic reaction. The MnBi fraction in terrestrial mineral samples is much below the 20% w/w. Therefore, under earth conditions, up to now only the production of pure MnBi using dust technology (such as thin tablets and by growing small mono-crystals) was possible[107].

Magnetic properties of Mn-Bi alloy

The magnetic properties of the MnBi alloy have been extensively studied due to the high magnetic mono-axis anisotropy (2.23107 erg/ cm^3 at 500 K) of the LTP phase and the magneto-optic properties of the QHTP phase, which can be used in permanent magnets and magneto-optic memory devices. The LTP phase exhibits magnetic torques of 4.0 and 3.95µB/Mn. At 550 K magnet-crystal anisotropy 9.0 T and demagnetizing ability 1.8 T have been observed, values which are very interesting as far as high temperature applications are concerned[108].

Hysteresis Loop

By drawing the magnetization curve of the hysteresis loop, as a function of the externally applied magnetic field (H), it is easy to represent the macroscopic properties of the materials. The characteristics of the loop suggest the kind of applications that the material[9] can be exploited. In Figure B6.9 the hysteresis loop M(H) at room temperature of the Mn-Bi alloy can be seen, which was used as a catalyst to produce carbon nanotubes.

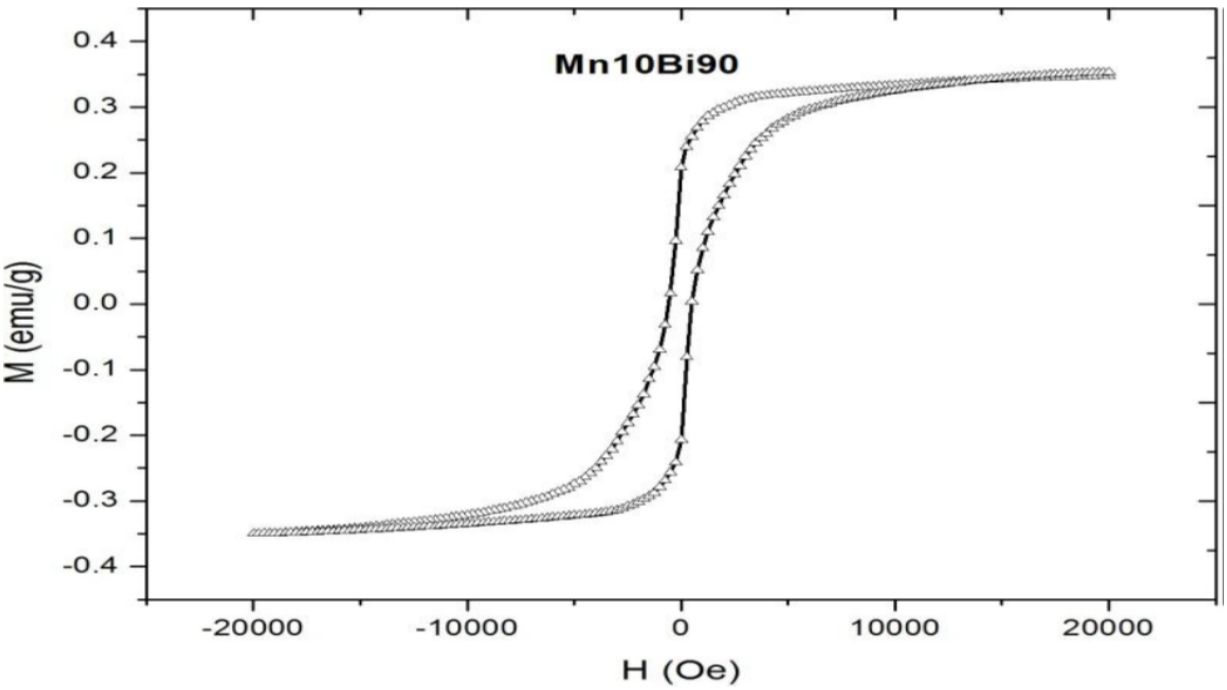

Figure B6.9: *Hysteresis loop curve for the Mn-Bi alloy*

B7. Graphene oxide (GO)

Graphene had been studied theoretically, by Wallace[111], only in 2010 Novoselov and Geim were awarded with Physics Nobel Prize because they managed to isolate graphene from graphite for the first time, using a simple mechanical way[110]. The difficulty was not just to compose graphene but to isolate large graphene sheets, thermodynamically stable so that the study and characterization of its properties would be possible.

It turned out very rapidly that this exceptional material showed many significant properties. Due to the fact that holes and electrons in graphene have potential for high carrier movements, this unique material formed an intriguing field for physics[112] as far as properties such as half-integer quantum Hall effect at room temperature[113,114], spin transport[115], high elasticity[116], electromechanical modulation[117], ferromagnetism[118] are concerned. The main target and interest after the first experiments took place on micromechanically cleaved graphite, a method which led to low yields, will be to establish ways for more massive graphene production, meaning towards the direction of large scale production[118,119,120]. Up to date, chemical vapor deposition was used to form and transfer the as-prepared films to arbitrary substrates[109] and has led to remarkable results considering the crystalline quality of the layers, as well as the derived mechanical and electrical properties. Regardless this fact, the issue of the controllable single or multi-layer large-scale deposition remains to be further investigated and solved. Here should be underlined the significance of good graphene adhesion to the substrate.

Nevertheless, the basic disadvantage of graphene is its chemical inertia in different solvents, a fact that restricts its usage in forming novel hybrid materials. Therefore, many research groups have turned the tide towards the production of graphene oxide (or graphite oxide or graphitic acid), which began decades ago[121,122]. First, the British chemist Brodie[123], in 1859, studied the behavior of graphite, the effect of a strong oxidant ($KClO_4$) and by the presence of an also strong acid (HNO_3). According to Brodie, the ingredients of the final material were carbon, hydrogen and oxygen at a 61.04:1.85:37.11 ratio, having that way achieved to increase the mass of the initial graphite quantity. The repeated oxidation procedures resulted in a further increase of oxygen, reaching to a limit after four oxidation reactions. In the end, Brodie concluded to a final material, which can be dispersed in water neutral or alkaline pH, but not acid, naming it “graphitic acid”. After 40 years, Staudenmaier[124] optimized the chemical oxidation of graphite increasing the presence of oxygen in the final material using the same oxidation reaction as Brodie did. Finally, Hummers and Offeman[125] developed a different graphite oxidation method using $KMnO_4$ as oxidant and dense sulfuric acid (H_2SO_4) as acid, achieving this way the same graphite oxidation levels. As a result, other similar graphite oxidation methods have been examined, but the thing that needs to be marked is that graphite oxidation depends on the oxidants which take place in the reactions, the graphite form and the reaction conditions. In order to comprehend the reactions taking place in graphite oxidation, it is much easier to study the reactions of the oxidizing means that are used during the graphite oxidation. Brodie and

Staudenmaier use nitric acid which is commonly used as an oxidant in surface modification using aromatic rings, such as carbon nanotubes by formation of groups such carboxyl-groups, accompanied by a gas release NO_2/N_2O_4[126,127]. On the contrary, in Hummers method, $KMnO_4$ and H_2SO_4 react with each other producing manganese heptoxide, as seen in the following reactions and which is considered to be a strong oxidant when comes to touch with organic compounds.

$$\mathbf{KMnO_4 + 3H_2SO_4 \rightarrow K^+ + MnO_3^+ + H_3O^+ + 3HSO_4^-}$$

$$\mathbf{MnO_3^+ + MnO_4^- \rightarrow Mn_2O_7}$$

In general, graphite appears with different morphologies while the most common to achieve the best oxidation is the one of graphite flakes, which contains a large number of localized defects that are only useful during oxidation process. The graphite oxide structure is quite complex and for this reason many models have been developed. According to Hofmann and Holst[128] a large number of epoxy-groups has been developed (C_2O) as represented in Figure B7.1. An alternation of this graphite oxide structure model is the one of Ruess in 1946 who suggested the existence of hydroxyl-groups along the length of the graphite sheets[129]. With this model it is verified successfully that the hydrogen percentage according to stoichiometric analysis, as previously mentioned, and also includes the presence of sp^3 carbon atoms in relation to the previous model which consists only of sp^2 hybridized carbon atoms (see Figure B7.1).

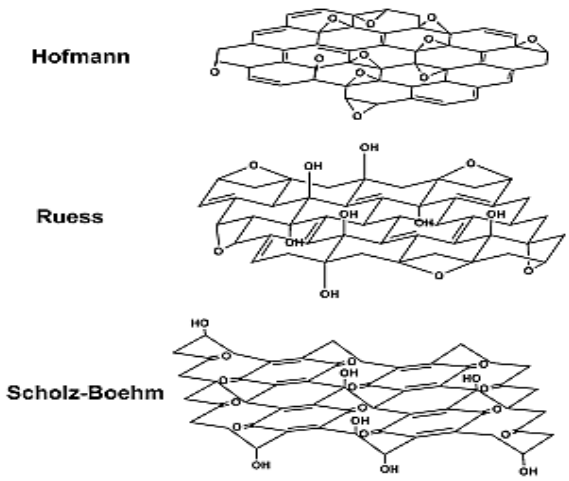

Figure B7.1: *Structural graphite oxide models*[109]

In the end, in Foster model which is the most prevailing one, epoxy- and carboxyl-groups are only formed on the edges of the material sheets[130,131]. As a conclusion, graphite oxide is a derivative of graphite, which contains oxygen groups (hydroxyl-, epoxy-, carboxyl-groups), which are covalently bind on its surface while this material restrains its laminate structure

with a larger interlayer space than the one in the initial graphite, because of the presence of water molecules between its sheets.

The graphite oxide structure leads to properties such as expansion (hydration) and intercalation. Following this, graphite oxide is a material which can host in its interlayer space several molecules, as large length carbon chains, transition metals, various hydrophilic molecules as well as polymers, forming this way promising hybrid materials as far as applications with "clever" properties are concerned[132].

The dispersion of graphite oxide in a solution is significant in the formation of derivatives and depends on the kind of the solvent but also on its surface modification which occurs during the oxidation. Up to date, it has been found that the larger the polarity of the surface is, the better the dispersion in polar solvents (like water) will be[133]. In figure B7.2 the interaction between graphite oxide and water, as well as other solvents is observed.

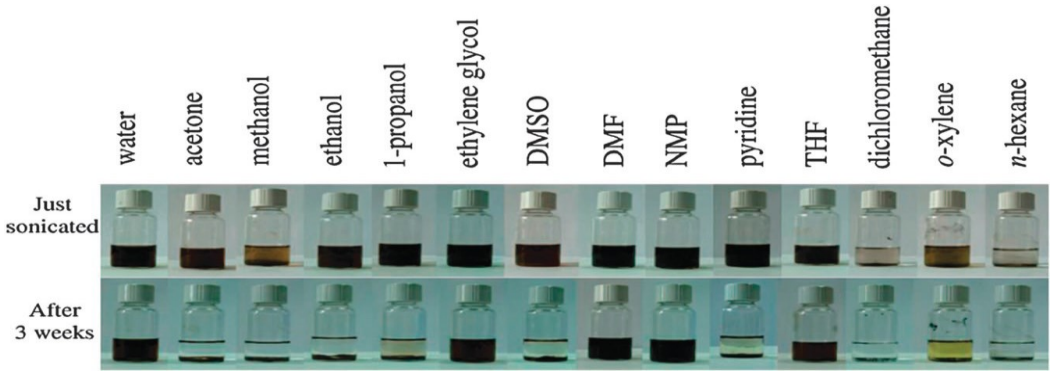

Figure B7.2: *Dispersion of Graphite oxide in water and 13 organic solvents directly after sonication treatment (on the top) and after 3 weeks of the treatment (bottom)*[211]

The presence of polar groups on the surface of graphite oxide makes it a unique material which can host a variety of molecules (organic and inorganic) in its interlayer space, such as hydrocarbon chains[133], transition metal ions[132], polymers and other hydrophilic molecules[134].

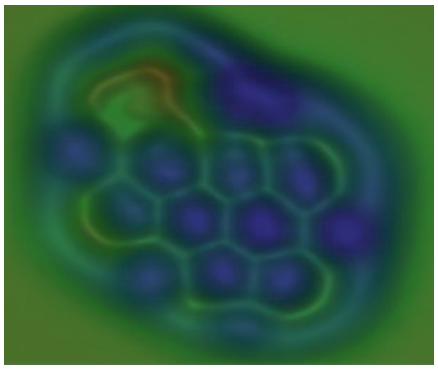

Figure B7.3: *Graphite oxide bonds by Atomic Force Microscopy (AFM)*[135]

Adding various groups in graphite oxide sheets via covalent or non-covalent bonds leads to production of chemically modified graphene (CMGs) with the cause to be used for various

applications because of its unique properties. The chemical procedures that are followed to modify chemically these 2-D nano-structures are summarized in two categories[136]:

- Attachment of chemical groups on the functional groups of graphite oxide sheets via covalent bond formation.
- Non-covalent attachment of molecules on the external graphitic surface of the sheets.

1) Covalent attachment: On the surface of graphite oxide sheets there are functional oxygen groups, such as epoxy-, hydroxyl- and carboxyl-groups[137]. The chemical modification of the graphite oxide surface by various molecules can be achieved with various ways, because of the molecules property to be selectively adjusted on one or more functional graphite oxide groups[137] via the following pathways:

i) ***Covalent connection of organic molecules with the carboxyl-groups which have been developed on graphite oxide surface.*** Small organic molecules are connected covalently with the carboxyl-groups of the graphite oxide. The conduction reactions often demand the activation of the acid positions. Adding constantly nucleophilic molecules (amines or hydroxyls), covalent bonds are formed with the active graphite oxide sheets groups via amides or esters[138].

ii) ***Nucleophilic substitution reactions between organic molecule amine groups and epoxy-groups which have been developed on the surface of graphite oxide.*** The groups that prevail in such reactions are the epoxy-groups of graphite oxide sheets as following: the terminal amine-groups ($-NH_2$) of various organic molecules are attached on the graphite oxide sheets via ring opening reactions of the epoxy-groups. The method is established as the most promising one amongst other methods, to produce large quantities of chemically modified graphite oxide, as the nucleophilic substitution reactions are performed in room temperature and in aqueous means. All types of aliphatic and aromatic amines, amino-acids, amino-terminal biomolecules, ionic liquids, polymer compounds of low molecular weight and xylene have been used to form graphite oxide derivatives via this method.

2) Non-covalent attachment: Non-covalent chemical modification of graphite oxide sheets is based on the formation of van deer Waals or π-π interactions between the groups of the graphite oxide sheet and multi-aromatic molecules. This kind of bonding is formed between bio-molecules[139], aromatic multi-cyclic derivatives[137] and in graphite oxide sheets via π-π interactions. These materials have often biological and medical applications.

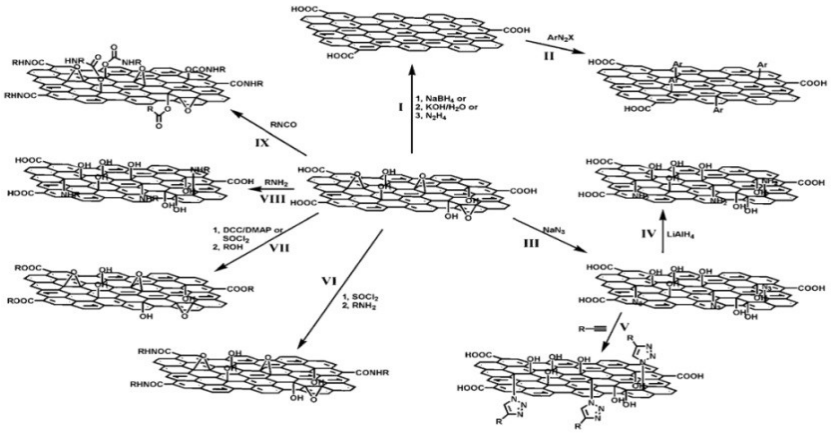

Figure B7.4: *Chemical courses which are followed by the chemical modification of graphite oxide*[211]

Graphite oxide is an electrically insulating material because of the sp^3 hybridized carbon atoms in its network. The reduction of graphite oxide to reduced GO (rGO) can improve its electrical properties[141]. On the sheets of graphite oxide there are some functional groups which contain oxygen. During the reduction process these groups depart at a high level, which leads to the formation of rGO, as observed in Figure B7.5.

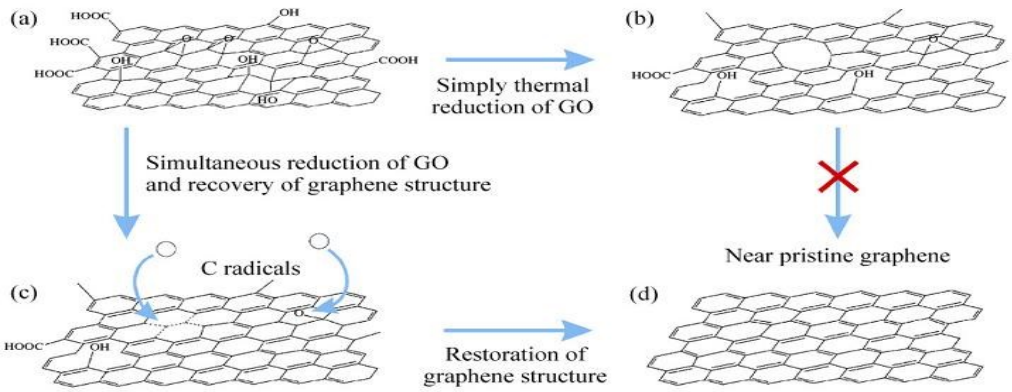

Figure B7.5: *Schematic representation of a graphite sheet (GO) before and after (rGO) reduction*[140]

Many methods to reduce graphite oxide have been developed. The main methods are chemical and thermal reduction.

Chemical reduction includes the exposure of graphite oxide in various chemical substances, such as hydrazine (hydrazine monohydrate[141,142], dimethylhydrazine[154,143], anhydrous hydrazine[144]), hydrides (sodium borohydride[145,146], sodium hydride[147]), hydroquinone[145,148] and π-phenylen-diamine[138], under different reaction conditions (temperature and time). In Figure 16 the way is presented, according to which the reduction in epoxy-groups of graphite oxide with hydrazine molecule is done.

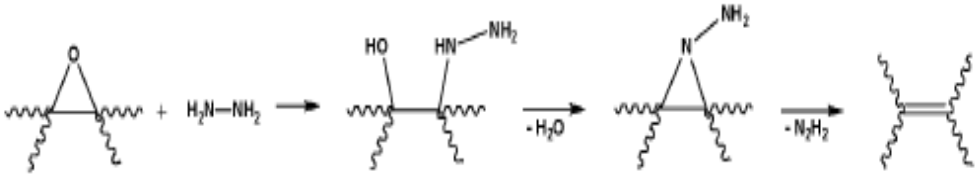

Figure B7.6: *Schematic representation of graphite oxide reduction using hydrazine*[109]

Thermal reduction forms a sufficient and economical method in order to produce graphene of high specific surface[149,150]. Heating the graphene oxide at 1050°C CO_2 gas pressure is released which leads to pressure increase. It has been estimated that pressure increases by 40 MPa when the temperature is 300°C and at 1000°C the pressure reaches 130MPa. Considering the fact that only a pressure increase around 2.5 MPa is capable of separating two graphene sheets, it is understood that the material is subjected to total exfoliation. The produced[109] material "TEGO" is found to exhibit specific surface ranging from 600-900 m^2g^{-1} via BET method.

Other methods that have been used for the reduction of graphite oxide are electrochemical reduction[151] and photo-thermal reduction[152].

Graphite oxide reduction to graphene (rGO) can improve its electric properties and to recompose the lattice. The non-covalent chemical modification of the reduced graphene oxide sheets is based on creation of van der Waals bonds or on π-π interactions between the groups of the reduced graphene oxide sheet and small molecules or polymers[153].

B8. Prussian-Blue Analogues

Introduction

One of the aspects of modern materials science that has been captivating scientific interest is low-dimensional systems[162] mainly because of their physical, chemical and biological properties. Several applications for photo-physical and electrical systems, electro-chromic devices[154-157], catalysis, molecular separation, gas storage devices, drug-delivery and as materials[158-161] and biosensors appear to be appealing. The formation of the products as well as their properties can be easily manipulated by changing simple external parameters (temperature, magnetic field, pressure light irradiation etc.)[162]. Therefore we have been lead to create novel materials such as Prussian Blue analogues (mixed valence poly-cyanides) which can switch from room temperature ferromagnetism to zero thermal expansion. The transition metal cyanides furthermore show interesting physical properties, such as photomagnetism[163], charge-transfer transition[164], photo-induced structural transition[165], negative thermal expansion[166], reduced-pressure induced spin transition[167]. The importance of incorporating Prussian Blue Analogues into tangible in real life applications arouses the issue of controlling properties like crystal size, shape, morphology etc. Also, one of the significant features of the transition metal cyanides is the potential to control the valence state of the transition metal sites[168].

Photo-magnetization

The photo-magnetic effect is the effect in which a material acquires (and in some cases loses) its ferromagnetic properties in response to light. The current model for this phenomenon is a light induced electron transfer, accompanied by the reversal of the spin direction of an electron. This leads to an increase in spin concentration, causing the magnetic transition[169]. Currently the effect is only observed to persist (for any significant time) at very low temperature. But at temperatures such as 5K, the effect can still exist for several days[170].

The energy diagram of the transitions between the ground state and the magnetic state can be observed in Figure B8.1; solid arrows are indicative of the absorption of photons and dashed arrows represent non radiative processes[170]. The magnetization and demagnetization (were not demagnetized thermally) occur through intermediate states as shown (right). The magnetizing and demagnetizing wavelengths provide the energy for the system to reach the intermediate states which then relax non-radiatively to one of the two states[170] (the intermediate state for magnetization and demagnetization are different and so the photon flux is not wasted by relaxation to the same state from which the system was just excited). A direct transition from the ground state to the magnetic state cannot be accomplished, and this leads to the magnetized state being metastable and persisting for a long period at low temperatures[170].

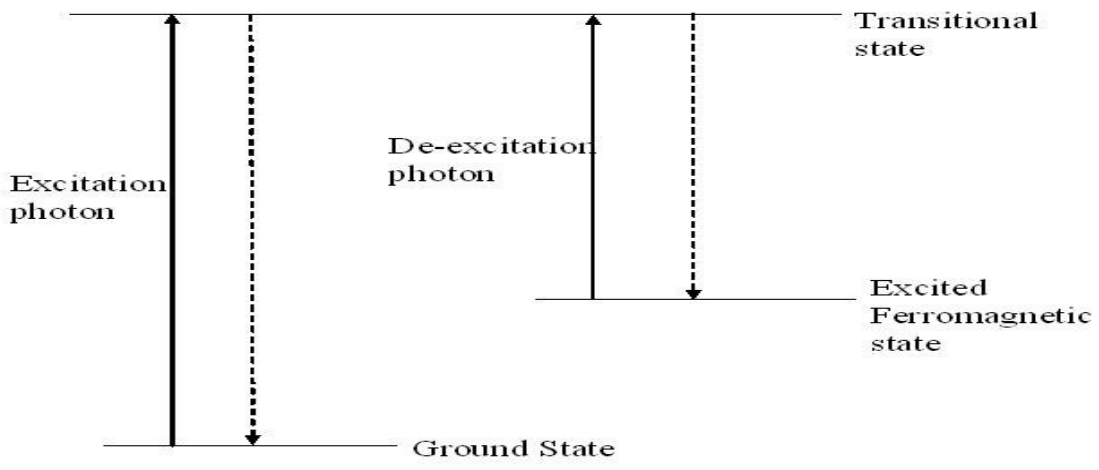

Figure B8.1: *Energy diagram of the transitions between the ground state and the magnetic state*[170]

Structure and Properties

The prototype transition metal hexa-cyanide is Prussian Blue (iron(III) hexa-cyano-ferrate(II)), which is the oldest coordination compound reported in the scientific literature[171]. This highly insoluble polymeric inorganic semiconductor has fascinated chemists since its discovery. The intense blue color, which was known to be unusual of ferric ion and ferro-cyanide ion solutions used in its preparation, was ascribed to an "oscillation of valence"[172].

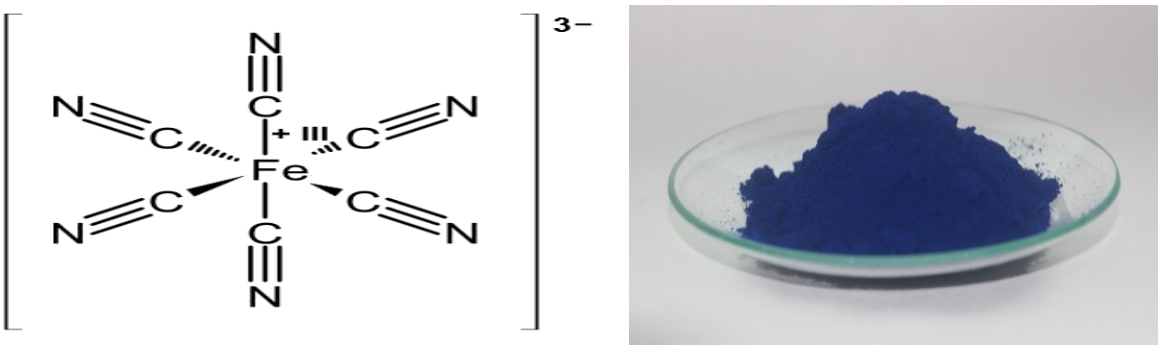

Figure B8.2: *Ferro-cyanide ion (left) and Prussian Blue pigment (right)*[172]

One of the most promising groups of molecular photo-magnetic materials is Co-Fe Prussian Blue analogues (i.e. compounds with the same structure and similar chemical make-up to Prussian-Blue[173]. A Prussian Blue analogue has a chemical formula $M_{1-2x}Co_{1+x}[Fe(CN)_6]\bullet zH_2O$ where x and z are variables (z may be zero) and M is an alkali metal. Prussian Blue Analogues have a face centered cubic structure.

The structure should be non-stoichiometric[173]. In this case the iron molecules are randomly replaced by water (6 molecules of water per replaced iron). This non-stoichiometric structure is necessary to the photo-magnetism of Prussian blue analogues as regions which contain an iron vacancy are more stable in the non-magnetic state and regions without a vacancy are more stable in the magnetic state. By illumination using the correct

frequency one or other of these regions can be locally changed to its more stable state from the bulk state, a fact which triggers the phase change of the entire molecule. By using the appropriate frequency in order to create excitation of the other type of region, the reverse phase change can be accomplished.

Prussian Blue Analogues exhibit several magnetic properties, which depend on their transition metal ion such as high Tc magnet[169,170], high Curie temperature values, spin glass behavior[173], magnetic pole inversion[171,172] and photo-magnetic behaviors[174,175]. Furthermore, they appear to have recently studied functions[175-178] such as pressure induced -CN group flip, zero thermal expansion and hydrogen storage[179]. Additionally, they show several electrochromic[180,181], photophysical[182] and possible analytical applications[183]. In order, to investigate these properties thin films of PBAs should be experimentally prepared. So far, commonly used techniques, such electrochemical deposition[184-187], casting from colloidal solution[188], as well as dip coating[189], do not appear to be the optimal ones due to the fact that they do not allow full control of the thickness in the nanometer scale. This issue was recently solved by the application of the Langmuir-Blodgett/Schaefer (LB or LS) technique.

One well-established method so as to form molecular architectures, such as PBAs is the Langmuir-Blodgett/Schaefer technique (described below in paragraph B.9). The formed materials show electrical and optical properties that are not possible to realize in conventional isotropic materials. The preparation of stable, molecularly ordered LB-films involves the following aspects: chemical synthesis, film preparation, physical characterization and film modification as well. The LB-films' structure[190] can be examined and defined accurately using Scanning Tunneling Microscopy (STM). In spite of the fact that a single monolayer shows two-dimensional characteristics, we are able to produce three-dimensional structures by performing subsequent depositions of certain thin film-layers, which could potentially consist even of different chemical compounds[190]. The advantage of the LB-method will be that it does not have to include and deal with thermal evaporation and sputtering. Furthermore, it can be applied at room temperature and in general under conditions that do not require the presence of vacuum[190].

Although a single monolayer shows two-dimensional characteristics, even three-dimensional structures can be formed, deriving from subsequent deposition of certain thin film-layers, which may even consist of different chemical compounds[191]. The advantage of the LB-method will be that it does not have to include and deal with thermal evaporation and sputtering. Furthermore, it can be applied at room temperature and in general under conditions that do not require the presence of vacuum[191].

The chemical stability, bi-chromic reactions, ease of preparation, and low cost of PB or its analogues modified electrodes make them obvious candidates for application in electro-chromic displays. Since such devices depend on electron and ion transport, the switching times depend on voltage and the amount of material on the electrodes. Also, PBAs can be

considered for energy storage and battery applications. Although the PBA battery has a low energy density it is advantageous due to its low cost and the highly reversible nature of the electrode reactions[192].

Up to now, the Langmuir-Blodgett technique has been applied in order to prepare ultrathin films containing highly oriented structures, the number of layers of which can be controlled at the molecular level[193]. The use of LB to form films which consist of Prussian-Blue, amphiphilic azobenzene cations and a smectite-clay leads to products the magnetic properties of which can be controlled by photo-illumination[194]. Furthermore, hybrid films of clay mineral and cationic compounds (e.g. Iron (II) complex cation) which were formed by the use of LB technique turned out to be stable structures, with any kind of cationic compound to be able to be incorporated inside the film and the density of the cations in the film can be controlled by the concentration of the clay dispersed in the solution[194]. Also, the same technique has been used to compose a multi-layer film of clay, Co-Fe Prussian-Blue and Di-dodecyl-dimethyl-ammonium bromide (DDAB) as an amphiphilic cation in order to exhibit that this way, magnetic thin films can be formed[195]. What is more, comparison in the magnetization of Prussian-Blue inside LB hybrid-films also composed of clay nano-sheets and alkylammonium cations and that of polycrystalline Prussian-Blue showed an increase in the first case[196]. In addition to this, PBA structures, consisting of layers of nano-sized clay platelets[162] (DODA-clay-PBA films) exhibited novel magnetic properties that range from super-paramagnetic to spin-glass properties also showing blocking glass temperatures above 65 K.

B9. Langmuir–Blodgett Technique

B9.1 Context

Over the last few years, being able to compose inorganic, organic or organic-inorganic molecules of desired structure and properties combined with thin films deposition technology enables the production of electrical, optical and bio-active materials and assemblies of several nanometers, an issue with large applications in sensors, screens and electronic circuits[197-199]. A thin film deposition can be achieved on a solid substrate using various techniques such as thermal evaporation, sputtering, electro-deposition, molecular beam epitaxy, adsorption from solution, self-assembly technique and Langmuir-Blodgett technique[200].

Langmuir-Blodgett technique is a very promising and advantageous synthetic method because it allows[109]:

- Precise control of the layer thickness
- Formation of multi-layer structures of various layer structures
- Homogeneous single layer deposition in large areas and surfaces
- Single layers deposition on every solid substrate, hydrophilic or hydrophobic.

B9.2 Theory

Langmuir Films

Langmuir films consist of surface active agents or surfactants trapped at the interface between two dissimilar phases, either liquid-liquid or liquid-gas[201]. Surfactants are molecules which are amphiphilic, meaning molecules that are composed of a hydrophilic part and a hydrophobic part. Hydrophilic groups consist of groups such as carboxylic acid, sulphates, amines and alcohols[201]. These are all attracted to polar media such as water and the forces acting upon them are predominantly coulomb type ($1/r^2$). Hydrophobic (or oleophilic) groups such as hydrocarbon chain, fats and lipids are much less (if at all) water soluble and the forces acting upon them are predominantly van der Waals ($1/r^{12}$ and $1/r^6$). Amphiphilic molecules are trapped at the interface because they possess these two totally different types of bonding within the one molecular structure[201].

When surfactants, which are dissolved in a non-aqueous volatile solvent, are applied onto a polar liquid surface, the solvent evaporates, leaving the surfactants oriented at the liquid-gas interface[201]. The hydrophilic head groups pull the molecule into the bulk of the water and the hydrophobic tail groups point to the air. A surface monolayer is only constructed if the amphiphilic balance of the molecule is correct; that is the balance between hydrophilic and hydrophobic parts. If the hydrophobic tail group is too short (not hydrophilic enough) the molecule will be dragged into the water and will be dissolved while,

on the other hand, if there is no hydrophilic part, the molecules may form thicker multilayer films on the surface or even evaporate[201].

The spontaneous spreading will continue to the point where the monolayer surface pressure equals the equilibrium spreading pressure[201]. This is the exact time when the monolayer has covered the whole surface and further solution drops will remain in the monolayer as floating lenses, due to the fact that no more spreading can be done. As a matter of fact, any material that has not been dispersed should be removed or else it may be deposited as bulk aggregates dipped into the monolayer[201].

Whenever the barrier is moving over the water surface the molecules come closer together and eventually form a compressed, ordered monolayer. The film produced by using this method is known as Langmuir film[201].

Langmuir-Blodgett-Schaefer: History

Langmuir-Blodgett films consist of monolayers stacked sequentially onto a solid substrate. A solid substrate is lowered into the water, breaking through the Langmuir film, provided that certain criteria have been met, the Langmuir film attaches itself to the substrate, coating it in a mono-molecular layer. Once the first layer has been deposited, further layers may be deposited on each subsequent pass of the surface through the air-water interface. Multilayers can therefore be deposited to produce a film, the thickness of which is the product of the individual molecular chain length and the number of times that the substrate has crossed the air-water interface[201].

The first scientific attempt and interest for molecular single-layers belongs to Benjamin Franklin, who observed, after having spread some oil on a pond, that one used teaspoon full of oil exhibited a calming influence over half an acre of water[201]. Considering a full teaspoon as 5 ml, this could lead one to the conclusion a film of thickness 2.5×10^{-7} m (about 100 layers) was covering half an acre (2,000 m^2). He reported this to the Royal Society of London in 1774.

More modern researches on molecular films were performed with Agnes Pockels, who worked on a kitchen trough due to her realization of cleanliness significance took into consideration the first containment of a single layer by means of a barrier. More extended investigations were carried out by Devaux, Rayleigh and Hardy. They were the ones who confirmed the molecular nature of the films formed this way. Langmuir did a deep research on the molecules pressure-area relationship on an aqueous surface[201]. What he realized was that the areas which were occupied by molecules such as alcohols, esters and acids did not depend on the length of the hydrocarbon chain, indicating at the same time that only the hydrophilic head groups were to be found into the sub-phase. Finally, Catherine Blodgett, having worked with Langmuir on floating monolayer properties, developed the technique of transferring the films onto solid substrates constructing, this way, multilayer films[201]. His results were released in 1934, 1935 and 1939.

The research around the formation of a monolayer in the surface between water and air was originally initiated by Langmuir in 1917, while the deposition of the films was studied by Blodgett (vertical dipping) and Schaeffer (horizontal dipping), where they both worked with Langmuir.

In general, all compounds may roughly be divided in two categories, substances that are water soluble or water insoluble[201,109]. The first ones are usually polar, being characterized for example by an non-homogeneous charge-distribution which can be defined by a dipole moment, μ through the equation μ=q x r, where q will be the charge carried by the parts that form the dipole and r the distance between them. Molecular polarity depends on the electronegativity difference between atoms in the compound and the asymmetry of the structure of the compound. An example will be the case of water molecule, where each of the two hydrogen atoms shares an electron pair with the oxygen atom (Figure B9.1). Due to that, the geometry of the shared electron pairs in the outer shell of the oxygen leads to the molecule's V-shape.

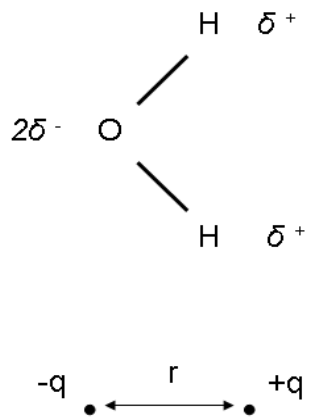

Figure B9.1: *Instant water molecule dipole*[109]

The strong electron-withdrawing tendency of the oxygen atom leads to local negative charge. This is found on the vertex of the V shaped molecule while the two hydrogen atoms stand with a local positive charge[109]. Despite of the fact that the water molecules are neutral, this charge separation allows the formation of a permanent dipole. The properties of water as a solvent depend on the attraction between its electrical dipole and the charge of the solute. In symmetrical molecules, where two bonding atoms share equally the electrons as in the benzene ring, C=C, or C-C long chains, do not possess any dipole moment and for that they are called non-polar[109]. Most of non-polar molecules are water insoluble (hydrophobic) at room temperature. The majority of the monolayer-forming substances which were used by the pioneers of this method consist of two parts: one part that is in favor of water and which, if found alone, will dissolve in water and a second part which exhibits the opposite property. Such molecules which consist of a hydrophilic and a hydrophobic part are called amphiphiles or surface active agents (surfactants). The hydrophobic part of surfactants consists of hydrocarbons or fluorocarbon chains while the hydrophilic part consists of a polar group such as –COOH, -OH, $-NH3^{+}$, $-PO_4^{-3}$, $(CH_2)_2NH_3^{+}$ etc.

The behavior of surfactants in a solution and in the water-air interface is defined by the physical-chemical properties of the hydrophilic-hydrophobic groups, considering size, shape, and hydration of the hydrophilic head. The most common prototypes of surfactant are the long chain fatty acids. An example of such a molecule is arachidic acid $C_{20}H_{40}O_2$, which is shown in figure B9.2.

Figure B9.2: *Arachidic Acid molecule*[109]

The long hydrocarbon chain forms the hydrophobic part (non-polar) and the carboxylic acid group (-COOH) the asymmetric polar hydrophilic (asymmetric polar) head of the surfactant. Langmuir indicated that these molecules do not constitute spheres but on the contrary they show high length/cross-section aspect ratio[109]. The balance between the chain length and / or the force of the polar group is the factor that offers those molecules the ability to float offering them the possibility to form a monolayer. In case the hydrocarbon chain turns out to be too long or the polar group too strong, then the molecule will dissolve.

Further investigation of the above leads to a conclusion that the hydrocarbon chain, which is used to form a monolayer should be big enough[198] in order to form the insoluble monolayer[202,203]. A general rule would be that carbon chains should have more than 12 carbon atoms. If the chain is smaller than that and insoluble into water, the amphiphilic part on the water surface tends to form micelles. These micelles are water soluble and prevent the formation of a monolayer on the air-water surface. On the other side, if the chain length is too big, the amphiphilic part tends to crystallize on the water surface and consequently does not form a monolayer. It is hard to define the optimal chain length due to the fact that the monolayer formation ability depends on the polar part.

Usually, most monolayer forming surfactants are brought onto a sub-phase, after having been dissolved in a proper solvent (often chloroform). With the term “sub-phase” the substance on which the monolayer will be created is defined. For the majority of the classic Langmuir-Blodgett experiments as sub-phase demineralized-deionized water with an 18.5MΩ resistivity is chosen. This low ion-content assures rules out the possibility for the polar head of the surfactant to get hybridized with minerals contained in natural water and therefore leave the properties of the monolayer undisturbed without any contaminants. Afterwards, very small amounts of the solvated surfactant are sprayed onto the sub-phase. In practice, this function is accomplished by spraying the surfactant on the sub-phase surface and waiting for the solvent (e.g. chloroform) to evaporate. Only then the organic molecules are able to compress and form a bi-dimensional solid. In fact, the driving force for this behavior will be the reduction of the free energy of the system. Due to this fact, when the surfactant comes in touch with water it accumulates on the air-water surface, leading to a reduction in water’s surface tension[204].

Surface tension

A description of the physics of the air-water interface, the forces that take place as well as the simple way to measure them, follows. The water molecules as they exist in liquid state are attracted to each other by electrostatic forces, known as van der Waals forces. Despite the fact that water molecule is electrically neutral, the distribution of charge in the molecule is not symmetrical a fact that leads to the creation of an instant dipole. This way, polar molecules are attracted to each other, an issue which justifies the cohesion of water molecules and contributes to viscosity and surface tension[205]. Van der Waals forces keep water in the liquid state. This only happens to the point at which thermal agitation becomes violent so as to break van der Waals bonds at the temperature of 100°C. It is easily understood that the bulk water liquid state is held through the isotropic cohesion between water molecules (Figure B9.3a) where every single molecules of the bulk liquid state is equally and uniformly pulled or push in all directions of space by its nearby H_2O molecules[205]. Therefore, the net applied force acting on each molecules (forgetting about gravity for a moment) is zero. As far as the boundary between the water liquid bulk state and the air gas bulk state is concerned, surface states by nature are at the boundary of two situations, representing a kind of 'transition' between pure bulk and the outside condition, and because of this they are different from the pure bulk (this applies equally to solid-solid or liquid-liquid interface of different materials). This 'transition' or interface states are very often simply structurally different, although this structural difference frequently leads to dramatically altered properties as compared to the pure bulk material. In that respect water is no exception, the surface water molecules behave quite differently from the bulk. In Figure B9.3 drawings are shown which we should take into consideration about air-water interfaces where the water molecules are the black dots, the forces acting on them would be the arrows, the bulk is represented by the grey zone and the interface exhibited by the lighter zone. As far as the first state (a) is concerned, the water molecules which are found at the top, at the boundary between air and water, are under the action of lateral and downward cohesion forces, an issue that takes place in a zero gravity environment[109].

Molecules exhibit a preference in being in the bulk where no net force act, than being on the surface, due to the net force pulling them inwards and therefore move until they construct a shape where the number of surface versus bulk atoms is decreased to a minimum, a flat leveled surface in a container (in the presence of gravity) or a sphere (in zero gravity)[109]. This initial diffusion of molecules from surface to bulk to reach the equilibrium state is going to lower the mean atomic separation and because of that increase the force between molecules at the surface. This force that appears and acts on any surface is called surface tension γ and is measured in N/m. Equally the surface tension is considered to be an excess free energy/unit area and counted in J/m^2. The surface tension is analogous to the vapor pressure, constant in a solid-gas interface, in dependence though with temperature. The surface tension on the other hand, decreases as the temperature ascends unlike the vapor pressure which increases with raising temperature. Furthermore, solids can

also show free surface energy although the direct measurement of this by the same techniques as with the solids is not excluded[201,202].

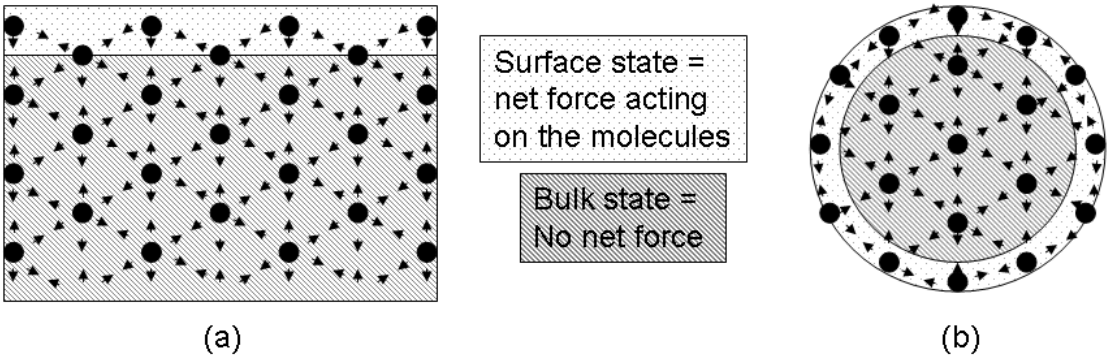

Figure B9.3: *Schematic representation of the origin of surface tension (a) for liquid inside a container (b) for liquid in a zero gravity environment (for both cases before equilibrium)*[109]

As mentioned earlier, the water-air surface possesses one additional free energy that comes from the molecule difference between the surface and the mass. This free energy is countable by the surface tension measurements[208,209]. When an amphiphilic compound in an insoluble in water solvent is placed on a water surface, the solution is quickly dispersed to occupy the available space. While the solvent evaporates, a monolayer is formed (Figure B9.4).

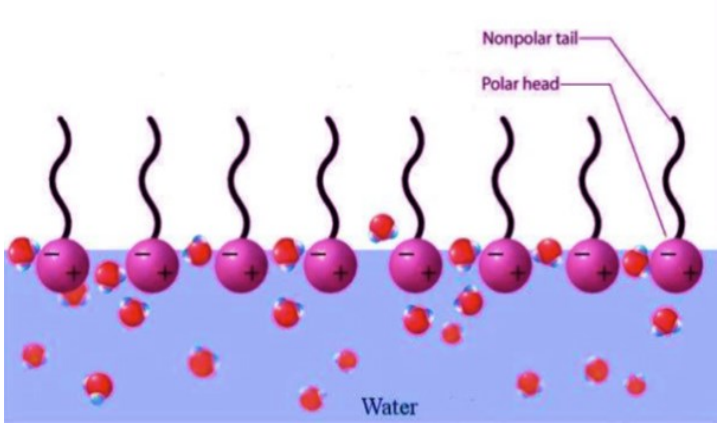

Figure B9.4: *Formation of the surfactant on water surface*[109]

On the other hand though, water contamination may possibly lead to alternation of the surface tension. Furthermore, the existence of a molecular film on a liquid surface will also affect the surface tension. Theoretically, surface pressure Π is stated as the difference between the surface tension of pure sub-phase (e.g. water) and the same sub-phase completely covered by molecules ($\Pi=\gamma_0-\gamma$). Under usual circumstances, surface pressure is measured by usage of the Wilhelmy plate[109]. According to the method, a plate, usually made of paper, is partially immersed in water (Figure B9.5). In the end, the total force which is

applied on the plate will be the sum of three forces: the gravity and the surface tension both heading downwards and the buoyancy of the plate, heading upwards. Therefore, the received equation will be:

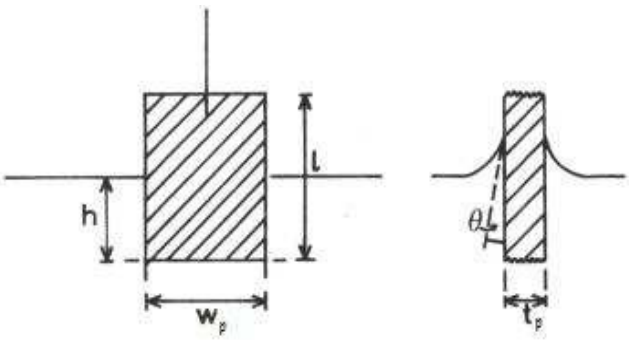

Figure B9.5: *Wilhelmy plate*[109]

$$F = F_{Gravitation} + \gamma \cos\theta .P - F_{Buoyancy}$$

$$F = m_P g + \gamma \cos\theta .P - m_l g ,$$

where the size of the plate is defined by l_p, w_p and t_p , ρ_p is the plate density, and P the perimeter of the plate. As the plate is immersed to a depth h in a liquid of density ρ_l, the net downward force is given by the following equation[109]:

$$F = \rho_p g l_p w_p t_p + 2\gamma(t_p + w_p)\cos\theta - \rho_l g t_l w_l h,$$

where γ is the liquid surface tension, θ he contact angle of the liquid on the solid plate and g the gravitational constant. The surface pressure can be extracted by measuring the change of force F acting on a plate without and with a molecular film present at the surface. In case where the plate is completely wetted by the liquid then the angle θ turns into zero, with cosθ = 1) and therefore, the surface pressure is acquired by the following equations:

$$F_0 = F_G + 2\gamma_0(t_p + w_p) - F_B$$

$$F = F_G + 2\gamma(t_p+w_p) – F_B$$

$$\Pi = \gamma_0 – \gamma = (F_0 – F)/2(t + w)$$

The method's sensitivity can be increased by using a very thin plate. The force is calculated by measuring the changes in the mass of the plate, which is directly coupled to a sensitive electro-balance. The monolayer can be formed at a stable surface pressure as well, which is activated using computer control and the engine of the device which is responsible for the movement of the barrier, a fact which is really helpful in the case when the film deposition is performed on a solid substrate.

The methods: Langmuir-Blodgett and Langmuir-Schaefer

As discussed earlier, when one injects a few micrograms of surfactant on the air-water interface the first thing that is going to occur will be the spreading of the molecules all over the free surface area. After the application of an external force on the floating surfactant molecules, they will be lead to change their positions within the trough and in the end, if the compression is sufficient, they shall form a solid film[109]. The exhibited monolayer compression undergoes several phase transitions that are two-dimensional analogues to solid, liquid and gas phase (Figure B9.6). In agreement with this, the phase diagram of a surfactant can be easily extracted by measuring a (Π-a) isotherm, which means extracting a relation curve concerning the pressure versus area per molecule while keeping temperature stable.

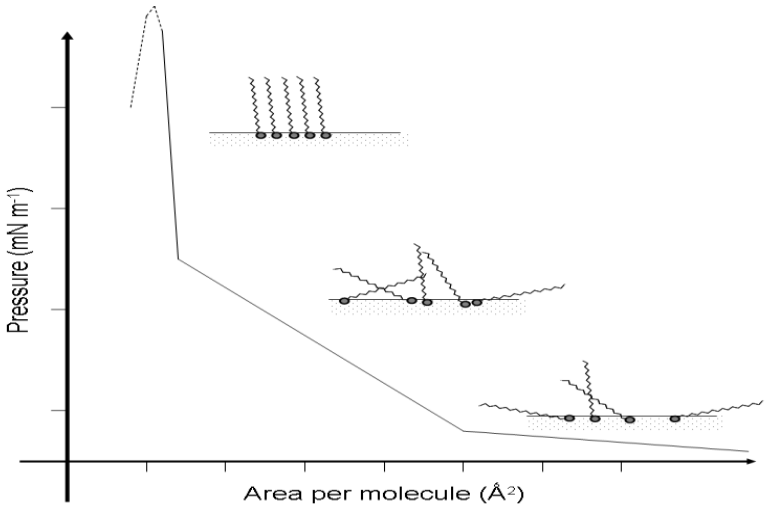

Figure B9.6: *Surface pressure in relation with area isotherm for a long chain organic molecule*[109]

In a usual run, after the molecules have been dispersed on the surface and the carrier solvent has evaporated, a two-dimensional gas phase is established, deriving from large distances between the molecules. What follows the solvent evaporation is the situation where the barrier is able to move in order to compress the molecules, as long as the pressure via surface is changing and observed. The pressure-area isotherm allowed Langmuir to prove the existence of different phase transitions for different kinds and combinations of systems.

In the gas phase the area per molecule is relatively large. Due to this fact, the floating surfactant molecules hardly interact with each other[109]. As a matter of fact, since we are aware that every molecule possesses an energy kT (kT/2 per degree of freedom) this will force them to move and collide with other molecules, as well as on the wall of the container exactly as it happens with a perfect 2D gas. One can estimate the pressure of this 2D gas by using the ideal gas law (PV=NkT); if taken into consideration that P is the pressure of the 2D gas, A the total container area, N the number of molecules and kT the Boltzmann constant

times and T the temperature, then the gas law turns into PA=NkT. A first transition from gas to liquid can be observed during the motion of the barriers. This exists for values of surface area estimated according to the size of the long axis of the molecules. As far as this state is concerned, the molecules are found arranged in a coherent way but still loosely packed. Further compression leads to the next phase transition at which liquid turns to solid state. Molecules found under these conditions themselves closely packed[109]. If one applies more pressure, this has as a result the instant and abrupt ascend in surface pressure, which is exactly what occurs in the case of a 3-D solid. By further increase in compression, a monolayer 'collapse' follows[109].

The 'collapse' can be realized and observed as a sharp breaking of the solid state. In case the collapse takes place, one can realize a decrease in pressure which leads in turn to the reformation of the monolayer into a double layer or triple layer which in the end turns into a micro-crystallite. It is obvious (Figure B9.7) that the increase in pressure on a well-defined and ordered compact layer leads to the formation of cracks (left middle and bottom panels), while further compression has as result the molecules turn-over.

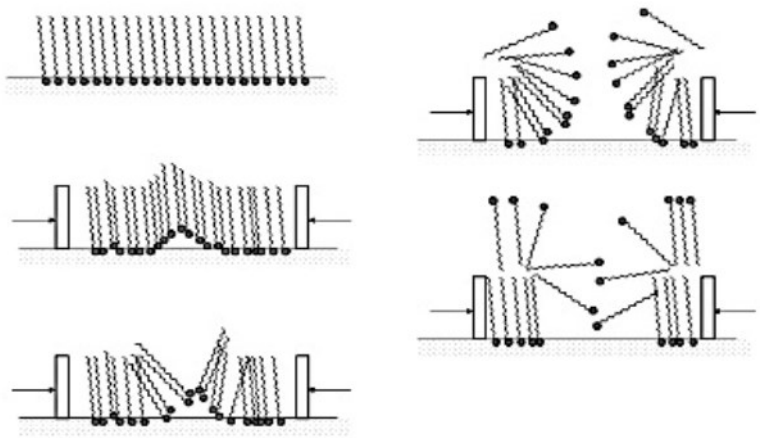

Figure B9.7: *Schematic representation of the 'collapse': further increase in the applied pressure might lead to overlapping and the formation of double or triple-layer or even crystallite[109]*

As a logical assumption it is considered that in order to make a deposition, the phase which will be chosen is intended to be the solid state. Finally and in order to perform the depositions on a solid substrate, one can use two methods: the Langmuir-Blodgett (vertical deposition) and the Langmuir-Schaefer (horizontal deposition) methods, with the first being the most common one (Figure B9.8). In order to perform a successful deposition, it is of great significance to achieve a fine meniscus and maintain a stable transfer speed. In the case where the transfer speed is relatively slow, the orientation and packing of the single layer is going to be preserved and stabilized during the deposition, allowing it to be transferred on the solid substrate. In case of the speed of dipping being too fast, then the monolayer cannot be successfully deposited. Therefore, its crystalline structure is not maintained while in the worst case no deposition takes place in the end[210].

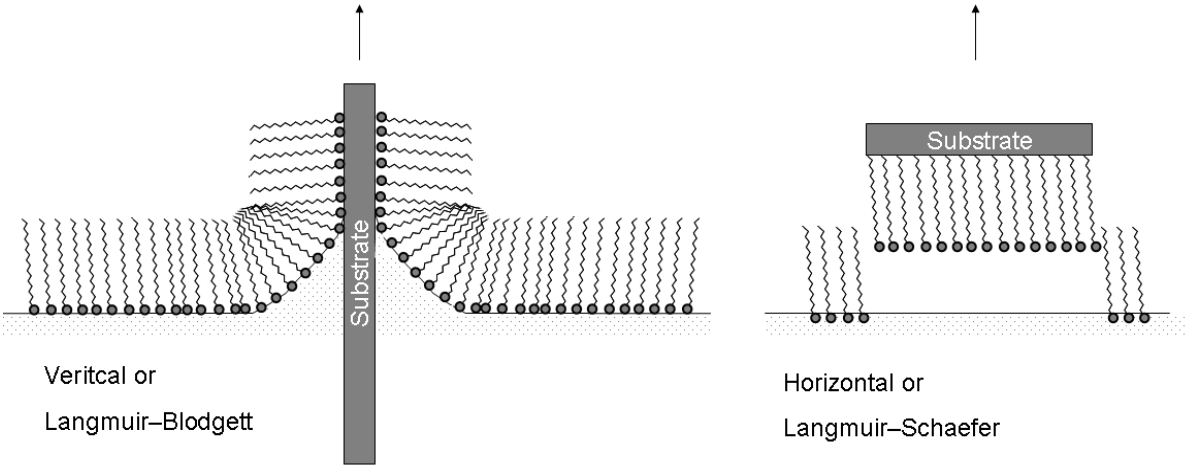

Figure B9.8: *Schematic representation of the vertical (Langmuir-Blodgett) and horizontal (Langmuir-Schaefer) multilayer films transfer method*[109]

The most common vertical deposition deals with an immersion (down-stroke movement) and emersion (upstroke movement) of the solid substrate, which occurs in a repeated way and leads to the formation of the multilayer (Figure B9.9), the so-called Y-type and consists of a sequence of surfactant layers with alternating hydrophobic-hydrophobic and hydrophilic-hydrophilic interaction. It is expected that the pre-mentioned structure leads to the formation of the most stable films. Despite of this, X and Y type films can also be formed using only down-stroke or up-stroke movement to achieve deposition. This method can be achieved by the usage of surfactants which consist of a slightly hydrophilic head group or a slightly polar-end alkyl chain.

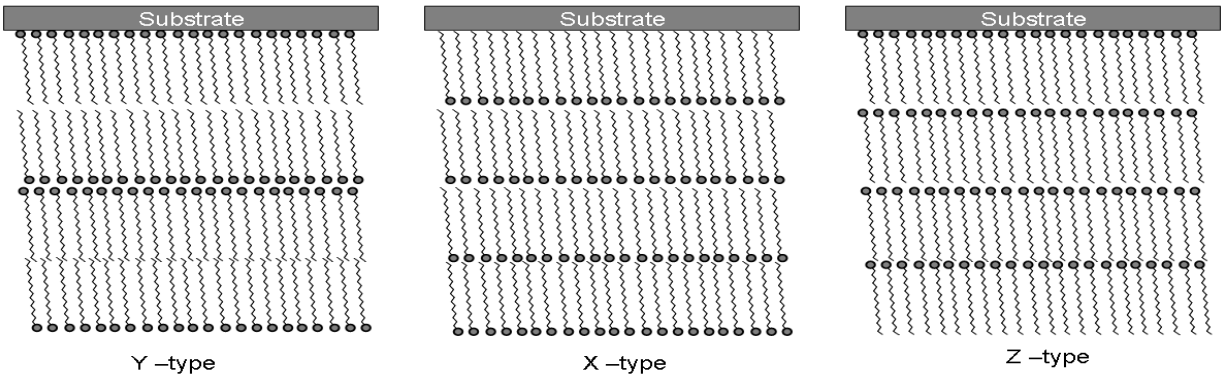

Figure B9.9: *Y, X and Z-type of multilayer deposition (y-type is center-symmetric while the X and Z are non-center-symmetric)*[109]

The second deposition method, which was used here, will be the horizontal dipping method which is widely known as the Langmuir-Schaefer method (Figure B9.8). This process is usually used and preferred when dealing with rigid films. According to this method the

rigid substrate is being moved very slowly at very low speed towards the surface, usually at ~2-4 mm/min, the monolayer is deposited and then lifting it up at ~1-2 mm/min to the point where substrate and water are apart[109]. In this type of deposition, the monolayer structure and orientation are preserved, leading to the formation of an X-type film.

Self-assembly

The term self-assembly refers to the independent organization of structural elements in patterns or structures without external interference and can be observed in every size scale. The self-assembly phenomenon can be described as the spontaneous formation of complex structures out of pre-designed structural units that contain multiple energy scales and a large number of degrees of freedom. This method[211] is encountered in nature by the spontaneous organization of various biological molecules, while in nanotechnology, is used for the organization of nano-dimensional elements (nanoparticles, monomers, polymers, in ordinal form, forming powerful bonds with the substrate and weak bonds between the elements[212].

Certain molecular groups, when absorbed on respective surfaces, form self-assembly monolayers, the so-called SAMs. These procedures lack central control on the individual structural units (molecules). On the contrary, the structure control is distributed in the whole system. All structural units, despite their only regional interaction, contribute equally to the self-assembly of the system. Structures which derive from self-assembly of a system's structural units constitute the new structural units for a totally new self-assembly at a higher level. Finally, self-assembly procedures can be accompanied, in each case, by spontaneous symmetry breaking phenomena and phase transitions as the system transcends from an initial disorder state to a well-defined order state.

When referring to self-assembly monolayers (or SAMs) one means the molecular systems of high order which are formed by absorption of a surfactant on a specific substrate. Surfactant compounds consist of low molecular length alkyl-groups (10 to 20 methylene groups), which on one edge have a group (head) that strongly interacts with the solid surface (e.g. mercaptane groups, -SH) and leads to bond formation (Figure B9.10).

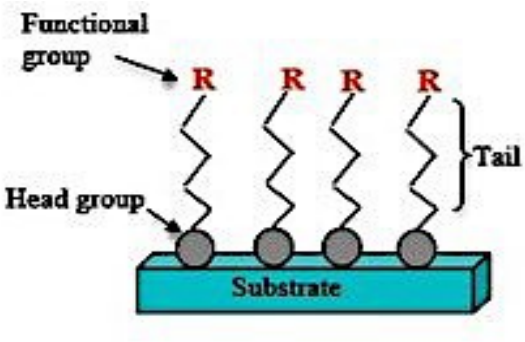

Figure B9.10: *SAMs' structure: head group interacts with the substrate and R is the functional alkyl-group*[211]

SAMs exhibit a variety of characteristic properties:

(i) they are easy to prepare,
(ii) one can easily adjust their properties by simply changing their structure in molecular level and
(iii) they are useful as structural units for constructing more complex structures.

SAMs have been the subject of intense research because they offer a unique opportunity to comprehend self-assembly phenomenon, the interface phenomena as well as procedures related to the interactions between molecules, molecules-surface and molecules-solvent such as soppy, paste, lubricating and corrosion. Furthermore, SAMs have various applications, such optics and electronics, as means of controlling the hydrophilic-hydrophobic surface character, in molecular identification, in nanotechnology, in drugs transfer and, recently, in bio-sensors[212,213].

B10. Characterization Techniques

In order to study the properties of various forms of carbon nanotubes as well as of all the chemically modified derivatives of theirs, such as oxidized and chemically modified carbon nanotubes, a variety of experimental analytical techniques can be used. The techniques which were used in this thesis are the following: X-Ray Diffraction (XRD), Raman spectroscopy, Differential Thermal Analysis (DTA), Thermo-gravimetric Analysis (TGA), Scanning Electron Microscopy (SEM), Transmission Electron Microscopy (TEM), Ultraviolet-Visible (UV-Vis) Spectroscopy, Infrared Spectroscopy (IR), Mössbauer Spectroscopy, Superconducting Quantum Interference Device (SQUID) and Vibrating Sample Magnetometer (VSM).

B10.1 X-Ray Diffraction (XRD)

The German professor Wilhelm Conrad Röntgen (1845-1923) in 1895 at Würzburg University (Franken) discovered the X-rays while performing experiments in order to study ionization due to collision phenomena. During these experiments which were being performed at high voltage (30-50 kV), the researcher observed that a piece of paper covered by fluorescent material was glowing for as long as the cathode tube was operational, even when that paper would be transferred to a nearby classroom. At a certain moment, Röntgen saw the image of his palm on the fluorescent screen, where the bones where absorbing more radiation than the surrounding tissue. This unknown radiation was initially named X and after the researcher's death, Röntgen radiation. For this discovery he was awarded with Nobel Prize in Physics in 1901.

The X-Rays are electro-magnetic radiation which forms part of the electro-magnetic spectrum. The electromagnetic radiation is an energy form which spreads in space and can overlap with atoms altering their energy state. The radiation consists of two square waves, which have the same frequency and same wavelength. One wave is a pulse electric field and the other one a pulse magnetic field. In vacuum, the wave spreading speed is equal to the light speed c. The wavelength λ of the electromagnetic radiation and its frequency ν are connected with the formula[214]: $c = \lambda \times \nu$.

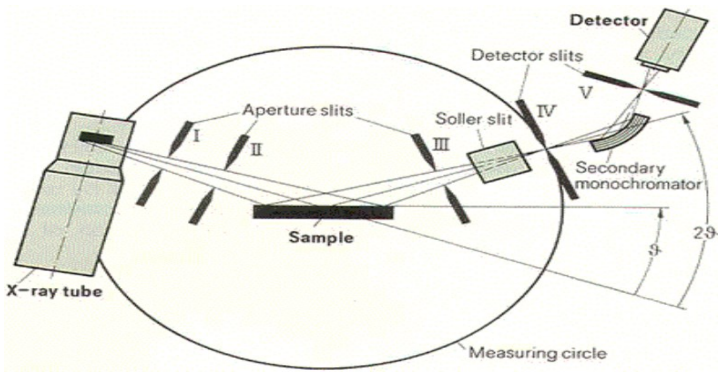

Figure B10.1: *Operation of an X-Ray Diffraction device*[214]

The most common way to produce X-Rays is the collision of high energy electrons on the surface of a high atomic number target metal. These electrons while colliding to the target excite the electrons of the internal metal layers causing them to be abstracted. This “gap” in the internal atom layer is covered by electrons of higher energy external layers and the energy difference between the two layers is released by the transmission of a photon (X-Rays)[215].

The wavelengths of the X-Rays are of the same size class as the distances between the atoms in crystal materials and so the crystals act like diffraction barriers for the X-Rays. In Figure B10.2, the electron beam while hitting the crystal surface scatters partially by the atoms on the first layer. Another part is scattered by the second and the procedure continues, leading to contribution phenomena. The demand so as to have contribution was initially expressed by W. L. Bragg: $\eta \times \lambda = 2 \times d \times \sin\theta$, where: η is an integral which defines the class of the produced radiation, λ the wavelength of the incidental beam of X-Rays, d the distance between the levels at the under-study crystallographic direction and θ the angle between the incidental beam and the reflective crystal level (Bragg Angle).

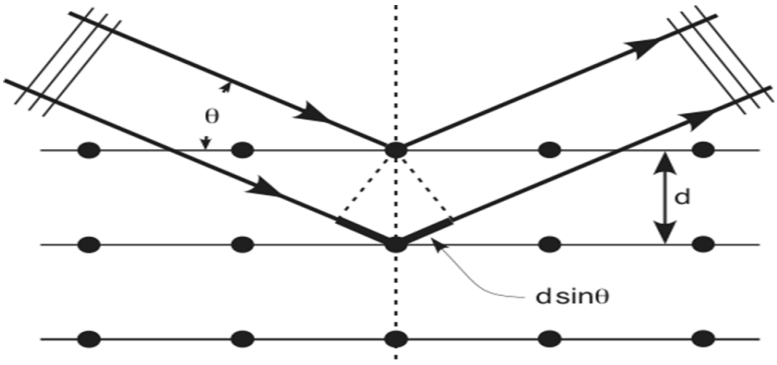

Figure B10.2: *X-Ray Diffraction of a crystal*[215]

From the Bragg’s law it is clear that the diffraction angle depends on the distance between the net-levels on the corresponding crystallographic direction. Different level groups inside a lattice exhibit different values of the distance between them. The distance d_{hkl} between two levels, measured in 90° to the levels angle, depends on the level’s Miller indicators (h, k, l) and the lattice constants (A, B, C). Their exact function depends on the crystallographic system[215].

B10.2 Raman Spectroscopy

Raman spectroscopy is based on the diffusion phenomenon of a beam of light through a transparent substance. If a mono-chromatic radiation beam is used almost the whole energy which is diffused in the sample will have the same radiation intensity as the incidental radiation (Rayleigh diffusion), but also, one part of it will be altered to have distinguished frequency values above and below of the incidental radiation (Raman diffusion, which was observed in 1928).

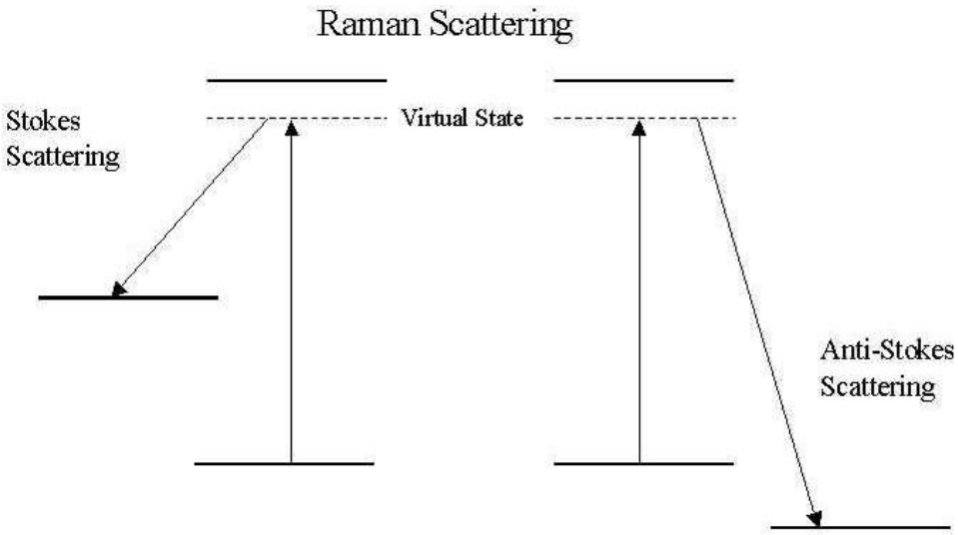

Figure B10.3: *Stokes and Anti-Stokes lines*[216]

In modern Raman spectroscopy lasers of specific frequency values are used as radiation source. The beam which is going to pass through the sample will endure two kinds of diffusion. Stokes lines are called the spectrum lines having lower frequency than that of the incidental laser radiation and are caused by the collision between photons and molecules which are in the ground energy state. Anti-Stokes lines are called the spectrum lines which have relatively higher frequency and are caused by the collision between photons with molecules which are in excited energy states, resulting in the transfer of the excess of energy to photons and the return of molecules to their initial ground-state. (Figure B10.3)

When radiation of frequency ν irradiates molecules, molecules are being subjected to elastic refraction. A sensor receives the refracted photons of energy h x ν and of frequency ν. In reality though, there can be an exchange of energy during the non-elastic collisions between photons and molecules and then the molecules gain or lose an amount of energy, according to the laws of quantum-mechanics. Whenever there are changes in the vibrating or rotating molecule energy then a difference between two allowed states is observed. In the Raman phenomenon the quantum energy changes derive from the ability of a chemical molecule to become polarized, which means that the atom or molecule has the ability to be subjected to a separation of positive and negative charge centers in an electric field[216].

According to the classical theory, the Raman phenomenon can be described as following: the intensity of the electric field (E) from the electro-magnetic wave depends on the time, as it is seen in the function:

$$\mathbf{E = E_o \cos 2\pi \nu_o t \ (1)},$$

where E_o is the vibration width and ν_o is the laser frequency. If a bi-atomic molecule is radiated with this light, then an inductive bi-polar torque can be caused,

$$\mathbf{P = \alpha E = \alpha E_o \cos 2\pi \nu_o t \ (2),}$$

where α is a susceptibility constant of polarization (polarizability) of the molecule (or polarity). If the molecule is vibrating with a frequency ν_m then the nuclear shift q is written as:

$$q = q_o \cos 2\pi\nu_m t \quad (3)$$

For small vibration widths, α has linear relation to the q. Therefore, it can be written that

$$\alpha = \alpha_o + (\theta\alpha/\theta q)_o q_o + \ldots (4)$$

The quantity α_o is the polarity in balance state and $(\theta\alpha/\theta q)_o$ is the change rate of the polarity in relation to change of the variable q. Combining the relations (2), (3) and (4) the following function is received:

$$P = \alpha_o E_o \cos 2\pi\nu_o t + (\theta\alpha/\theta q)_o q_o E_o \cos 2\pi\nu_o t \cos 2\pi\nu_m t =$$

$$\alpha_o E_o \cos 2\pi\nu_o t + 1/2(\theta\alpha/\theta q)_o q_o E_o [\cos\{2\pi(\nu_o + \nu_m\} + \cos\{2\pi(\nu_o - \nu_m)t\}] \quad (5)$$

According to the classical theory, the first part shows a swinging bi-pole, which radiates at frequency ν_o, the same as the frequency of the stimulator (Rayleigh scattering), while the second one refers to the Raman scattering, of frequency $\nu_o + \nu_m$ (anti-Stokes) and $\nu_o - \nu_m$ (Stokes). If the quantity $(\theta\alpha/\theta q)_o$ equals zero then only the first term of the equation survives, giving exclusively elastic scattering. Therefore, in order for the Raman scattering to exist a change in polarity during the vibration is necessary[217].

Raman scattering is a very weak and rare phenomenon; only one of ten billion incidental photons are scattered by Raman. The weak nature of the phenomenon requires the existence of very powerful radiation sources such as a laser.

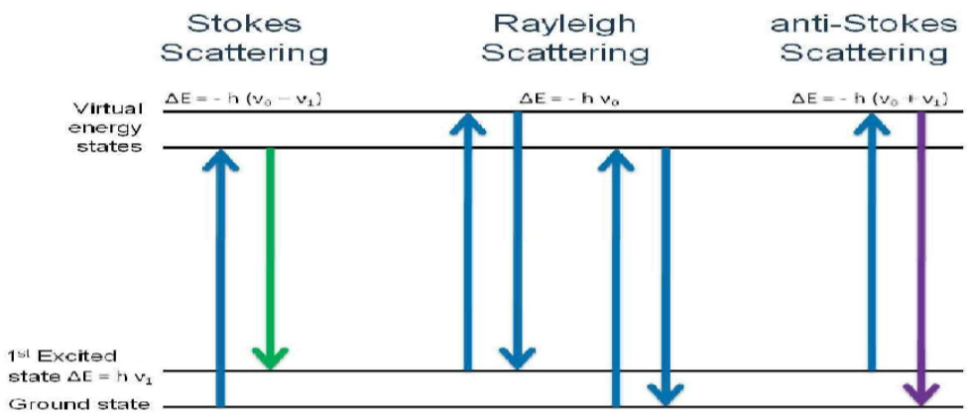

Figure B10.4: *Rayleigh, Stokes and anti-Stokes scattering*[217]

Using Raman spectrometry we are able to define the identity of the material, the phases of which it consists, whether it has obtained impurities etc. Usually, a Raman spectrum is a separate fingerprint of a specific molecule or material and can be used for its quick identification or separation from other molecules or materials via special tables which contain Raman spectra[217].

B10.3 Thermal Analysis

When a substance is heated it undergoes a change in its state such as phase change (fusion, evaporation etc.), cracking etc. These changes are almost always followed by temperature changes or (and) sample mass changes, which are studied and analyzed using thermal analysis techniques. Thermal analysis includes various techniques with which we can measure one or more physical properties of a substance or of the products of its cracking, when this substance is heated or cooled at stable heating or cooling rate. The phenomena taking place during the thermal analysis of a sample are separated into two categories, physical and chemical.

There are approximately a hundred thermal analysis techniques. In table 4 the main thermal analysis techniques, their international abbreviation and the property that is changing during the thermal treatment of the sample are included[214, 215].

Table B10.1. *Thermal Analysis Techniques*[214]

TECHNIQUE	ABBREVIATION	PROPERTY
Differential Thermal Analysis	DTA	Temperature
Differential Scanning Calorimeter	DSC	Enthalpy
Thermal-gravimetric analysis	TGA	Mass
Thermal-mechanical analysis	TMA	Mechanical Properties
Thermal-optometry or Thermal-microscopy		Optical properties
Thermal-magnetometer	TM	Magnetic properties
Thermal-electrometer		Electric properties
Thermal-acoustic-meter	TS	Acoustic properties

- ***Differential Thermal Analysis (DTA)***

In differential thermal analysis (DTA), the examined sample and the reference material (which is usually a-aloumina) are subjected to a controlled heating or cooling program which is usually linear in correspondence with time. Initially there is zero differential temperature between the sample and the reference sample, as long as the sample does not undergo any physical or chemical change. If, however, any procedure between the sample and the reference sample takes place, then a differential temperature (ΔT) is developed (Figure B10.5).

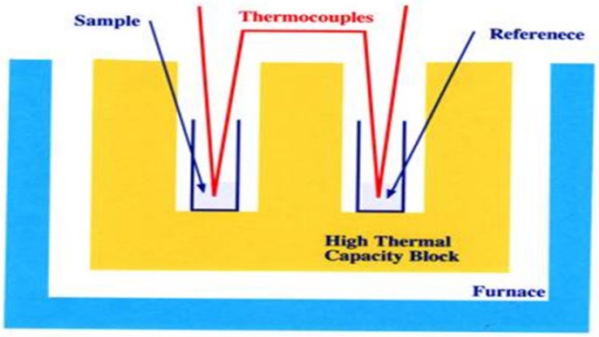

Figure B10.5: *Schematic representation of the DTA device*[215]

This way, in an endothermic change (e.g. when the sample is fused) the sample temperature is lower than that of the reference material. This is a transition state, because by the time the procedure is complete, the sample will have again zero differential temperature compared to the reference material. Considering an endothermic procedure (ΔH>0, e.g. fusion) that takes place in the region S, during the phenomenon of which, the sample temperature TS will be lower than the reference temperature TR. The differential temperature will be ΔT=TS-TR. The area A is analogous to the ΔH of the procedure and are related to with the function ΔH=A*K/m, where m is the sample mass and K the device calibration constant. In Figure B10.6 a typical DTA curve which was described above can be seen[215].

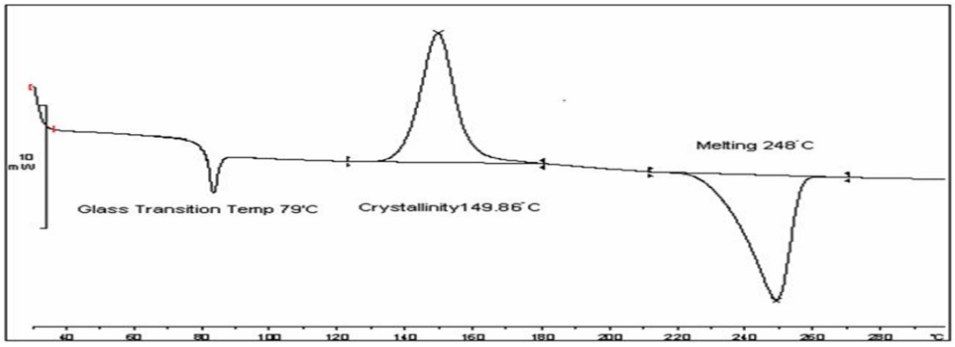

Figure B10.6: *Typical DTA curve*[215]

- ## *Thermal-gravimetric Analysis (TGA)*

Thermal-gravimetric analysis examines the mass change of a sample as a function of temperature. There are some materials thermal transitions which lead to mass change, such as absorption, adsorption, sublimation, evaporation, oxidation and deformation. TGA is used to characterize the decomposition and thermal stability of materials under various circumstances and to examine the kinetics of physical-chemical procedures which come up in samples. The characteristics of a material's mass change depend at high extend by the enforced experimental conditions. Factors such as sample mass, volume and physical form, shape and the nature of the sample holder, atmospheric pressure and the scanning rate are of greater influence to the characteristics recorded in the TG curves.

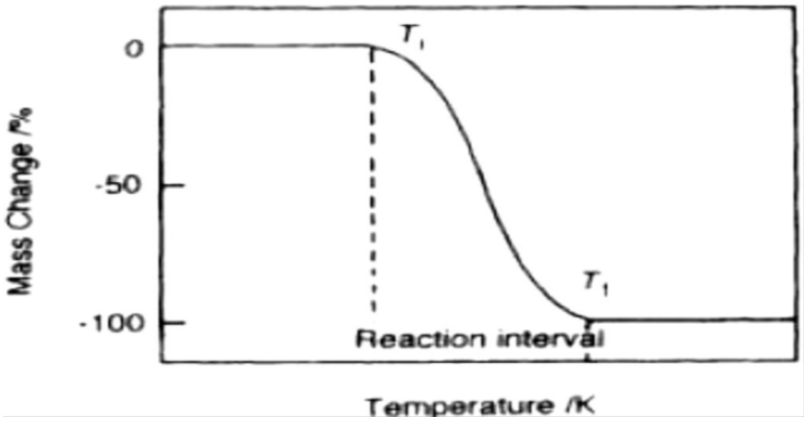

Figure B10.7: *TG curve for 1-D change*[215]

The TG curves are printed as mass change (Δm) expressed as % percentage on the vertical axis and the temperature (T) on the horizontal. The schematic representation of a one stage procedure is given in Figure B10.7. The procedure is characterized by two temperatures T_i and T_f, which are called decomposition and final temperature respectively. T_i represents the lower temperature at which it is possible to detect the beginning of mass change for certain experimental conditions. All of the same, the temperature T_f stands for the lower temperature, at which the responsible for the mass change procedure is completed. The values of T_i and T_f do not really matter as the initial temperature as well as the differential temperature (T_i-T_f) do not have a specific value, but depend on the experimental conditions.

B10.4 Scanning Electron Microscopy (SEM)

Scanning electron microscopy (SEM) is based on the interaction of an electron beam with atoms on the surface of a solid, usually in vacuum environment. The electrons are accelerated using voltage from 5 to some tens of keV and their beam scans the under examination sample surface via electrostatic deviation systems. The information is received by scanning electrons or electromagnetic radiation that is transmitted secondarily from the sample surface. The electronic of photonic signals are collected and driven to a cathode tube screen after certain amplification. The electron microscopy operates with different methodology depending on the secondary signal that is used to display the information.

The scanning electron microscopy is used for topographical surface studies in solids (metals, semi-conductors, insulators, polymers etc.) as long as they are stable in a vacuum measurement environment and their surface is not physical-chemically modified by the electron beam. The surface analysis which is achieved can reach 250 Å[9].

In Figure B10.8 the scanning electron microscope way of function can be seen. Initially, the electrons of thee beam are produced by a heated cathode and then accelerated by differential voltage and via electronic “lenses” are headed and focused to form the image. The electrons interact with the sample atoms and produce some signal (secondary and back-scattered electrons, X-Rays, Auger electrons), of which information about the morphology of

its surface, its composition etc. is received. When the beam electrons interact with the sample they lose energy from the scattering and the absorptions while entering inside it, at 100 nm to 5 μm depth from its surface and this depends on the beam energy and the materials density. The kinds of interaction which are observed are the elastic scattering (Rutherford scattering), the non-elastic scattering which leads to transmittance of electro-magnetic radiation (visible and X-Rays) out of the excitations and the de-excitations of the sample atoms.

The scattered electron and the radiation can be measured by appropriate sensors. The spec on a CRT screen scans the screen in synchronization with the electron beam and its brightness is formed by the reinforced signal of the sensor[9].

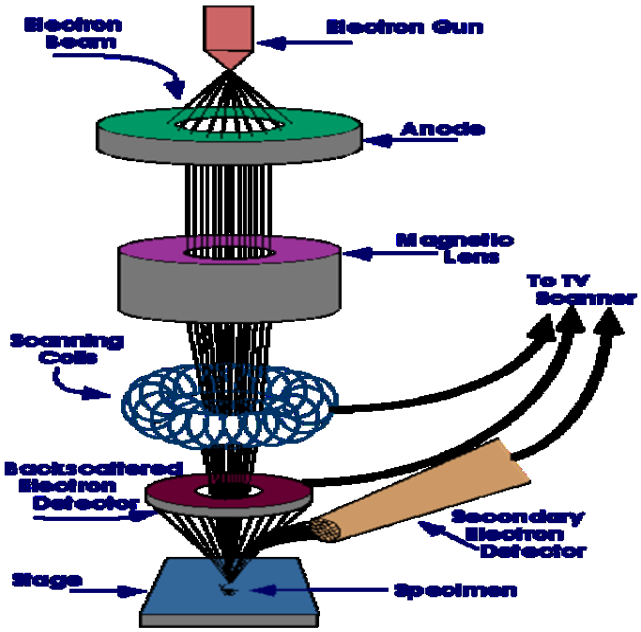

Figure B10.8: *Function diagram of the SEM microscope*[9]

B10.5 Transmission Electron Microscopy (TEM)

Transmission electron microscopy is a microscopy technique at which an electron beam is transmitted through a significantly thin sample and which interacts with the sample while it passes through. Due to the interaction with the electrons which are transmitted through the sample, an image is formed, which is magnified and focused by a monitoring device, such as a fluorescent screen, on a photographic film layer or can be detected by a sensor such as an LCD photo-camera[214, 215, 216].

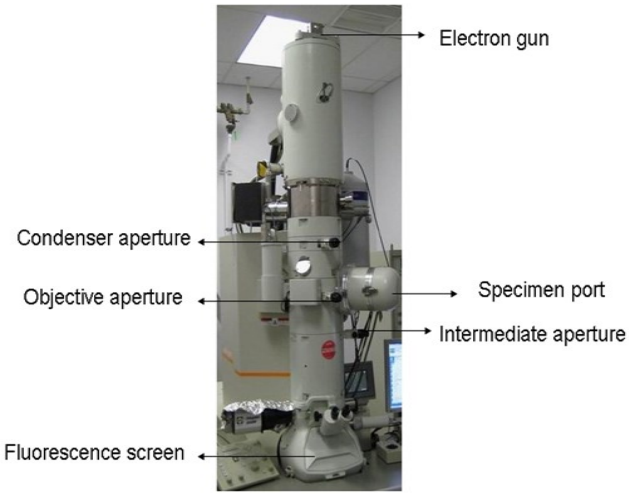

Figure B10.9: *TEM function*[218]

In Figure B10.9 the function of the transmission electron microscope is observed. The voltage also has to be large so that it will allow the electrons to pass through the sample. The sample should be placed on a base which should be electrically conductive allowing that way the electrons' passing-through.

From the top down, the TEM consists of an emission source, which may be a tungsten filament, or a lanthanum hexaboride (LaB_6) source. For tungsten, this will be of the form of either a hairpin-style filament, or a small spike-shaped filament. LaB_6 sources utilize small single crystals. By connecting this gun to a high voltage source (typically ~100–300 kV) the gun will, given sufficient current, begin to emit electrons either by thermionic or field electron emission into the vacuum. This extraction is usually aided by the use of a Wehnelt cylinder. Once extracted, the upper lenses of the TEM allow for the formation of the electron probe to the desired size and location for later interaction with the sample[218].

Manipulation of the electron beam is performed using two physical effects. The interaction of electrons with a magnetic field will cause electrons to move according to the right hand rule, thus allowing for electromagnets to manipulate the electron beam. The use of magnetic fields allows the formation of a magnetic lens of variable focusing power, the lens shape originating due to the distribution of magnetic flux[218]. Additionally, electrostatic fields can cause the electrons to be deflected through a constant angle. Coupling of two deflections in opposing directions with a small intermediate gap allows for the formation of a shift in the beam path, this being used in TEM for beam shifting. From these two effects, as well as the use of an electron imaging system, sufficient control over the beam path is possible for TEM operation. The optical configuration of a TEM can be rapidly changed, unlike that for an optical microscope, as lenses in the beam path can be enabled, have their strength changed, or be disabled entirely simply via rapid electrical switching, the speed of which is limited by effects such as the magnetic hysteresis of the lenses. The electro-magnetic lenses are used to concentrate and focus the beam[218].

The electron beam is focused on the sample with the assistance of two concentrating lenses. Afterwards, the electrons are focused at the objective aperture, where the diffraction image of the sample is formed. After that, a system of intermediate lenses magnifies more the diffraction image (75000 times of magnification). The electro-magnetic lenses are used to concentrate and focus the beam. The final image can be seen on a screen or recorded on a photographic plate [218].

B10.6 Mössbauer Spectroscopy

Mössbauer spectroscopy is a versatile technique[219] that can be used to provide information in many areas of science such as Physics, Chemistry, Biology and Metallurgy. It provides precise information about the chemical, structural, magnetic and time-dependent properties of a material. Key to the success of the technique is the discovery of recoilless gamma ray emission and absorption, now referred to as the "Mössbauer Effect", after its discoverer Rudolph Mössbauer, who first observed the effect in 1957 and received the Nobel Prize in Physics in 1961 for his work.

The Mössbauer Effect

Nuclei in atoms can undergo different energy level transitions, which are often associated with the emission or absorption of a gamma ray. These energy levels are influenced by their surrounding environment, both electronic and magnetic, which in turn can change or split these energy levels. These pre-mentioned energy levels' changes can provide information about the atom's local environment within a system and ought to be observed using resonance-fluorescence. There are, however, two major obstacles in obtaining this information: the 'hyperfine' interactions between the nucleus and its environment are extremely small, and the recoil of the nucleus as the gamma-ray is emitted or absorbed prevents resonance[219].

In a free nucleus during emission or absorption of a gamma ray it recoils due to conservation of momentum[219], with a recoil energy ER. This recoil is shown in Figure B10.10. The emitted gamma ray of a free nucleus has a total energy which is less than the nuclear transition energy by the amount of ER[219] and in order to be resonantly absorbed by another nucleus of the same kind it should have a total energy which must be greater than the transition energy by an amount equal to the ER due to the recoil of the absorbing nucleus. To achieve resonance the loss of the recoil energy must be overcome in some way.

Figure B10.10: *Recoil of free nuclei in emission or absorption of a gamma-ray*[219]

As the atoms will be moving due to random thermal motion the gamma-ray energy has a spread of values ED caused by the Doppler-effect. This leads to a gamma-ray energy profile as shown in Figure B10.11. To produce a resonant signal the two energies need to overlap and this is shown in the red-shaded area. This area is shown exaggerated as in reality it is really small and impractical as a technique.

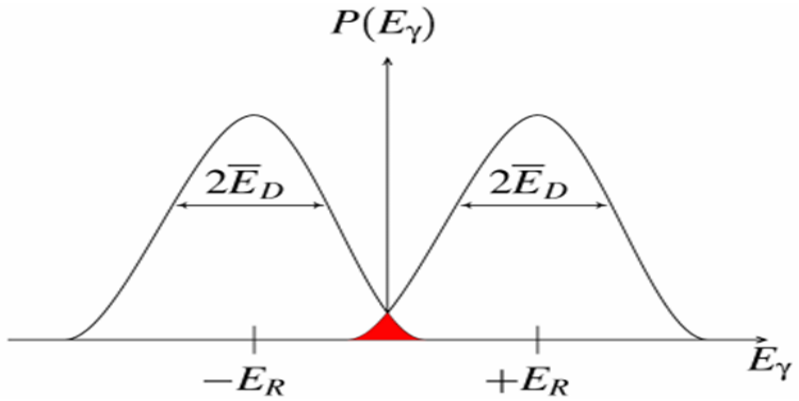

Figure B10.11: *Resonant overlap in free atoms: the overlap shown shaded is greatly exaggerated*[219]

What Mössbauer discovered is that when the atoms are found within a solid matrix the effective mass of the nucleus could be much greater. The recoiling mass can be now effectively the mass of the whole system if certain conditions are present, making ER and ED very small[219]. If the gamma-ray energy is small enough the recoil of the nucleus is too low to be transmitted through the solid as a phonon (the quantized harmonic vibrations of the solid lattice) and so the whole system of atoms in the solid recoils, making the recoil energy practically zero: a recoil-free event. In this situation, as shown in Figure B10.12, if the emitting and absorbing nuclei are in a solid matrix the emitted and absorbed gamma-ray have almost the same energies: resonance[219].

Figure B10.12: *Recoil-free emission or absorption of a gamma-ray when the nuclei are in a solid matrix such as a crystal lattice*[219]

As resonance only occurs when the transition energy of the emitting and absorbing nucleus match exactly, the effect is isotope specific[219]. The relative number of recoil-free events (and therefore the power of the signal) is significantly dependent on the gamma-ray energy and so the Mössbauer effect is only detected in isotopes with very low lying excited states[219]. At the same time the resolution is dependent upon the lifetime of the excited state, two factors that limit the number of isotopes which can be used successfully for Mössbauer spectroscopy. The most used one is ^{57}Fe, which has both a very low energy gamma-ray and long-lived excited state, which meets both requirements well[219]. Figure B10.13 shows the isotopes in which the Mössbauer effect has been detected.

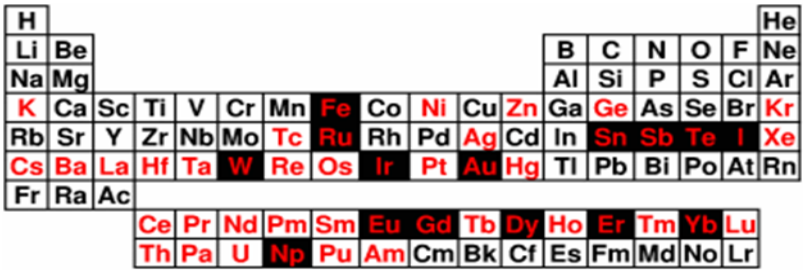

Figure B10.13: *Elements of the periodic table which have known Mössbauer isotopes (shown in red font)*[219]

The energy levels in the absorbing nuclei can be modified by their environment in three main ways: by the Isomer Shift, Quadruple Splitting and Magnetic Splitting[219].

The isomer shift arises due to the non-zero volume[219] of the nucleus and the electron charge density due to s-electrons within it. This leads to a monopole (Coulomb) interaction, altering the nuclear energy levels. Any difference in the s-electron environment between the source and absorber thus produces a shift in the resonance energy of the transition. This shifts the whole spectrum positively or negatively depending upon the s-electron density, and sets the centroid of the spectrum[219]. As the shift cannot be measured directly it is quoted relative to a known absorber. The isomer shift can be used to determine valence states, ligand bonding states, electron shielding and the electron-drawing power of electronegative groups[219]. As an example, the electron configurations for Fe^{2+} and Fe^{3+} are $3d^6$ and $3d^5$ respectively. Thus, the high spin ferrous ions have less s-electrons at the nucleus due to the greater screening of their excess of d-electrons relative to the case of the high spin ferric ions. Despite of this, ferrous ions have larger positive isomer shifts than ferric ions.

Nuclei in states with an angular momentum quantum number I>1/2 have a non-spherical charge distribution[219]. This produces a nuclear quadruple moment. In the presence of an asymmetrical electric field (produced by an asymmetric electronic charge distribution or ligand arrangement) this splits the nuclear energy levels[219]. The charge-distribution is justified by a single quantity called the Electric Field Gradient (EFG).

In the case of an isotope with a I=3/2 excited state, such as ^{57}Fe or ^{119}Sn, the excited state is split into two sub-states $m_I=\pm1/2$ and $m_I=\pm3/2$. This is shown in Figure B10.14, giving a two-line spectrum or "doublet".

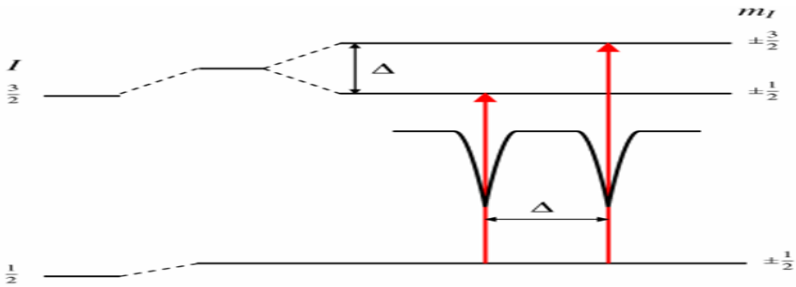

Figure B10.14: *Quadruple splitting for a 3/2 to 1/2 transition. The magnitude of quadruple splitting, Delta, is shown*[219]

The magnitude of splitting, Delta, is related to the nuclear quadruple moment, Q, and the principle component of the EFG, Vzz, by the relation Delta=eQVzz/2 in the case of an axially symmetric EFG (Vxx=Vyy).

In the presence of a magnetic field the nuclear spin moment experiences a dipolar interaction with the magnetic field i.e. Zeeman splitting. There are many sources of magnetic fields that can be experienced by the nucleus. The total effective magnetic field at the nucleus, B_{eff} is given by:

$$\mathbf{B_{eff} = (B_{contact} + B_{orbital} + B_{dipolar}) + B_{applied}}$$

The first three terms exist due to the atom's own partially filled electron shells. $B_{contact}$ is due to the unbalanced s-electrons density at the nucleus, $B_{orbital}$ is due to the orbital moment, and $B_{dipolar}$ is the dipolar field due to the spin. This magnetic field splits nuclear levels with a spin of I into (2I+1) sub-states. This is shown in Figure B10.17 for ^{57}Fe. Transitions between the excited state and ground state can only occur where m_I changes by 0 or 1. This gives six possible transitions for a 3/2 to 1/2 transition, giving a sextet as illustrated in Figure B10.15, with the line spacing being proportional to Be_{ff}.

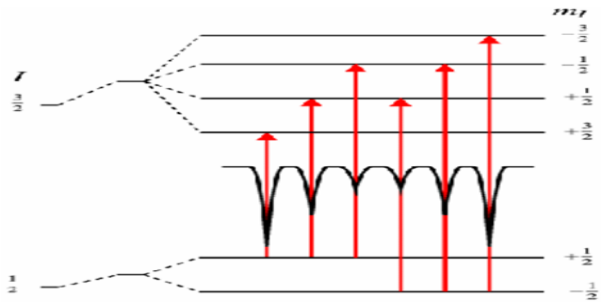

Figure B10.15: *Magnetic splitting of the nuclear energy levels*[219]

The line positions are related to the splitting of the energy levels, but the line intensities are related to the angle between the Mössbauer gamma-ray and the nuclear spin moment

These interactions, Isomer Shift, Quadruple Splitting and Magnetic Splitting, alone or in combination are the primary characteristics of many Mössbauer spectra[219]. If emitting and absorbing nuclei are in identical, cubic environments then the transition energies are identical and this produces a spectrum as shown in Figure B10.16: a single absorption line.

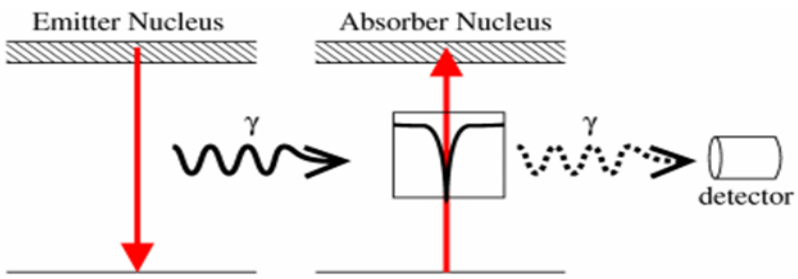

Figure B10.16: *Simple Mössbauer spectrum from identical source and absorber*[219]

B10.7 Superconducting quantum interference device (SQUID)

A SQUID (Superconducting Quantum Interference Device) is a very sensitive magnetometer used to measure extremely low magnetic fields[220]. It is based on superconducting loops which contain Josephson junctions (a Josephson junction is a device which consists of two superconductors coupled by a weak link). SQUIDs are sensitive enough to measure fields as low as 5 aT (5×10^{-18} T) within a few days of averaged measurements[220]. Their noise levels are as low as 3 fT•Hz-½. For comparison, a typical refrigerator magnet produces 0.01 Tesla (10^{-2} T), and some processes in animals produce very small magnetic fields between 10^{-9} T and 10^{-6} T.

There are two main types of SQUID: direct current (DC) and radio frequency (RF). RF SQUIDs can work with only one Josephson junction, which might make them cheaper to produce, but are less sensitive.

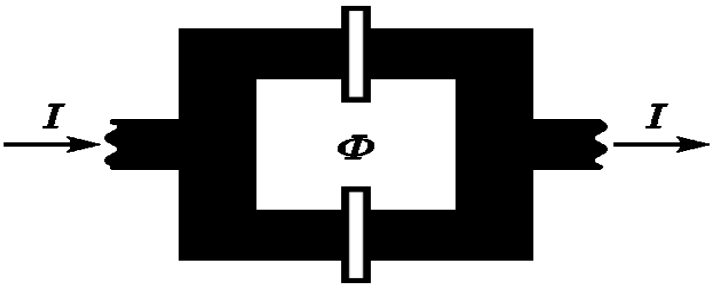

Figure B10.17: *Diagram of a DC SQUID. The current I enters and splits into the two paths, each with currents Ia and Ib. The thin barriers on each path are Josephson junctions, which together separate the two superconducting regions. Φ represents the magnetic flux threading the DC SQUID loop*[220]

In figure 10.18 an electrical schematic of a SQUID is observed, where I_b is the bias current, I_0 is the critical current of the SQUID, is the flux threading the SQUID and is the voltage response to that flux. The X-symbols represent Josephson junctions.

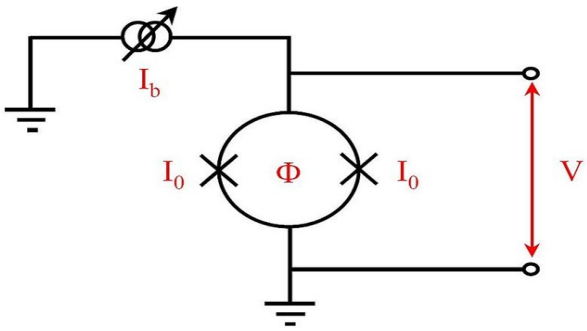

Figure B10.18: *Electrical schematic of a SQUID*[220]

The DC SQUID was invented in 1964 by Robert Jaklevic, John J. Lambe, James Mercereau, and Arnold Silver of Ford Research Labs[220] after Brian David Josephson postulated the Josephson Effect in 1962, and the first Josephson junction was made by John Rowell and

Philip Anderson at Bell Labs in 1963[220]. It has two Josephson junctions in parallel in a superconducting loop.

The RF SQUID was introduced in 1965 by Robert Jaklevic, John J. Lambe, Arnold Silver, and James Edward Zimmerman at Ford[220]. It is based on the AC Josephson effect and uses only one Josephson junction. It is less sensitive compared to DC SQUID but is cheaper and easier to manufacture in smaller quantities. Most fundamental measurements in bio-magnetism, even of extremely small signals, have been made using RF SQUIDS[220]. The RF SQUID is inductively coupled to a resonant tank circuit. Depending on the external magnetic field, as the SQUID operates in the resistive mode, the effective inductance of the tank circuit changes, thus changing the resonant frequency of the tank circuit[220].

The traditional superconducting materials for SQUIDs are pure niobium or a lead alloy with 10% gold or indium, as pure lead is unstable when its temperature is repeatedly changed. In order to realize superconductivity, the entire device needs to operate within a few degrees of absolute zero, cooled with liquid helium[220]. "High-temperature" SQUID sensors are more recent and they are constructed of high-temperature superconductors, particularly YBCO, and are cooled by liquid nitrogen which is cheaper and more easily handled than liquid helium. They are less sensitive than conventional "low temperature" SQUIDs but good enough for many applications[220].

SQUID measures also magnetic moments of substances in addition to the strength of magnetic fields. It is this property of the SQUID which was mainly used during this dissertation so as to investigate magnetic properties of the formed hybrid materials.

B10.8 Vibrating Sample Magnetometer (VSM)

A vibrating sample magnetometer is one of the scientific instruments which measures the materials' magnetic properties and was invented in 1955 by Simon Foner in MIT.

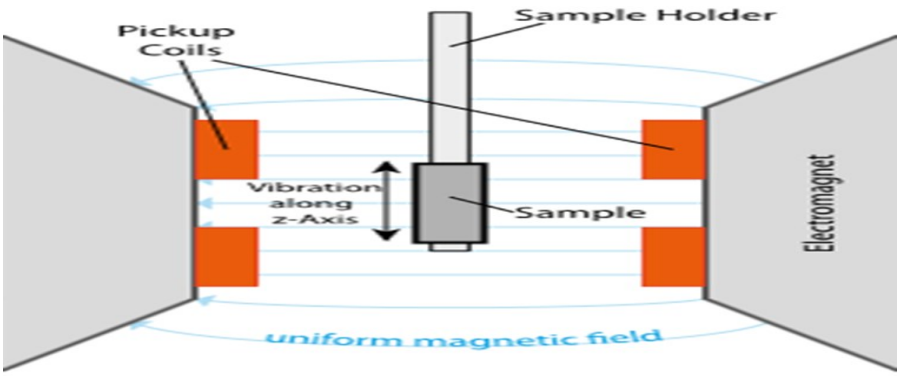

Figure B10.19: *Schematic representation of VSM function*[221]

Vibrating Sample Magnetometry (VSM) is based on Faraday's law which states that an electromagnetic force is generated in a coil when there is a change in flux linking the coil[221].

In the measurement setup, a magnetic sample is moving in the proximity of two pickup coils as indicated in Figure B10.20.

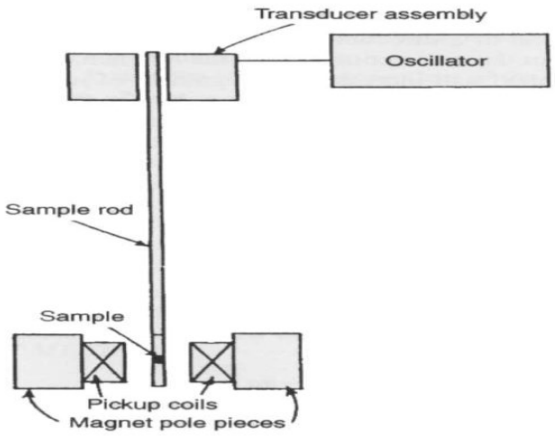

Figure B10.20: *Schematic representation of a VSM*[222]

The oscillator provides a sinusoidal signal that is translated by the transducer assembly into a vertical vibration. The sample which is fixed to the sample rod vibrates with a given frequency and amplitude (60 Hz and 1 mm, respectively). It is centered between the two pole pieces of an electromagnet that generates a magnetic field H_o of high homogeneity[222]. Field strengths of several Tesla are commonly possible with laboratory VSM systems. Stationary pickup coils are mounted on the poles of the electromagnet[222]. Their symmetry center coincides with the center of the sample. Hence, the change in magnetic flux originating from the vertical movement of the magnetized sample induces a voltage U_{ind} in the coils. H_0, being constant, has no effect on the voltage but is necessary only for magnetizing the sample[222]. According to Faraday the voltage in a single winding of the pickup coil can be written as

$$U_{ind} = -\theta\Phi/\theta t \qquad (1)$$

where Φ is the magnetic flux. For the pickup coils with a flat surface A and n_w windings, equilibrium 1 gives

$$U_{ind} = -nwA\theta B/\theta t \qquad (2)$$

When we bring the sample into the homogeneous field H_0, it will be magnetized and have the magnetization *M.* The magnetic flux density *B* near the sample is now

$$B = \mu_0(H_0 + M) \qquad (3)$$

where *M* is defined by the resulting magnetic moment *m* per volume unit.

$$M = dm/dV \qquad (4)$$

In the constant magnetic field H_0 we have

$$\theta B/\theta t = \theta M/\theta t \qquad (5)$$

The change of magnetic flux linking the coils is therefore proportional to a number of quantities: the frequency ω of the vibration and its amplitude Z, the magnetic moment of the sample m and the distance to the pickup coils y_0. Furthermore, U_{ind} can be increased by increasing the number of windings n_w and the number of pickup coils n_c used in the setup. Also, the geometry of the sample influences the induction.

$$U_{ind}(t)\alpha - m\omega Z y_0 n_w n_c G\cos(\omega t) \quad (6)$$

where G is a geometric factor of the sample[222]. The measurement setup is sensitive even to very low magnetic moments. Today's Vibrating Sample magnetometers are able to detect magnetic moments of down to the μemu range[222].

B10.9 Infrared Spectroscopy (IR)

Infrared Spectroscopy is widely used in materials and organic chemistry due to the fact that it is easy to obtain compound spectra and compare them with certain known organic compound spectra. In principle, every time infrared radiation hits a material it is able to pass through, scatter or to be absorbed. The absorbed infrared radiation usually excites molecules in higher quantum vibration states. In order for this to be accomplished, the difference between the vibration energy levels and the radiation energy should be equal.

The theory behind this is simple: in the IR spectrum, absorptions take place, which derive from bond bending, stretching, wagging, rocking, twisting, scissoring or vibrating which has the tendency to change and to absorb strongly in the infrared spectrum. The bond stretching refers to the length change while the bending vibrations refer to the angle change that is exhibited by the bonds. Absorption zones can also derive by other vibrating ways such as distortion, swinging etc. A linear molecule, which consists of N atoms, vibrates with 3N-5 different basic vibrations, while a non-linear molecule using 3N-6 different vibrations.

The quantitative function that relates light intensity that goes through the sample and its concentration inside the solution is given by the Beer-Lambert-Bouguer law:

$$I = I_0 \exp(-\alpha c\, l),$$

where I_0 is the intensity (energy) of the radiation which falls on the sample, c the concentration, l the thickness of the sample and α the absorption coefficient $\log(I_0/I) = \varepsilon\, c\, l$, where ε is called depreciation coefficient. The law is valid for monochromatic light and for low concentrations. Usually spectrometers recorder the spectrum in linear form, on the vertical axis of which we find %transmittance while on the horizontal axis frequencies as wavenumbers are observed.

IR spectroscopy is mostly used in the range of 4000-650 cm^{-1}, nevertheless quite some useful data can be acquired, as far as the structure of many organic compounds is concerned, if one observes the far infrared (far-IR) spectrum (400-10 cm^{-1})[223]. The far-IR spectrum is the zone of electromagnetic absorbance of Deuterium, Tritium, the organic

compounds skeleton distortions, the twist vibrations of organic compounds, the vibrations of several molecular structures, the hydrogen bonds (200-50 cm^{-1}) etc. In this part of the spectrum though the IR-spectrometer sensitivity is limited and the absorption intensities are too low, which leads to the interference and covering of the absorption bands by "noise". The incapability of common IR-spectrometers, as well as this of other spectroscopy methods, was defeated using the Fourier Transform IR Spectroscopy, FT-IR (Figure B10.21).

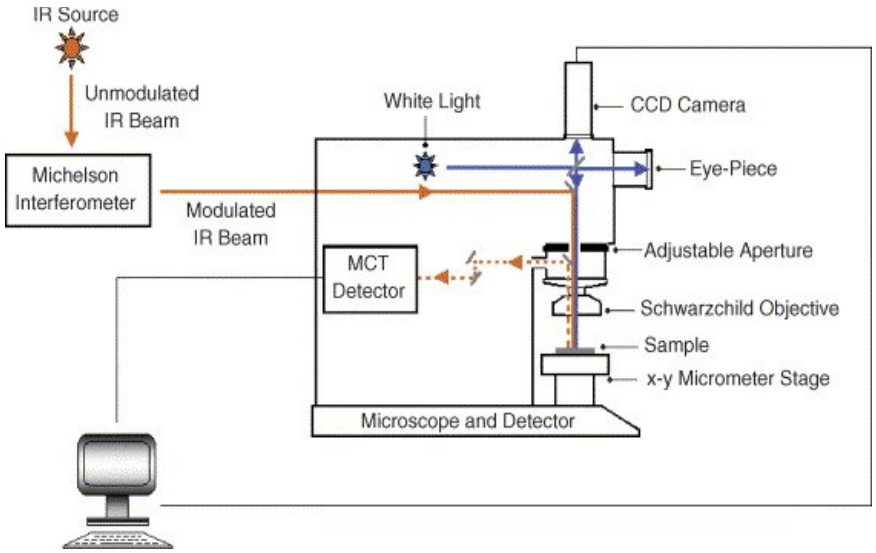

Figure B10.21: *FT-IR spectrometer*[223]

The explanation of infrared spectra is not an easy task due to the fact that it requires high experience and experimenting in order to acquire knowledge on absorption bands, even on those of simple organic compounds[224]. What is more, there is a variety of literature and tables for the majority of organic compounds. Several points should be taken into consideration when trying to interpret IR spectra[224,225]:

i) Drastic group absorptions are usually to be found in the range of 4000-1500 cm^{-1}.
ii) The absorbance of bands, lines or peaks are categorized according to their intensity to strong (s), medium (m), weak (w) and broad (br). This is about a qualitative comparison and should be performed under the same conditions of concentration, scanning time etc.
iii) Many characteristic groups give weak absorptions which are difficult to distinguish.
iv) The comparison of unknown compounds' spectra with known compounds spectra can lead to positive results in order to certify them. Theoretically, the two spectra should resemble.
v) The skeleton absorbance appears in the area below 1500 cm-1, although the exact interpretation of theirs is trickier.
vi) The characteristic groups give one or more absorptions that depend on the nature and position inside the molecule.

vii) The IR tables with the characteristic absorptions (drastic groups and skeleton) of organic compounds are in accordance with general absorbance estimations, according to scientific literature[223,224].

B10.10 Ultraviolet Spectroscopy (UV-Vis)

Ultraviolet–Visible (UV-Vis) has to do with the absorption spectroscopy or reflectance spectroscopy in the ultraviolet-visible spectral region. This means it uses light in the visible and adjacent (near-UV and near-infrared (NIR)) ranges. The perceived color of the chemicals involved is directly affected by the absorption or reflectance in the visible range. Molecules can undergo electronic transitions in this region of the electromagnetic spectrum. This technique measures transitions from the ground state to the excited state[226].

The principle of the method is simple: molecules which contain π-electrons or non-bonding electrons (n-electrons) can absorb the energy in the form of ultraviolet or visible light to excite these electrons to higher anti-bonding molecular orbitals. The more easily excited the electrons are, the longer the wavelength of light it can absorb.

The device which is used in ultraviolet-visible spectroscopy is called a UV/Vis spectrophotometer. This instrument is intended to measure the intensity of light passing through a sample **I**, and compares it to the intensity of light before it passes through the sample $\mathbf{I_o}$. The ratio $\mathbf{I/I_o}$ is referred to as transmittance, and is usually expressed as a percentage **(%T)**. The absorbance **A** is based on the transmittance according to the formula[226]:

$$\mathbf{A = -\log(\%T/100\%)}$$

The UV-visible spectrometer can also be modified to measure reflectance. In this case, the spectrophotometer measures the intensity of light reflected from a sample **(I)**, and compares it to the intensity of light reflected from a reference material $\mathbf{(I_o)}$. The ratio $\mathbf{(I/I_o)}$ is then referred to as reflectance, and is usually expressed as a percentage **(%R)**.

A spectrophotometer is composed of a light source, a holder for the sample, a diffraction grating in a monochromator or a prism in order to separate the different wavelengths of light, and a detector. The radiation source is often a Tungsten filament (300-2500 nm), a deuterium arc lamp, which is continuous over the ultraviolet region (190-400 nm), Xenon arc lamp, which is continuous from 160-2000 nm as well as light emitting diodes (LED)[229] for the visible wavelengths. The detector will typically be a photomultiplier tube, a photodiode, a photodiode array or a charge-coupled device (CCD). Single photodiode detectors and photomultiplier tubes are used with scanning monochromators, which filter the light so that only light of a single wavelength reaches the detector at one time. The scanning monochromator moves the diffraction grating to "step-through" each wavelength so that its intensity will be measured as a function of wavelength. Standard monochromators are used with CCDs and photodiode arrays. Considering the fact that these instruments are composed

of many detectors grouped into one or two dimensional arrays, they exhibit the ability to collect light of different wavelengths on different pixels or groups of pixels simultaneously[226].

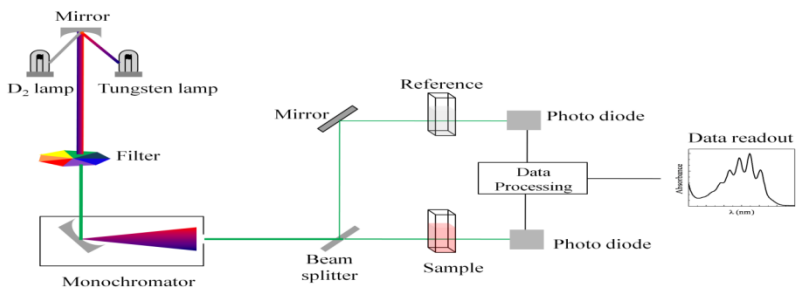

Figure B.10.22: *Schematic representation of UV- visible spectrophotometer*[225]

A spectrophotometer can be either single beam or double beam. In a single beam all of the light passes through the sample cell, so $\mathbf{I_o}$ should be measured by removing the sample. This was the earliest design and is still commonly used in both teaching and industrial labs. As far as double-beam instruments are concerned, the light is being split into two beams before reaching the sample. The one will be used as the reference beam while the other beam is passing through the sample. The intensity of the reference beam will be considered as 100% Transmission (or 0% Absorbance), and the displayed measurement is the ratio of the two beam intensities. There are also double-beam instruments that have two detectors (photodiodes)[226].

As far as sampling for UV/Vis spectrometry is concerned, samples are most often liquids, although the absorbance of gases and even of solids can also be measured. Samples are typically placed in a transparent cell, known as a cuvette. Cuvettes are typically rectangular in shape, commonly with an internal width of 1 cm (this width becomes the path length, in the Beer-Lambert law)[226]. Test tubes are also able to be used as cuvettes in some instruments. The type of the used sample container used must allow radiation to pass over the spectral region of interest. The most widely applicable cuvettes are made of high quality fused silica or quartz glass because these are transparent throughout the UV, visible and near infrared regions. Glass and plastic cuvettes are also common, although glass and most plastics absorb in the UV, which limits their usefulness to visible wavelengths[226].

The above method is most commonly used to determine in a quantitative way concentrations of an absorbing species in solution, using the Beer-Lambert law:

$$\mathbf{A = \log_{10}(Io/I) = \epsilon cL},$$

where **A** is the measured absorbance, in Absorbance Units (AU), $\mathbf{I_o}$ will be the intensity of the incident light at a given wavelength, **I** is the transmitted intensity, **L** the path-length through the sample, and **c** the concentration of the absorbing species. For each species and

wavelength, **ϵ** is a constant known as the molar absorptivity or extinction coefficient. This constant is a fundamental molecular property in a given solvent, at a particular temperature and pressure, and has units of 1/M*cm or often AU/M*cm. The absorbance and extinction ϵ are sometimes defined in terms of the natural logarithm instead of the base-10 logarithm.

Applications

UV/Vis spectroscopy is commonly used in quantitative analytical chemistry for the quantitative determination of different compounds, such as transition metal ions, highly conjugated organic compounds, and biological macromolecules[226]. Spectroscopic analysis in solutions, as well as solid and gas studies are commonly carried out. Solutions of transition metal ions can be colored (i.e., absorb visible light) because d-electrons within the metal atoms can be excited from one electronic state to another[226]. The color of metal ion solutions is strongly affected by the presence of other species, such as certain anions or ligands. For instance, the color of a dilute solution of copper sulfate is a very light blue, while adding ammonia intensifies the color and changes the wavelength of maximum absorption (λ_{max}). Organic compounds, especially the ones which exhibit a high degree of conjugation, can also absorb light in the UV or visible regions of the electromagnetic spectrum. The solvents for these determinations are often water for water-soluble compounds, or ethanol for organic-soluble compounds[226]. Although not all solvents are suitable for use in UV spectroscopy organic solvents may have significant UV absorption. In spite of the fact that charge transfer complexes also give rise to colors, the colors are often too intense to be used for quantitative measurement.

B10.11 X-ray photoelectron spectroscopy (XPS)

X-ray photoelectron spectroscopy (XPS) is a surface-sensitive quantitative spectroscopic technique that measures the elemental composition at the parts per thousand range, empirical formula, chemical state and electronic state of the elements that exist within a material[227]. XPS spectra are acquired by irradiating a material with a beam of X-rays while at the same time measuring the kinetic energy and number of electrons that escape from the top 0 to 10 nm of the material being analyzed[227]. XPS demands high vacuum (P ~ 10-8 millibar) or ultra-high vacuum (UHV: P < 10-9 millibar) conditions, although a current area of development is ambient-pressure XPS, in which samples are analyzed at pressures of a few tens of mbar[227].

XPS is a surface chemical analysis technique that can be used to analyze the surface chemistry of a material in its as-received state, or after some treatment, for example[227]: fracturing, cutting or scraping in air or Ultra High Vacuum (UHV) to expose the bulk chemistry, ion beam etching to clean off some or all of the surface contamination (with mild ion etching) or to intentionally expose deeper layers of the sample (with more extensive ion etching) in depth-profiling XPS, exposure to heat to study the changes due to heating,

exposure to reactive gases or solutions, exposure to ion beam implant, exposure to ultraviolet light[227].

In principle XPS detects all elements. In practice, using typical laboratory-scale X-ray sources, XPS detects all elements with an atomic number (Z) of 3 (lithium) and above. It cannot easily detect hydrogen (Z = 1) or helium (Z = 2)[227].

Detection limits for most of the elements (on a modern instrument) are in the range of parts per thousand. Detection limits[227] of parts per million (ppm) can be obtained, but demand special conditions: concentration at top surface or very long collection time (overnight).

XPS is typically used to analyze inorganic compounds, metal alloys, semiconductors, polymers, elements, catalysts, glasses, ceramics, paints, papers, inks, woods, plant parts, make-up, teeth, bones, medical implants, bio-materials, viscous oils, glues, ion-modified materials and many others[227]. Less routinely it is used to analyze the hydrated forms of some of the above materials by freezing the samples in their hydrated state in an ultra-pure environment, allowing or causing multilayers of ice to sublime away prior to analysis[227]. Such hydrated XPS analysis allows hydrated sample structures, which may be different from vacuum-dehydrated sample structures, to be studied in their more relevant as-used hydrated structure.

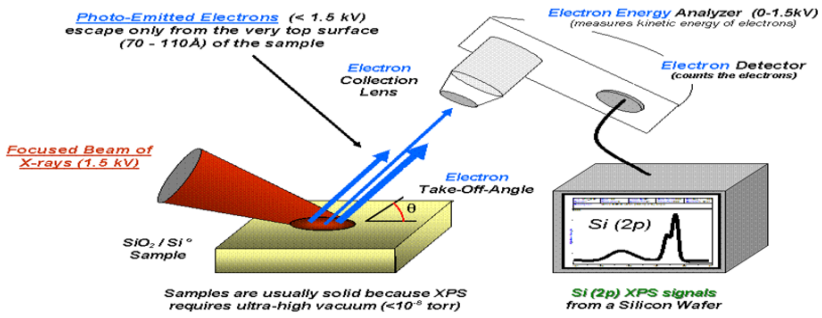

Figure B10.23: *Basic components of a monochromatic XPS system*[227]

XPS is used to measure[227]:

- elemental composition of the surface (top 0–10 nm usually)
- empirical formula of pure materials
- elements that contaminate a surface
- chemical or electronic state of each element in the surface
- uniformity of elemental composition across the top surface (or line profiling or mapping)
- uniformity of elemental composition as a function of ion beam etching (or depth profiling)

XPS can be performed using a commercially built XPS system, a privately built XPS system, or a synchrotron-based light source combined with a custom-designed electron energy analyzer. The ability to heat or cool the sample during or prior to analysis is relatively common[227]. Because the energy of an X-ray with particular wavelength is known (for aluminum Kα X-rays, E_{photon} = 1486.7 eV), and because the emitted electrons' kinetic energies are measured, the electron binding energy of each of the emitted electrons can be determined by using an equation that is based on the work of Ernest Rutherford (1914)[227]:

$$E_{binding} = E_{photon} - (E_{kinetic} + \Phi)$$

where $E_{binding}$ is the binding energy (BE) of the electron, E_{photon} is the energy of the X-ray photons being used, $E_{kinetic}$ is the kinetic energy of the electron as measured by the instrument and is the work function of the spectrometer (not the material)[227]. This equation is essentially a conservation of energy equation. The work function term is an adjustable instrumental correction factor that accounts for the few eV of kinetic energy given up by the photoelectron as it becomes absorbed by the instrument's detector. It is a constant that rarely needs to be adjusted in practice.

A typical XPS spectrum is a plot of the number of electrons detected (sometimes per unit time) (Y-axis, ordinate) versus the binding energy of the electrons detected. Each element produces a characteristic set of XPS peaks at characteristic binding energy values that directly identify each element that exists in or on the surface of the material being analyzed. These characteristic spectral peaks correspond to the electron configuration of the electrons within the atoms, e.g., 1s, 2s, 2p, 3s, etc. The number of detected electrons in each of the characteristic peaks is directly related to the amount of element within the XPS sampling volume. To generate atomic percentage values, each raw XPS signal must be corrected by dividing its signal intensity (number of electrons detected) by a "relative sensitivity factor" (RSF), and normalized over all of the elements detected. Since hydrogen is not detected, these atomic percentages exclude hydrogen. In order to count the number of electrons during the acquisition of a spectrum with a minimum of error, XPS detectors must be operated under ultra-high vacuum (UHV) conditions because electron counting detectors in XPS instruments are typically one meter away from the material irradiated with X-rays. This long path length for detection requires such low pressures[227].

XPS detects only those electrons that have actually escaped from the sample into the vacuum of the instrument, and reach the detector. In order to escape from the sample into vacuum, a photoelectron must travel through the sample. Photo-emitted electrons can undergo inelastic collisions, recombination, excitation of the sample, recapture or trapping in various excited states within the material, all of which can reduce the number of escaping photoelectrons. These effects appear as an exponential attenuation function as the depth increases, making the signals detected from analytes at the surface much stronger than the signals detected from analyses deeper below the sample surface. Thus, the signal measured

by XPS is an exponentially surface-weighted signal, and this fact can be used to estimate analytical depths in layered materials[227].

XPS is routinely used to determine[227]:

- What elements and the quantity of those elements that are present within the top 1-12 nm of the sample surface
- What contamination, if any, exists in the surface or the bulk of the sample
- Empirical formula of a material that is free of excessive surface contamination
- The chemical state identification of one or more of the elements in the sample and also give information on local bonding of atom
- The binding energy of one or more electronic states
- The thickness of one or more thin layers (1–8 nm) of different materials within the top 12 nm of the surface
- The density of electronic states

Part C: Experimental

C1. Synthesis of carbon nanotubes encapsulating superconducting tin nanowires (Sn@CNTs) using the CCVD method

C1.1 Chemical Reagents and apparatus

The chemical reagents, their molecular formula, the company which they were provided and the apparatus that were used during the experiments are described below:

- Acetylene gas (C_2H_2) of 99.9% purity (Linde HELLAS)
- Argon gas (Ar) of 99.999% purity (Linde HELLAS)
- Tin Oxide (SnO Sigma Aldrich, 99+%), Tin Dioxide (SnO_2, Sigma Aldrich, 99%) and metallic Tin (Sn, Koch Light Lab., 99.999%)
- Tubular furnace (Carbolite)
- Quartz tube of 2.2cm diameter and 90cm length
- Two mass flow meters (Omega Engineering, FMA-A2000 series)
- Ceramic (alumina) crucibles (95% purity)
- Hydrochloric Acid (HCl 0.1M, Merck).

C1.2 Experimental procedure

Superconducting tin nanowires encapsulated in carbon nanotubes were synthesized by catalytic decomposition of acetylene over tin-based catalysts (tin monoxide, tin dioxide and pure tin) in a fixed bed flow reactor at various temperatures ranging from 500°C up to 1000°C. Metallic tin (Koch-Light Lab., 99.999%), SnO (Aldrich, 99+ %) and SnO_2 (Aldrich, 99.9%) were used as catalysts. In a typical run, about 100 mg of the catalyst powders were placed in an alumina boat within a quartz tube, with an inner diameter of 2.2 cm and length of 90 cm, located in a resistance furnace (see Figure C1.1). Sample was heated up to certain temperature (for example 700°C) in Argon atmosphere. At this temperature acetylene as a carbon precursor was admixed with the carrier gas (Argon) at a flow rate of 10 cm^3/ min and 90 cm^3/ min, respectively. 60 min later, the C_2H_2 gas flow was stopped, and the ceramic boat was cooled down to room temperature in the Argon atmosphere. The deposited materials were finally collected from the ceramic boat. Additionally, the products obtained from the same procedure as above using as variable different times of acetylene flow (30 minutes, 1 hour, 1,5 hours and 2 hours) at 700°C were investigated. The obtained materials were denoted as Sn@CNTs30min, Sn@CNTs60min, Sn@CNTs90min and Sn@CNTs120min.

Figure C1.1: *the CCVD setup (Dept. Mater. Sci. Engineer., Univ. Ioannina)*

C1.3 Purification of Sn@CNTs samples

The next step after the preparation of the samples in CCVD was the cleaning of hybrid nanowires from the unreacted tin oxides (catalyst). Initially, 20 ml of hydrochloric acid (0.1 M) is shed into a beaker which contains the Sn@CNTs sample so that the whole unreacted SnO_2 is completely diluted. The solution is placed into a sonication bath for 15 minutes and then was stirred for 2 hours so that every remaining unreacted catalyst (SnO, or SnO_2) was removed. In the next step centrifugation was performed at 3500 rpm for 15 minutes to separate carbon nanotubes (Sn@CNTs) from the diluted tin oxides. The precipitate was then washed with water, stirred for another 15 minutes, centrifuged for 15 minutes at 3500 rpm and re-dispersed in water. Finally, the mixture was spread on a glass plate in order to dry and the final powdered product was collected.

C2. Synthesis of carbon nanotubes encapsulating Tin-Lead nanowires (SnPb@CNTs) using the CCVD method

C2.1 Chemical Reagents and apparatus

The chemical reagents, their molecular formula, the company which they were provided and the apparatus that were used during the experimental procedure are described below:

- Acetylene gas (C_2H_2) of 99.9% purity (Linde HELLAS)
- Argon gas (Ar) of 99.999% purity (Linde HELLAS)
- Tubular furnace (Carbolite)
- Quartz tube of 2.2cm diameter and 90cm length
- Two mass flow meters (Omega Engineering, FMA-A2000 series)
- Ceramic (alumina) crucibles (95% purity)
- Sodium Chloride (NaCl Merck 99.5%, 106404)
- SnPb alloy 61% w/w in Sn and 39% w/w Pb (typical "solder")
- Silver Nitrate ($AgNO_3$, ACS reagent, Sigma Aldrich, ≥99.0%)

C2.2 Experimental procedure

Carbon nanotubes encapsulating superconducting SnPb alloy were composed by the catalytic chemical vapor deposition method, using acetylene as carbon source in an Argon atmosphere at flow rates of 10 cm^3/ min and 94 cm^3/ min respectively. A similar procedure like in the case of Sn@CNTs was followed (see above). The reaction temperature was set to 700°C while two reaction times, 30 and 60 min were chosen. Upon reaction at 700°C two cooling procedures were followed:

- *Fast cooling* by pouring off the final product powder of the CCVD from the ceramic directly in deionized water.

- *Slow cooling* by letting the final product to cool down at room temperature.

Initially, an alumina boat was used as a sample holder, which was cleaned thoroughly with acetone. Inside the boat 0.04 g of SnPb alloy (normal solder) and 0.16 g of NaCl (20% w/w SnPb alloy and 80% w/w NaCl) were placed. In the CCVD device, the quartz tube was cleaned prior to use and the catalyst within the boat was placed inside the tube. Argon and Acetylene gas bottles were connected to the mass flow-meters and the desired current flows were adjusted (10cm^3/min and 94cm^3/min for Acetylene and Argon respectively). The temperature was set to 700°C and two reaction times of 30 min and 60 min were used for each experiment. The reaction would take place in an inert atmosphere, therefore, an initial ten minutes Argon purging was performed in order for the oxygen to be completely removed. When the temperature of the furnace reached the desired value (T=700°C), the acetylene flow was begun and lasted for two different times (30 and 60min). Acetylene is

dangerous and explosive at high concentrations. For this reason a constant flow of the volatile ingredients is required so that no acetylene is trapped inside the tube, leading to a possible explosion.

When the acetylene flow was stopped, the device was cooled down either for three hours to the environment temperature, keeping the Argon flow constant (slow cooling) or after having been cooled fast and abruptly from 350°C (while the furnace temperature was decreasing) to room temperature by submerging the powder sample in a beaker of deionized water (fast cooling). The advantage of the fast cooling procedure is that NaCl is removed directly from the final product upon contacted with water while in the case of slow drying an addition step (see below) was followed for catalyst support removal (NaCl) and purification. In the case of the fast-cooling procedure the sample was received upon centrifugation and air-drying by spreading on a glass plate. The samples that were prepared are summarized in Table C2.1:

Table C2.1. *Description of the produced SnPb@CNTs samples*

	Product	Reaction Temperature (^{o}C) in CCVD	Reaction Time (min) in CCVD	Cooling procedure
1	SnPb@CNT_30FC	700	30	Fast
2	SnPb@CNT_60FC	700	60	Fast
3	SnPb@CNT_30SC	700	30	Slow
4	SnPb@CNT_60SC	700	60	Slow

C2.3 Sodium Chloride (NaCl) removal and purification of SnPb@CNTs

SnPb@CNTs samples prepared using the slow-cooling procedure, were cleaned from sodium chloride with the following procedure: In a beaker, 30 ml of distilled water were added and the powder sample was poured off slowly. The dispersion was stirred for 10 and the system was centrifuged at 3000 rpm for 10 minutes in order to separate the SnPb@CNTs from aqueous NaCl solution. The same procedure was followed several times. To be sure for the complete removal of NaCl, each time aqueous solution of the centrifugation (supernatant) was shed into a beaker and it was examined whether sodium chloride had remained by the use of silver nitrate ($AgNO_3$). In case there was still NaCl in the supernatant, then by adding $AgNO_3$ a white precipitate (AgCl) was observed due to the reaction:

$$\mathbf{NaCl + AgNO_3 \rightarrow AgCl + NaNO_3}$$

Finally, the system was spread on a glass plate in order to dry and the final powdered product (SnPb@CNTs) was collected.

C3. Synthesis of carbon nanotubes encapsulating Manganese-Bismuth (Mn-Bi) nanorods (MnBi@CNTs) using the CCVD method

C3.1 Chemical Reagents and apparatus

The chemical reagents, their molecular formula, the company which they were provided and the apparatus that were used during the experimental procedure are described below:

- Acetylene gas (C_2H_2) of 99.9% purity (Linde HELLAS)
- Argon gas (Ar) of 99.999% purity (Linde HELLAS)
- Tubular furnace (Carbolite)
- Quartz tube of diameter 2.2 cm and 90 cm length
- Manganese-Bismuth alloy and
- Sodium Chloride (NaCl) of 99.5% purity (MERCK, 106404)
- Silver Nitrate ($AgNO_3$, ACS reagent, Sigma Aldrich, ≥99.0%)
- Bismuth needles 99.99% purity (Alfa Aesar)
- Manganese powder-325 mesh 99.3% purity (Alfa Aesar)

C3.2 Synthesis of Mn-Bi alloy

In order to synthesize the MnBi alloy (10%w/w Mn and 90% Bi) the following where used:

- 9 gr Bismuth needles 99.99% purity (Alfa Aesar)
- 1 gr Manganese powder-325 mesh 99.3% purity (Alfa Aesar)

Initially, 9 g Bismuth was grinded with 1 gr Manganese (10% w/w Mn-90% w/w Bi), are placed in a porcelain capsule and inserted into an oven for 30 minutes at 800°C. Below, the composition conversion from % w/w to atomic % as well as the alloy phase diagram is observed:

Table C3.1. *Conversion from % w/w to atomic % for MnBi alloy*[108]

weight % to Atomic % convertion			
Element	Atomic Weight	Weight %	Result
Element 1:Mn	54.94	10%	29.71
Element 2: Bi	208.98	90%	70.29

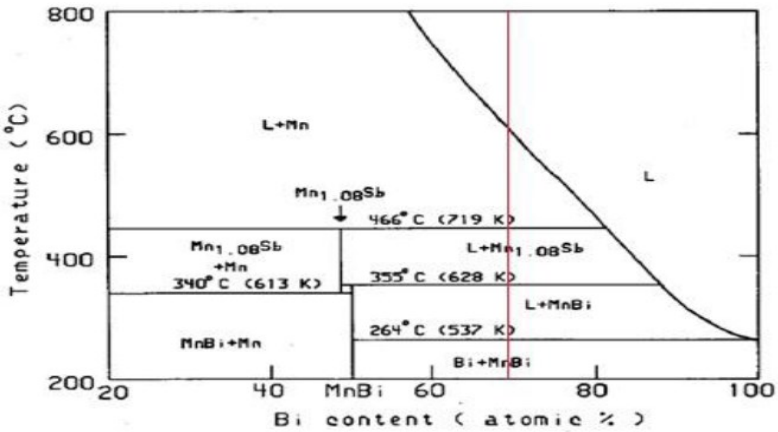

Figure C3.1: *Phase diagram of MnBi alloy*[108]

C3.3 Experimental procedure

Carbon nanotubes were synthesized by the Catalytic Chemical Vapor Deposition method, using as carbon source the acetylene in an inactive Argon atmosphere at flow rates 10 cm^3/ min and 94 cm^3/ min respectively. The catalytic substrate which was used was the MnBi alloy at reaction temperatures 700°C and 800°C for different times of acetylene flow (15 minutes, 30 minutes, 1 hour and 1.5 hours).

Initially and for every run, 40 mg of MnBi alloy and 160 mg of NaCl are grinded and placed, after becoming a fully homogeneous mixture, in an alumina (Al_2O_3) boat (before usage is thoroughly cleaned with acetone) (Figure C3.2). The quartz tube (diameter 2.2 cm and length 90 cm), which is placed inside the furnace, was cleaned also prior to use with acetone. Afterwards, the alumina boat is placed in the center of the tube, which is air-sealed so that no oxygen from the atmosphere can pass through it. The edges of the tube are connected with special digital flow-meters (in order to achieve constant gas flow) that are attached in an Argon (Ar) and an Acetylene bottle (C_2H_2).

Figure C3.2: *The sample before entering the furnace*

The parameters according to which the nanotube synthesis is achieved are chosen via the device. In the first experiments, the temperature of 700°C was chosen for various reaction times 15 min, 30 min, 1 h and 1.5 h, while for the rest of the experiments the temperature of 800°C for the same reaction times was selected. Initially, Argon flow is let to pass through the quartz tube for 10 minutes (since the reaction takes place in an inert atmosphere), so

that our system is emptied of oxygen and the inactive atmosphere is established. After the furnace has reached the required temperature, a controlled acetylene flow was set for different time flows. The acetylene is dangerous and in large concentrations explosive so, a continuous volatile ingredients flow must be ensured so that there will not be any danger of explosion. By the time the acetylene flow is stopped, the system is let to cool down to room temperature keeping the Argon atmosphere constant. Finally, the nanotubes in which the MnBi alloy is encapsulated are collected (Figure C3.3).

Figure C3.3: *The CCVD product*

C3.4 Sodium Chloride (NaCl) removal and purification of MnBi@CNTs

Next stage after preparing the samples using the CCVD method was the removal of NaCl. Initially, the sample is separated into two equal quantities so that the one stays for further characterization and the other one to be cleaned and characterized as well. In a beaker, 30 ml of distilled water are added and the sample is left to stir for 10 minutes so as to remove the aggregates and to clean more easily. Afterwards, centrifugations at 3000 rpm were performed for 10 minutes in order to separate carbon nanotubes from NaCl. The aqueous solution is poured off into a beaker and was examined whether sodium chloride had remained by the use of silver nitrate ($AgNO_3$). In case there was still NaCl in the supernatant, then by adding $AgNO_3$ a white precipitate (AgCl) was observed due to the reaction:

$$\mathbf{NaCl + AgNO_3 \rightarrow AgCl + NaNO_3}$$

Finally, the system was spread on a glass plate in order to dry and the final powdered product (MnBi@CNTs) was collected (Figure C3.4).

Figure C3.4: *The solid product after drying*

C4. Synthesis of 'Kish' Graphene Oxide monolayers using the Langmuir-Blodgett (LB) technique

C4.1 Chemical Reagents and apparatus

The chemical reagents, their molecular formula, the company which they were provided and the apparatus that were used during the experimental procedures are described below:

- Graphite (Kish, Grade 200, Graphene Supermarket)
- Millipore ultrapure water (18.2 M Ω)
- Methanol (CH_3OH, UV-grade, Sigma Aldrich)
- Nitric acid (HNO_3, 65 wt%, puriss, Sigma Aldrich)
- Sulfuric Acid (H_2SO_4, 98 wt%, Sigma Aldrich)
- Potassium Chlorate ($KClO_3$, ACS reagent>99.0%, Carl Roth)
- LB apparatus (from Nima Technology, model 312D, with a pressure sensor and dipper mounted at the center of the trough and two barriers which compress symmetrically to the center of the trough)
- TEM grids (copper grids, 2000 mesh, Plano GmbH)

C4.2 Pristine 'Kish' graphite

Graphite oxide (GO) is usually made by reacting graphite powder with strong oxidants such as a mixture of concentrated sulfuric acid, nitric acid and potassium chlorate. After oxidation, the carbon sheets are decorated by carboxylic acid groups at the edges and phenol, hydroxyl and epoxide groups mainly at the basal plane. The reaction breaks the π-π conjugation at those sites, which can be partially recovered by either chemical or thermal methods to yield again graphene (also known as reduced graphene oxide or chemically prepared graphene). Lately, GO has become a promising material for polymer reinforcement, graphene-related electronics applications and many others[229]. Here for the first time, graphene oxide was prepared using Kish graphite, that was then deposited on TEM grids (copper grids, 2000 mesh, Plano GmbH) using the Langmuir-Blodgett technique in order to form monolayers. The dependence and impact of time, injected concentration and quantity of injected material on the formation of thin graphene oxide monolayers was examined.

Kish graphite is one of the by-products of steel-making process. It can be acquired when carbon crystalizes from molten steel during the steel manufacturing procedure. Natural Kish graphite is also known to form a perfect inexpensive starting material[228] for synthesis of:

• Graphene Intercalation Compounds

• Graphene Oxide

• Graphene hybrid materials

Kish graphite which was used in this series of experiments was grade 200. This grade of Kish graphite works well for making Scotch Tape graphene. As observed in the following SEM images, Kish graphite grade 200 consists of flakes where the size ranges between 0.7-2 mm and therefore, is a good candidate for graphene oxide production due to the many structural defects that it exhibits.

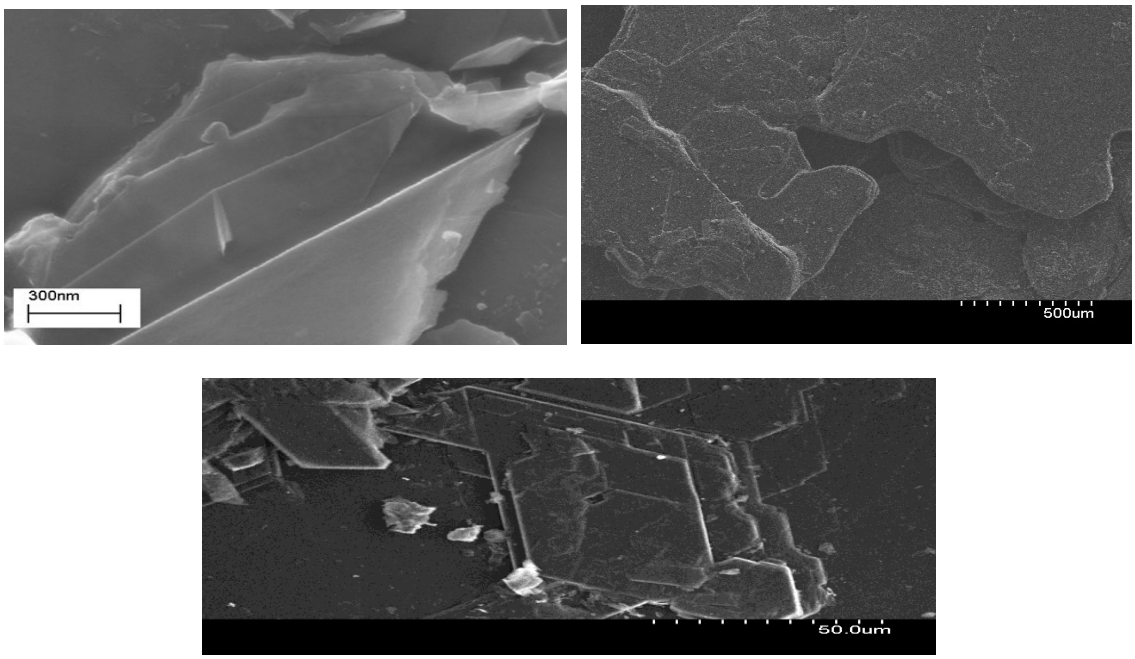

Figure C4.1: *SEM images of Kish graphite grade 200*

C4.3 Preparation of 'Kish' Graphene Oxide

'Kish'-GO was prepared using a modified Staudenmaier method[124]. According to this method, 1 gram of Graphite (Kish, Grade 200, Graphene Supermarket) was placed in an 100 ml round flask-20 ml Nitric Acid (HNO_3, 65 wt%, puriss, Sigma Aldrich) and 40 ml Sulfuric Acid (H_2SO_4, 98 wt%, Sigma Aldrich) were then added to the flask and the system was stirred for 30 minutes in an ice bath (0^oC). Afterwards, 20 grams of Potassium Chlorate ($KClO_3$, ACS reagent>99.0%) were slowly added, while the system being in the ice bath and the new system was left stirring for 18-20 hours. The next day, the system was transferred into a 500 ml conical flask which contained 200 ml of deionized water. The mixture was then centrifuged at 4000 rpm for 3-10 minutes and finally rinsed with deionized water until pH >=6.5. The final sediment was re-dispersed in water with mechanical agitation or mild sonication using a table-top ultrasonic cleaner, giving a solution of exfoliated GO. Finally, GO was spread on a glass surface and left to dry. The procedure was repeated another two times in order to have three complete cycles of oxidization. In all three cycles, samples were stored as to be used for the LB experiments.

C4.4 Deposition and formation of 'Kish' GO monolayers using the LB

When the aqueous solution of GO is directly applied onto a water surface, most of the material sinks into the sub-phase. Methanol is a good solvent for the LB experiment since it disperses GO well and spreads on a water surface rapidly. A deionized (DI) water/methanol mixture with an optimal ratio of 1:5 was used for most LB experiments[229].

A quantity of approximately 120 mg (121.59 mg) of 'Kish'GO (triple-oxidized) was mixed with 10 ml water, stirred for 20 minutes and sonicated for another 2 minutes. Afterwards, the sample was centrifuged for 20 minutes at 5800 rpm. The liquid was separated from the solid which was dispersed into 10 ml water and sonicated for 2 minutes. Another centrifugation was followed at 5800 rpm for another 20 minutes. Separation of liquid-solid and dispersion of the solid into 5 ml water and 25 ml methanol was also performed while the system was stirred for another 1.5 hour. As a last cycle, the solution was centrifuged at 5800 rpm for 20 min to further remove smaller GO sheets. Liquid was separated from solid and the solid was re-dispersed into 5 ml water and 25 ml methanol (1:5 water/methanol), stirred for 24 hours and sonicated for 10 minutes.

In order to determine the final 'Kish' GO concentration that was used in each experiment, the initial GO mass was known, the final supernatant solution that was separated from the solid GO was gathered in a beaker, left to dry and the remaining solid was weighted. The mass difference between initial GO mass and of the dried one would give each time, divided by the final known solution (water-methanol 1:5) volume the GO concentration. In this way the initial GO concentration was estimated to be 115 mg/30 ml solution (5 ml H_2O and 25 ml CH_3OH), which after doing the appropriate math leads to a concentration value of 3.8 mg/ml, quite higher than the reported concentration which is demanded or required[229] in order to a sufficient Langmuir-Blodgett surface coverage.

Alternately, when 'Kish' graphene oxide (triple oxidized) was weighed (12,5 mg), placed into a beaker, mixed with a water-methanol solution 1:5 (total 125 ml), left to stir for 1 hour, sonicated for 30 minutes and stirred again for 2 hours-in order to use in the LB experiments-the final concentration would be 0.1 mg/ml.

Afterwards, the trough (Nima Technology, model 312D, see Figure C4.2) was carefully cleaned with chloroform and then filled with DI water. 'Kish' GO dispersion was slowly spread onto the water surface drop-wise using a glass syringe. Generally, the solution was spread with speed of 50 µL/ min up to a total of 15 mL. A GO film with faint brown color could be observed at the end of the compression. The film was compressed by barriers at a speed of 20 cm^2/ min. The dimensions of the trough are 20 cm × 25 cm. Typical initial and final surface areas were around 200 and 70 cm^2, respectively. Various volumes of GO as well as various concentrations, were dispersed on the water surface and the change of pressure was monitored while compressing by closing the barriers. Finally, depositions on TEM copper grids and on Silicon wafers were accomplished, before and after compression, in order to

examine samples with Transmission Electron Microscopy (TEM). Films were transferred onto the hydrophobic copper grids (substrate) by horizontal dipping (Langmuir-Schaeffer approach). Each time the substrate was lowered into the LB trough and was allowed to touch the air-water interface in a very gentle dip of max 0.5 mm below the water level.

- Initial area: 200 cm^2
- Final area: 70 cm^2
- Speed= 20 cm^2/min
- Gain= 0.8

C4.5 Evaluation of the LB isotherms

The Π – a isotherm, which is measured and extracted in the LB, leads to essential and interesting knowledge as well as understanding about the dependence of conditions used for the LB trough experiments on the formed materials, the interactions between the particles on the surface and the deposition on certain substrates. Each isotherm is received by monitoring the change in surface pressure as a function of the area per molecule and the time of the effect, while compressing or de-compressing the barriers of the trough and alternating, therefore, the pressure of the floating material on them. During the procedure, the temperature remains stable, while the only parameters changing with each other are surface and pressure, the free parameters for a 2D phase diagram. A Langmuir-Blodgett trough was used for all series of tests that were performed for this study (Figure C4.2). The LB apparatus was obtained from Nima Technology, model 312D, with a pressure sensor and dipper mounted at the center of the trough and two barriers which compress symmetrically to the center of the trough.

Figure C4.2: *Langmuir-Blodgett trough*

C5. Development of low-dimensional Prussian-Blue Analogues using the 'inverted' LB method

C5.1 Chemical Reagents and apparatus

The chemical reagents, their molecular formula, the company which they were provided and the apparatus that were used during the experimental procedure are described below:

- Potassium tetra-cyano-platinate (II) hydrate ($C_4K_2N_4PtxH_2O$, Sigma Aldrich)
- Copper Chloride ($CuCl_2x2H_2O$, Sigma Aldrich)
- Dimethyl-dioctadecyl-ammonium (DODA)
- Millipore ultrapure water (18.2 M Ω)
- LB apparatus (from Nima Technology, model 312D, with a pressure sensor and dipper mounted at the center of the trough and two barriers which compress symmetrically to the center of the trough)
- TEM grids (copper grids, 2000 mesh, Plano GmbH)
- Silicon Nitride grids (frame thickness 100 μm and film thickness of 5 nm, PLANO GmbH)
- Highly oriented pyrolytic graphite HOPG (size 10mmx10mm, 2.0mm thickness, Goodfellow Cambridge Ltd)

C5.2 Experimental procedure

The same LB trough as in the previous case was used, cleaned thoroughly using chloroform and filled the sub-phase with a $CuCl_2$ water solution (in some tests de-ionized water was used). Dimethyl-dioctadecyl-ammonium (DODA) bromide was used as surfactant, which acts as an amphiphilic cation, although the idea of using it was rejected after some preliminary tests due to the fact that it did not assist the anticipated reaction on the surface. The injected material was in each case Potassium tetra-cyano-platinate (II) hydrate ($C_4K_2N_4PtxH_2O$, molecular weight: 377.34 g/mol), the initial concentration of which was C=15mg/8ml water-ethanol solution (1:3). Ethanol was used to assist the floating of the injected material, so that it would not sink and react this way below the surface. Before injecting the tetra-cyanide, an inclined (~50°) quartz slide was partially submerged inside the trough. The idea was to let the injected material reach more smoothly with the $CuCl_2$ surface and form a PBA monolayer on the surface instead below it. In a typical run, the trough would be filled with copper chloride, barriers would be at the position where the initial area was 200-300 cm^2 approx., 100 μl of DODA were spread on the surface and target pressure was set at a specific value. The barriers closed or opened in order to reach the set value and then the injection of 0.8-1 ml tetra-cyanide was performed. The tetra-cyanide while reaching the surface of the copper chloride sub-phase reacts according to the cationic exchange reaction as mentioned before.

The barriers would move again in order to stabilize again at the selected target pressure. The evaluation of each procedure derived from the received isotherm. Each isotherm shows the change in the applied surface pressure, the relative area change (increasing while barriers opened or decreasing when they would close) in correspondence to the experiment time.

In the end, the produced films were deposited on TEM copper grids, on Silicon Nitride grids and on Silicon wafers, before and after compression, in order to examine samples with Transmission Electron Microscopy (TEM). Films were transferred onto the hydrophobic grids (substrate) by horizontal dipping (Langmuir-Schaeffer technique). Each time the substrate was lowered into the LB trough and was allowed to touch the air-water interface in a very gentle dip of max 0.5 mm below the water level. Also, for the characterization of the films using X-Ray Photoelectron Spectroscopy (XPS) the films were also deposited onto Highly Oriented Pyrolytic Graphite (HOPG) through horizontal dipping as well.

C5.3 Evaluation of the LB isotherms

The Π – a isotherm is measured and extracted from the LB Technique. Each isotherm is received by monitoring the change in surface pressure as a function of the area per molecule and the time of the effect, while compressing or de-compressing the barriers of the trough and alternating, therefore, the pressure of the floating material on them. As mentioned before, the temperature remains stable during each procedure, while the only parameters changing with each other are surface and pressure, the free parameters for a 2D phase diagram.

C6. Experimental Setup of the Characterization Techniques - Specimen preparation

- ***X-Ray Diffraction***

The study of the samples by using the X-Ray diffraction was accomplished by a diffraction-meter D8 AdvanceBruker, department of Physics, University of Ioannina. Radiation CuKa (40 kV, 40 mA, $\lambda_{K\alpha}$) and the monochromator system of diffracted beam were used. The X-Ray diffraction diagrams were measured in the area of 2θ angles between 2° and 80° using a rotation step 0.02^o and time of 2 sec per step. All samples measured with the above diffraction-meter were in fine-grained powder form.

- ***Raman Spectroscopy***

Raman spectra were measured with the instrument Micro-Raman Renishaw system RM 1000, using excitation laser beam at 532 nm (Nd-YAG). Power between 0.5 to 1 mW of 1 μm focus was used, so that to avoid photo-decomposition phenomena of the under examination samples. The specific spectrometer was equipped with an optical microscope with magnifying lenses 50x and 100x for the beam focusing. Using the 100x lens the beam diameter that hits the sample is focused in a diameter 1 μm approximately. All the samples measured were in fine-grained powder form.

Figure C6.1: *Raman device (Dept. Mater. Sci. Engineer., Univ. Ioannina)*

- ***Differential Thermal Analysis & Thermogravimetric Analysis***

For the DTA/TG measurements, the device DTA/TG Perkin-Elmer Pyris-Diamond of the department of Materials Science and Engineering, University of Ioannina was used. For the measurements, 3 mg of the sample were used, which were placed inside a platinum capsule on one side of the thermal-scale while on the other side a-alumina was used as reference sample. The speed of temperature increase was 5^oC/min and the measurements took place in the air and in nitrogen atmosphere. All the measured samples were in fine-grained powder form.

Figure C6.2: *DTA-TGA device (Dept. Mater. Sci. Engineer., Univ. Ioannina)*

- ***Scanning Electron Microscopy (SEM)***

The SEM images were received using the scanning electron microscope, JEOL JSM-5600 V from DEMOKRITOS Institute, Athens. The under study samples were coated by a thin layer made from a conductive metal (Au), so as to avoid charging problems which would affect the quality of the received images. All the samples were in the form of fine-grained powder.

- ***Transmission Electron Microscopy (TEM)***

The TEM images were obtained by using a JEOL JEM-2100F microscope (at operating voltage of 200 kV), which was also equipped with an extra EDAX sensor. All the measured samples were in the form of fine-grained powder. During the preparation of the samples a drop from the respective solutions of the nanotubes in hexane was added on a holey carbon grid and was left in room temperature in order for the solvent to evaporate. The received images are typical and representative of the tested samples.

Additionally, Transmission Electron Microscopy (TEM) served a powerful technique towards the characterization and examination of the on-grid deposited GO and PBA. The Transmission Electron Microscope (JEOL) of Deutsches Elektronen Synchrotron (DESY) of Max Planck Institute Hamburg was used to observe the nature and structure of the GO on the surface, the ordering of the flakes forming monolayers, the overlapping of the flakes leading to double/triple layers or nano-crystals as well as the crystallinity of the samples, using Selected Area Electron Diffraction (SAED). The samples were deposited on Copper TEM grids (G2786C, Plano GmbH) and Silicon Nitride (Frame thickness of 100 μm and film thickness of 5 nm, Plano GmbH). The TEM images were obtained by using a Phillips/FEI CM-12 microscope operating at 80 kV.

- ***^{119}Sn-Mössbauer spectroscopy***

^{119}Sn Mössbauer spectroscopy served a powerful and complementary to XRD technique so as to identify and characterize the Sn local environment and formal oxidation state in

Sn@CNTs solids. Mössbauer measurements were performed using a constant acceleration spectrometer with $Ba^{119}SnO_3$ source maintained at room temperature (Physics Department, University of Ioannina). A Pd filter was used to eliminate the 25.2 keV X-ray radiation. A liquid helium/nitrogen cryostat (MD306 Oxford Instruments) was used to control the measuring temperature at 80K. Suitable computer programs were used to fit the experimental spectra using Lorentzian line shapes.

- ***Superconducting quantum interference device (SQUID)***

SQUID measurements were performed using the Superconducting Quantum Interference Device of Palacky University (Czech Republic), in temperature range from 2 to 6 K with applied magnetic fields up to 1 T. The powder samples (SnPb@CNTs samples) were contained in transparent gelatine capsules. H_{ext} was 20 Oe and Mass Magnetization (M) as a function of Temperature (T) and Magnetic Field (B) was studied in comparison with the respective ones for the Sn@CNTs.

- ***Vibrating Sample Magnetometer (VSM)***

The isothermal measurements of the magnetization were collected in room temperature, in liquid Nitrogen temperature using the Vibrating Sample Magnetometer of VSM LakeShore 730, which was equipped with a low temperature cryostat (Janis). All the measured samples were in the form of fine-grained powders.

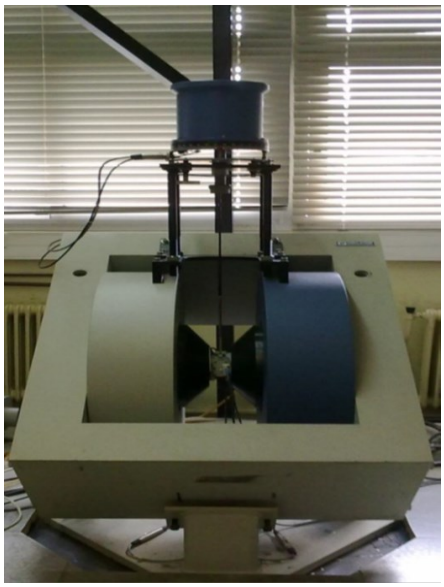

Figure C6.3: *VSM device (Dept. Physics., Univ. Ioannina)*

- ***Infrared Spectroscopy (FTIR)***

Infrared spectroscopy (IR) was used to characterize and evaluate the quality of the produced graphene oxide. The Potassium Bromide (KBr) platelet technique was used and the IR-patterns of the composed GO were obtained by the FT-IR-Spectrometer (Perkin-Elmer GX)

of the Department of Materials Science and Engineering, University of Ioannina. The final spectra were obtained in the range of 400-4000 cm^{-1}. Each spectrum was the average of 64 scans collected with 2 cm^{-1} resolution. Samples were in the form of KBr pellets. By admixing 5 wt% of the sample powder with KBr (95%) in an agate mortar a homogeneous mixture of fine-grained powder was formed. The powder mixture was placed in a mold and compressed axially using a hydraulic SPECAC press in order to produce pellets of 1 cm diameter and 1-1.5 mm height.

- ***X-Ray Photoelectron Spectroscopy (XPS)***

XPS spectra were collected at room temperature on a SSX-100 (Surface Science Instruments) spectrometer equipped with a monochromatic Al K α X-ray source (h ν = 1486.6 eV) and operating at a base pressure of 3×10^{-10} mbar (Zernike Institute for Advanced Materials, University of Groningen, the Netherlands). The energy resolution was set to 1.3 eV and the photoelectron take-off angle was 37°. A flood gun providing 0.1 eV kinetic energy electrons in combination with a Mo grid placed above the sample was used to compensate for the charging of the sample. Binding energies are reported ± 0.1 eV.

- ***Ultraviolet-Visible Spectroscopy (UV-Vis)***

Ultraviolet-Visible Spectroscopy was applied in order to prove that after each deposition of one monolayer of the on-surface formed PBA on a quartz-glass substrate the absorption of UV-radiation would be increased in a linear way as the thickness of the deposited mater would rise. For this purpose the UV-Vis Spectrometer (SHIMADZU UV-2700, capable of 8 Absorbance measurements and suited for measuring low transmittance samples)) of Center for Free-Electron Laser Science (CFEL, DESY Hamburg) was used.

Part D:

Results and Discussion

D1. Carbon nanotubes encapsulating superconducting tin nanowires (Sn@CNTs)

In this chapter, the development of carbon nanotubes encapsulating tin superconducting nanowires by employing the conversional method of catalytic chemical vapour deposition (CCVD) over different tin containing solids is described. The role of tin-containing catalysts [metallic tin (Sn), tin oxide (SnO) and tin dioxide (SnO_2)], as well as the effect of the reaction time and temperature during the CCVD in the overall quality and quantity of the produced nanowires were investigated in detailed. The characterization was performed using various analytical techniques including X-Ray Diffraction (XRD), Raman Spectroscopy, Differential Thermal (DTA) and Thermogravimetric Analyses (DTA/TGA), Mössbauer Spectroscopy, Scanning Electron Microscopy (SEM) and Transmission Electron Microscopy (TEM).

The X-ray diffraction (XRD) patterns of all CCVD products prepared at different reaction times and different reaction temperatures using tin oxide powder catalysts (SnO_2 or SnO) are shown in Figures D.1.1 and D.1.2. For comparison the standard X-Ray Diffraction patterns of β-Sn (JCPDS 4-0673) and SnO_2 (JCPDS 2-1337) are also present in each diagram. In figures 1.1(a) and (b) the diffraction patterns of the products received for various reaction times (30min, 60min, 90min and 120min) and at 700°C using SnO_2 and SnO respectively as catalyst are shown, while in Figures D1.2 (a) and (b) the corresponding diffraction patterns of the products received for various reaction temperatures (600°C, 700°C, 800°C and 900°C) and for 1h of acetylene flow, using SnO_2 and SnO, respectively, are also presented. All patterns (for both SnO and SnO_2 catalysts) show the presence of β-Sn (JCPDS 4-0673) and SnO_2 (JCPDS 2-1337) while β-Sn was the only phase observed in the case that metallic tin was used as catalyst (pattern not shown here). Based on the relative intensities of the diffraction peaks, a rough estimation of the amount of β-Sn and SnO_2 phases in every sample can be achieved. From the diagrams it is obvious that β-Sn is formed in higher amount in the case of SnO_2 catalyst as compared to nanowires formed on SnO catalyst. Moreover, the XRD patterns of nanowires produced using SnO_2 indicate that after 90 minutes of acetylene flow the characteristic peaks of tin dioxide is almost absent, which leads to the conclusion that all SnO_2 quantity reacted and the tin is found probably inside carbon nanotubes. In general, all XRD patterns shows the characteristic peaks of metallic tin that is probably encapsulated within carbon nanotubes (as also revealed from TEM images shown below), as well as the reflections of tin dioxide peaks that arise from either unreacted catalyst or byproduct of the reaction. In fact, in the case of using SnO as catalytic substrate, the presence of SnO_2 is justified if one takes into consideration the disproportionation of SnO at temperatures above 500°C in equimolar quantities of β-Sn and SnO_2 according to the reaction[141,179]:

$$\mathbf{2SnO \rightarrow Sn + SnO_2}$$

This phenomenon leads to products of higher percentage of partially Tin-filled carbon nanotubes compared to the samples produced using SnO_2 as catalyst, a fact also supported

by Sn-Mössbauer spectroscopy and TEM results. Considering the temperature effect, using SnO_2 as catalyst, the optimal temperature at which tin Dioxide peaks are not to observe turns out to be 900°C, while in the case of SnO this is observed at 800°C.

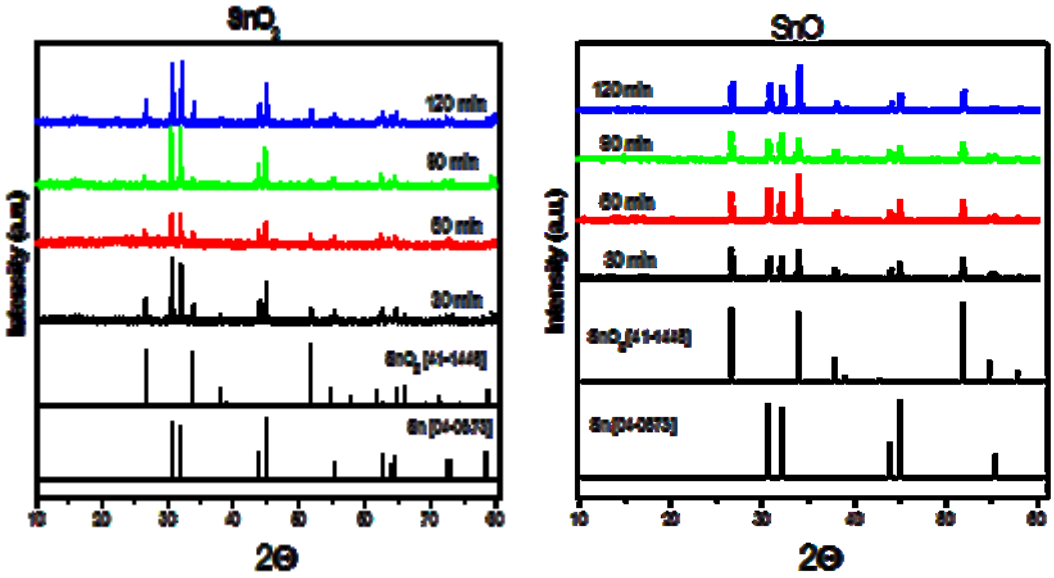

(a) (b)

Figure D1.1: *XRD patterns of Sn@CNTs products prepared using (a) SnO_2 and (b) SnO as catalyst for different reaction times*

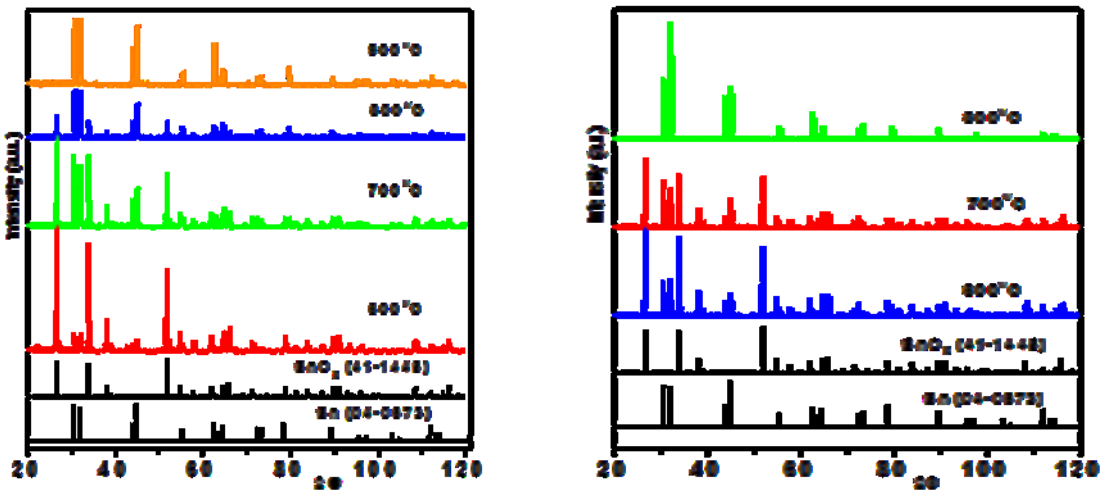

(a) (b)

Figure D1.1: *XRD patterns of Sn@CNTs products prepared using (a) SnO_2 and (b) SnO as catalyst for different reaction temperatures.*

Sn-Mössbauer spectroscopy formed a powerful and complementary to XRD technique in order to identify and characterize the Sn local environment and formal oxidation state in Sn@CNTs hybrid solids. Mössbauer spectra obtained at 80 K for three representative

products obtained using Sn (a), SnO (b) and SnO_2 (c) solids at 800°C and for 60min are shown in Figure D1.3. The spectrum of Sn@CNTs prepared using metallic tin shows one quadruple doublet with a line width at half maximum equal to 0.40 mm/s. The analysis of the spectrum gave a small quadruple splitting parameter (QS) and an isomer shift (IS) value equal to 2.54 mm/s (see Table D1.1). These hyperfine parameters are typical and characteristic for β-Sn. In the case of Sn@CNTs produced over SnO_2 and SnO catalyst solids, two contributions are observed indicating the presence of two Sn containing phases. Analysis of the corresponding spectra shows that these phases are β-Sn and SnO_2 (see Table D1.1). Their quantitative relative ratio can accurately be measured from the corresponding Mössbauer spectral areas. Accordingly, the SnO_2/ β-Sn percent ratio was found to be 0.59 and 1.00 in Sn@CNTs (over SnO_2) and Sn@CNTs (over SnO) respectively, an issue explained by the disproportionation of SnO as mentioned above ($2SnO \rightarrow Sn + SnO_2$). As presented below (see TEM and SEM results) when SnO and SnO_2 are used as catalysts the amount of *in-situ* formed β-Sn controls the degree of encapsulation within carbon nanotubes.

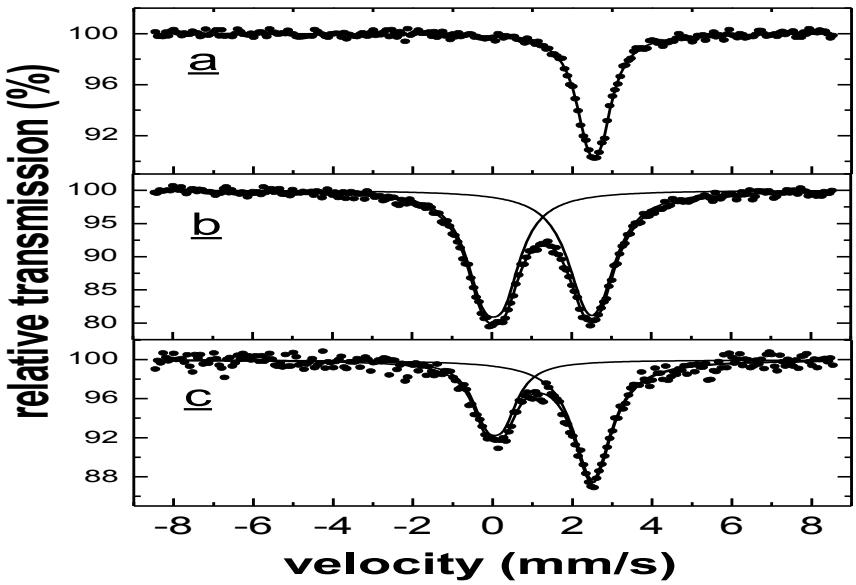

Figure D1.3: *Mössbauer spectra of Sn@CNTs products obtained using Sn (a), SnO (b) and SnO_2(c) solid catalysts at 700°C and for 60min of acetylene flow*

Table D1.1. *Mössbauer effect spectral data at 80 K*

Sn@CNTs samples from	IS (mm/s)	GA/2 (mm/s)	QS (mm/s)	Area (%)
Sn	2.54	0.40	0.32	100
SnO	0.04	0.53	0.53	51
	2.56	0.59	0.38	49
SnO_2	0.05	0.42	0.45	37
	2.50	0.58	0.00	63

The estimated errors on the Mössbauer parameters are ±2 on the last significant digit for isomer shift (IS) and quadrupole splitting (QS) and ±5 for half width at half maximum (GA/2) and for the spectral area.

The Mössbauer spectra of all samples were obtained and the data that were collected are summarized in Figure D1.4. It appears that for the investigated reaction temperature range, the Sn@CNT products on both SnO and SnO_2 catalysts show an increase in the % tin content along with the temperature increase. It should be emphasized here that in the case of using SnO as a catalyst, the final nanotubes contain higher percentage of metallic tin than in the case of using SnO_2 at the same reaction temperature, a fact which is justified if one takes into account the already mentioned disproportionation of SnO at temperatures higher than 500°C. This finally leads to higher percentage on nanotubes containing tin, with most of them though being partially filled, as exhibited by the TEM images that follow.

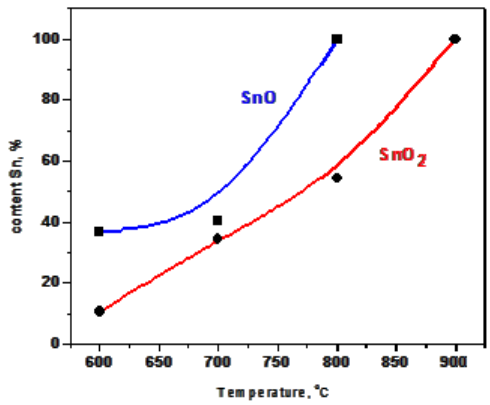

Figure D1.4: *Content) of Sn(0) in nano-crystalline Sn@CNT products at various reaction temperatures using SnO and SnO_2 solid catalysts*

All products were investigated using scanning (SEM) and transmission electron microscopy (TEM). Figure D1.5 shows SEM images of Sn@CNTs solids over different catalysts (pure Sn, SnO_2 and SnO). From these images we can obtain a rough estimation of the dimensions of carbon nanotubes. The produced nanotubes exhibit a diameter between 20

and 40 nm and length up to 5 µm. Moreover, from these images it is clear that in case of SnO_2 catalysts the CNT are almost fully filled while those obtained from SnO catalysts are only partially filled (see Figure D1.5b).

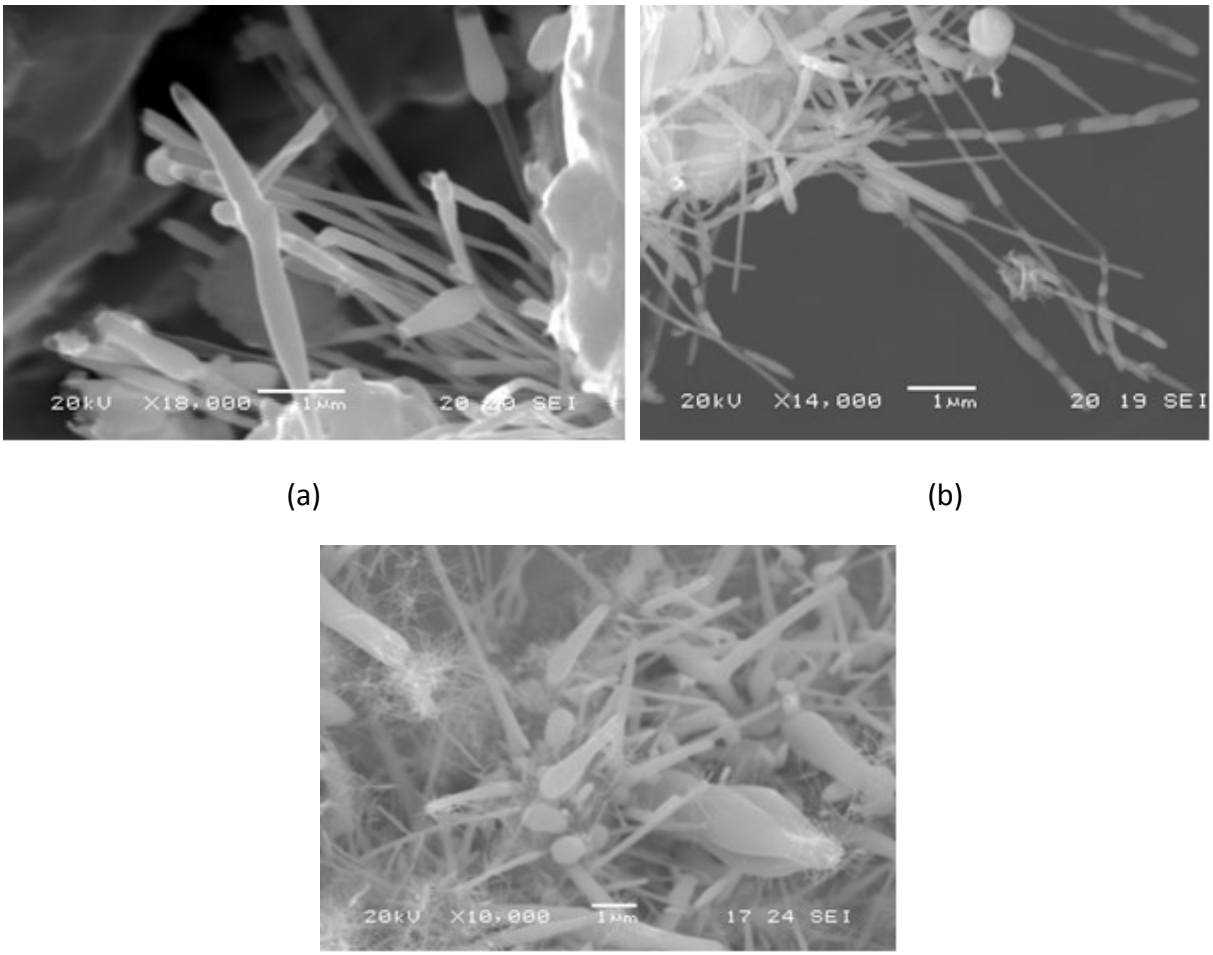

Figure D1.5: *Representative SEM images of β-Sn filled CNT made from (a) SnO_2, (b) SnO and (c) Sn catalysts produced at 700°C for 60min of acetylene flow.*

The above results were confirmed by TEM and representative images are shown in Figure D1.6. It is confirmed by TEM that in the case of SnO_2 catalysts the CNTs are almost fully filled (a) while those obtained from SnO catalysts are only partially filled (b). Unequivocal proof of the nature of the encapsulated phase within CNT comes from selected area electron diffraction (SAED) analysis. Figure D1.6a (inset) shows a typical SAED pattern which can be fully indexed to metallic β-Sn, taken from the darker (filled with Tin) part of the nanotubes. Moreover, the characteristic regular diffraction spots indicate that these are in fact single crystals. It is important to note here that in a large area of the sample under TEM observation, no β-Sn phase outside CNT was observed. In other words, in the cases of SnO and SnO_2 catalysts all the in situ formed β-Sn is encapsulated within CNT in the form of single crystalline nanowires. These results are strongly supported by differential thermal analysis (DTA, see below).

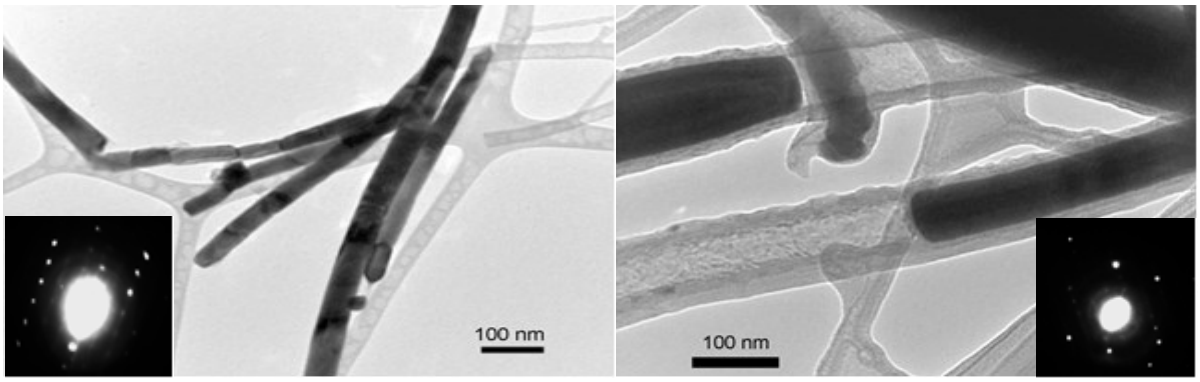

(a) **(b)**

Figure D1.6: *TEM and the respective SAED images of Sn@CNTs produced at 700°C for 60min of acetylene flow using SnO_2 (a) and SnO (b) as catalysts*

The thermal behavior of the β-Sn hybrid nanowires was investigated using differential thermal analysis (DTA). Figure D1.7 shows DTA traces of Sn@CNTs solid prepared using SnO as precursor (for 30 minutes of acetylene flow at 700°C) and of pure commercial metallic Sn served for comparison purposes. In markedly contrast with bulk Sn, the β-Sn nanowires encapsulated within CNTs show large hysteresis (93°C) between melting and crystallization temperature. The same exactly profiles are observed over five heating-cooling DTA cycles (see Figure D1.7) while interestingly, similar behavior has been observed in the case of Ge nanowires encapsulated within carbon nanotubes[238]. This super-cooling behavior is not yet fully understood and worth further investigation, although it is believed that is due to the presence of a kinetic barrier for homogeneous/heterogeneous crystallization within the nanotubes. A final point is that the absence of any crystallization signal between 200-230°C strongly suggests that there is no bulk metallic Sn present, in full agreement with TEM results.

Figure D1.8 shows the DTA/TGA diagrams taken in air of a representative sample prepared using tin dioxide as catalyst, for 30 minutes reaction time at 700°C. From the curves and at the temperature range between 380 και 500°C an 8% weight increase is observed, which is caused by the oxidation of metallic Tin that is present inside the carbon nanotubes in the form of nanowires. At higher than 500°C temperatures, the destruction of carbon nanotubes is observed due to their thermal decomposition, which is accompanied by a 3% weight loss. The thermal decomposition might be caused at even lower temperatures (≈450°C), however is not visible since at these temperatures the antagonistic effect of oxidization of tin prevails (an effect that causes increase in the mass of the system and therefore this method cannot be used to determine the carbon nanotube yield with accuracy). Similar results were observed for all the other products.

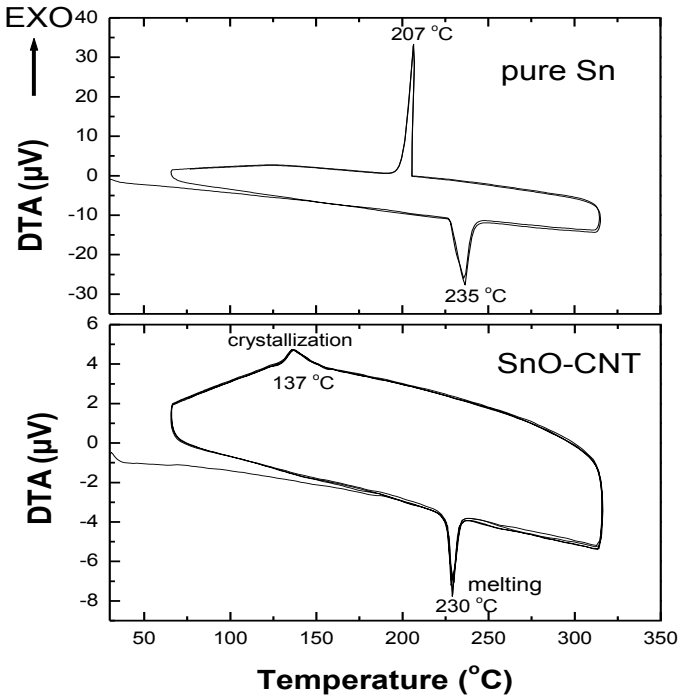

Figure D1.7: *DTA curves of pure metallic Sn and Sn@CNTs (prepared using SnO solid) under nitrogen flow with a heating rate of 5°C/min (5 cycles)*

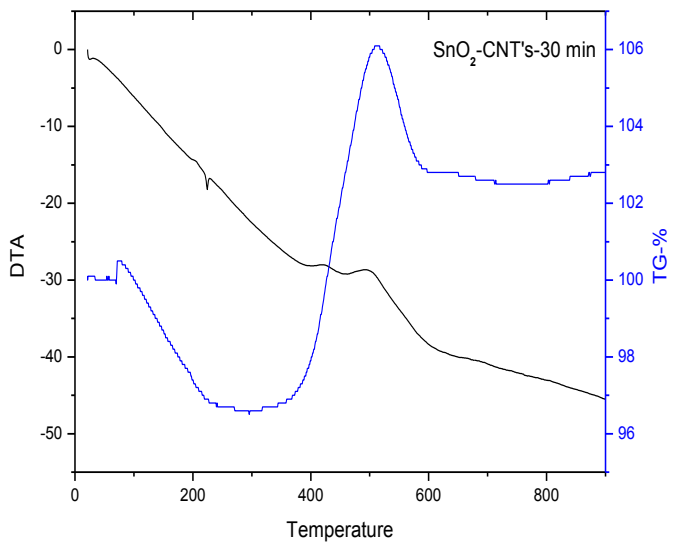

Figure D1.8*: DTA/TG curves of a Sn@CNTs sample prepared using SnO_2 for 30 minutes of acetylene flow at 700°C*

A very powerful method for the characterization of carbon deposits, and more specifically for CNTs, is Raman spectroscopy as it has been reported for both single-wall (SWNTs) and multi-wall carbon nanotubes MWCNTs[235,236]. Figure D1.9 shows the Raman spectra of the as-grown CNTs on different Sn-based catalysts (Sn, SnO and SnO_2) using an

Nd: YAG laser at 532 nm. The spectra are characteristic for the respective nanotubes; they do not change significantly if the laser spot is scanned over the nanotube samples. In the Raman-shift range 1200–1800 cm^{-1}, two peaks are observed at 1350 and 1595 cm^{-1} corresponding to graphite D- and G-bands, respectively (Figure D1.9). The G-band corresponds to the tangential stretching (E_{2g}) mode of highly oriented pyrolytic graphite (HOPG) and can be used to assess the degree of crystallinity/graphitization, while D-band at 1354 cm^{-1} originates from disorder in the sp^2-hybridized carbon atoms, characteristic for lattice distortions in the curved graphene sheets and/or tube ends[236,237]. The relative intensity of D and G bands (I_D/I_G), reveals the degree of disorder and it was found to be 0.83 (Sn@CNT over metallic tin), 0.90 (Sn@CNT over SnO catalyst) and 0.86 (Sn@CNT over SnO_2 catalyst). These values are similar to those reported (I_D/I_G = 0.85–1.3) in the literature for CNTs prepared using acetylene[230,231]. Concerning the Sn@CNT sample and in order to prove the presence of carbon nanotubes dispersed in the whole mass of the metallic tin, the sample was cut to access an inside surface of the bulk material. The Raman spectrum taken from these internal surfaces shows the presence of D- and G-bands and confirms that carbon nanotubes are formed and distributed homogeneously in the mass of melted tin during the reaction. A second proof comes from measuring the hardness of the composite material. An 80% increase in Vickers hardness of Sn-CNT compared to the pure metallic tin was observed indicating reinforcement of metallic tin due to the presence of carbon nanotubes.

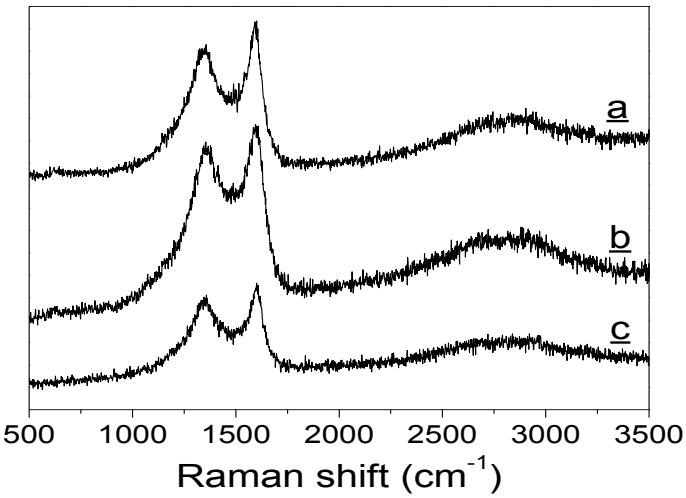

Figure D1.9: *Raman spectra of Sn@CNTs over metallic tin (a), SnO (b) and SnO_2 (c) samples at 700°C for 30min of acetylene flow*

In Figure D1.10 that follows the Raman spectra of Sn@CNTs produced over SnO_2 in comparison with the respective ones for the nanotubes produced over SnO for different reaction times (30min, 60min, 90min and 120min) at 700°C are exhibited. Here again in the Raman-shift range 1200–1800 cm^{-1}, the two peaks are observed at 1350 and 1595 cm^{-1} corresponding to graphite D- and G-bands for both products. In table D1.2 the relative

intensities I_D/I_G concerning each product using SnO or SnO_2 for each reaction time are calculated. The obtained values indicate the fine quality of the products.

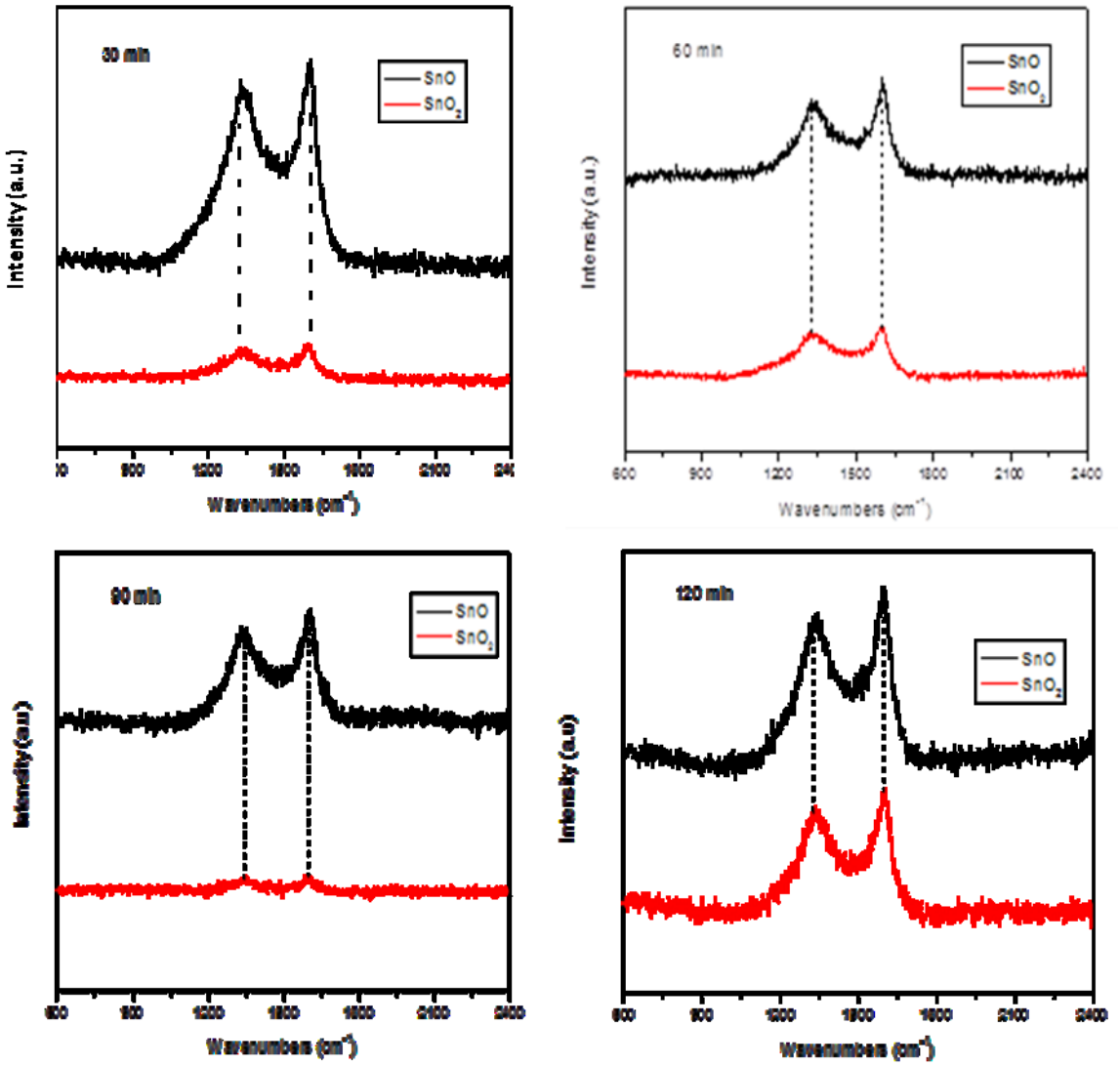

Figure D1.10: *Raman spectra of (Sn@CNTs) products using SnO and SnO_2 as catalysts after 30, 60, 90 and 120 minutes of acetylene flow at 700°C*

Table D1.2. *I_D/I_G intensities ratio of Sn@CNTs products prepared over SnO_2 and SnO catalysts at various reaction times*

Acetylene flow time (minutes)	I_D/I_G	
	SnO_2	SnO
30	0.78	0.90
60	0.86	0.77
90	0.81	0.85
120	0.84	0.84

As a conclusion, the role of tin-containing catalysts [metallic tin (Sn), tin oxide (SnO) and tin dioxide (SnO_2)], as well as the effect of the reaction time and temperature during the CCVD in the quality and quantity of the produced nanowires were investigated in details. Electron spectroscopy measurements showed that the produced nanowires covered with nanotubes have a diameter between 20 and 40 nm and length up to 5 μm, while unreacted catalyst particles (SnO_2) are also observed. The XRD patterns revealed the characteristic peaks of metallic tin (β-Sn) that was encapsulated in carbon nanotubes, as well as the reflections of tin dioxide (unreacted catalyst). However, after 90 minutes of acetylene flow the characteristic peaks of tin dioxide in the XRD patterns are almost absent, which leads to the conclusion that all SnO_2 reacted and lies potentially in the form of metallic tin inside carbon nanotubes. In the case of using SnO as catalyst, the presence of SnO_2 is justified if one takes into account the disproportionation of SnO at temperatures above 500°C which yields equimolar quantities of β-Sn and SnO_2 according to the reaction: $2SnO \rightarrow Sn + SnO_2$. This phenomenon leads to products of carbon nanotubes filled partially with metallic tin compared to the samples produced using SnO_2 as catalyst where filling is more continuous, a fact in agreement with Mössbauer-effect spectral data. Considering the effect of temperature, using SnO_2 as catalyst, the optimal temperature at which tin dioxide peaks are absent seems to be 900°C, while in the case of SnO the same phenomenon is observed at lower temperature (800°C). Concerning the quality of the outer of carbon nanotubes surrounding metallic tin nanowires using Raman spectroscopy, the I_D/I_G ratio of all samples was calculated. The ratio ranges between 0.77 and 0.90, which confirms the fine overall quality of the produced CNTs. The TGA analysis indicated that the produced Sn@CNTs were formed at a yield around 11% w/w.

D2. Carbon nanotubes encapsulating Tin-Lead nanowires (SnPb@CNTs)

In this chapter, tin-lead superconducting nanowires were developed in the interior of carbon nanotubes by applying the conversional catalytic chemical vapour deposition method over common solder (61 wt% Sn, 39 wt% Pb) impregnated in NaCl. Carbon nanotubes encapsulating superconducting SnPb alloy were composed by CCVD, using acetylene as carbon source. A similar procedure like in the case of Sn@CNT was followed (see above). The reaction temperature was set to 700°C while two reaction times, 30 and 60 min were chosen. Upon reaction at 700°C two coolling procedures were followed: *fast cooling* by pouring off the final product powder of the CCVD from the ceramic boat directly in deionized water and *slow cooling* by letting the final product to cool down at room temperature. The advantage of the fast cooling procedure is that NaCl is removed directly from the final product upon contacted with water while in the case of slow cooling an additional step (see below) was followed for catalyst support removal (NaCl) and purification. The Tin-Lead alloy was used as a catalyst and it is noteworthy that only tin acts as a catalyst, while lead is inactive. Sodium chloride was used as substrate for the immobilization (impregnation) of the SnPb alloy, as since it is also inactive and can be easily removed with water. Lead was chosen because of its higher superconducting critical temperature (Tc) than that of compared to tin and so it is expected to increase the critical temperature of the alloy. The critical temperature of Lead is 7.05 K and that of Tin 3.7 K. To achieve critical temperature of Tin, pumping over liquid Helium atmosphere is required, while, in order to realize that of for Lead only dipping in liquid Helium is required. The final products were denoted as SnPb@CNTs. A fully structural, physicochemical and morphological characterization was performed using a combination of analytic techniques including X-Ray Diffraction (XRD), Raman Spectroscopy, Differential Thermal and Thermogravimetric Analysis (DTA/TGA), Mössbauer Spectroscopy, Superconducting Quantum Interference Device (SQUID), Scanning Electron Microscopy (SEM) and Transmission Electron Microscopy (TEM).

X-ray diffraction was used to prove the successful integration of Sn inside carbon nanotubes and the existence of NaCl before its removal as well as its absence after removal. Figure D2.1 shows the XRD patterns of SnPb@CNT_30FC and SnPb@CNT_60FCsamples. In both X-Ray diagrams, the characteristic peaks of metallic Tin (β-Sn, JCPDS 04-0673) and of SnO_2 due to the tin oxidation by the atmospheric oxygen, most likely during the cooling procedure are observed. Metallic tin (or a tin-rich containing phase) is most probably located in the interior of nanotubes as revealed from TEM images (see below). The absence of any reflections from NaCl indicated that the later was efficiently removed upon contact of the sample with the water bath. Finally, a small intensity peak at 37° is observed and could be attributed to a phase of SnPb alloy found in the products, which is difficult to observe in most XRD patterns due to noise.

In Figure D2.1, the X-Ray patterns of SnPb@CNT_30SC and SnPb@CNT_60SC for 30 min and 60 min acetylene flow before and after sodium chloride removal and purification are presented. Before cleaning, the characteristic NaCl peaks at 31°, 45°, 55° (SnPb@CNT_30SC-NaCl) are observed. After cleaning (SnPb@CNT_30SC), the characteristic NaCl peaks are not observed, a fact that indicates that removal of NaCl was successful.

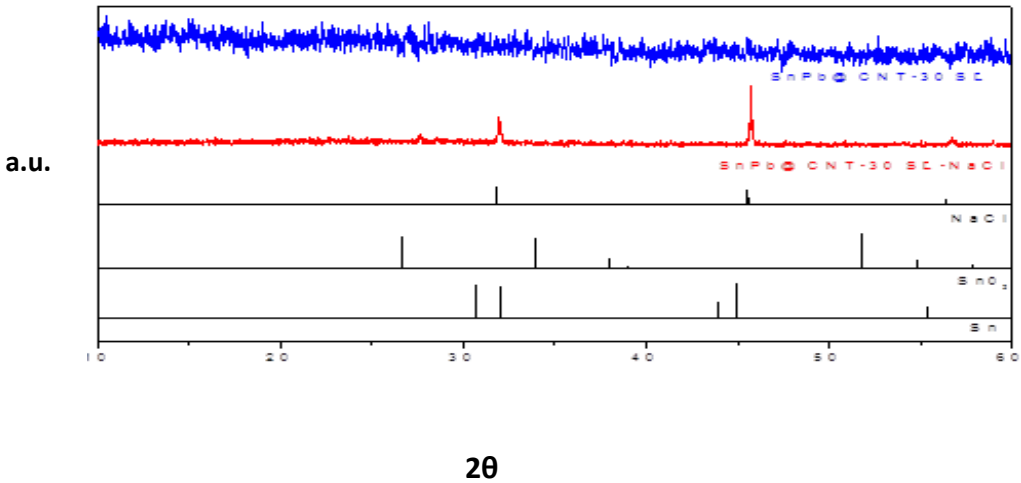

Figure D2.1: *XRD patterns of SnPb@CNT-30SC before and after removal of NaCl*

In Figure D2.2 the X-Ray patterns of SnPb@CNT_60SC-NaCl and SnPb@CNT_60SC for 60 min acetylene flow before and after NaCl removal are shown. Here also, the characteristics NaCl reflections are not observed in the SnPb@CNT_60SC proving its successful removal.

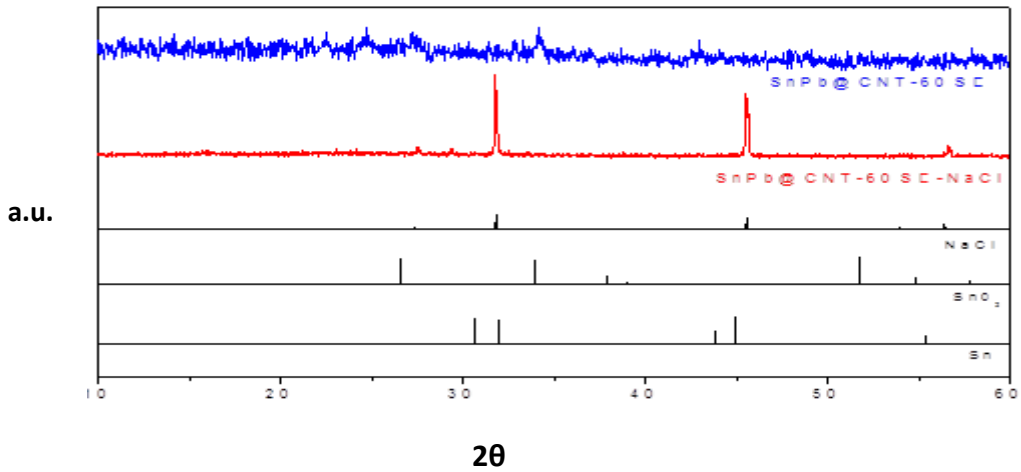

Figure D2.2: *XRD patterns of SnPb@CNT_60SC-NaCl and SnPb@CNT-60SC*

In Figure D2.3 the XRD patterns of SnPb@CNT_30FC and SnPb@CNT_60FC products after NaCl removal are exhibited. The absence of any reflections from NaCl indicates that all NaCl was successfully removed after abrupt contact with water (submerging abruptly the CCVD product into a beaker of water, while the furnace temperature was at 350°C, without the need of any other purification process.

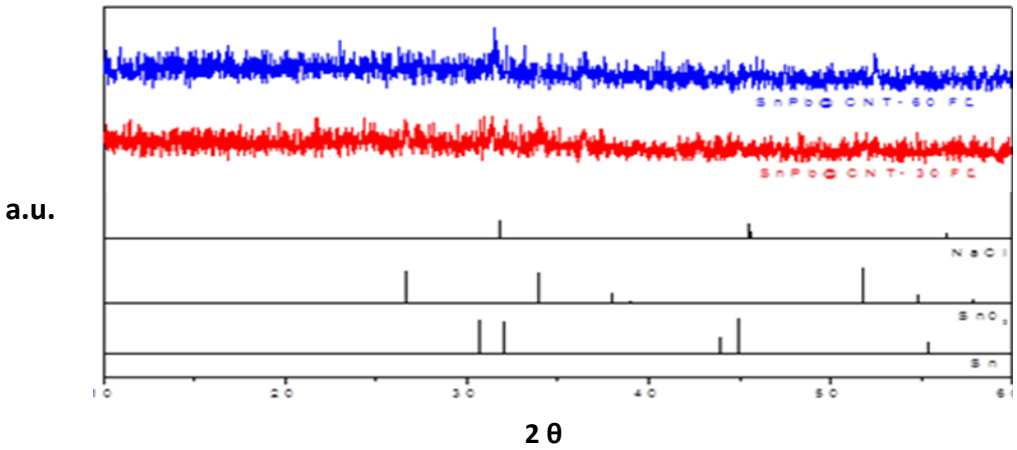

Figure D2.3: *XRD patterns of SnPb@CNT_30FC and SnPb@CNT_60FC products after NaCl removal*

After the XRD analysis one can reach to the conclusion that NaCl is successfully removed in the case of fast cooling as well as compared to the slow cooling procedure. This indicates that since the sodium chloride removal sufficiency is equal, the fast cooling is the most preferable procedure, as it does not require many stages.

In Figure D2.4, Raman spectra of SnPb@CNT_30SC and for SnPb@CNT_60SC samples upon slow cooling at room temperature (SC) for 30 min and 60 min, respectively are shown while Figure D2.5 show the Raman spectra of SnPb@CNT_30FC and for SnPb@CNT_60FC (fast cooling samples) at room temperature (FC) for 30 min and 60 min, respectively. In all spectra, the two characteristic peaks at 1300 and 1600 cm^{-1} are observed, which correspond to D and G bands respectively[236,237], characteristic for the hybridization of carbon atoms in the nanotubes surrounding the metallic nanowires. The G band is attributed to tension vibrations (sp^2) of E_{2g} type of highly oriented pyrolytic graphite (HOPG), while D band originates from the disorder of the hexagonal graphitic lattice in the curved graphite sheets and/or on the edges of CNTs (sp^3 hybridization)[230,231]. The ratio of the relative intensities R=ID/IG reveals the degree of disorder in the graphitic lattice. Low values below 1 are indicative of a high quality graphitic structure while values above this value testify for a large number of structural defects. According to the received spectra, the ratio I_D/I_G was calculated (Table D2.1) for all the samples and was found to range between 0.88 and 0.92, a fact that confirms the fine quality of the formed carbon nanotubes. From the calculated ratios I_D/I_G it is observed that the quality of nanotubes is not affected by the final drying procedure of the sample (slow or fast cooling at room temperature). These results are in total agreement with the already discussed XRD data and are quite important indicating that even with less composition stages (fast cooling) carbon nanotubes of the same quality are produced, while the removal of sodium chloride is successfully accomplished as well.

Table D2.1. *Relative intensity ratios I_D/I_G for different acetylene flow times*

Samples	Acetylene flow time (min)	SnPb I_D/I_G
SnPb@CNT_30FC	**30**	**0,90**
SnPb@CNT_60FC	**60**	**0,88**
SnPb@CNT_30SC	**30**	**0,92**
SnPb@CNT_60SC	**60**	**0,88**

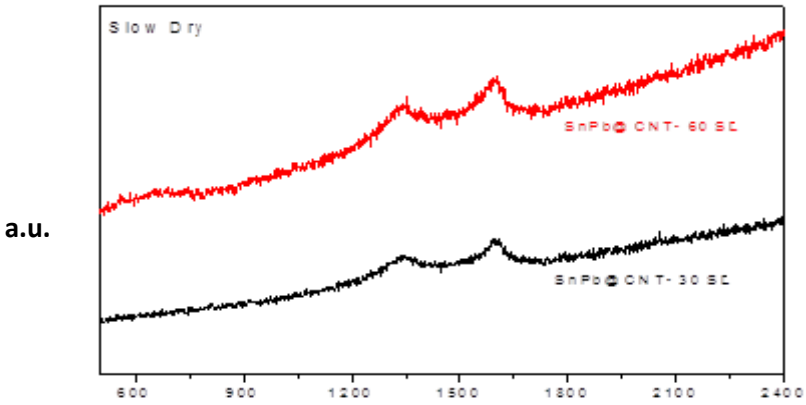

a.u.

Raman shift (cm^{-1})

Figure D2.4: *Raman shifts of SnPb@CNT_30SC and SnPb@CNT_60SC*

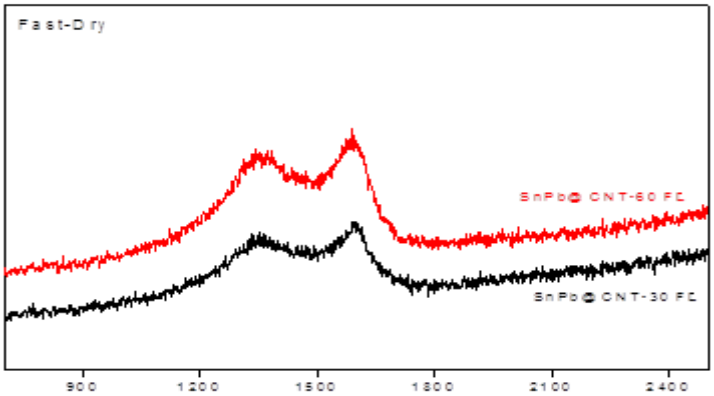

a.u.

Raman shift (cm^{-1})

Figure D2.5: *Raman spectra of SnPb@CNT_30FC and SnPb@CNT_60FC*

A TGA diagram of a representative sample (SnPb@CNT_60FC) is shown in Figure D2.6. Between 380 and 600°C an increase of 6% w/w in the sample is observed due to the oxidation of metallic tin and/or lead which exist inside of nanotubes (see TEM results below) in the form of nanowires. At temperatures above 600°C destruction of carbon nanotubes occurs due to thermal decomposition, which is followed by a 3% weight loss. The thermal decomposition of course, may be caused at even lower temperatures (starting from ~450°C), however it is not visible since at these temperatures, the competitive phenomenon of tin oxidation prevails which causes a weight increase. The results for the other samples were similar.

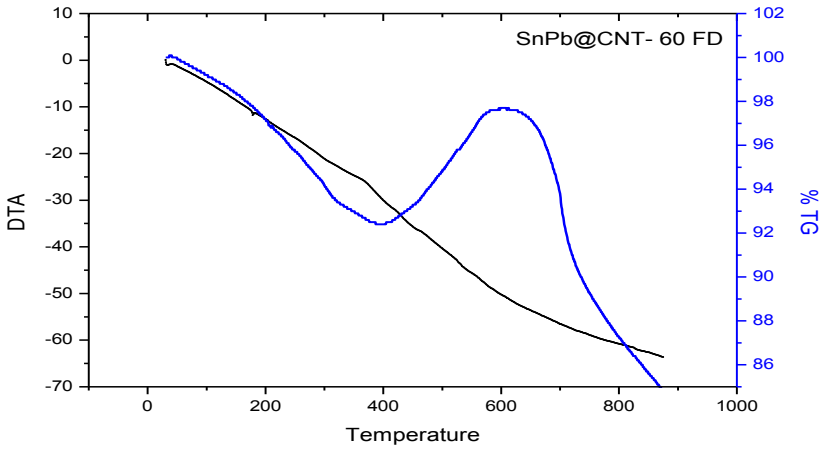

Figure D2.6: *TGA curve of SnPb@CNT_60FC*

In Figure D2.7 a DTA diagram of the sample SnPb@CNT_30SC is observed. Three cycles of heating and cooling were performed in order to examine the behavior of the nanowires inside carbon nanotubes. At 180°C the melting point of the solder which appears to be found in the final product is observed. At 250°C one can observe the melting point of metallic tin, being relatively close to the melting point of pure tin (237°C). As the temperature decreases, the crystallization temperature of tin is observed at higher temperature (240°C) compared to that of pure tin (207°C) (see Chapter D1 above), showing a little hysteresis from the realized melting point. Finally, at 155-160°C the crystallization point of the SnPb alloy is also observed. The same temperatures are obtained after three subsequent DTA cycles.

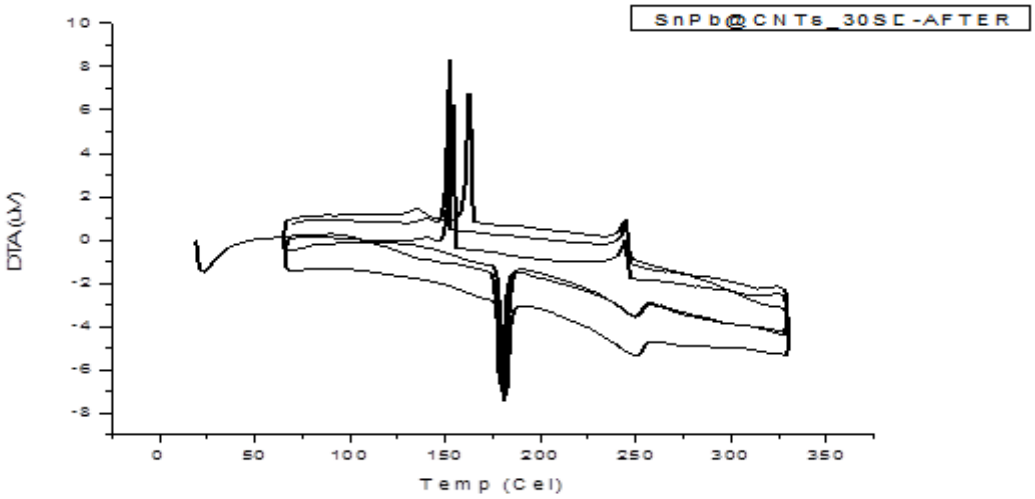

Figure D2.7: *DTA diagram of SnPb@CNT_30SC*

Representative SEM images of the sample SnPb@CNT_30SC at different product magnifications confirm the formation of homogenous carbon nanotubes inside of which metallic nanowires have been formed. Nanotubes have a diameter which varies between 46.9 and 52.3 nm (as seen in Figure D2.9), while their length extended up to 2 µm. In Figure D2.10 individual nanotubes are also seen to come out of the main mass of the catalyst. As it is observed, most of the nanotubes are fully filled with metallic nanowires, however, there are some nanotubes which are partially filled.

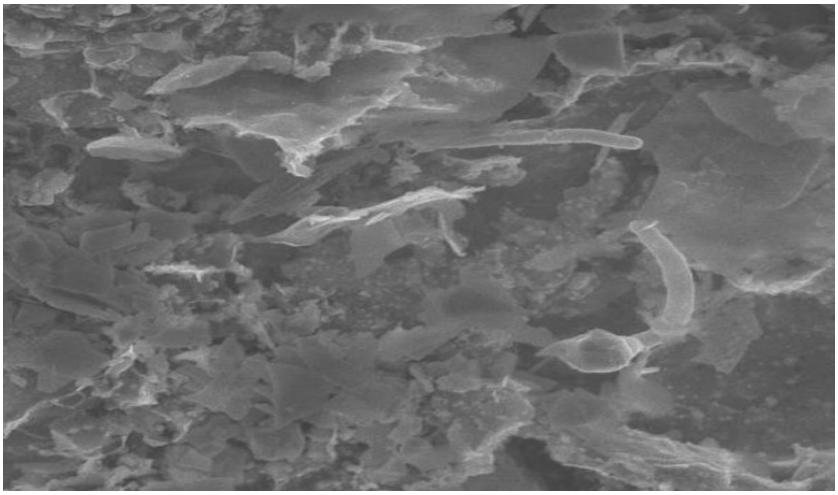

Figure D2.8: *SEM Image of individual carbon nanotubes filled with SnPb (SnPb@CNT-30SC sample)*

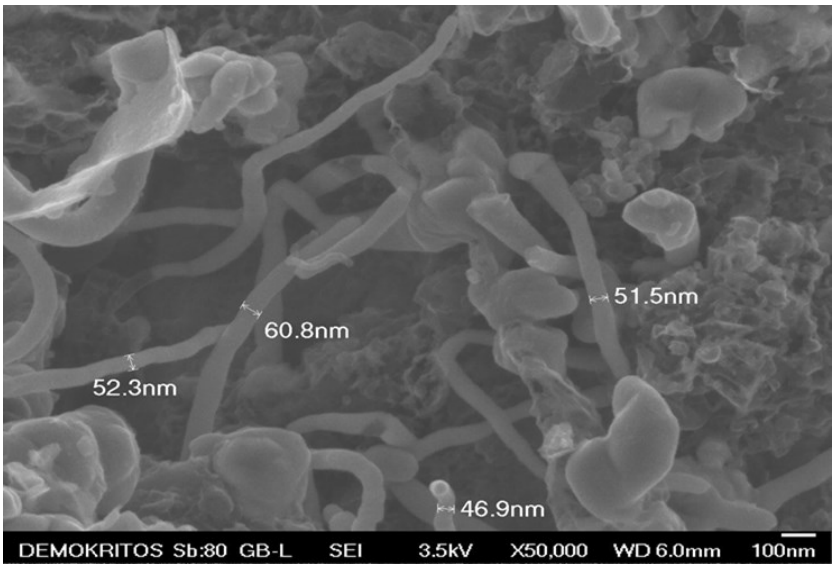

Figure D2.9: *SEM Image of individual carbon nanotubes filled with SnPb (SnPb@CNT-30SC sample)*

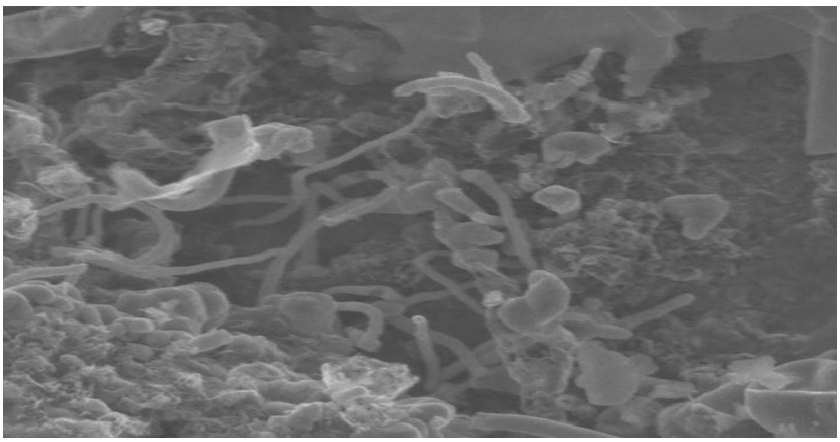

Figure D2.10: *SEM Image of individual carbon nanotubes filled with SnPb (SnPb@CNT-30SC)*

Furthermore, representative TEM images of the received products at various magnifications confirm the formation of homogeneous carbon nanotubes filled with metallic nanowires. The nanotubes have a diameter between 91 nm and 181 nm and length to 5μm. As it is observed in the following TEM images, most of the carbon nanotubes are fully filled with SnPb nanowires (Figures D2.11 and D2.12). There are though, some regions (as seen in Figure D2.14) where carbon nanotubes are partially filled. In Figure D2.14 it is noticed that a nanotube appears to be like a bottle, fully filled with metallic nanowire on one edge. Furthermore, it must be underlined that, the observed final edges (tips) of Tin-Lead nanowires are fully covered by well graphitized carbon shells (Figure D2.16). The latter implies that nanowires are protected by atmospheric oxidation and therefore they can exist in air atmosphere for a long time. This is very important for future potential applications.

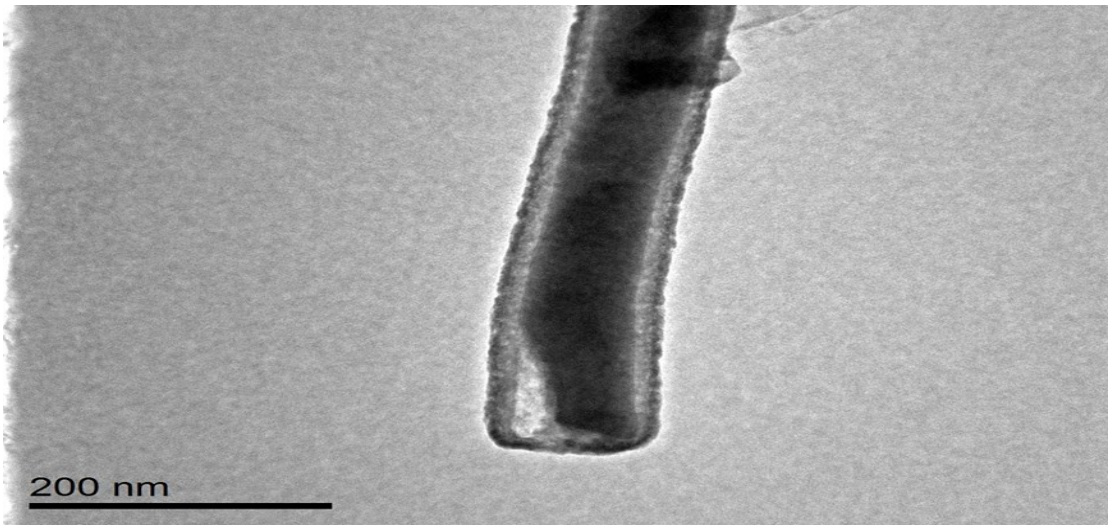

Figure D2.11: *TEM image of the SnPb@CNT-30SC product*

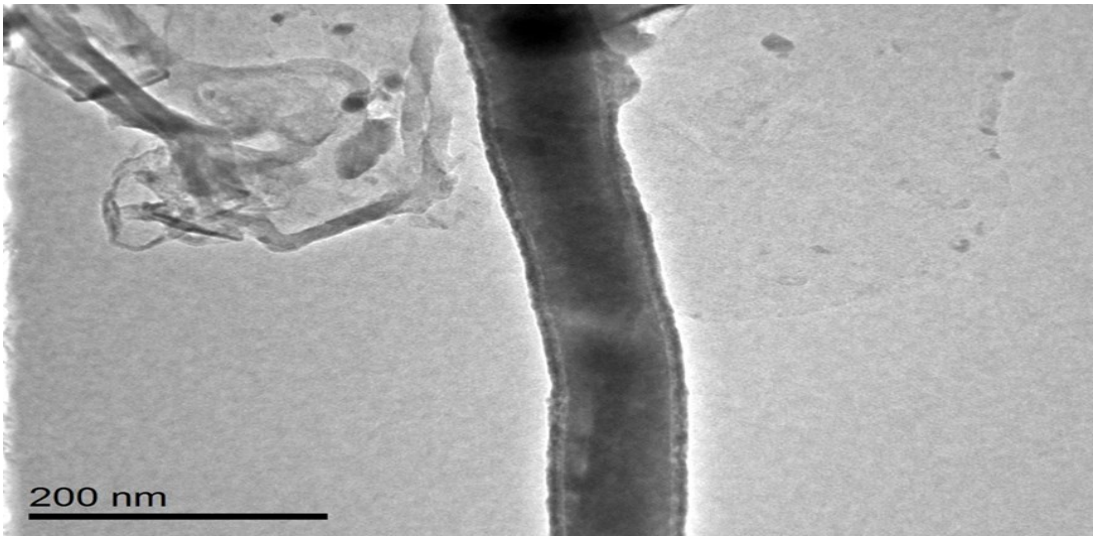

Figure D2.12: *TEM image of the SnPb@CNT-30SC product*

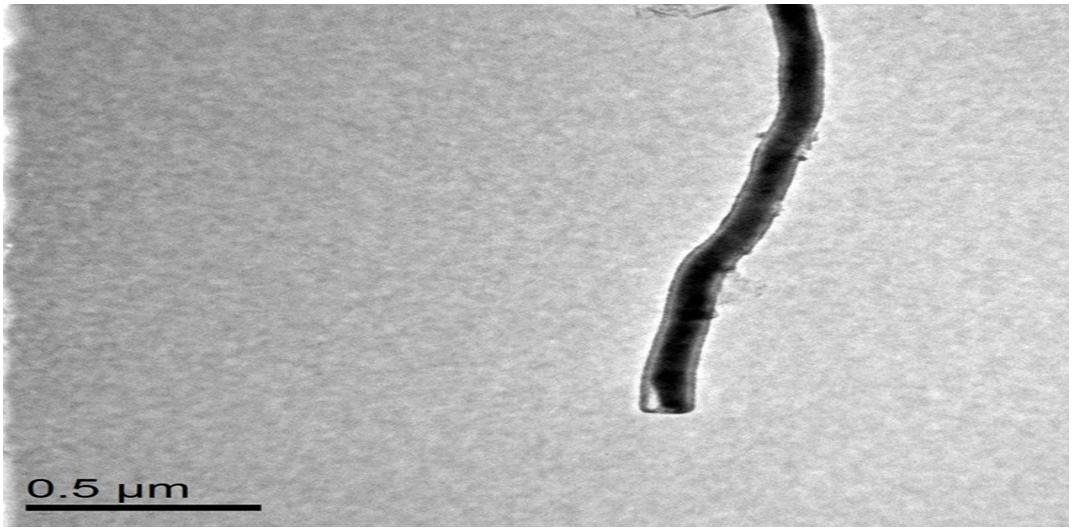

Figure D2.13: *TEM image of the SnPb@CNT-30SC product*

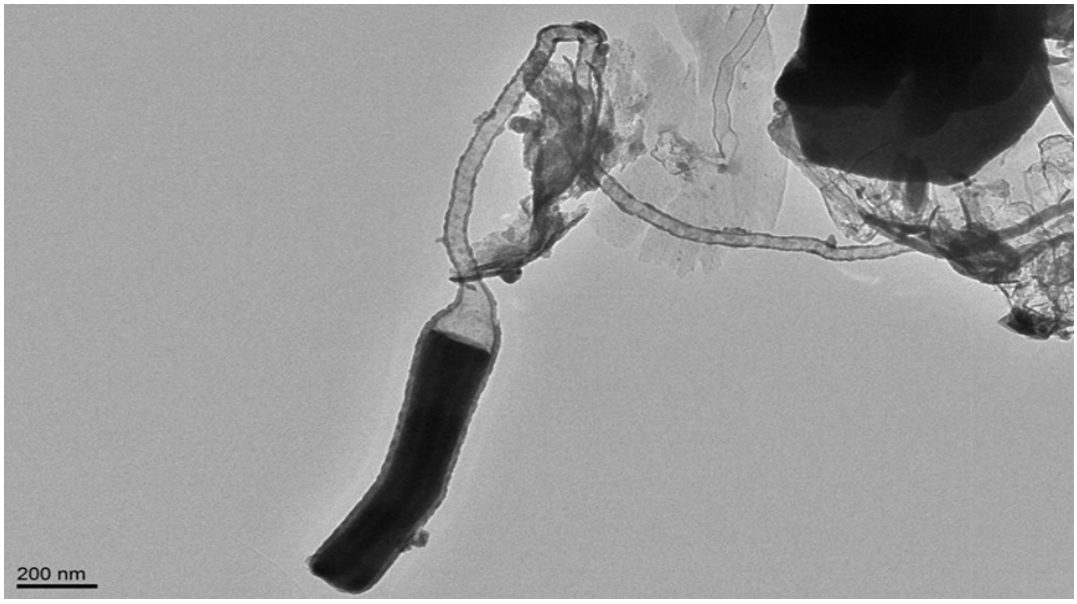

Figure D2.14: *TEM image of the SnPb@CNT-30SC product*

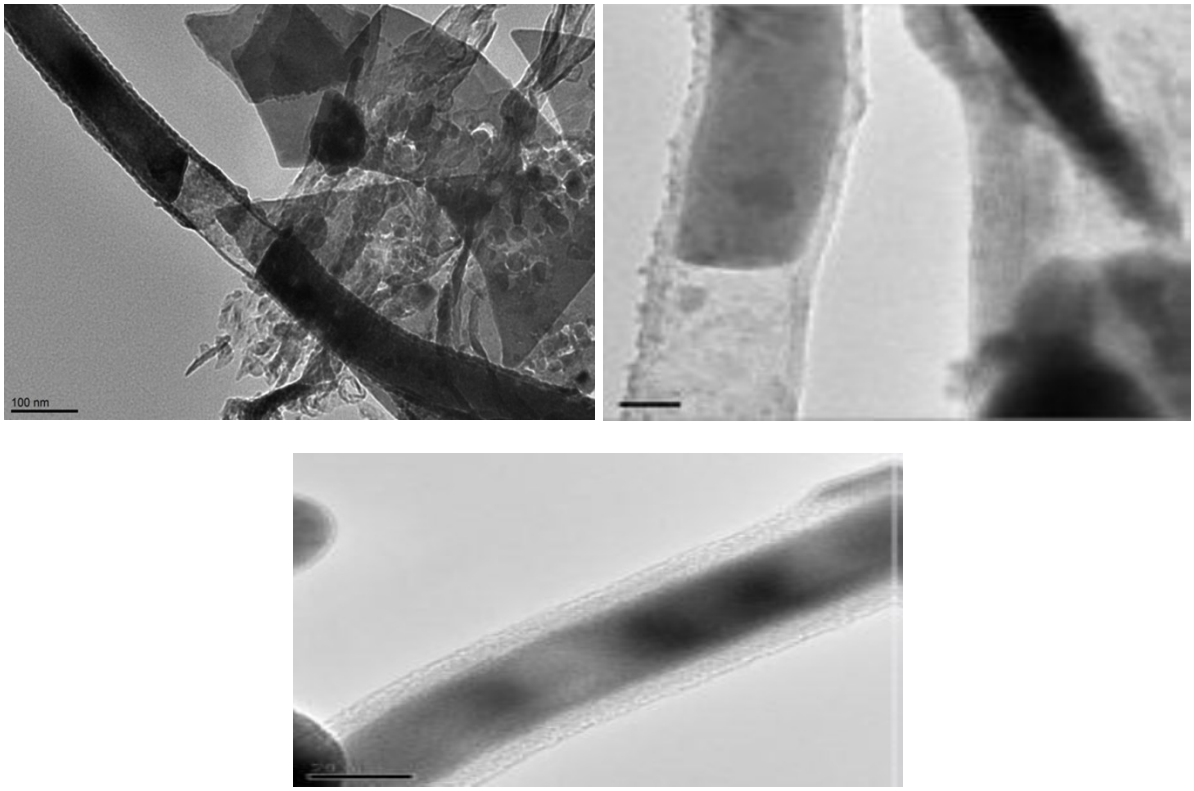

Figure D2.15: *TEM image of the SnPb@CNT-30SC product*

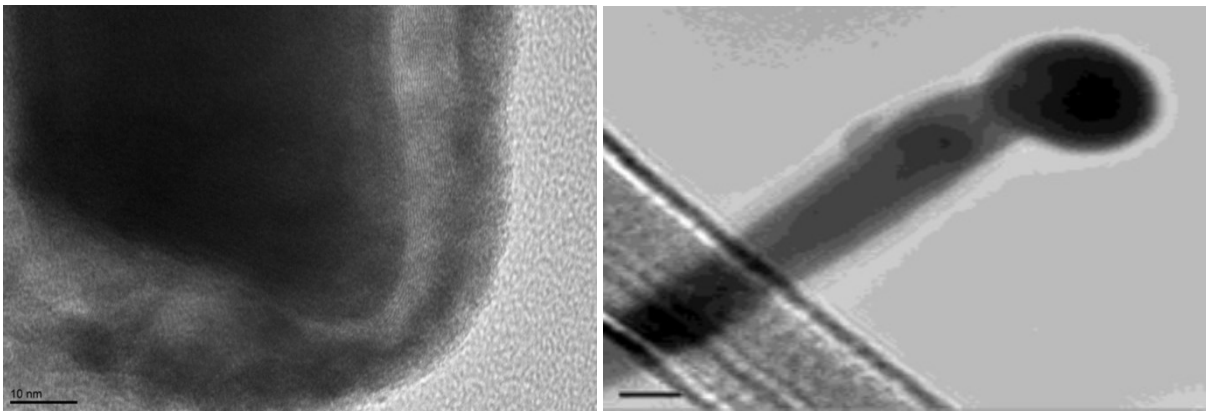

Figure D2.16: *TEM image of a nanowire edge (SnPb@CNT-30SC)*

Additionally, TEM images were also obtained and the images in Figure D2.17 indicate the existence of partially and fully filled carbon nanotubes. Moreover, D2.17 image exhibits the formation of a forest of dense carbon nanotubes which are filled with metallic nanowires indicating the high yield of the proposed procedure.

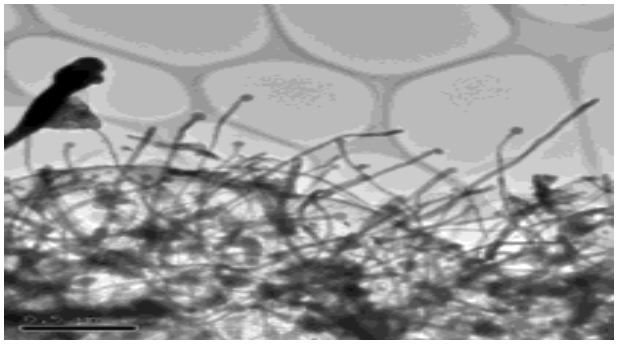

Figure D2.17: *High resolution TEM images of the SnPb@CNT-30SC product*

The Energy Dispersive X-ray spectrum (EDX) of a representative sample is shown in Figure D2.18. This was taken from an individual tube. Quantitative analysis shows that the atomic ratio Tin/Lead is estimated to be 22 to 1. This indicates that probably two (or more) different tin-rich phases are located within the carbon tube and not the initial solder composition (61 wt% Sn, 39 wt% Pb). In fact, a similar phenomenon was observed when carbon-encapsulated Sn-Pb nanowires were generated by electrolysis of graphite in molten LiCl containing these metals[239]. A distinctive profile for the metal cores in which Sn predominates at one end and Pb at the other of the individual nanowires was also observed.

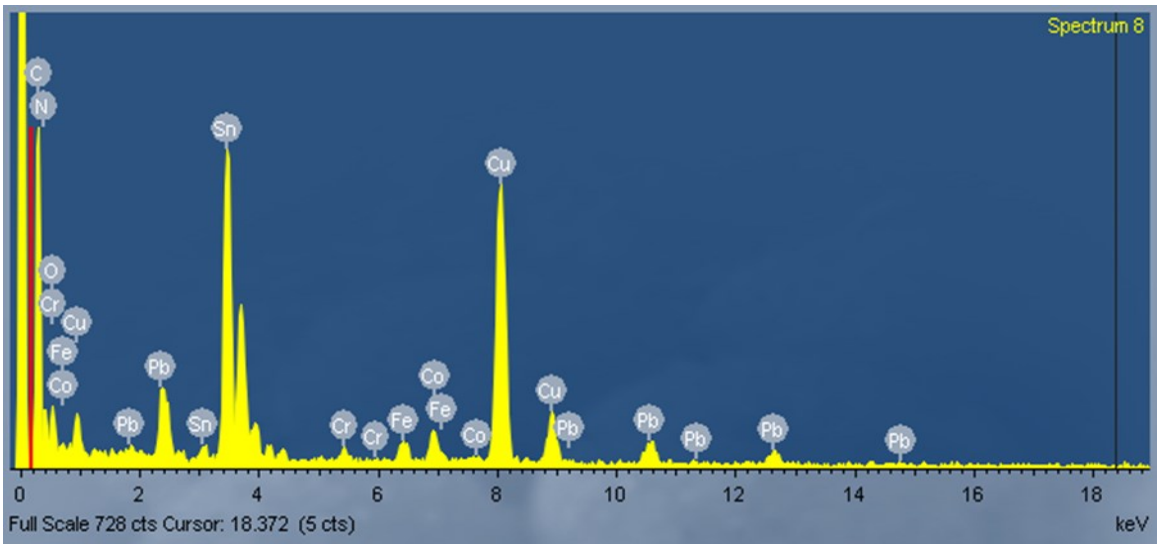

Figure D2.18: *Energy Dispersive X-ray spectroscopy (EDAX) pattern* of *SnPb@CNT_30SC*

Sn-Mössbauer spectroscopy served again a powerful and complementary to XRD technique in order to identify and characterize the Sn local environment and the formal oxidation state of the different tin phases in SnPb@CNTs samples. Mössbauer spectra obtained at 80 K for SnPb@CNT_30SC and SnPb@CNTs _60SC in comparison with the initial solder (pure SnPb alloy) are shown in Figure D2.19.

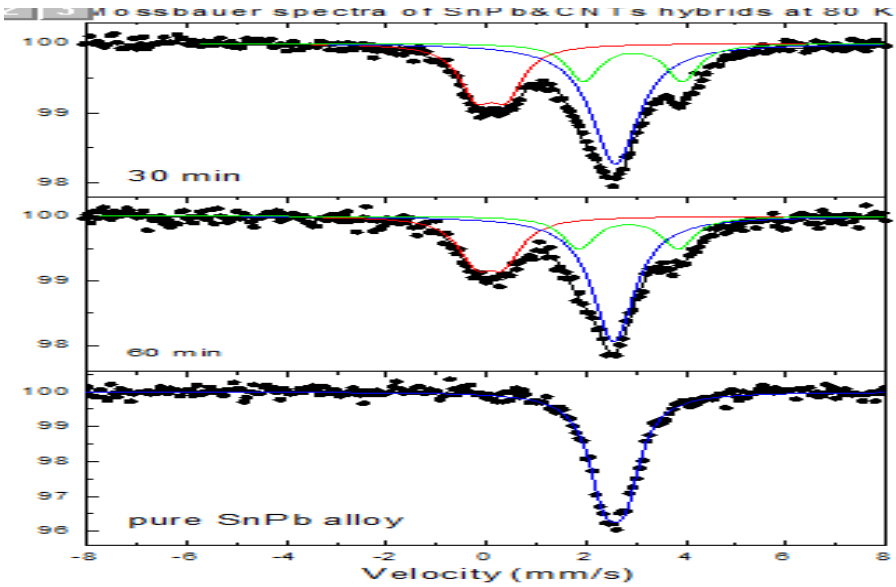

Figure D2.19: *Mössbauer spectra obtained at 80 K for SnPb@CNTs _30SC, SnPb@CNTs _60SC and pure SnPb alloy*

Table D2.2. *Mössbauer effect spectral data at 80 K*

SnPb@CNTs samples from	**IS (mm/s)**	**GA/2 (mm/s)**	**QS (mm/s)**	**Area (%)**
SnPb pure alloy	2.56	0.48	0.00	100
SnPb@CNTs _30SC	0.10 2.59 2.94	0.41 0.58 0.39	0.61 0.00 1.99	51 28 21
SnPb@CNTs _60SC	0.07 2.55 2.85	0.44 0.52 0.39	0.57 0.00 1.99	52 28 20

The spectra of both SnPb@CNTs samples show three singlets indicating the presence of three Sn containing phases, while in the pure SnPb alloy spectrum only one singlet (Δ or QS=0) doublet is observed showing an isomer shift at 2.56 mm/s. Analysis of the corresponding spectra shows that the two phases are β-Sn (blue line) and SnO_2 (red line). The % SnO_2/beta-Sn area coverage ratio which is exhibited by the two Sn-containing phases is 28:51 and 28:52 for SnPb@CNTs_30SC and for SnPb@CNTs_60SC respectively. Furthermore, for both spectra there is also a third quadruple doublet (green line) that is equal to 21% and 20% for each sample that corresponds to a potentially new phase of Tin. This unknown Sn-phase consists of Tin atoms being in close contact with Pb atoms forming a new layer as revealed from STEM-EDX mapping (see below).

In Figure D2.20 the SQUID measurements [mass magnetization *versus* temperature (left) and magnetic field B (right)] of a representative sample (SnPb@CNTs_30SC) are demonstrated. From the analysis of the magnetization measurements, it follows that the critical (superconducting after transition) temperature (T_C) is around 7.05 K and the critical magnetic field (H_C) is 0.095 T (950 Gauss) that is due to a lead-rich phase. For bulk lead, T_C is equal to 7.2 K and H_C is equal to 0.08 T at 0 K (0.069 T at 2 K after extrapolation following simple relation valid for Type-I superconductors). This increase in the critical field is a direct result of the reduced diameter of the nanowires and especially of this lead phase[240-242] that is confined inside the nanotube. A second (smoother) step is also observed with a Tc at 3.7 K which originates from a β-tin phase. Thus, the superconductivity surely stems from Pb or Pb-doped Sn.

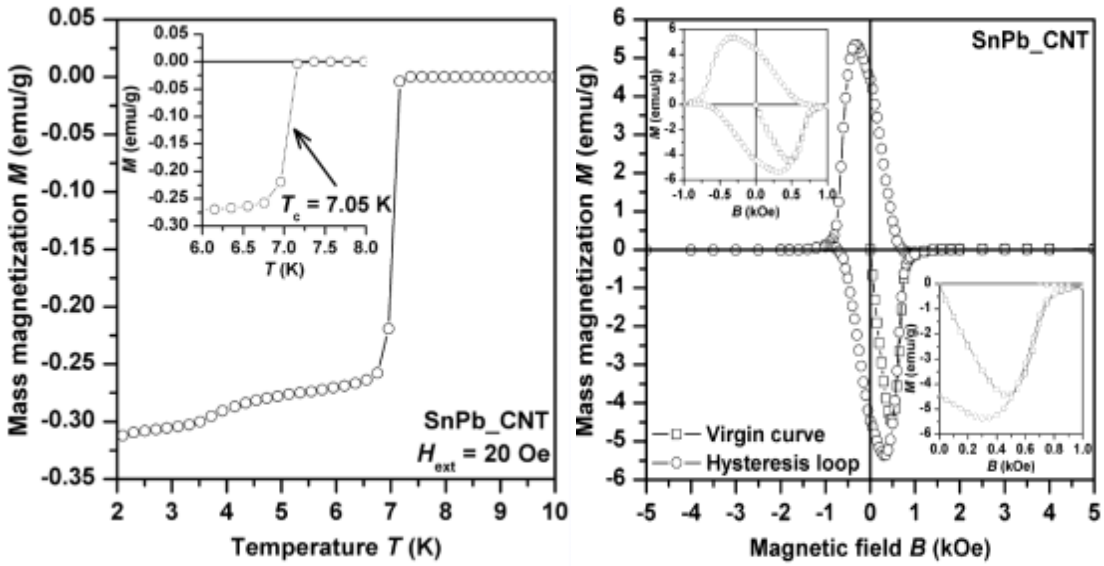

Figure D2.20: *Mass Magnetization Mass versus Temperature T (left) and Magnetic Field B (right)*

In order to prove the sustainability of the theory about the new phase which is probably located inside CNTs, STEM and HRTEM measurements were also performed. In Figure D2.21 a HRTEM image of a filled CNT is observed. The nanotube is fully filled and the diffraction pattern taken from the darker tip indicates that the Sn/Pb nanowire inside the nanotubes is multi-crystalline as suggested by the dim rings-spots pattern. Furthermore, the receive diffraction from the tip crystal (Figure D2.21) fits a cubic structure along [011], with a=4.94Å, which can be attributed to lead (Pure Pb has an fcc structure of a=4.93Å).

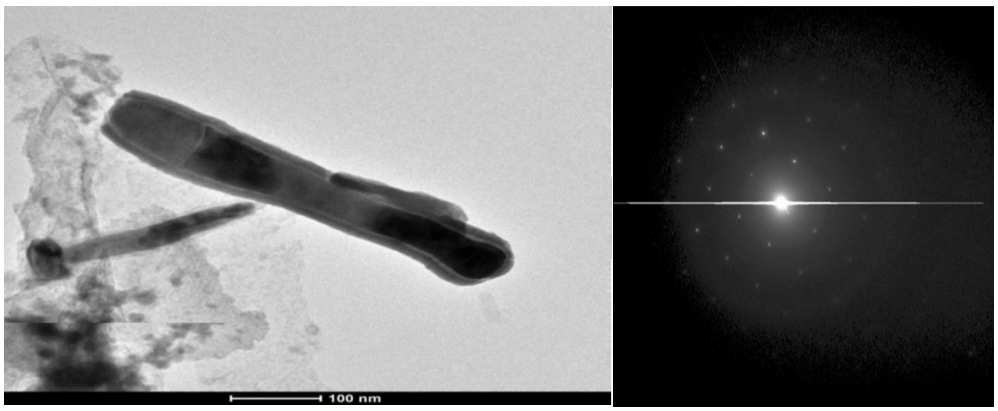

Figure D2.21: *HRTEM image of a filled nanotube and diffraction from one tip of a filled nanotube SnPb@CNTs_30SC (the darker tip)*

In addition to this, Figure D2.22 shows another HRTEM image from a tube tip which accompanied by the received diffraction pattern exhibited that the crystal has the same [011] pattern that fits the structure of lead.

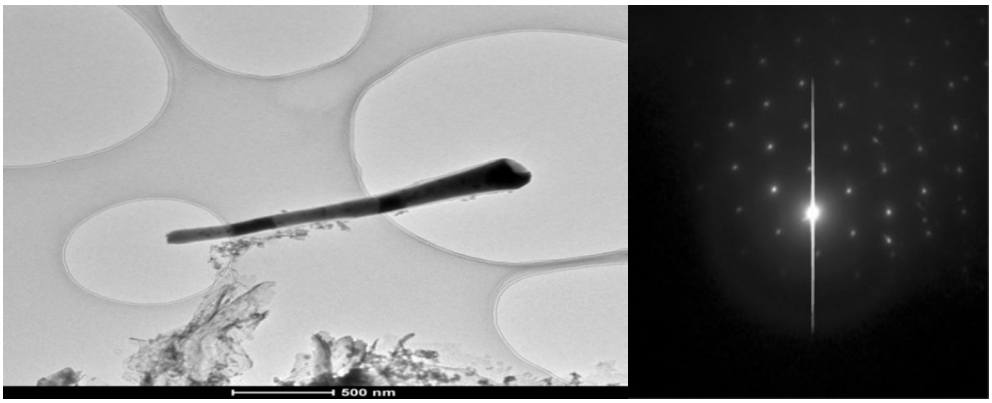

Figure D2.22: *HRTEM of a nanotube (left) and diffraction image from a tube tip (SnPb@CNTs_30SC)*

STEM-EDX mapping of one single carbon nanotube filled with metallic nanoparticles is depicted in Figures D2.23 and Figure D2.24. It is clear that the distribution of the elements Pb, Sn and O (due to SnO_2) is confirmed and it is obvious that Sn, SnO_2 and Pb all co-exist inside the CNT. Lead distribution can be observed in Sn-majored areas whereas the opposite is happened for tin. In spite of the fact that this can be attributed to multi-scattering of the X-Rays deriving from heavy elements and could be considered to be noise/background, the presence of both elements strongly suggest the formation of SnPb nanowires in the interior of carbon nanotubes. Furthermore, from Figure D2.24 it seems that lead is located mainly in the outer surface of the nanowire which in turn gives rise to the formation of a new Pb-doped tin phase that was also revealed from Mössbauer spectroscopy.

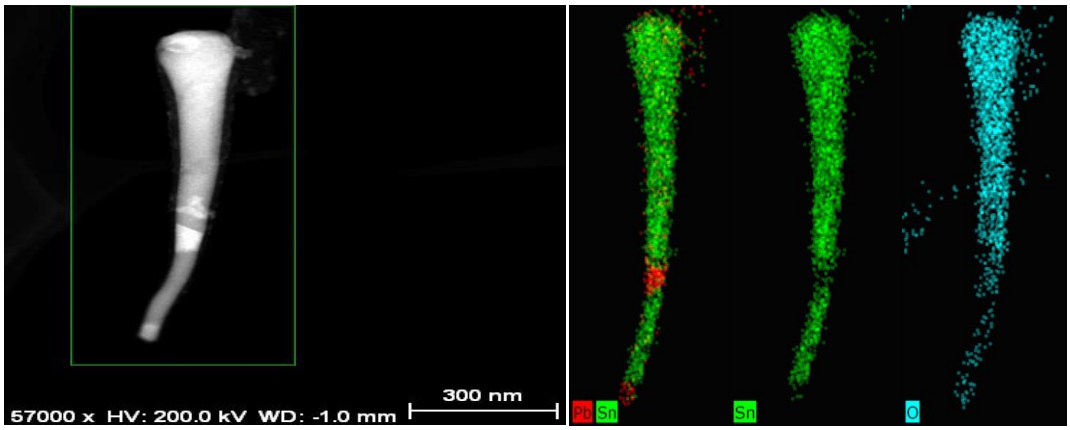

Figure D2.23: *The STEM-EDX mapping of a single CNT (SnPb@CNTs_30SC), containing nanoparticles is presented. SnO_2, Sn and Pb distribution is confirmed which clarifies that the filled crystal is composed of different materials*

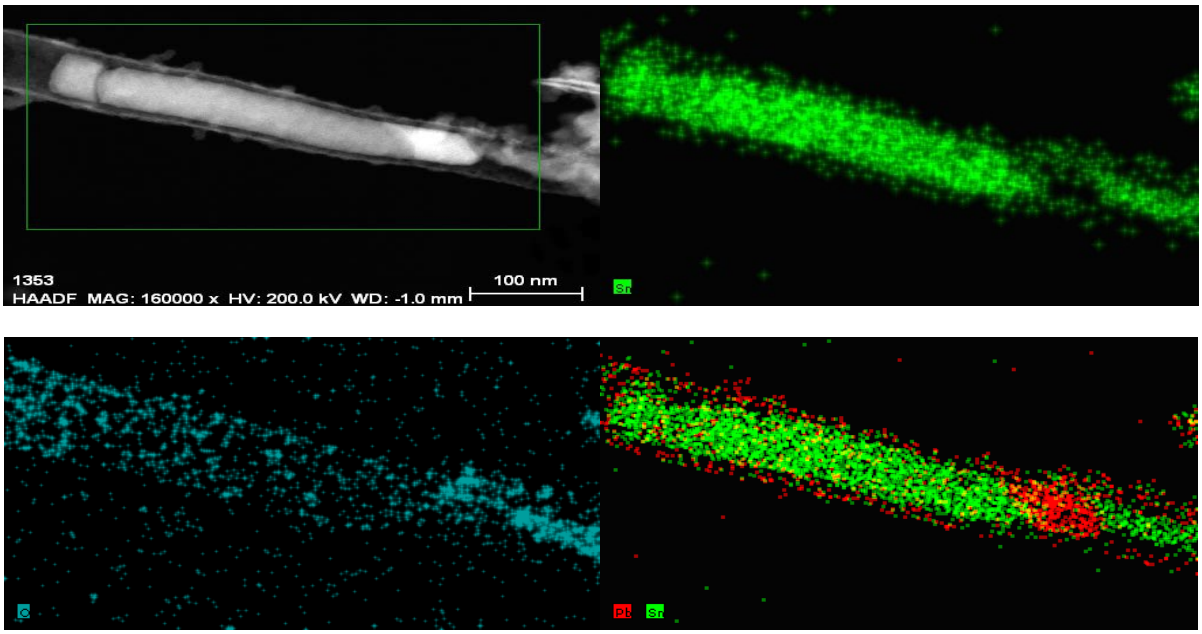

Figure D2.24: *The STEM-EDX mapping of SnPb@CNTs_30SC*

As previously mentioned, lead was used due to its higher critical temperature than that of tin and is therefore expected to increase the critical temperature of the alloy. From the XRD patterns the existence of the characteristic β-Sn which is encapsulated inside carbon nanotubes as well as the successful NaCl removal after washing is confirmed. The SEM and TEM images showed that the nanotubes exhibit a diameter that ranges from 46.9 to 181 nm and length up to 5μm. As it can be observed from the TEM images, most of carbon nanotubes are fully filled with tin-lead nanowires. There are certain regions though where carbon nanotubes are partially filled. All the observed final edges (tips) of the tin-lead nanowires are totally covered by nanotubes shell, a fact that indicates that nanowires are protected in every spot by atmospheric oxidation and because of this they can stay in the air for a long time. Thermal analysis showed that the produced nanotubes are produced at a yield 9-10%w/w. From the EDAX spectrum it was estimated that the ratio tin to lead is 22:1. Raman shifts confirmed the fine quality of carbon nanotubes as the I_D/I_G ratio for all samples ranges between 0.88 and 0.92. From the I_D/I_G ratios it was observed that the quality of the produced carbon nanotubes is not affected by the type of the cooling process (fast or slow). This led to the conclusion that using less cooling stages (fast cooling) carbon nanotubes of the same quality are formed. From the analysis of the magnetization measurements, it follows that the superconductivity temperature (TC) is around 7.05 K and the critical magnetic field (HC) is 0.095 T (950 Gauss) that is due to a lead-rich phase This is significant because now and in order to realize superconducting state, there will no longer be needed to pump above liquid Helium. The Mössbauer spectra indicated the presence of two Sn containing phases, corresponding to β-Sn and SnO_2, as well as a third Sn-containing phase. This fact strongly suggests that there is an unknown Sn-phase, which consists of tin atoms being in contact with lead atoms forming a new layer, a conclusion which was remarkably supported by STEM-EDX.

D3. Synthesis of carbon nanotubes encapsulating Manganese-Bismuth (Mn-Bi) nanorods (MnBi@CNTs)

In this chapter, the characterization of carbon nanotubes that were grown encapsulating Manganese-Bismuth (Mn-Bi) nanorods using the CCVD method is described**.** The characterization was performed using various analytical techniques: X-Ray Diffraction (XRD), Raman Spectroscopy, Differential Thermal and Thermogravimetric Analyses (DTA/TGA), Scanning Electron Microscopy (SEM) and Transmission Electron Microscopy (TEM) and Vibrating Sample Magnetometer (VSM).

The main purpose of this part was the synthesis of low dimensional magnetic materials (like nanorods), which would be in the interior of carbon nanotubes and therefore would be protected against oxidation. Manganese-Bismuth alloy was chosen due to its interesting magnetic properties (it is ferromagnetic) and because of the fact that its melting point is lower than the used nanotube growth temperatures (700°C or 800°C). For this reason, Bismuth (Bi) was used, having Tm= 271.5^{o}C, as the second metal in the alloy, allowing in this way the lowering of its melting point, due to the fact that the melting point of Manganese is relatively high (1246°C). Furthermore, during the process and apart from the desired products, Bismuth forms oxides during the formation of carbon nanotubes, which can be easily removed with mild acid treatment. Here should be underlined that the presence of manganese oxide in the products before and after sodium chloride removal is justified since the formation of manganese oxide takes place during the preparation of the Manganese-Bismuth alloy in air atmosphere. Finally, sodium chloride was used as substrate for the immobilization (impregnation) of the MnBi alloy, since it is also inactive and can be easily removed with water.

In the following figures (Figures D3.1 and Figures D3.2) the X-Ray diffraction diagrams of the formed products, using MnBi alloy impregnated in NaCl as catalyst, for different reaction times (15-90 min) and for different temperatures (700°C-800°C) are seen. In both Figures we see the characteristic peaks of the Manganese-Bismuth alloy (JCPD 04-003-1943), Bismuth (JCPD 04-006-7762) and Manganese Oxide (JCPD 04-005-4310) which are all found in and out of the nanotubes. The intensities of the Manganese Oxide peaks are too low due to its low percentage in the alloy (10%). In Figure D3.1 the characteristic peaks of NaCl (JCPD 00-005-0628) are observed, while in Figure D3.2, after the sodium chloride removal of the nanotubes with distilled water, they are absent, confirming the successful removal of the substrate.

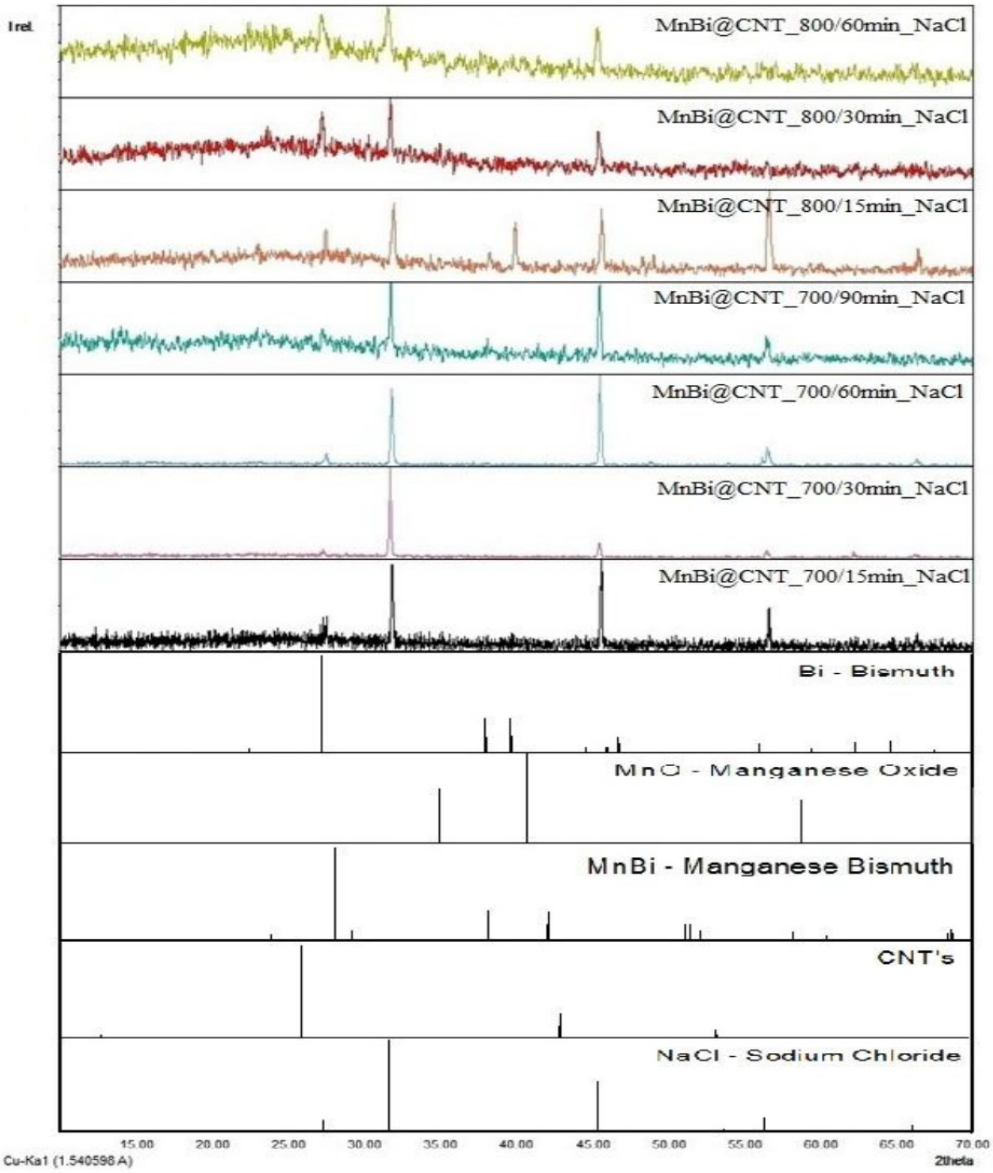

Figure D3.1: *X-Ray diffraction patterns for all samples before sodium chloride removal*

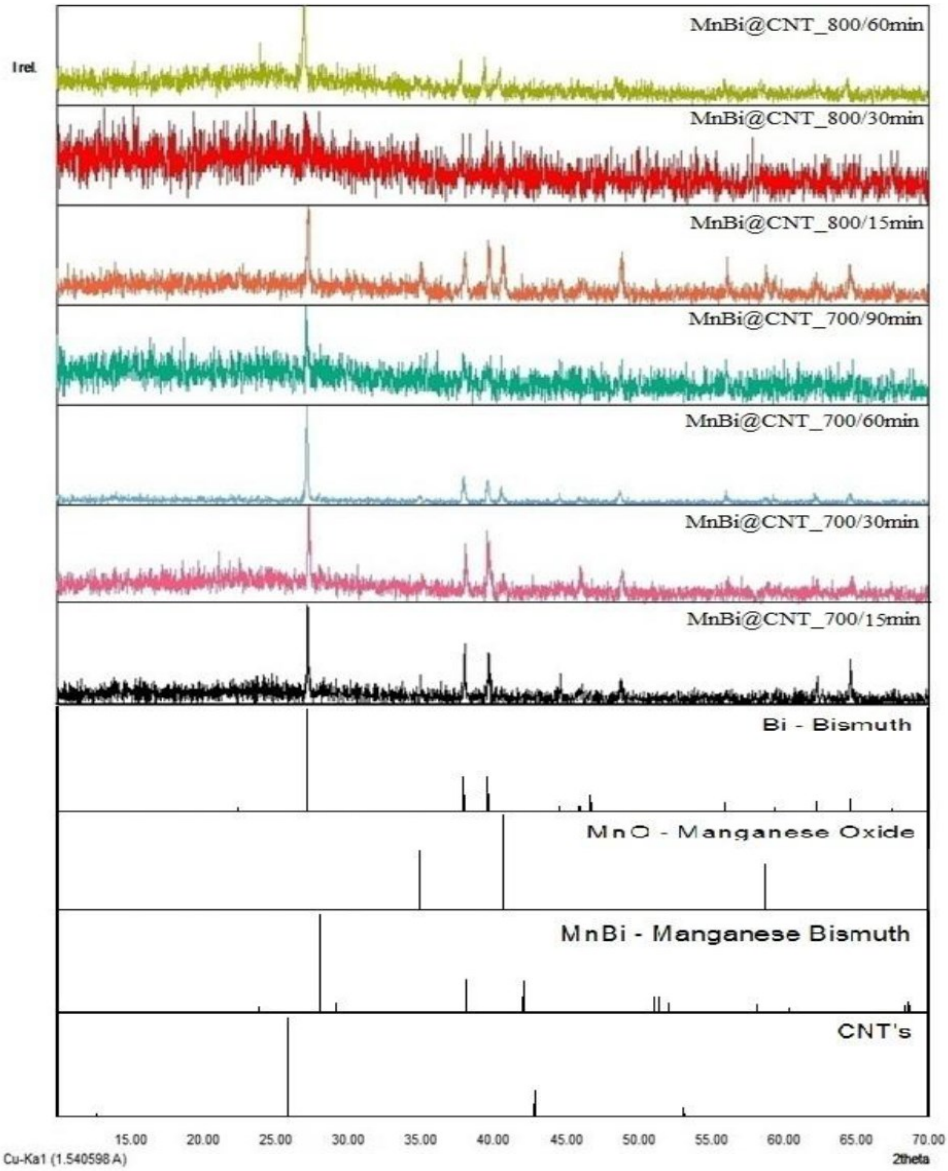

Figure D3.2: *X-Ray diffraction patterns for all samples after sodium chloride removal*

Raman spectra (Figures D3.3, D3.4, D3.5, D3.6 and D3.7) of carbon nanotubes grown using MnBi as catalyst for 15, 30, 60 and 90 minutes of acetylene flow follow. In all spectra, the characteristic peaks at 1300 and 1600 cm^{-1} corresponding to D and G bands respectively are observed, which are indicative of the hybridization of nanotubes carbon atoms[236,237]. The G band corresponds to tension vibrations (sp^2) of E_{2g} type of high symmetrical pyrolytic graphite (HOPG), while D band results from the disorder of the sp^2 hybridized carbon atoms, which is characteristic of the distortion in the hexagonal graphitic lattice of the curved graphitic sheets or/and on the edges of the CNTs (sp^3 hybridization)[230,231]. The ratio of the relative intensities of D and G bands ($R=I_D/I_G$) reveals the degree of disorder in the graphitic lattice. According to the received Raman spectra, the ratio I_D/I_G of the samples was calculated, which ranges between 0.91 and 0.98, confirming the fine quality of the composed nanotubes (Table D3.1).

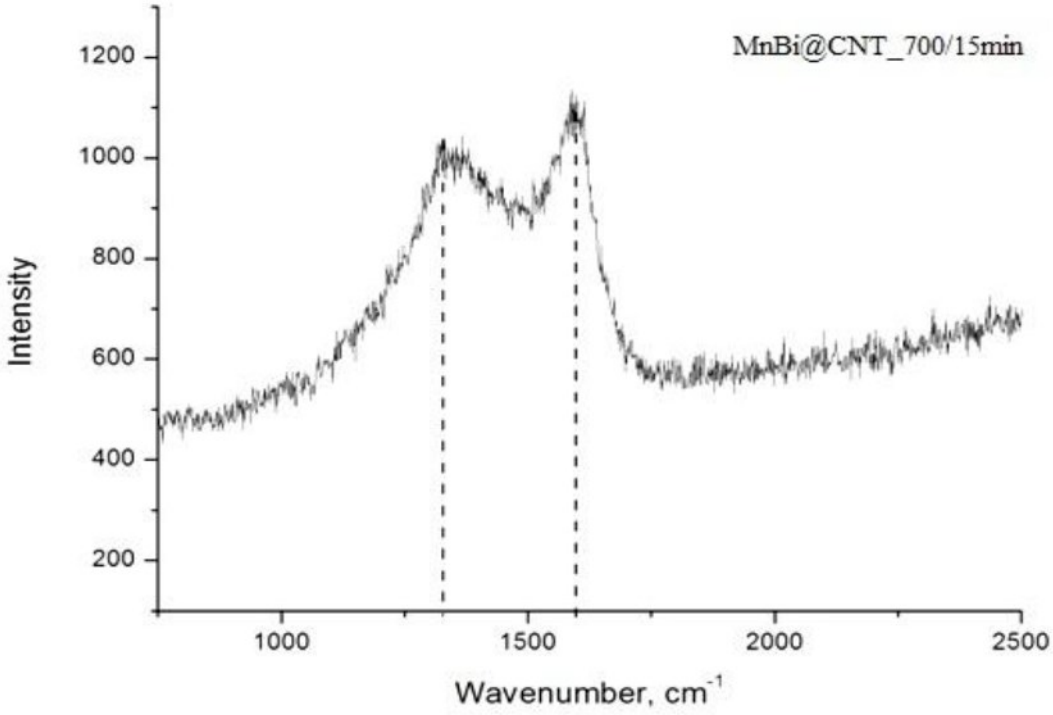

Figure D3.3: *Raman spectra of MnBi@CNTs after 15 minutes of acetylene flow at 700°C*

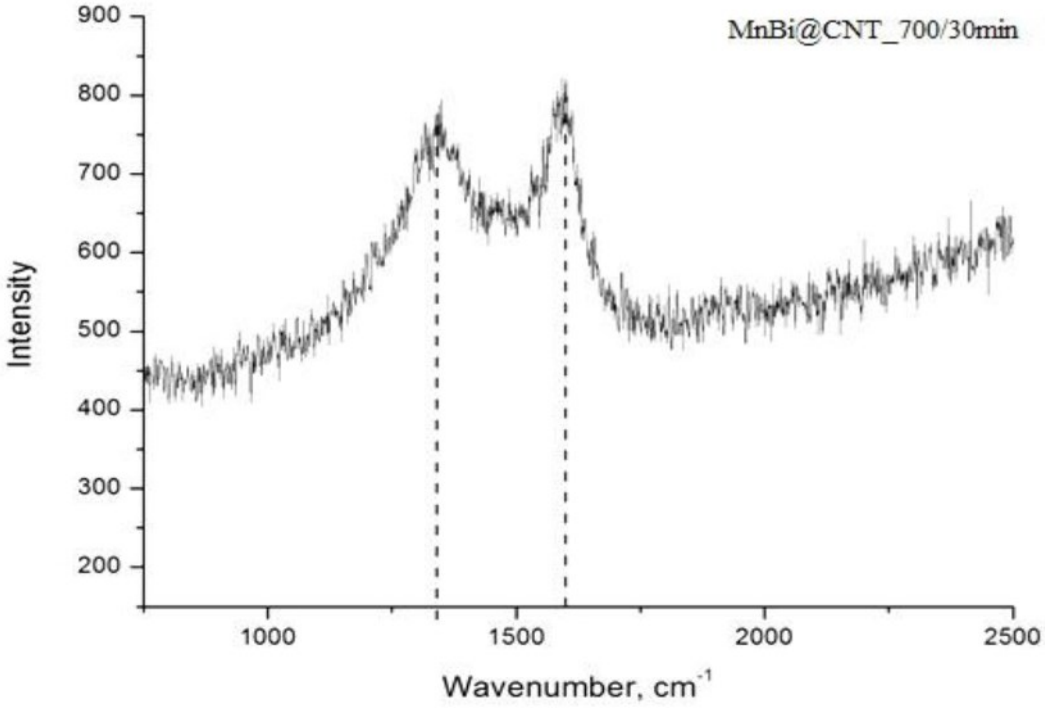

Figure D3.4: *Raman spectra of MnBi@CNTs after 30 minutes of acetylene flow at 700°C*

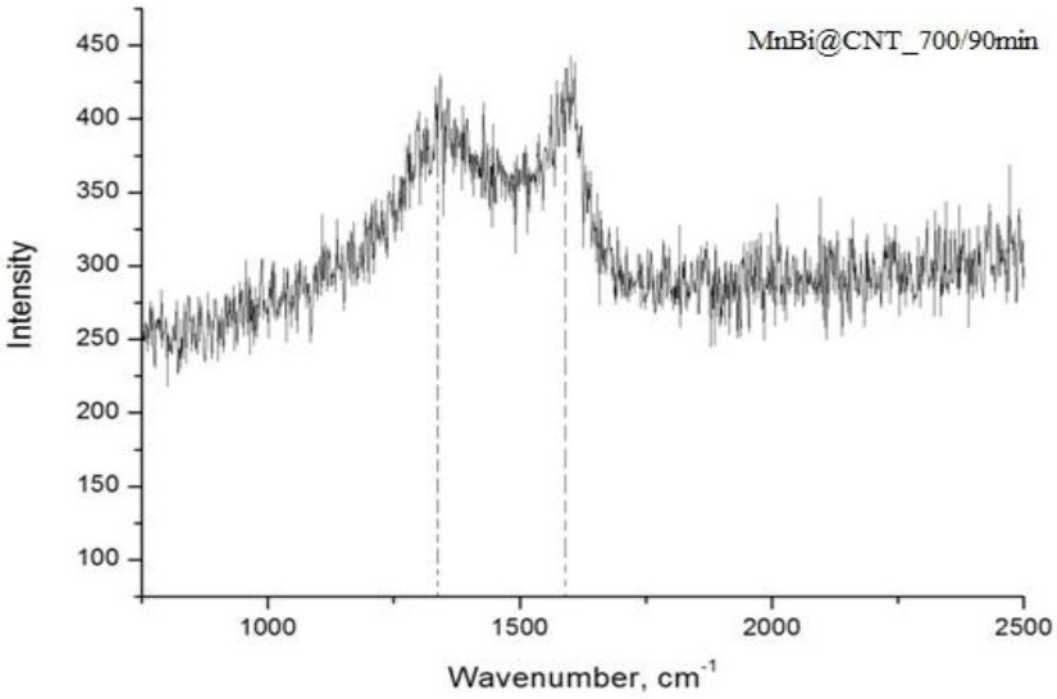

Figure D3.5: *Raman spectra of MnBi@CNTs after 1.5 hour of acetylene flow at 700°C*

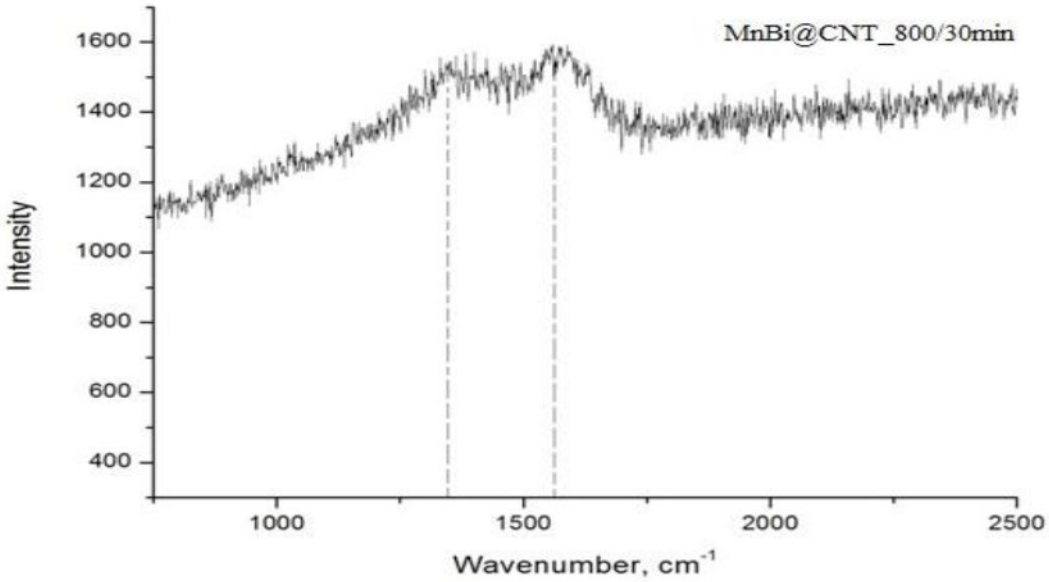

Figure D3.6: *Raman spectra of MnBi@CNTs after 30 minutes of acetylene flow at 800°C*

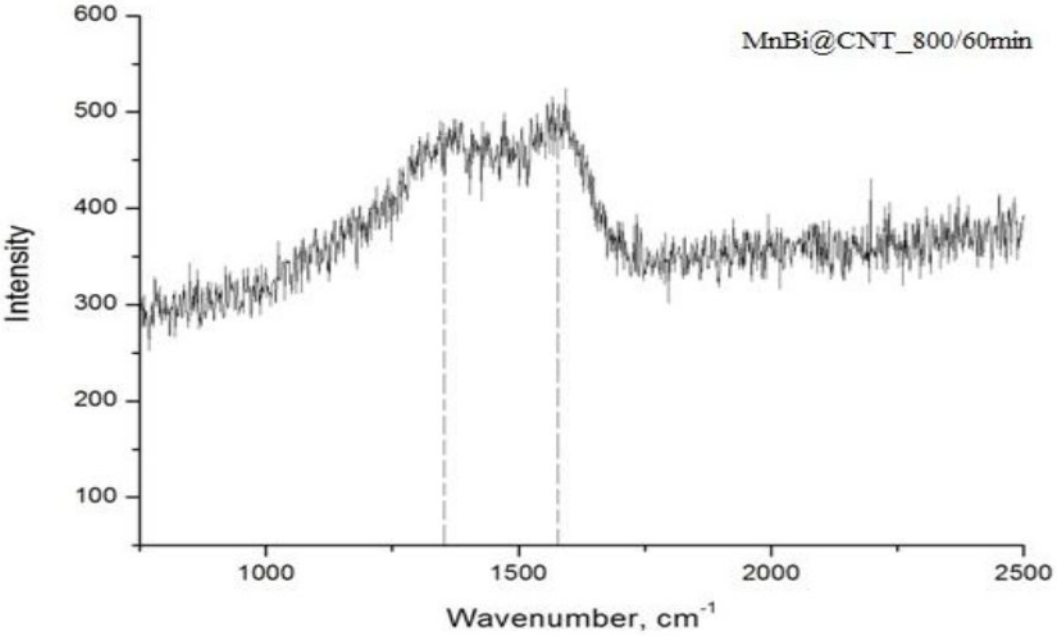

Figure D3.7: *Raman spectra of MnBi@CNTs after 1 hour of acetylene flow at 800°C*

Table D3.1. *I_D/I_G ratios of the composed nanotubes*

Acetylene flow time	Reaction Temperature	I_D/I_G
15 min	700°C	0.91
30 min	700°C	0.97
90 min	700°C	0.95
30 min	800°C	0.98
60 min	800°C	0.97

The thermal analysis diagram DTA/TG of a representative sample (using as catalyst MnBi alloy and NaCl for reaction time 1h at 800°C) is presented in Figure D3.8. At temperatures below 100°C the moisture is removed. This is a phenomenon which is accompanied by a reduction in the weight of the sample by 1% w/w. As it can be observed in the TG diagram, at a temperature between 500 and 800°C an increase by 1% in the sample weight occurs, which is caused by the oxidation of the ingredients Mn and Bi, which are found inside nanotubes. At temperatures above 380°C carbon nanotubes are decomposed due to their thermal cracking (combustion), which is accompanied by a 8% weight loss. Of course, the thermal combustion is possible to have been caused at lower temperatures (≈300°C), which is not visible because at these temperatures the oxidation of alloy prevails which leads to increase of the sample weight. As far as the rest of the samples are concerned, the results were similar.

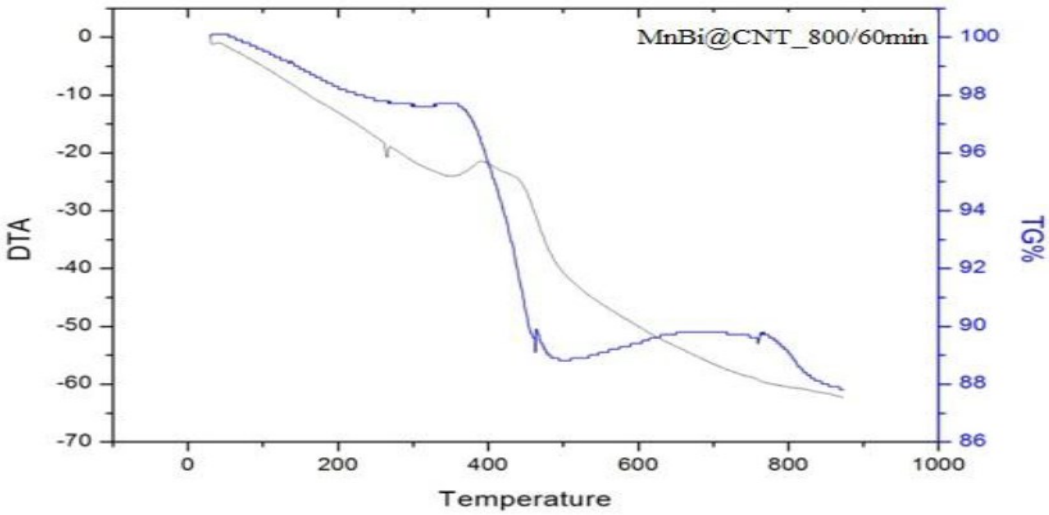

Figure D3.8: *DTA/TG diagram of MnBi@CNTs at 800°C for 1h of acetylene flow*

Representative SEM images (Figure D3.9, D3.10, D3.11) received from the products in various magnifications are seen below, which confirm the formation of carbon nanotubes. In these images, carbon nanotubes are observed, which have a tubular shape with different space settlements and are tangled with each other. From the first image it can also be observed that the diameter of the nanotubes ranges from 360 to 640 nm. Despite of that, in the last image it is obvious that there are some nanotubes with a much lower diameter, ranging from 25 to 108 nm.

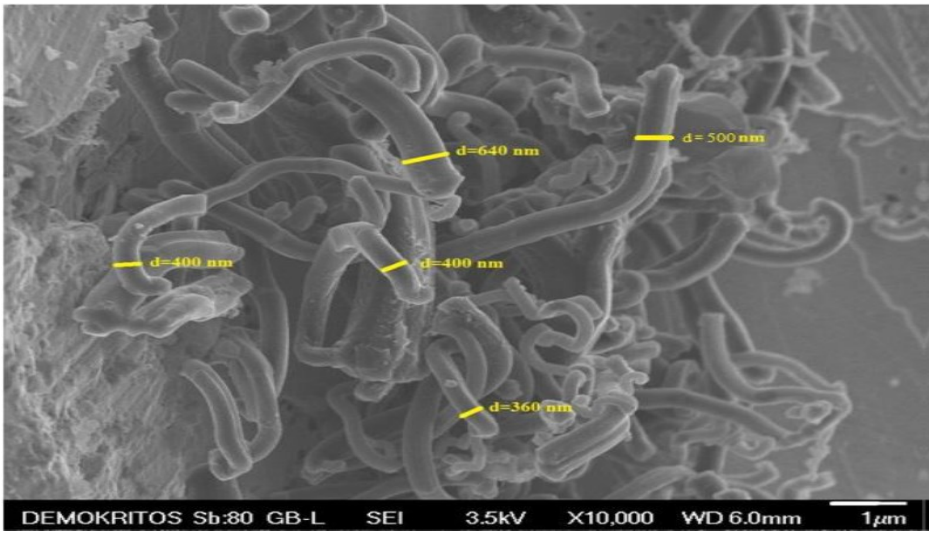

Figure D3.9: *SEM Image of MnBi@CNTs (at 700°C for 1h of acetylene flow) in which nanotubes diameters are observed*

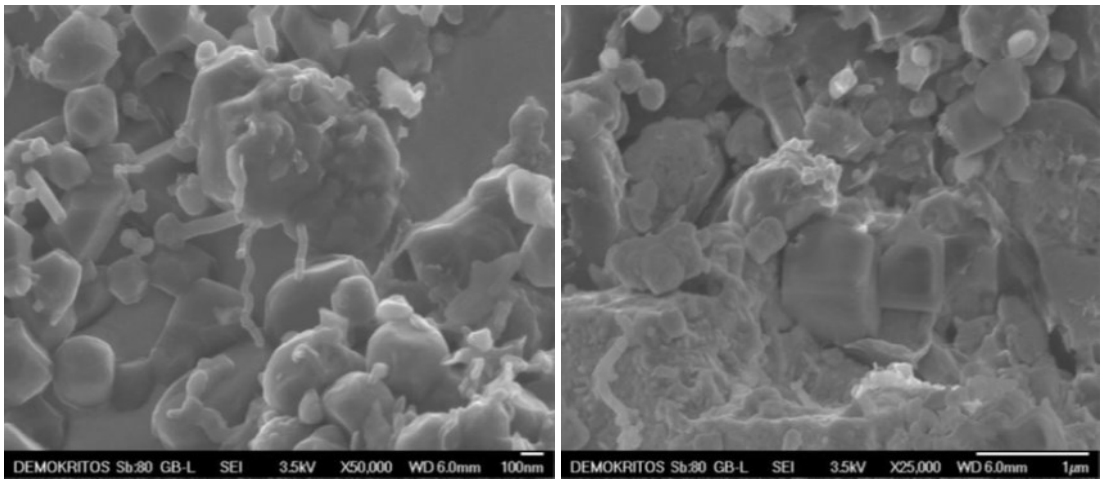

Figure D3.10: *SEM Images of MnBi@CNTs(at 700°C for 1h of acetylene flow)*

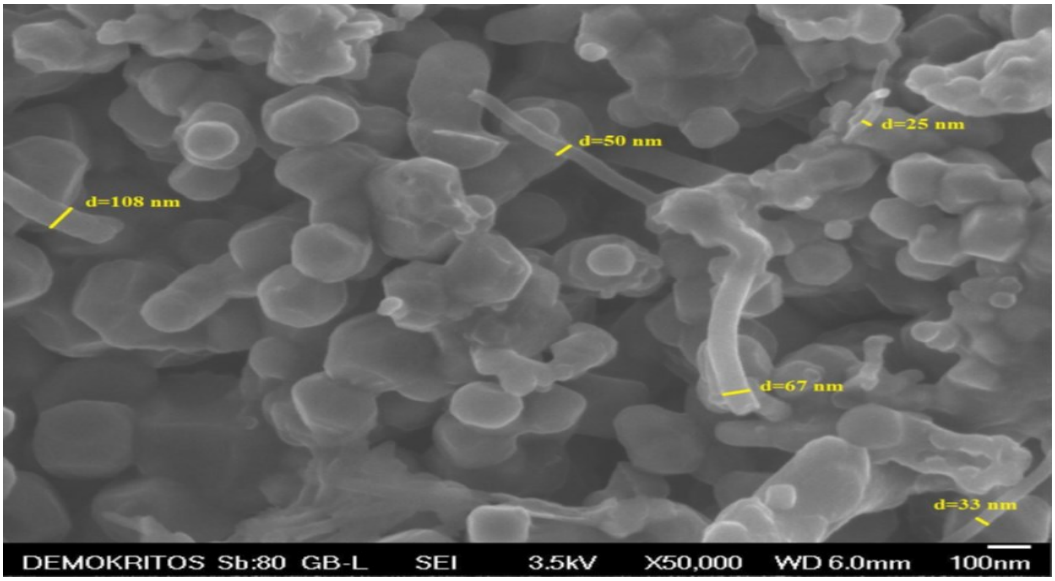

Figure D3.11: *SEM Image of MnBi@CNTs (at 700°C for 1h of acetylene flow), at which the nanotubes' diameters are observed*

Additionally, representative TEM images (Figure D3.12, D3.13, D3.14 and D3.15) of different magnifications of the products received confirm the formation of carbon nanotubes on the inside of which nanowires of MnBi are encapsulated. In Figure D3.14 nanowires of diameter between 150 to 485 nm are observed. Furthermore, it is noticed that the model according to which nanotubes were grown is the "tip-growth model", and therefore, it is understood that the interaction between the catalyst and the substrate was weak[16]. In Figure D3.14 many unreacted particles are seen together. Additionally, the length of nanotubes is found to be not more than 2 μm.

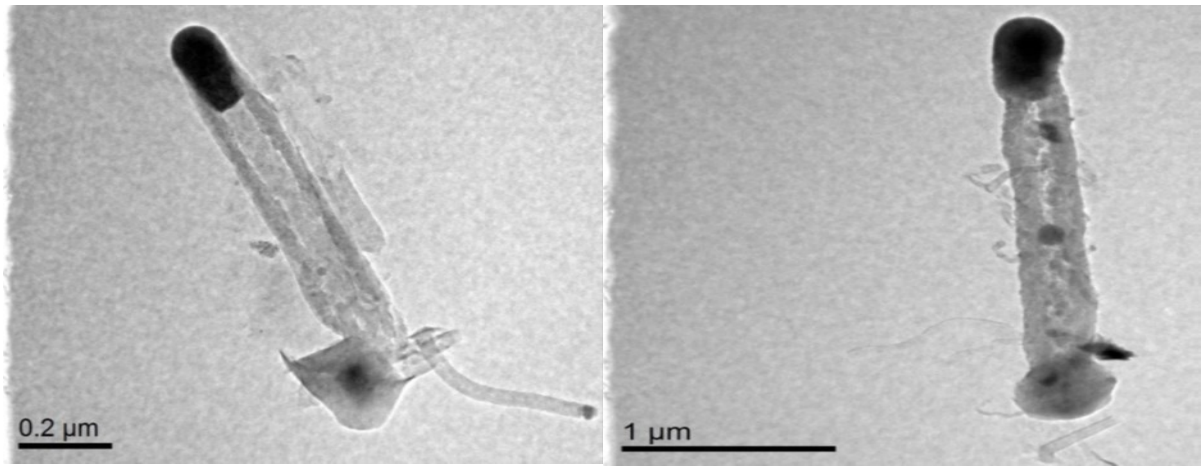

Figure D3.12: *TEM Images of MnBi@CNTs (at 700°C for 1h of acetylene flow)*

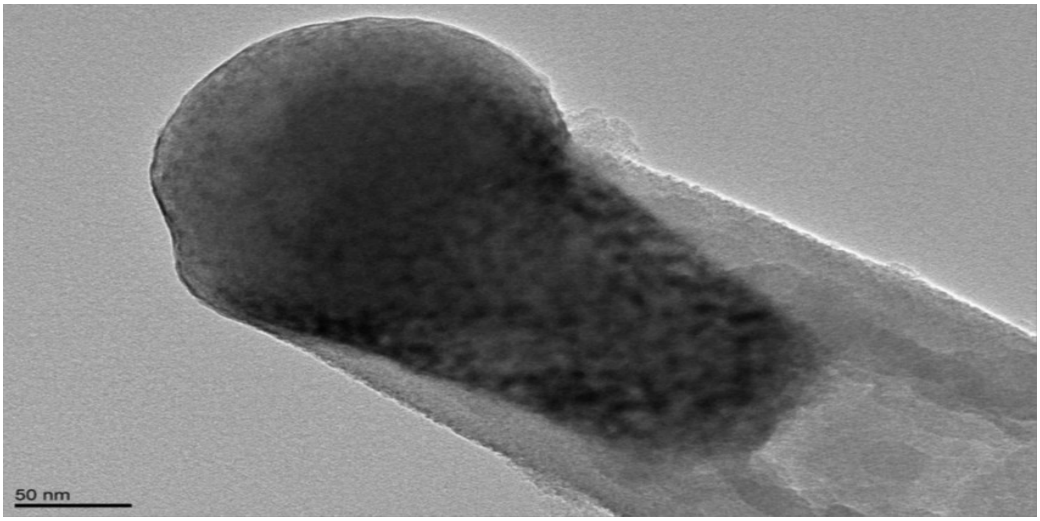

Figure D3.13: *TEM Image of MnBi@CNTs (at 700°C for 1h of acetylene flow)*

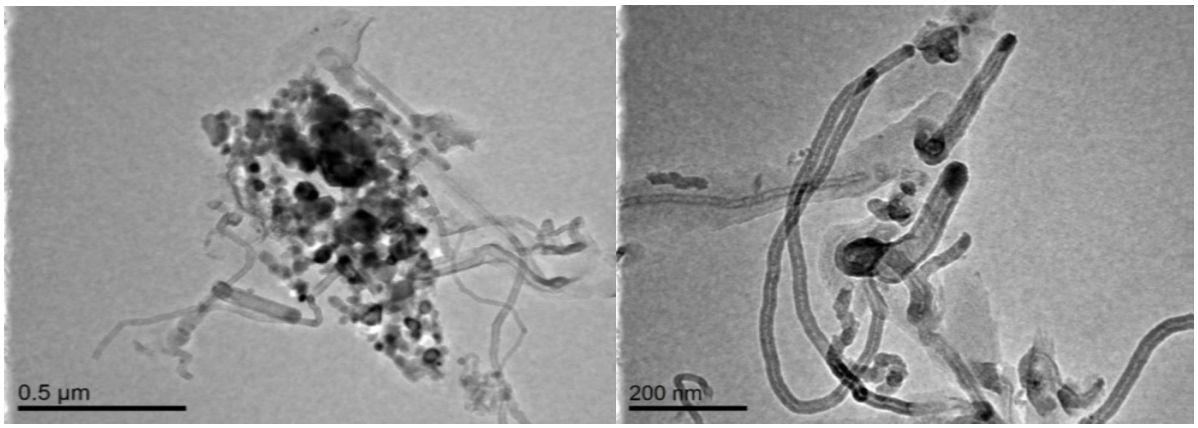

Figure D3.14: *TEM Images of MnBi@CNTs(at 700°C for 1h of acetylene flow)*

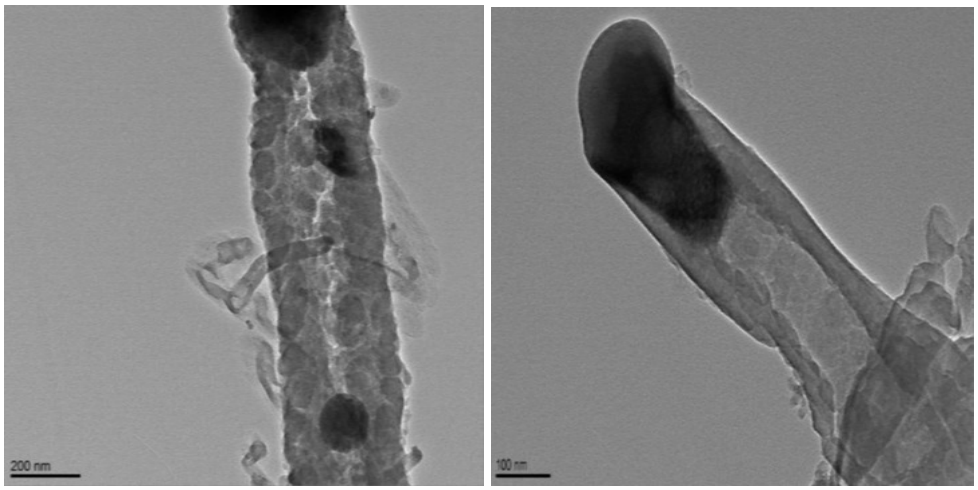

Figure D3.15: *TEM Images of MnBi@CNTs (at 700°C for 1h of acetylene flow)*

Finally, Vibrating Sample Magnetometer was used to investigate the magnetic properties of the sample. In Figure D3.16 three magnetization loops are given, one of pure MnBi alloy and the ones of MnBi@CNTs of 15 and 60 minutes acetylene flow at 700°C, which are typical ferromagnetic material loops. The green magnetization loop corresponds to MnBi alloy. The blue loop corresponds to 15 min acetylene flow and 700°C temperature. Due to the low acetylene flow time, the nanoparticles which are on the inside of the carbon nanotubes are relatively small offering this way no significant contribution to the magnetization. This is realized by the absence of an actual plateau. The red magnetization loop refers to 1 hour acetylene flow at 700°C. Because of the large time of acetylene flow, the nanowires which were grown on the inside of carbon nanotubes did not have the same growth rate as the nanotubes did, resulting to the formation of non-fully filled nanotubes and, therefore, the magnetization was lower than that of the alloy, but still remarkable to support the observation of magnetization of the MnBi@CNTs. More specifically, for the MnBi alloy, the saturation seems to be stable as the applied magnetic field approaches certain limit values (-20kOe to 20kOe) between the values -4.5emu/g and -4.5emu/g. This is expected since manganese alloy is expected to exhibit macroscopically magnetism after application of external magnetic field. On the other hand and for the case of MnBi@CNTs (60min), the received magnetization values range between 0.35emu/g and -0.35emu/g, much lower than those of this alloy. For the MnBi@CNTs (15min), the received magnetization values have a much lower range from 0.12emu/g to -0.12emu/g. It should be noticed that in both last cases, it appears that although the external magnetic field ranges between 20kOe and -20kOe, saturation has the potential to go even further, not being able though to give much higher values. Finally, the pure alloy exhibits the largest hysteresis compared to the cases of the nanorods encapsulated inside carbon nanotubes, followed by the relatively smaller but significant hysteresis of MnBi@CNTs (60min).

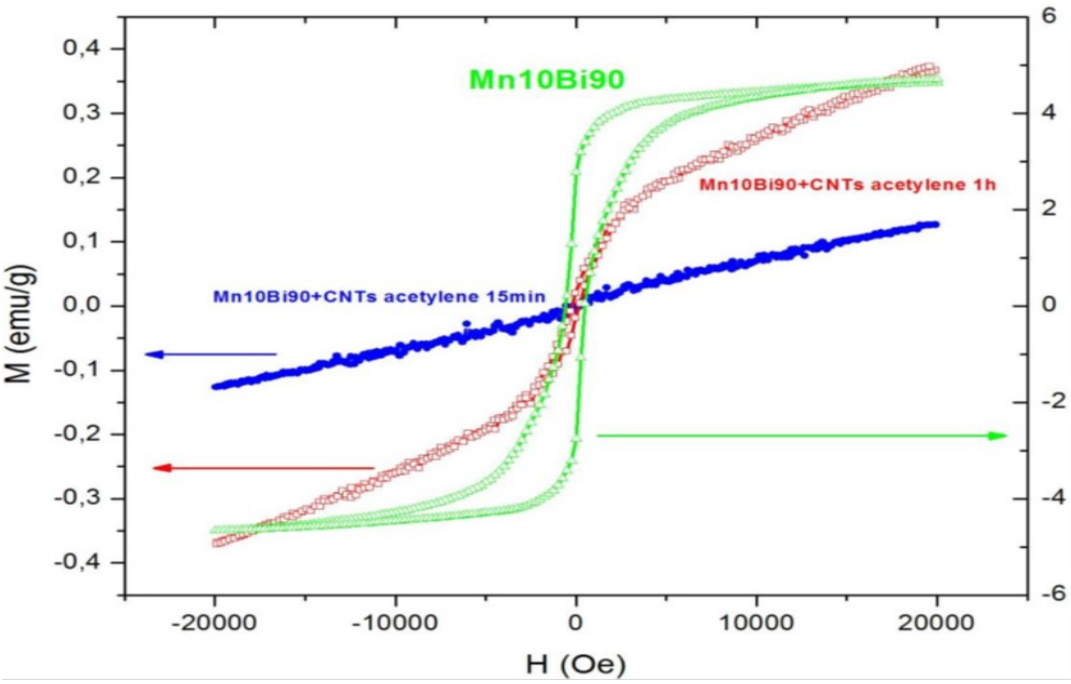

Figure D3.16: *Magnetization loops*

As a conclusion and according to XRD patterns, the existence of metallic bismuth and manganese phases, as well as alloy and oxide phases of them, which was expected to be present inside nanotubes, is confirmed. Observation of Raman spectra showed that the ratio I_D/I_G which was calculated for all sample was found to range between 0.91 and 0.98, confirming this way the fine quality of the produced carbon nanotubes. Furthermore, after sodium chloride removal, the characteristic NaCl (which was used as catalyst) peaks are absent. Thermal analysis data exhibited that the produced MnBi nanorods covered by carbon nanotubes gave a yield around 10%w/w. SEM images indicated that the diameter of the nanotubes ranges between 360 and 640 nm. Despite of that there are some nanotubes with a much lower diameter, ranging from 25 to 108 nm. From the TEM images nanowires of diameter between 150 to 485 nm were observed. According to VSM measurements, it was observed that by increasing reaction time, the magnetic signal is enhanced, due to the fact that while time passes, carbon nanotubes become more filled with the MnBi ferromagnetic alloy.

D4. Development of 'Kish' Graphene Oxide monolayers using the Langmuir-Blodgett (LB) technique

- ## Characterization of pristine 'Kish' GO

Graphite oxide (GO) is usually formed by reacting graphite powder with strong oxidants such as a mixture of concentrated sulfuric acid, nitric acid and potassium chlorate (Staudenmaier method). After oxidation, the carbon sheets are decorated by carboxylic acid groups at the edges and phenol, hydroxyl and epoxide groups mainly at the basal plane. GO has become a promising material for several applications as already mentioned. Among other sources 'Kish graphite' represents an outstanding precursor for the development of high-quality GO. Kish graphite, at one time, was a by-product of the steel-making process. The more modern steel making processes do not result in the generation of Kish graphite, but in earlier times it was produced during the cooling of molten steel. Some early researchers recognized the potential for using Kish graphite, which exhibited the phenomenon of micaceous cleavage (and in that respect, was perhaps a precursor to modern-day HOPG), for producing spectrometer crystals and also, for the making of atomically smooth surfaces[243]. The high impurity levels as well as the biggest flake size which usually goes up to 5 mm in overall dimension are the main advantages. Here for the first time, graphene oxide was prepared using 'Kish graphite' that was then deposited on TEM grids (copper grids, 2000 mesh, Plano GmbH) using the Langmuir-Blodgett technique in order to form monolayers. The dependence and impact of time, injected concentration and quantity of injected material on the formation of thin graphene oxide monolayers was examined. A combination of analytical techniques was used for the characterization of pristine 'Kish' GO as well as the produced monolayers including X-Ray Diffraction (XRD), Raman Spectroscopy, Differential Thermal Analysis (DTA) and Thermogravimetric Analysis (TGA).

Figure D4.1 shows the XRD patterns of the 'Kish' GO prepared after two and after undergoing three oxidation cycles. Pristine graphite (not shown here) shows a very sharp diffraction peak at $2\theta=26.7^{o}$, which corresponds to the diffraction of the (002) plane, being the interplanar distance, d_{002}=3.3 Å[5]. After graphite oxidation to GO, the (002) reflection of graphite disappears and a diffraction peak at $2\theta = 11.9^{o}$ is present (in both patterns), which corresponds to the diffraction of the 001 plane (d_{001} = 7.4 Å), indicative of the successful oxidation of graphite and the creation of oxygen-containing groups that are randomly distributed on the basal planes and edges of the graphene sheets. Comparison of the relative intensity of the two patterns leads to a conclusion that in the second case and after three cycles of oxidation, GO has a higher order probably due to higher degree of oxidation.

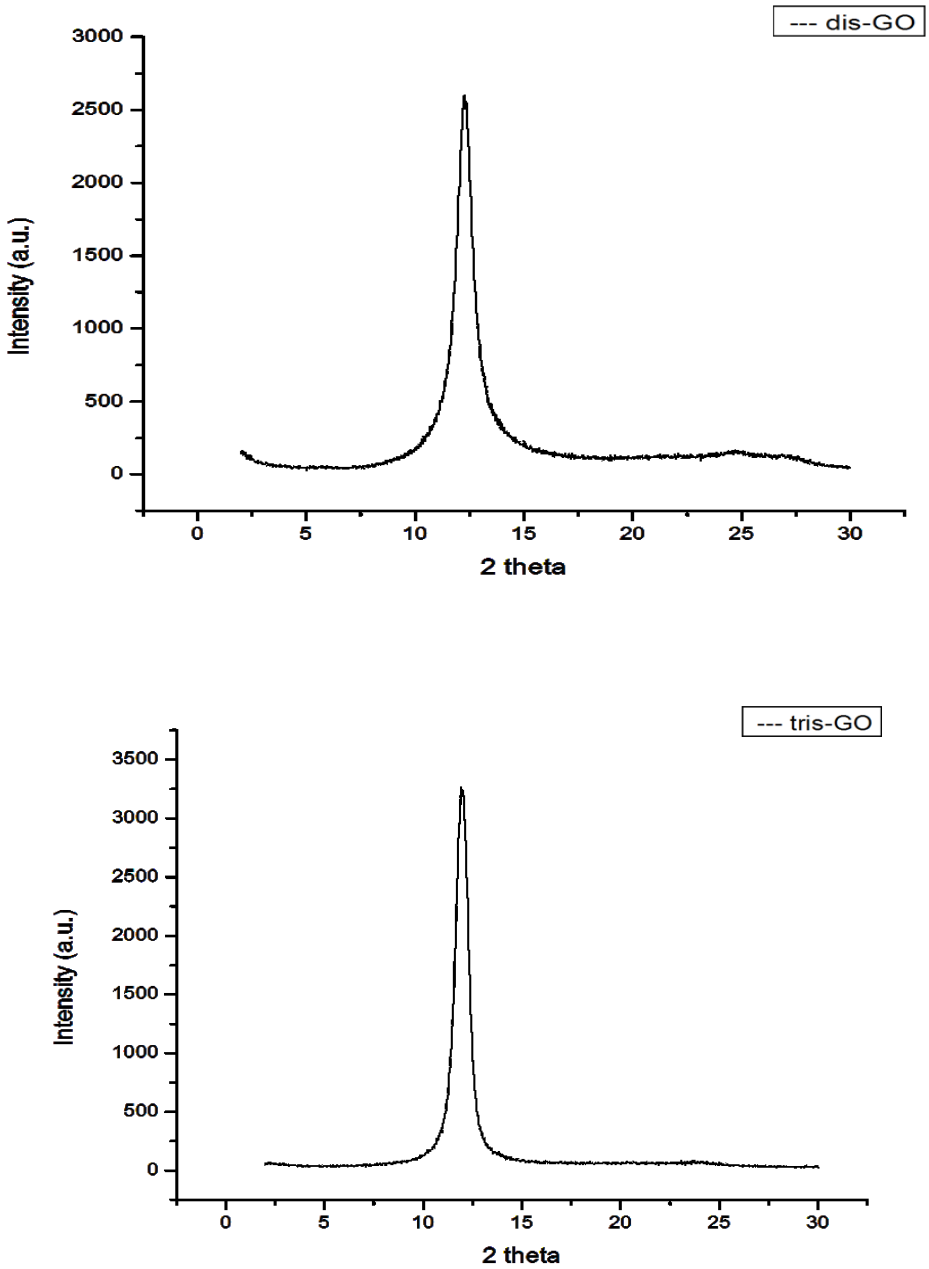

Figure D4.1: *XRD patterns of 'Kish' GO prepared after two and after three cycles of oxidation*

Contrary to graphite, which is an IR-inactive solid, the FTIR spectra of 'Kish' GO prepared after two or three oxidation cycles presents many peaks attributed to the oxygen-containing groups of GO (Figure D4.2) It is obvious that the peaks are more pronounced in the case where triple oxidation occurred indicative of the higher oxidation degree of the graphitic layers. The peak at 1627 cm^{-1} is attributed to –C=O stretching and the peak at 1395 cm^{-1} to –OH vibration. The peaks at 1060 cm^{-1} and 1215 cm^{-1} derive from C-O stretching while the peak at 970 $cm^{-1}$is attributed to epoxy groups. At the end, the peak at 815 cm^{-1} is attributed to the bending of C=O of carboxylic groups and the broader peak at 3430 cm^{-1} derives from the stretching vibrations of the hydroxyls of the same groups. As a comparison, in the case of

three oxidation cycles Kish-GO, most of the pre-mentioned peaks are of higher intensity compared to the respective ones of the two-oxidation cycles Kish- GO.

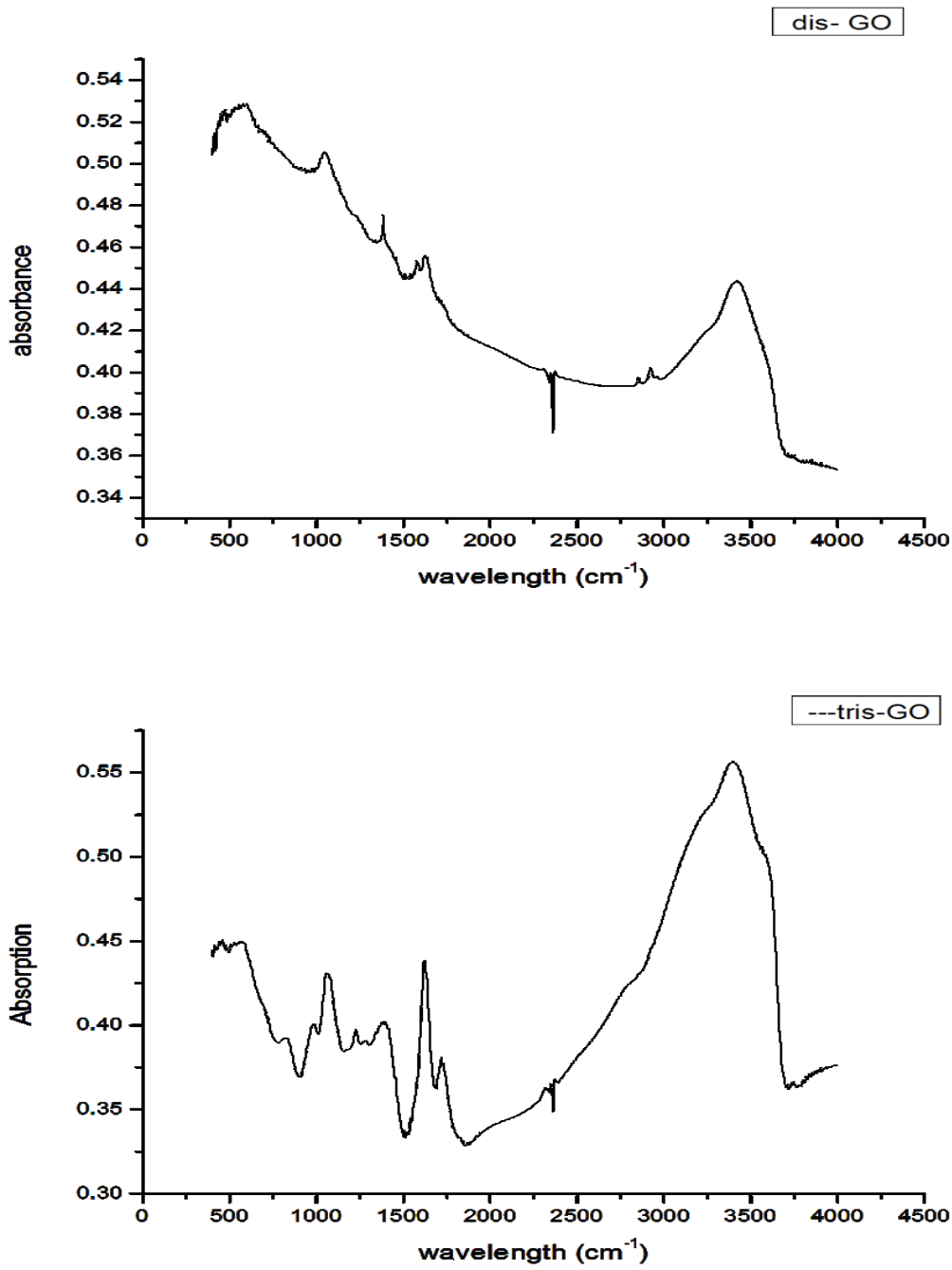

Figure D4.2: *IR patterns of 'Kish' GO after two and after three cycles of oxidation*

The quality of the produced Graphene Oxide was also investigated using Thermal Analysis. Two separate samples were examined, one of 'Kish' GO after two cycles of oxidation, using Staudenmaier Method and one of Graphene Oxide after three cycles of oxidation. The DTA/TGA curves are shown in Figures D4.3 and D4.4:

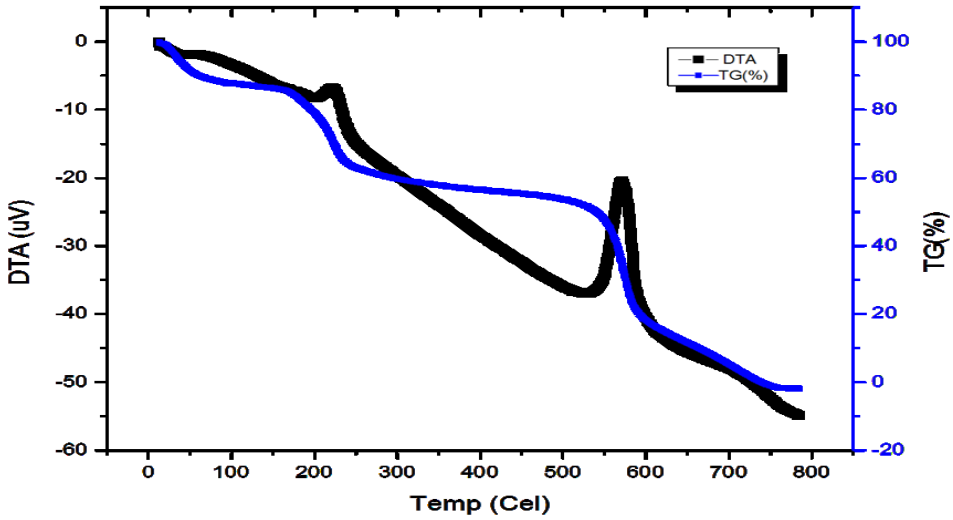

Figure D4.3: *DTA/TGA curves of 'Kish' GO after two oxidation cycles (dis-GO)*

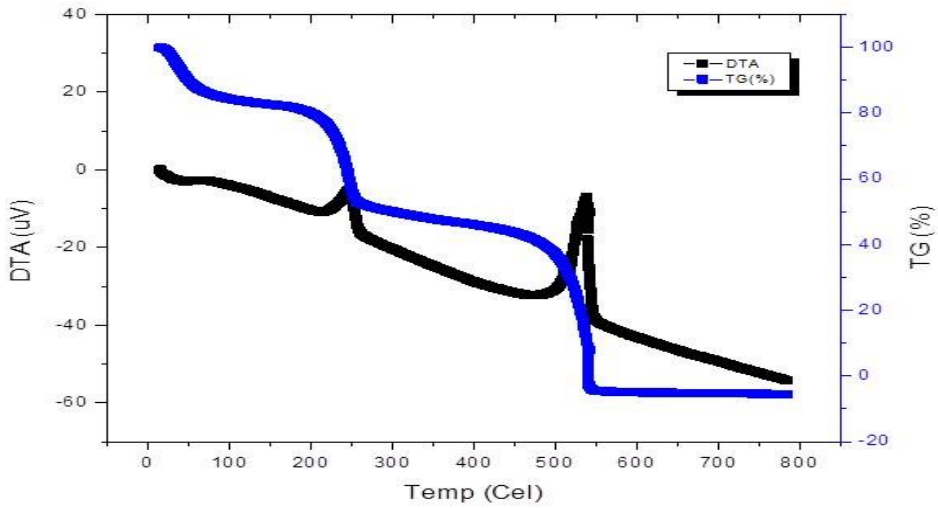

Figure D4.4: *DTA/TGA curves of 'Kish' GO after three oxidation cycles (tris-GO)*

In both DTA-TGA curves two significant and standard exothermic effects are observed: the first one at 230°C which is attributed to the thermal decomposition of oxygen-containing groups and indicates the loss of water and carbon dioxide release from the GO and the second one at 510°C which is connected with the combustion of the graphitic lattice. In the case of 2-cycle 'Kish' GO the weight loss at 230°C is ~30% w/w and at 510°C is ~50% w/w, while for temperatures below 120°C a weight loss of ~12% which is attributed to the physically absorbed water is observed. On the other hand and in the 3-cycle 'Kish' GO case, a ~12% weight loss is also observed below 120°C, again due to the absorbed water. At 230°C the mass loss attributed to the oxygen-containing groups is slightly increased (~35% w/w) due to the fact that the GO has undergone a higher degree of oxidation (three cycles instead

of two). Finally a ~50% weight loss at 510°C is observed due to the decomposition of the graphitic lattice as in the first case. In conclusion, XRD, FTIR and DTA/TGA data confirm the successful oxidation of the pristine 'Kish' graphite towards synthesis of GO while verify the higher oxidation degree of the sample after three oxidation cycles.

- **Evaluation of LB isotherms**

Sample concentration C=3.8 mg/ml

Aiming at testing the behavior of Kish-GO during the formation of monolayers and by the use of LB-method, different volumes of a standard Kish-GO concentration (C=3.8mg/ml, in a 1:5 water-methanol solution) where applied on an LB trough, which was filled with milliQ distilled and de-ionized water as a subphase. Beginning from 200cm^2 surface area, at 20cm^2/min barrier speed, several isotherms where received as observed in Figure D4.5.

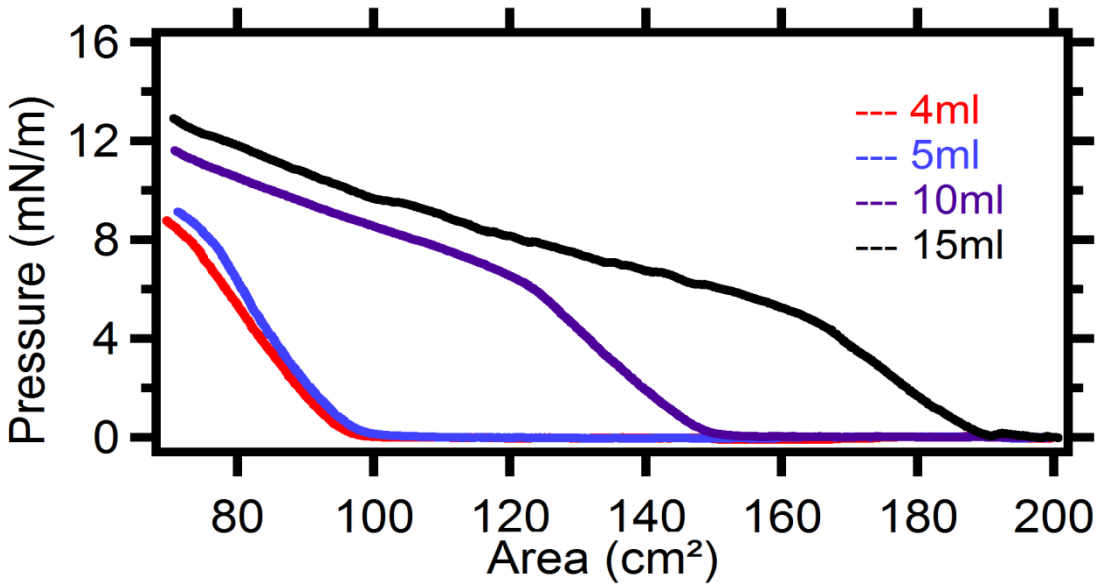

Figure D4.5: *Π-α isotherms of different volumes of 'Kish'-GO (3.8mg/ml)*

A summarized table of the first observed results follows (Table D4.1); from the table it is obvious that when we increase the amount of GO we inject, the final pressure is increasing (for the same surface difference). Here must be underlined though the fact that, although for injected 'Kish'-GO volumes of 4 ml and 5 ml the isotherms are almost identical, in the cases of 10 ml and 15 ml it appears that the pressure increases but not as steep as before, indicating that the GO flakes strongly interact with each other while in solid state, still giving though a pressure increase.

Table D4.1. *Differential area-injected volume-final pressure*

ΔA (cm^2)	V_{GO} (ml)	Final Pressure (mN/m)
130cm²	4ml	9mN/m
130cm²	5ml	9.4mN/m
130cm²	10ml	11.4mN/m
130cm²	15ml	13mN/m

Sample concentration C=5 mg/ml

The LB-method was applied again for different volumes of a standard Kish-GO concentration (C=5mg/ml, in a 1:5 water-methanol solution) allowing us to investigate the final pressure of a formed on the LB-trough monolayer at higher concentrations. The trough was filled with milliQ distilled and de-ionized water as a subphase. Beginning from 200cm^2 surface area, at 20cm^2/min barrier speed several isotherms where received as observed in Figure D4.6.

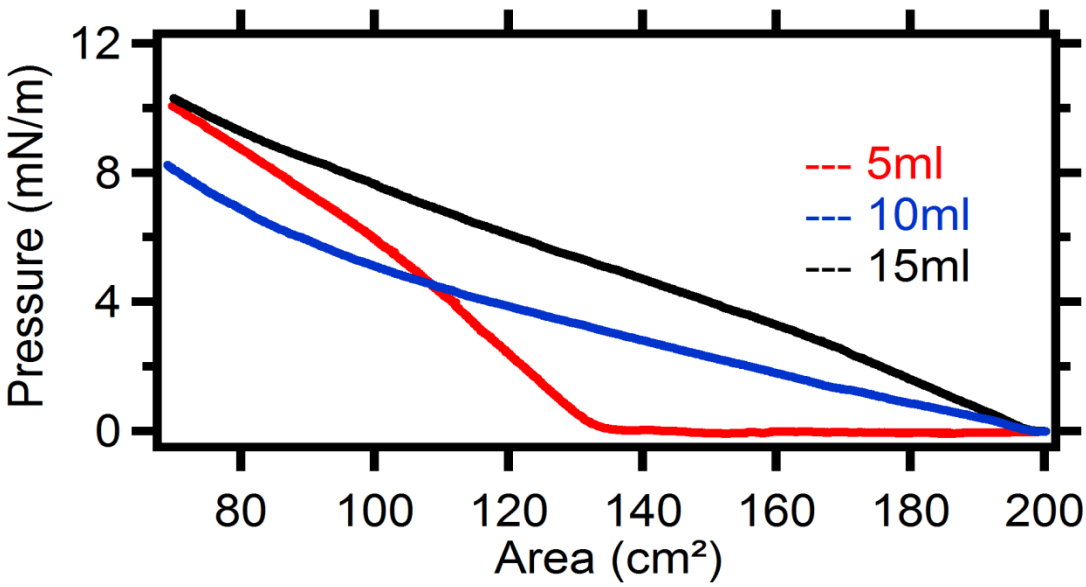

Figure D4.6: *Π-α isotherms of different volumes of 'Kish'-GO (5mg/ml)*

Table D4.2 summarize the results from these series of Π-α tests. The results indicate that the more GO we inject the higher the final pressure is for the same surface difference, although after injecting 15 ml GO the pressure seems to drop, indicating a possible collapsing in the finally achieved solid state. It appears though that the received isotherms at

even higher concentrations do not follow the expected Π-α isotherm pattern as the injected volume increases, a fact that indicates that the injected GO volume is already far from the one needed to cover the surface in order to create a solid state monolayer. This potentially leads to overlapping of 'Kish'-GO flakes, forming this way double or multi-layers.

Table D4.2. *Differential area-injected volume-final pressure*

ΔA (cm^2)	V_{GO} (ml)	Pressure (mN/m)
130	5	10.2
130	10	10.4
130	15	8.2

Sample concentration C=1 mg/ml

Several new depositions were also performed, this time not only injecting different GO volumes but also changing its concentration. The concentration of 1 mg/ml from this point will be regarded as C and gives a surface coverage very close to the reported in the literature GO values[152]. 5ml of 'Kish'-GO would be injected on the water subphase in order to investigate the impact of same amount of material of different concentrations on the final solid LB-monolayer. Beginning from initial area 200 cm^2, 20cm^2/min barrier speed and final area 70 $cm^2$and injecting slowly 5ml of 'Kish'-GO of different concentrations, the obtained isotherms are presented in Figure D4.7:

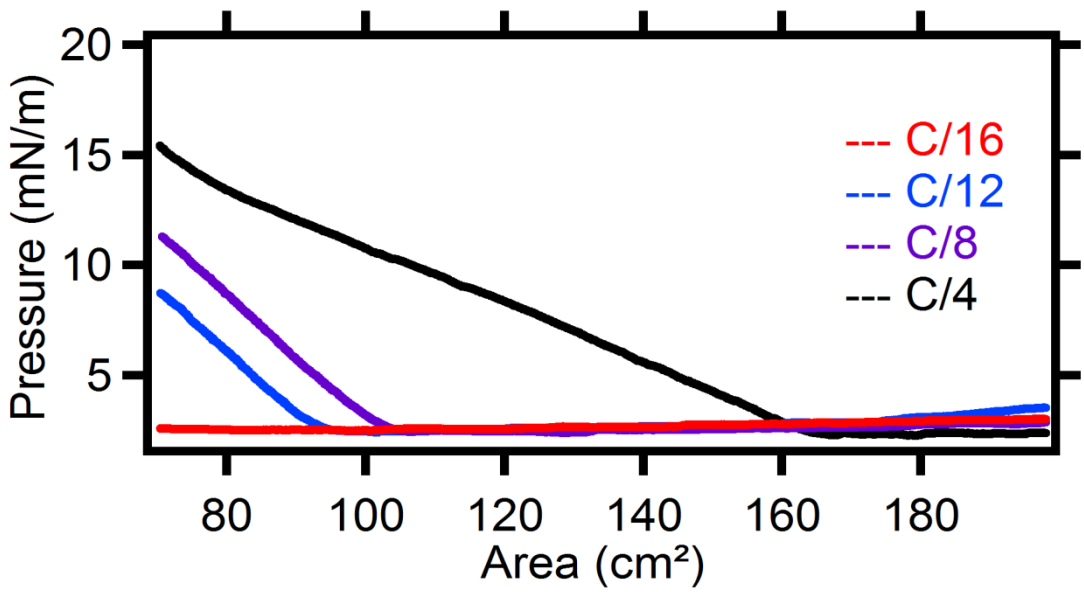

Figure D4.7: *Π-α isotherms of different concentrations of injected 'Kish'-GO of the same volume (5ml)*

The results of the received isotherms are summarized in the following Table D.4.3.

Table D4.3. *'Kish'-GO concentrations and final achieved pressure for the same injected volume*

Concentration (C=1 mg/ml)	V_{GO} (ml)	Pressure (mN/m)
C/4	5ml	15mN/m
C/8	5ml	12mN/m
C/12	5ml	9.5mN/m
C/16	5ml	2mN/m

Base on the above one can conclude that as the 'Kish'-GO concentration is decreasing and for the same injected volume, the final pressure of the formed monolayer is becoming less. The 'Kish'-GO molecules appear to switch through compression from gas phase forces to liquid and final to gas phase, following more cohesive isotherm patterns than those in the previous higher concentrations. Therefore and in order to investigate the behavior at even lower concentrations, C/48, was chosen, following the same experimental conditions as before (see Figure D4.8).

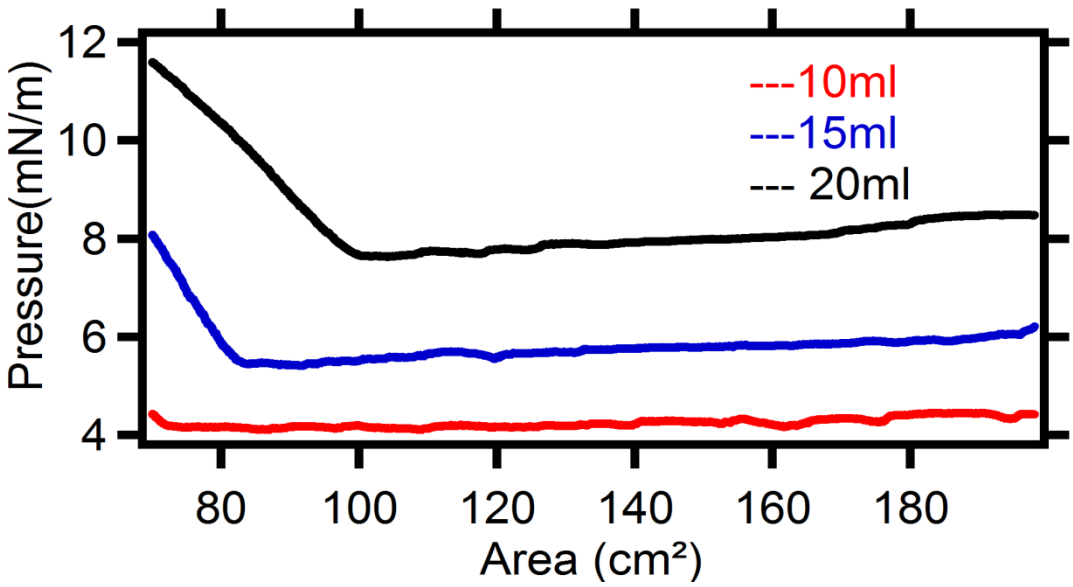

Figure D4.8: *Π-α isotherms received after injecting different volumes of 'Kish'-GO of concentration C/48*

Notably, after having spread the whole of GO volume each time and before compression, the pressure on the surface is far from 0 mN/m, a fact that indicates that the injected material is already exceeding the necessary molecule amount in order to have a homogeneous surface coverage, beginning (during compression) from gas phase to solid phase.

Finally, having lowered the concentration at C/64 and for the same conditions, the obtained isotherms are shown in Figure D4.9:

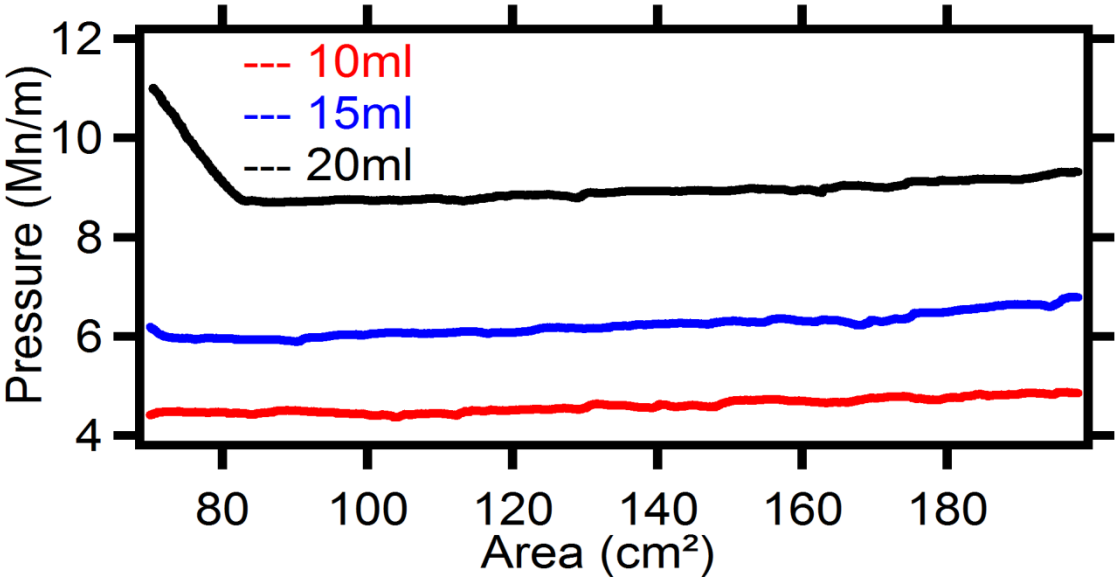

Figure D4.9: *Π-α isotherms received after injecting different volumes of 'Kish'-GO of concentration C/64*

In all of the above cases and due to the fact that the initial pressure before compressing stabilizes above 0 mN/m it should be concluded that 3.8mg/ml and 5mg/ml concentrations seem to be far from the desired ones in order to receive the expected patterns, leading to different isotherms each time. Notably, in all the above tests there was no use of glass (see below) during the injections, which could be the reason for which not so smooth and reproducible isotherms were received. Allowing the material to reach the subphase as smooth as possible and decreasing also the injection rate we could lead to better and more reproducible results (see below).

Sample concentration C=1 mg/ml (use of an inclined quartz-glass)

Langmuir-Blodgett technique was used one step further in order to control parameters that could be inhibiting the reproducibility of the tests, the floating of 'Kish'-GO on the water-subphase and the formation of the monolayer in the water-air interphase. Therefore, an inclined quartz-slide glass was partially submerged (for more details about the 'soft injection' see PBA chapter) in the subphase so as to allow a 'soft' injection of Kish-GO on the subphase and on which several volumes of 'Kish'-GO [dispersed in the same water-methanol solution (1:5)] would be injected, allowing floating to be more smooth and controllable. The rate at which the injections were done was roughly 10 μl per minute. In the first attempt 100 μl, 200μl, 500μl, 700μl and 1000μl (1ml) were injected. The received isotherms follow (Figure D4.10).

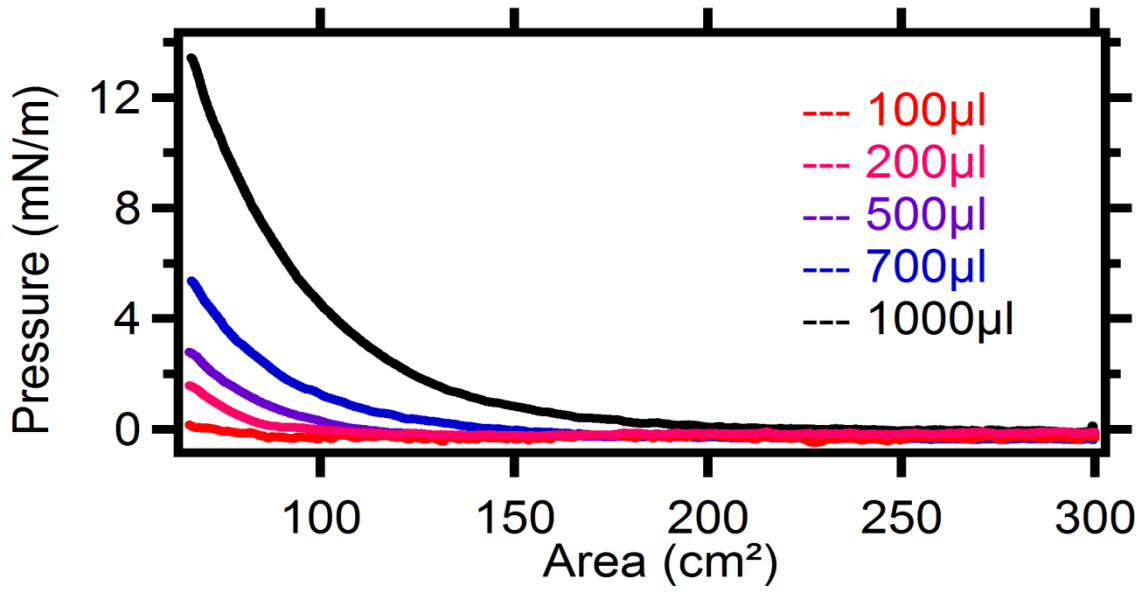

Figure D4.10: *Isotherms received for different GO volumes of concentration 1 mg/ml*

It appears that the use of glass as well as the injection of less than 1ml volume of GO leads to isotherms that follow the same increase pattern, being actually parallel to each other and going smoothly from gas phase through the liquid phase and in a steeper way to the final solid phase, forming the 'Kish'-GO monolayer on air-water interface.

Sample concentration C=0.5 mg/ml (use of an inclined quartz-glass)

The same conditions were followed at an even lower concentration, but now the 'Kish'-GO concentration would be 0.5 mg/ml and the injected volumes 50μl, 100μl, 200 μl, 500 μl and 1000μl. It appears that injecting less than 300 μl no significant rise in pressure occurs while after injecting 200 μl and above the increase in pressure is observed and the isotherm is rather steep at the area 100 cm^2 and below. The received isotherms are shown in Figure D4.11.

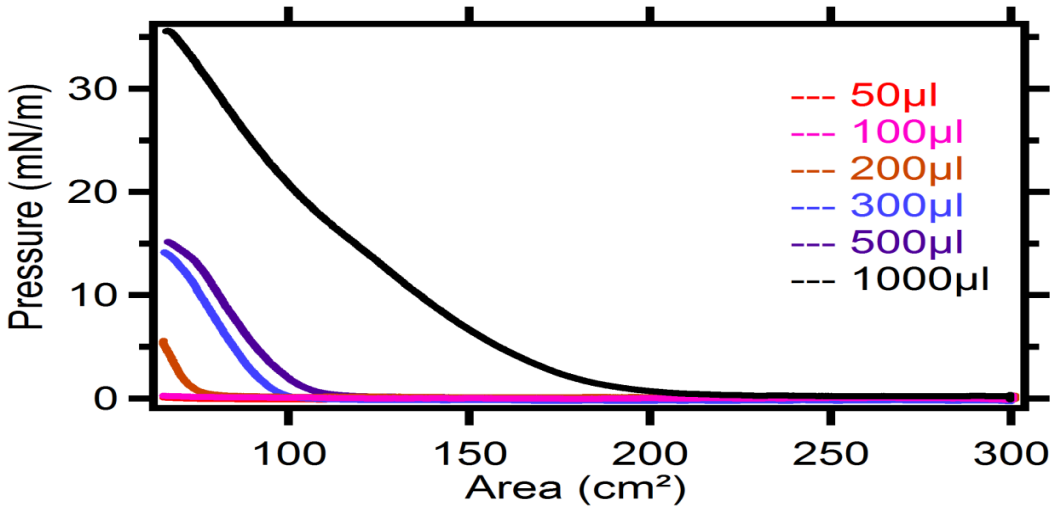

Figure D4.11: *Isotherms received for different GO volumes of concentration 0.5 mg/ml*

After this final series of tests at half concentration, the main conclusion is that although the injection of 50 and 100 µl of GO do not actually give any pressure increase, the injection of 200 µl of GO and above would give an even steeper isotherm than in the case of C=1 mg/ml, and the pressure rise begins at a smaller surface value. Notably after injecting 1000 µl of GO the received isotherm is not as steep as in the cases of less injected quantity though the pressure increase takes place 100 cm^2 approximately earlier (at 200cm^2).

- **Morphological and structural characterization of 'Kish' GO monolayers**

Transmission Electron Microscopy images were obtained in order to evaluate the structural characteristics and the overall quality of the deposited 'Kish' Graphite Oxide on the TEM grids in conjunction with the corresponding selected area diffraction patterns. After injecting different volumes of GO of 3.8 mg/ml concentration, the received TEM images as well as the diffraction patterns are shown in Figures D4.12-D4.14. The TEM images show large flakes of 'Kish'-GO having covered almost all the space of every TEM-grid window. The concentration at which the depositions were performed was high, therefore there are some darker regions that indicate a potential overlapping of GO flakes. This might have led to domains consisting of more than one monoatomic flake and form in this way double or multiple layers. As revealed by the received SAED patterns, the formed monolayer consists of domains that contain single crystals (spots pattern) and multi-crystalline parts as exhibited by the clear ring patterns. It is also observed that the size of the flakes varies from 2 µm to a few tens of µm.

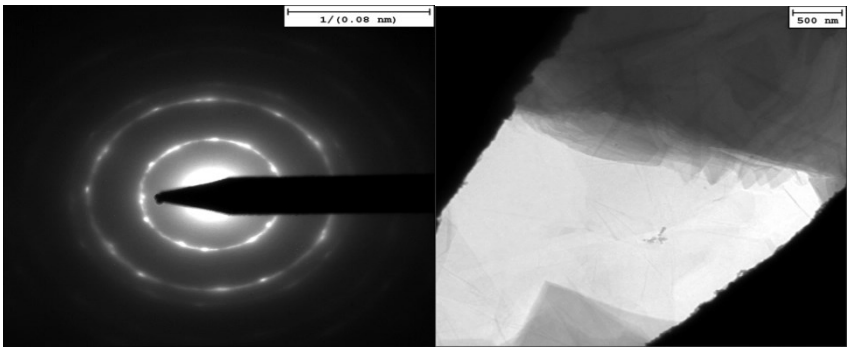

Figure D4.12: *TEM (right) and SAED (left) images of the formed monlayer deposited on Cu-grid, after injecting 4 ml of GO (3.8mg/ml) on the water subphase*

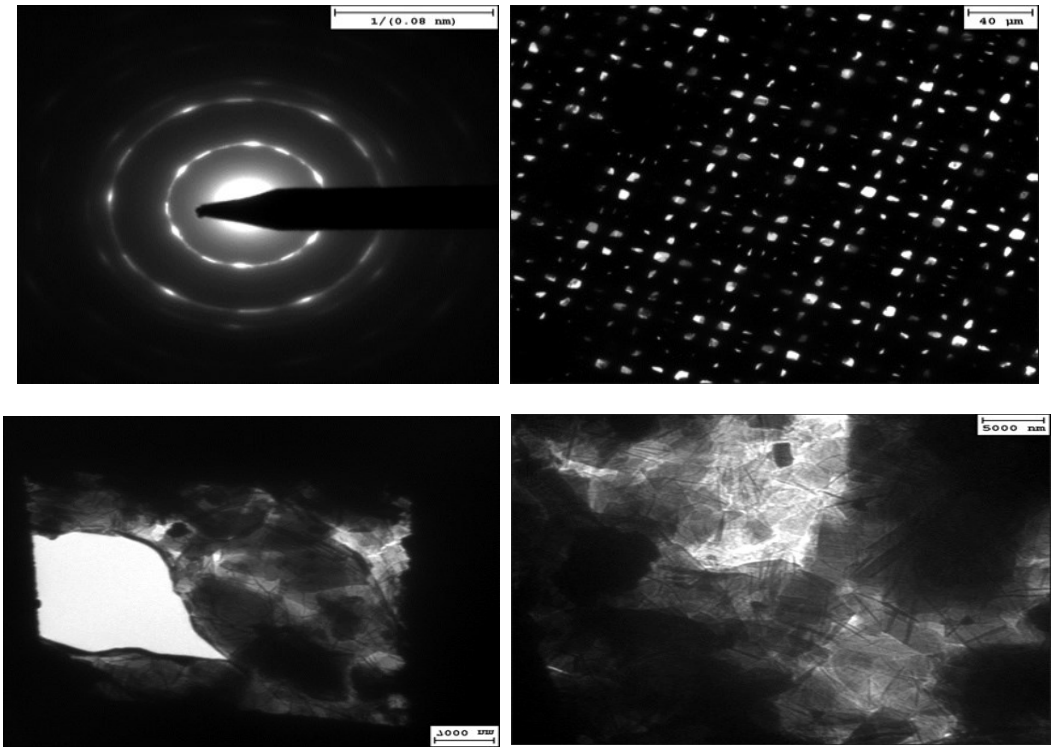

Figure D4.13: SAED (upper left) and *TEM images of the formed monolayer, deposited on Cu-grid and after injecting 5 ml of GO (3.8mg/ml) on the water subphase*

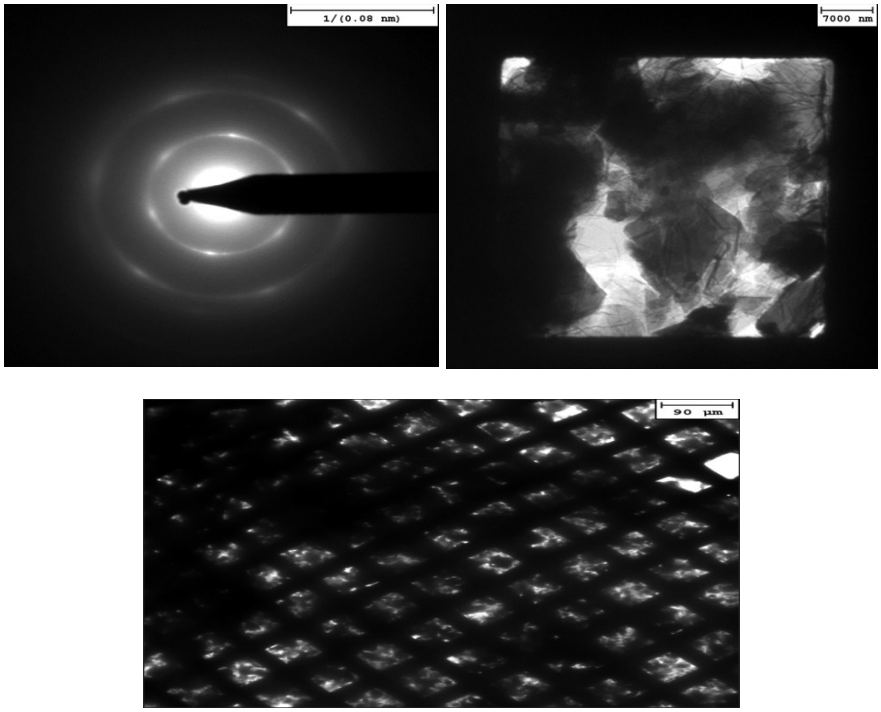

Figure D4.14: *SAED (upper left) and TEM images of the formed monolayer deposited on Cu-grid, after injecting 10 ml of GO (3.8mg/ml). The bottom image shows the copper grid, almost every window of which is covered with GO*

To conclude the study of concentration effect on the quality of the formed through the LB-method monolayer, the lower concentrations were investigated. TEM measurements on 'Kish'-Graphene Oxide samples, of 1mg/ml and 0.5 mg/ml concentrations were performed,

in order to examine the quality of the formed monolayers on the LB-trough and to determine whether they diffracts, verifying at the same time the single- or multi-crystalline nature of the deposited films. These concentrations were chosen due to the fact that they exhibited the optimal behavior after compression through the LB-method and therefore they represent fine candidates for a potential monolayer constitution. The depositions were accomplished on copper grids as well.

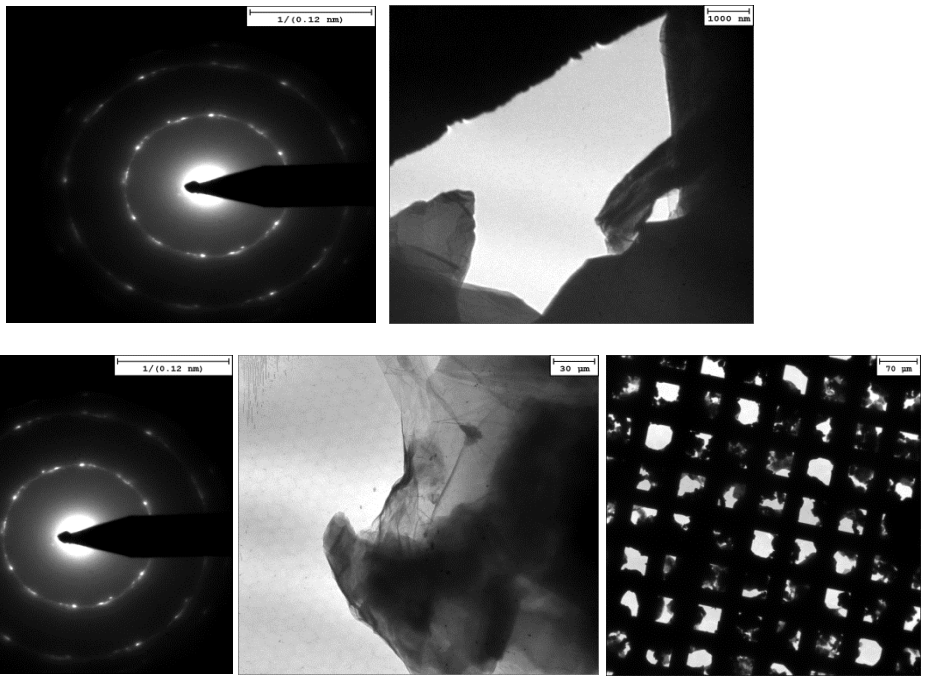

Figure D4.15: *TEM images of the 'Kish' GO samples of 0.5mg/ml*

In Figure D4.15 the TEM patterns are presented. The observation which enhances the previously acquired assumption is that the formed monolayer is composed by single crystals of various orientations. This derives from the decoding of the received diffraction patterns: typical homo-centric rings that are not continuous but consist of spots, a fact that strongly suggests that single-crystals of different orientations diffract, forming a multi-crystalline layer, close though to the potential diffraction pattern of a single crystal (the typical square-dot pattern). Notably, the diffraction has been taken from the thinner areas which can be observed in the large-scale images respectively. The final image is the one of the copper grid (bottom right) with the deposited 'Kish'-GO on it, with an approximate 50% coverage.

As a conclusion, 'Kish'-GO was successfully produced by the use of the Staudenmaier synthetic method. The formation of monolayers using the LB method was possible and controlling of surface coverage by different initial 'Kish'-GO concentrations was facile. All concentrations and injected volumes showed during TEM investigation fine diffraction, proving the crystallinity of 'Kish'-GO, ranging from multi-crystal monolayer (clear ring patterns) to dotted rings. This is indicative of multi-crystaline material that consists of differently oriented crystals, also containing single-crystalline domains (dotted ring patterns taken from the thinner monolayer areas, at 0.5 mg/ml).

D5. Development of low-dimensional Prussian-Blue Analogues using the 'inverted' LB method

The final fifth part of the thesis is an effort to develop low-dimensional Prussian Blue Analogues using the 'inverted' LB method. The main advantage of this technique is its ability to precisely control the film thickness (number of layers deposited) with molecular level accuracy. This control offered by the LB method is applied here to pursue the creation of truly bi-dimensional systems of Prussian blue analogues. It is important to note that, the aspect of restricted dimensionality was created through a self-limited 'on-surface' reaction. However, the nature of the deposited material synthesized in such a way remains partially three-dimensional as imposed by the coordination level of the precursor. The target here was to create a material which would be two-dimensional by nature. The planar geometry of a tetracyanide building block makes it a logical and suitable choice for the construction of a genuinely two-dimensional material. Cyclic (layer-by-layer) deposition (consecutive LS transfer) can be used to form stacks of the material in the third dimension (as demonstrated below).

A modified LS technique was used to synthesize PBA from precursors through an 'on-surface' reaction between a metal chloride sub-phase and potassium tetra-cyano-platinate(II). The proposed reaction is the following:

$$\mathrm{CuCl_2 + K_2Pt(CN)_4 \rightarrow CuPt(CN)_4 + 2KCl}$$

This is the well-known Lewis acid-base reaction which governs the synthesis of classic three-dimensional PBA, with the exception that the traditional hexacyanide group has been replaced with tetracyanide. Although the water-air interface already provides a two-dimensional surface, in order to ensure that truly two-dimensional material is created at the interface, a novel technique which we deem as an 'inverted' Langmuir method was employed. In a classic LB experiment where amphiphilic molecules are used as surface active agents, the packing goes from a two-dimensional gaseous, to liquid, and finally to solid state as the surface area is decreased. This is accompanied by discrete stepwise pressure rises. In the 'inverted' Langmuir method the barriers are initially closed, providing a restricted area on which a reaction can take place. The creation of the material then occurs by gently injecting an aqueous solution of potassium tetra-cyano-platinate(II) at the interface between air and a $CuCl_2$ aqueous subphase. As the solid PBA is formed at the interface, the surface pressure begins to decrease as the barriers are free to move and are being pushed by the newly created film. The term 'inverted' comes from the fact that the solid state material is formed during injection while decompressing as opposed to the solid product one would receive during compression (classical Langmuir method). The appeal of this approach is that the surface area only changes when necessary to compensate for the addition of newly formed film, which encourages an 'on-surface' reaction over an 'in-solution' reaction. Furthermore, the gentle addition of the tetracyanide compound was facilitated by injecting the material on an inclined quartz slide that was partially submerged in the subphase (see

Figure D5.1). This supports a slow reaction to occur, which also mediates the formation of a 2D film at the interface.

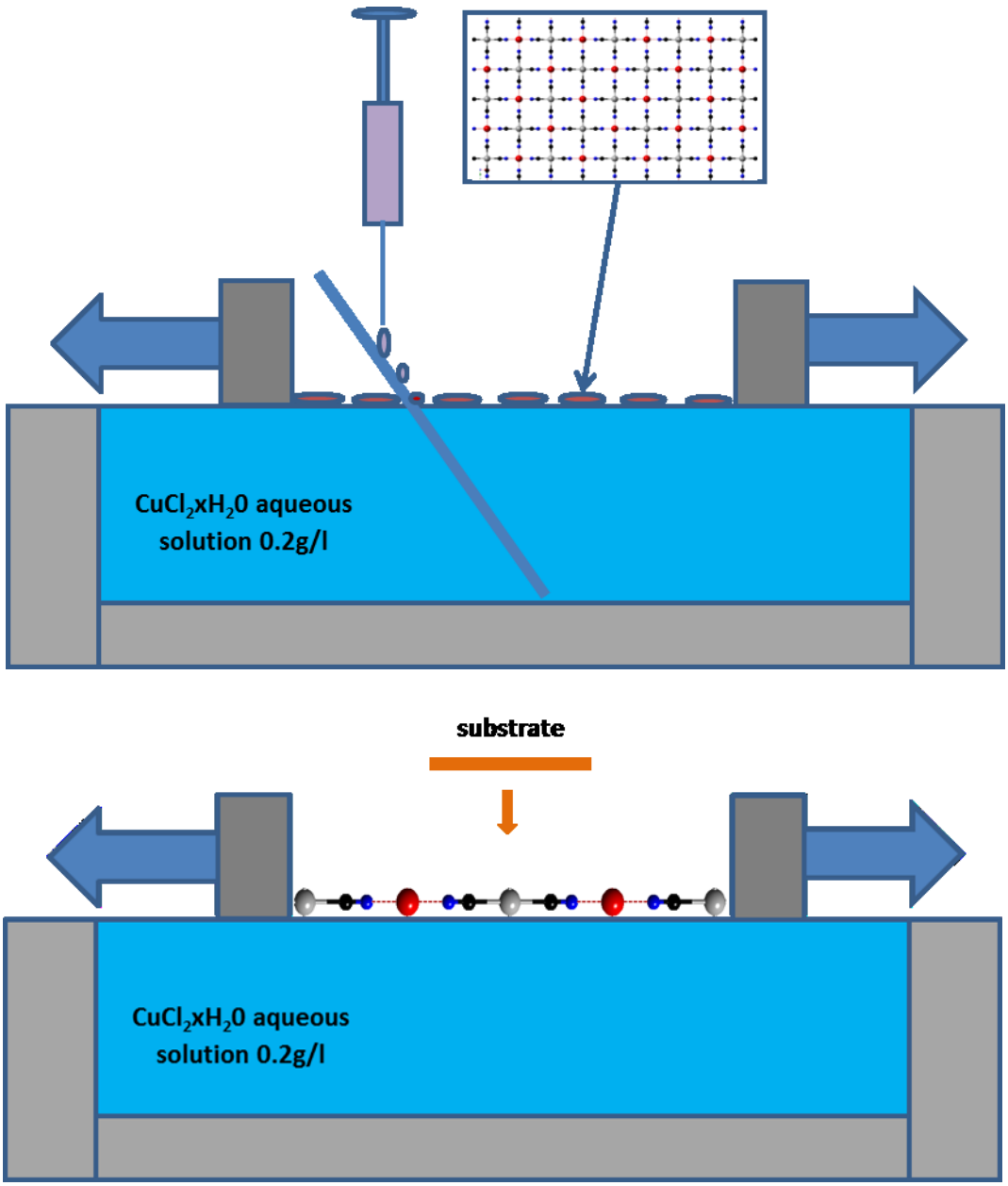

Figure D5.1: *Schematic representation of the 2D film formation using the 'inverted' Langmuir-Blodgett technique; the 'soft injection' of the tetracyanide on a piece of glass allows it to reach smoothly on the copper chloride surface and react slowly to produce the PBA, the formation is accomplished by de-compressing the barriers and deposition follows after dipping gently the substrate on the established PBA solid surface.*

The proposed structure for the formed 2D PBA network follows in Figure D5.2. Copper ions tend to substitute potassium ions, which derive from the dissolved in the water-ethanol mixture of the tetracyanide.

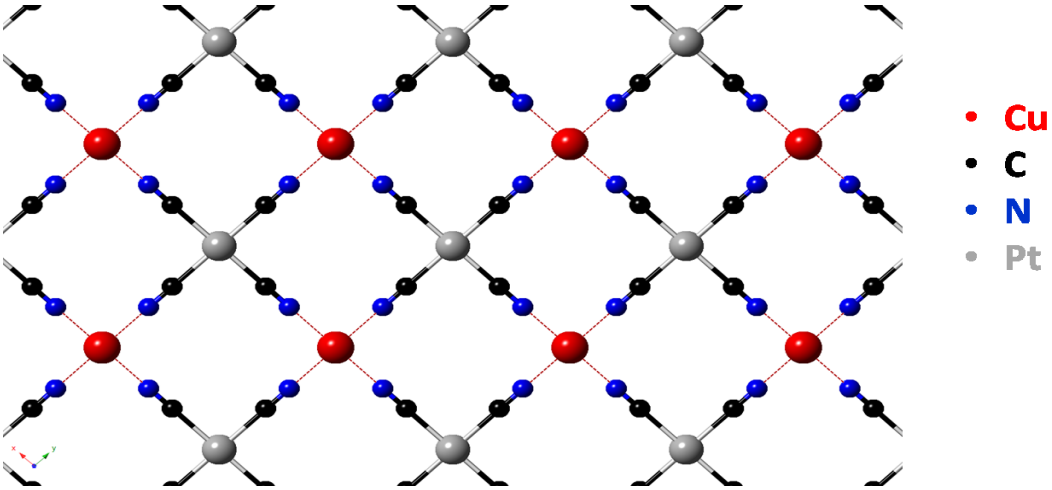

Figure D5.2: *Simulation of the formed 2D PBA network on the surface of the LB trough*

One of the most facile and powerful ways to characterize the air-liquid interface of an LB trough is by the so-called isotherm (Π-a) measurements where one performs a compression of the material floating at the interface at a fixed bath temperature. The presence of any material at the interface and its nature (area on surface per volume of injected material) will affect the surface tension of the liquid it floats on. By closing the trough barriers, the floating material is compacted. Although isotherm curves are often used to identify various phases of the material during compression, such analysis is not applicable to the 'inverted' Langmuir technique. Based on the discussion above the barrier movement is not expected to induce any further phase transitions (like in classic LB), but instead push the patches of solid material together until the formation of a close-packed film (see figure D5.3).

Before each test, the LB trough was cleaned thoroughly using chloroform and filled with the sub-phase, which would usually be an aqueous $CuCl_2$ solution 0.2g/l. The tetracyanide compound was injected with a concentration of 0.23mg/ml (which was the optimal chosen concentration, see Appendix for details) in a water-ethanol solution (1:3) at a rate of 10μl/min. Ethanol was used to assist the floating of the injected material, so that it would not sink or react below the surface. Before injecting the tetracyanide, a piece of quartz glass was submerged partially in the trough approximately forming a 50° angle with the horizontal axis and the barriers were placed at closed position (90 cm^2). These conditions were kept stable for all tests and the produced thin films were deposited on silicon nitride windows in order to examine samples with TEM. Films were transferred onto the hydrophobic substrates by horizontal dipping (LS technique) at a certain constant pressure. Each time the substrate was lowered into the LB trough and was allowed to touch the air-water interface in a very gentle dip of maximum 0.5 mm below the water level.

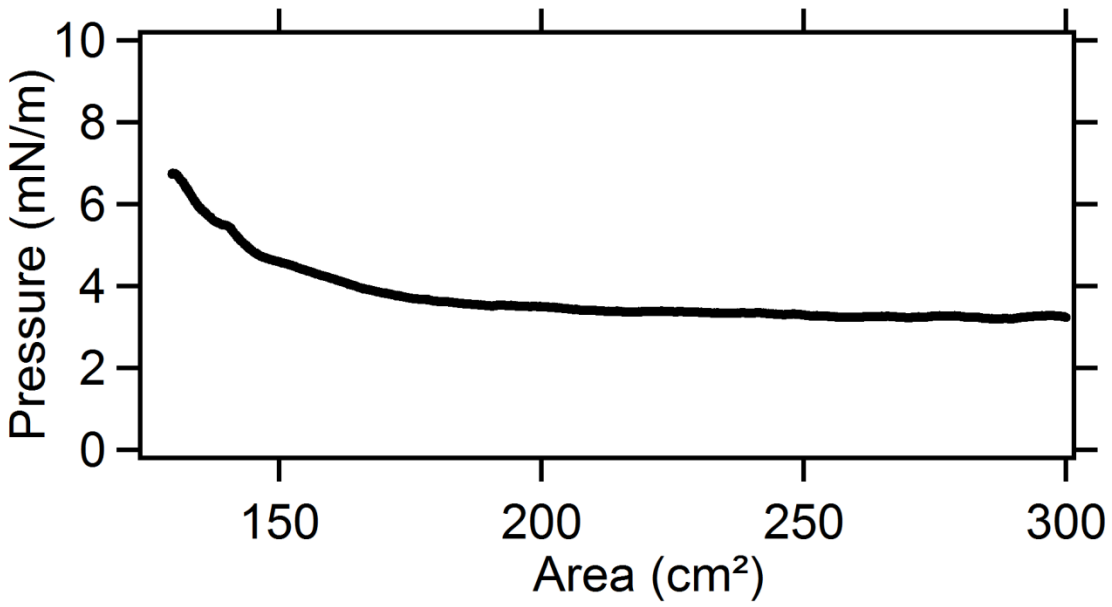

Figure D5.3: *Π-a isotherm after the 'inverted' LB method is applied; as the solid PBA is formed on the LB-surface the pressure begins to decrease as the barriers are free to move and are being pushed by the solid to be stabilized at the selected target pressure (3 mN/m)*

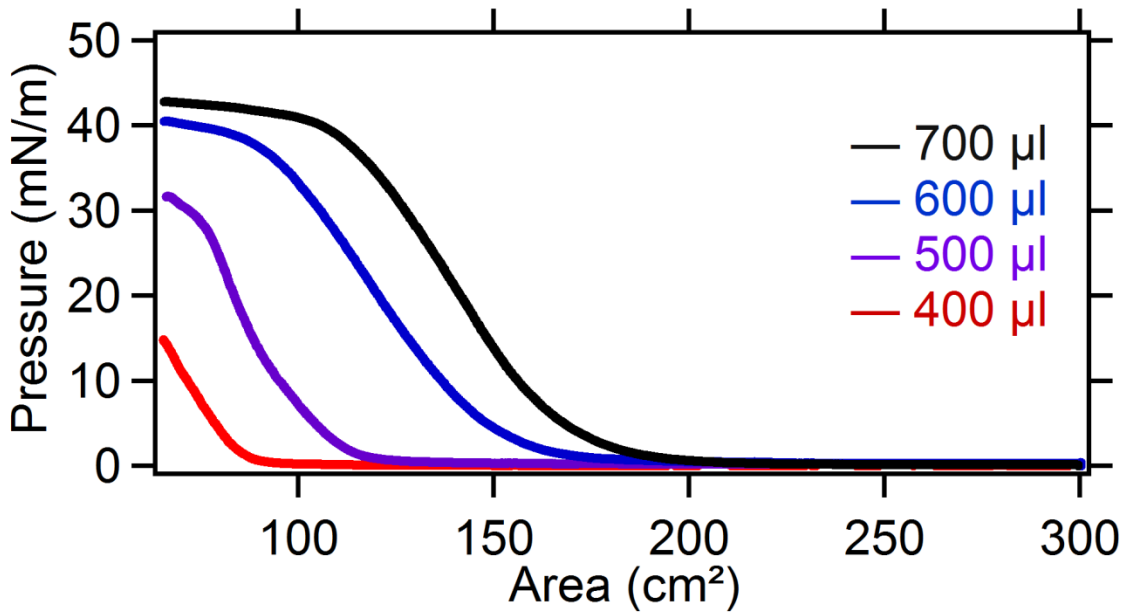

Figure D5.4: *Π-a isotherms after different volumes of injected potassium tetra-cyano-platinate (II) on the copper chloride subphase using an inclined quartz-slide; the isotherms follow the typical LB-isotherm with the formed monolayer to reach and stabilize at a final-pressure value of 43 mN/m at the established solid state*

Figure D5.4 displays isotherm curves of the two-dimensional PBA films on the air-liquid interface after applying the classical LB method. A pressure rise observed as a consequence of the close packing is described above. The area of 300 cm^2 corresponds to fully opened barriers whereas 60 cm^2 is reached when the barriers are at the closed position. The final pressure that was reached for fully closed barriers depends on the volume of injected reactant; for volumes lower than 300 µl (at 0.23 mg/ml) little to no change in surface tension was observed during compression meaning that the total area of created solid material was

less than 60 cm^2. Larger injection volumes lead to increased final pressure. A maximum surface pressure is observed around 40mN/m and saturation at this pressure implies that an irreversible collapse or overlapping of material has occurred at the interface. In a control experiment potassium tetra-cyano-platinate(II) was injected on pure water. No surface tension rise was observed, meaning that one of the reactants alone does not affect the surface properties, and therefore no material can be created at the interface. Only the combination of tetracyanide with an appropriate subphase can react so as to lead to the creation of material.

The formed PBA (after injecting 600 µl of tetracyanide at 30 mN/m, using the 'inverted' LB method and keeping the rest of the conditions stable) was transferred horizontally (the L/S method) onto various substrates for further analysis. In order to confirm the nature of the product, X-Ray Photoelectron Spectroscopy (XPS) was performed. XPS is a quantitative elemental analysis of surfaces (probing depth of 5-10nm), and so is well-suited to study the two-dimensional PBA films. If this is successful, the proposed reaction involves the substitution of potassium by copper, and so chlorine and potassium should be absent from the final product. Two potassium ions exist in each 'molecule' inside the tetracyanide salt, balancing with their positive charge the negative charge which derives from the platinum tetracyanide group. What one should expect from the reaction would be the replacement of the two potassium atoms by one copper ion (Cu^{+2}) or equally by two Cu^{+1} ions so as to equalize the charge difference inside the salt. On the other hand, platinum being connected with four cyanide groups before and after reaction, would be expected to retain its (+4) oxidative state. Figure D5.5 shows an XPS wide scan of the sample deposited on a boron-doped silicon wafer, where one can observe multiple peaks indicating the presence of various elements: Si and B from the substrate, and Pt, C, N, and Cu from the 2D PBA layer. Also visible is oxygen from water and other possible contaminants which are always present on samples exposed to ambient conditions. Notably, chlorine and potassium are not observed, which leads to the conclusion that the measured sample is the product of an interfacial reaction and not just precursor compounds floating at the interface. Photoelectron spectroscopy is not only a quantitative elemental analysis (by identifying which elements are in the sample in what quantity) but is also very sensitive to the chemical environment in which each probed element resides. From the shape of the peaks one can try to deduce the oxidation state for each observed element out of which it was found that the metals appear to be Cu(I,II) and Pt (IV).

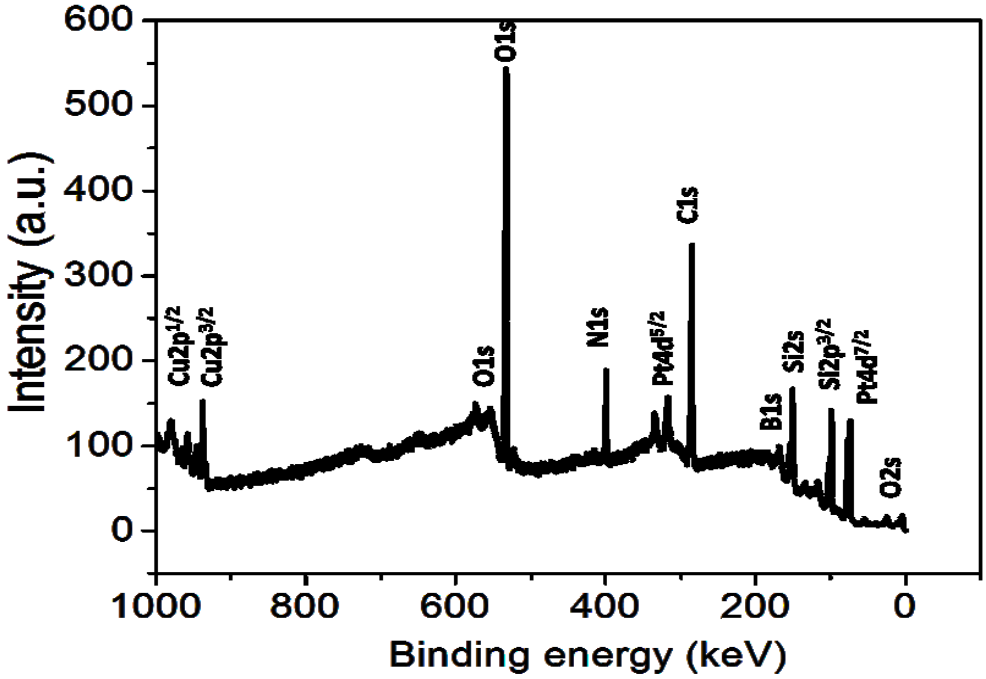

Figure D5.5: *XPS survey spectrum of PBA formed as described above using the 'inverted' LB, showing the reported characteristic peaks of the detected elements*

A multilayer structure was formed by consecutively depositing monolayers of PBA on a quartz plate. The formation of this multilayer film was followed by ultraviolet-visible absorption spectroscopy. A maximum absorption is observed at 280 nm, probably due to the charge transfer absorption band of the Pt-CN-Cu sequence (see figure D5.2). A measurement of the total trough area versus time at constant pressure (3mN/m as deposition condition and after having injected 600µl of tetracyanide, using the classical LB method) can be found in the Appendix, and testifies for a clear sequential deposition. The dependence of the maximum observed UV-absorption on the number of deposited monolayers of PBA is displayed in Figure D5.6 (lower panel), and reveals a linear relationship. This suggests that the same amount of material is transferred during each deposition. Additionally, the fact that the shape of the spectra in Figure D5.6 (top panel) is independent of the number of monolayers advocates that the monolayers in the stacked structure retain their two-dimensional nature. Both of these results prove that sequential deposition of 2D PBA is possible, and offers atomic level control over the film thickness.

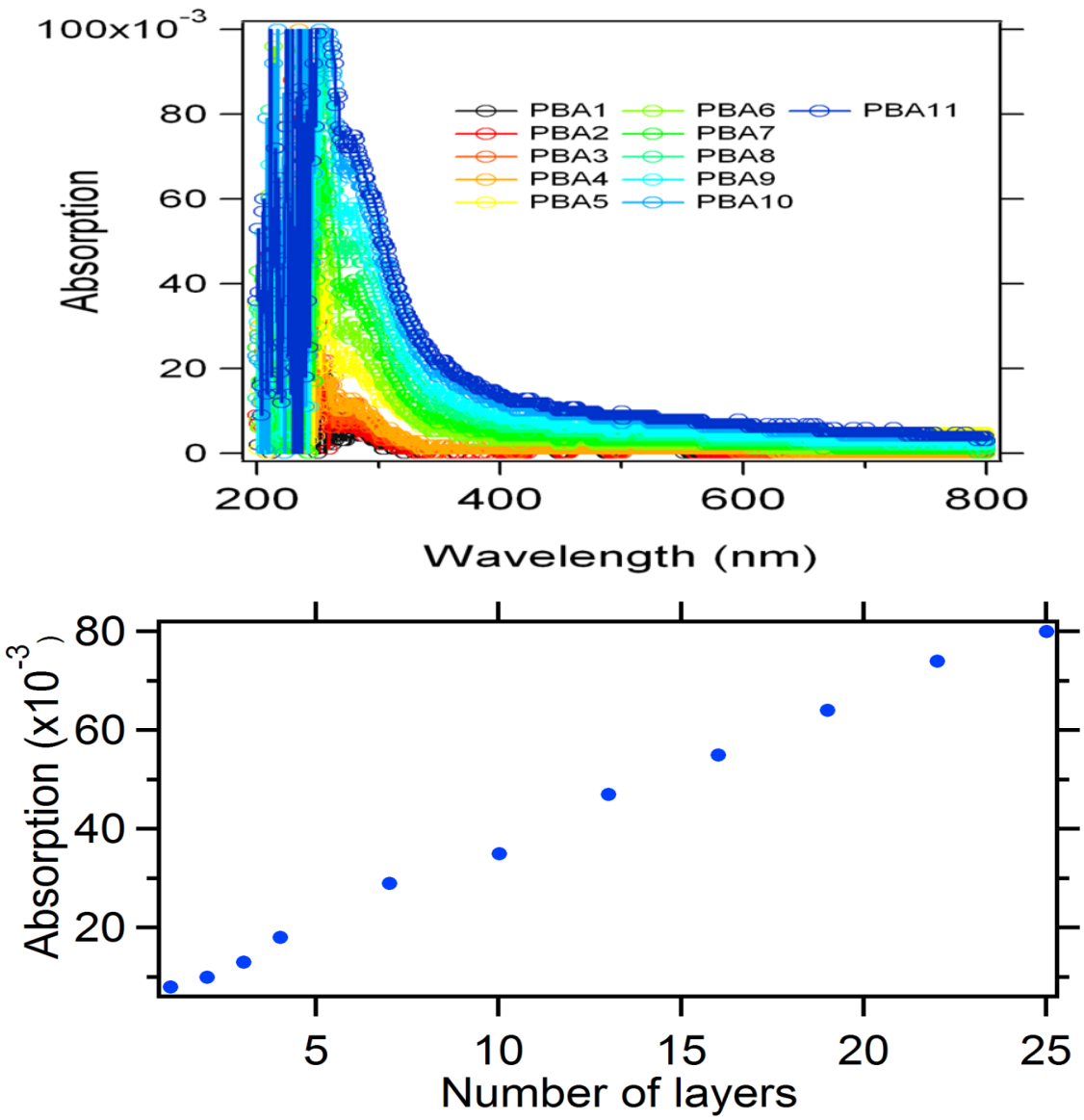

Figure D5.6: *Ultraviolet-visible absorption spectra of sequential deposited PBA (formed as described above) monolayers on a quartz-glass under constant pressure (top) and linear-dependence of the maximum absorption on the number of deposited monolayers of PBA (bottom)*

The morphology and crystallinity of the created material was analyzed using transmission electron microscopy (TEM) and selected area electron diffraction (SAED). Figure D5.7A shows a high magnification TEM micrograph of a single layer of PBA deposited on a silicon nitride window. All bright-field images showed extremely low contrast, which suggests that the PBA films are very thin. This is in support with the expected two-dimensional nature of the films. Additionally, almost all observed flakes were of the same contrast level, indicating uniformity in the sample thickness. A few very dark regions were observed, and are probably the consequence of partial layer collapse or folding. This is likely to have occurred during transfer onto the silicon nitride windows, as the smoothness of the LB isotherms in Figure D5.4 is indicative of the successful formation of a continuous film. The distribution of the nanocrystal areas is shown in inset of Figure D5.7A and reveals that a significant fraction

(over 15%) of the crystals was quite large (over 10,000 nm^2 in area). The average area was around 6,500 nm^2, while the median was around 2,100 nm^2. These roughly correspond to lateral sizes just over 80 nm and 45 nm respectively.

Two selected area electron diffraction patterns are shown in Figure D5.7B. The left side shows a representative pattern formed by diffracting from many flakes (such as that shown in Figure D5.7A), whereas the right side shows a single-crystal pattern from an individual flake. The broad, diffuse rings are due to scattering from the silicon nitride window[209]. This data suggests that each flake is crystalline, although with a random orientation relative to its neighbors, such that a collection of flakes results in a polycrystalline pattern. The tetragonal symmetry is supportive of the expected cubic structure (Figure D5.2).

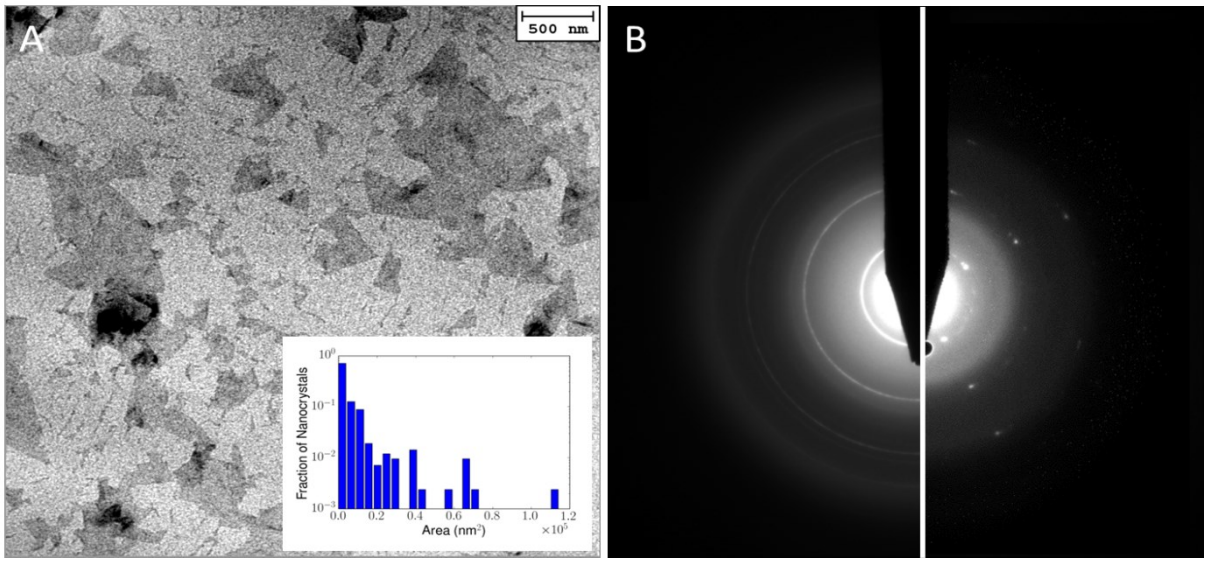

Figure D5.7: *(A) Bright-field transmission electron microscope images of the two-dimensional PBA (formed as described above) deposited on a silicon nitride window (B) selected area electron diffraction patterns revealing polycrystalline (left side) and single crystal (right side) domains*

The widths of the diffraction peaks contain information about structural imperfections in the crystals. For the majority of materials, the most significant contributing factors are the finite size of the crystalline domains and the strain leading to distortions from a perfect crystal structure. These effects can be identified by their different dependencies on the scattering angle, with the peak widths proportional to $1/\cos\theta$ and $\tan\theta$. By analyzing the peaks in the polycrystalline diffraction pattern with a Williamson-Hall plot (Figure A5 in the Appendix), it is determined that the strain is 1.9 % +/- 0.5 %, and the average size is 10.5 ± 2.6 nm. It is important to stress that the size determined by such an analysis cannot be interpreted as the true size of the flakes, but rather corresponds to an effective coherence length of the crystalline domains. It represents a lower bound on the particle size, as is evident from the fact that it is significantly smaller than the flake size observed in the bright-field images. The measured strain is quite large, which is likely due to inaccuracy in determining the peak widths because of their weak intensity and the significant background from the silicon nitride window.

Part E: Appendix

Several subphase and injected tetracyanide concentrations were tested in order to choose the optimal conditions for the performed tests. Beginning from a stable tertacyanide concentration (15mg/8ml) in a water-ethanol solution (1:3), several copper chloride concentrations where tested. The reason for this was that, using the 'inverted 'LB approach and injecting the tetracyanide on an inclined-quartz slide, the formed monolayer, having already been deposited on silicon nitride grids would not give strong diffraction signal on the TEM due to its thinness. Therefore and trying to reduce the signal from the subphase, the concentration of copper chloride had to be reduced to the point where it would not interfere with the received signal of the PBA itself. In order to achieve this, five different copper chloride concentrations were examined: 1 g/l, 0.5g/l, 0.2 g/l, 0.1 g/l and 0.01 g/l and depositions on TEM silicon nitride grids were accomplished. From SAED measurements it turned out that from the concentration of 0.2 g/l and below no actual diffraction signal due to the presence of $CuCl_2$ is observed. For this reason, the concentration of 0.2 g/l was the upper limit of the sub-phase concentration.

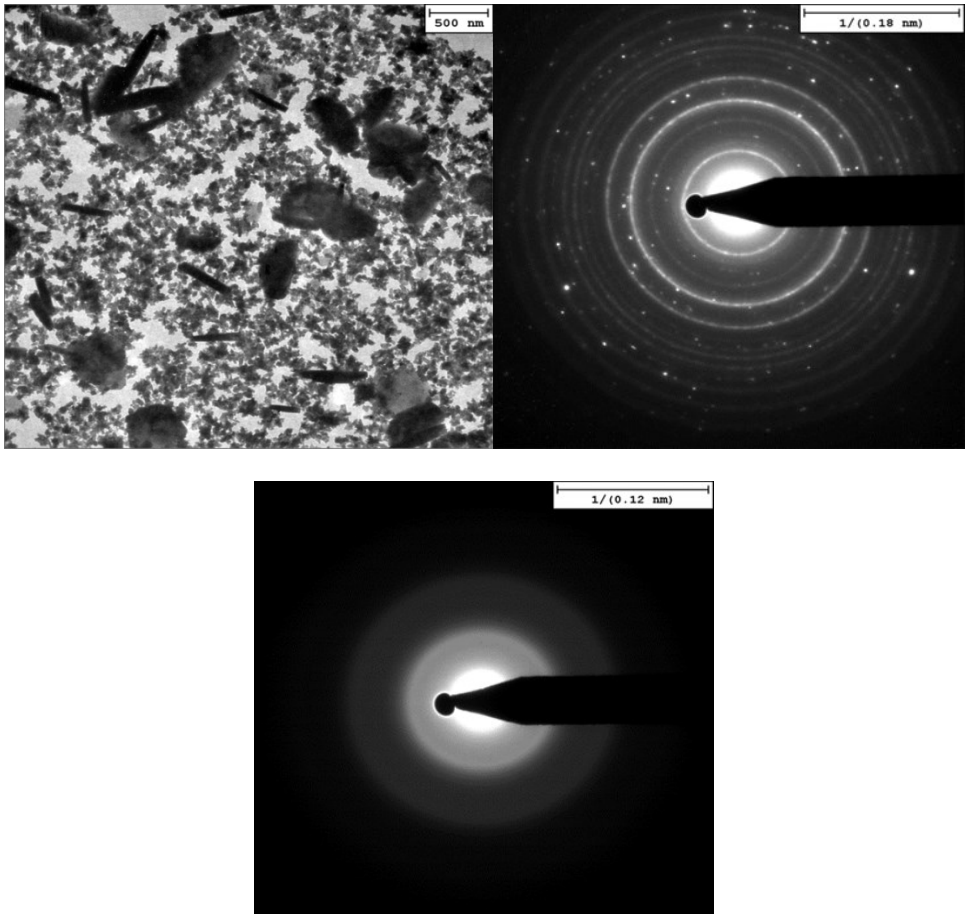

Figure A1: *TEM and SAED images of copper chloride solution with concentration above 0.2g/l; strong diffraction signal that could interfere with PBA's weaker signal (top) and diffraction pattern of copper chloride 0.2g/l where the observed dim rings derive only from the silicon nitride background*

Having chosen the optimal subphase concentration, various concentrations of the injected tetracyanide were tested so as to investigate the effect of tertacyanide concentration on the formed monolayer. Using again the 'inverted' LB and beginning from

closed barriers (90 cm^2) for the above conditions, different concentrations namely C, C/2, C/4, C/8 and C/16 with C being 15mg/8ml as before were examined. The injected volumes were chosen so as to keep the total amount of injected tertacyanide molecules stable for each test. The concentrated results are observed in table A1. As a result, tetracyanide concentration C/8 (0.23mg/ml) resulted in higher differential area, indicating that this should be chosen for the optimized PBA formation. This concentration value along with 0.2g/l concerning the copper chloride subphase would be kept stable for all tests, along with the use of the inclined quartz-glass slide for the 'soft injection'.

Table A1. *Effect of injected tertacyanide concentration on the final LB-area coverage*

Concentration of injected tetracyanide (mg/ml)	Injected volume (ml)	Differential LB-area ΔA (cm^2)
C	0.4	202
C/2	0.8	233
C/4	1.6	275
C/8	3.2	316
C/16	6.4	208

Figure A2 exhibits the change of surface pressure and LB-area during the sequential depositions of the formed monolayer on a quartz-glass substrate in order to measure the UV absorption. All depositions were performed under stable pressure (3mN/m) and after injection of 600 μl of tetracyanide. After each deposition on the quartz glass a part of the monolayer leaves the surface (steps of the red line), therefore the LB-barriers close to restore the decreased pressure and the total area-value becomes less. In the end the barriers cannot move anymore and the pressure stabilizes (black line).

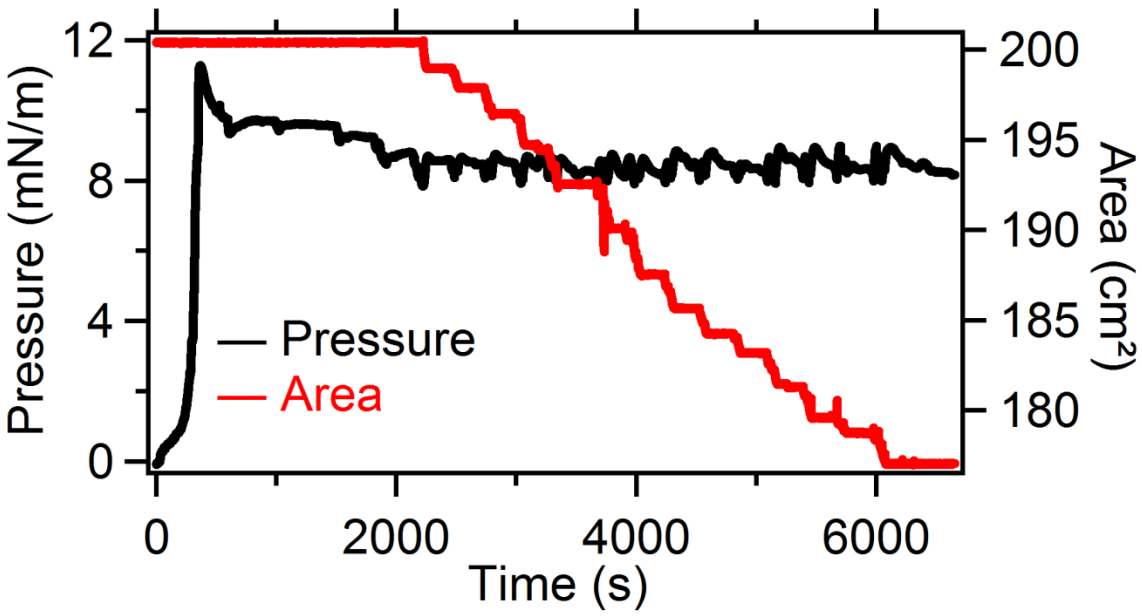

Figure A2: *Sequential deposition for ultraviolet-visible absorption spectroscopy test; after each deposition on the quartz glass a part of the monolayer leaves the surface (steps of the red line), therefore the LB-barriers close to restore the decreased pressure and the area-value becomes less. In the end the barriers cannot move anymore and the pressure stabilizes.*

In addition to the above and although the formed PBA appears to be stable enough as the time passes, the stability of the PBA monolayer as a separate test had to be examined and evaluated. Therefore, another test was performed injecting 600 microliters of the tetra-cyanide. The procedure which was followed was in this case the classic LB (beginning from totally open barriers) and included compression and expansion cycles in order to investigate if the system would reach the same high and low pressure values after every cycle. In this case and after ten cycles, the system exhibits a smooth, hyperbolic pressure decrease, which indicates that the formed PBA monolayer is rather stable with time, while slowly collapses after every compression-expansion cycle (Figure A3) and leads to a final 50% lower maximum pressure than the initially reached value during the first cycle.

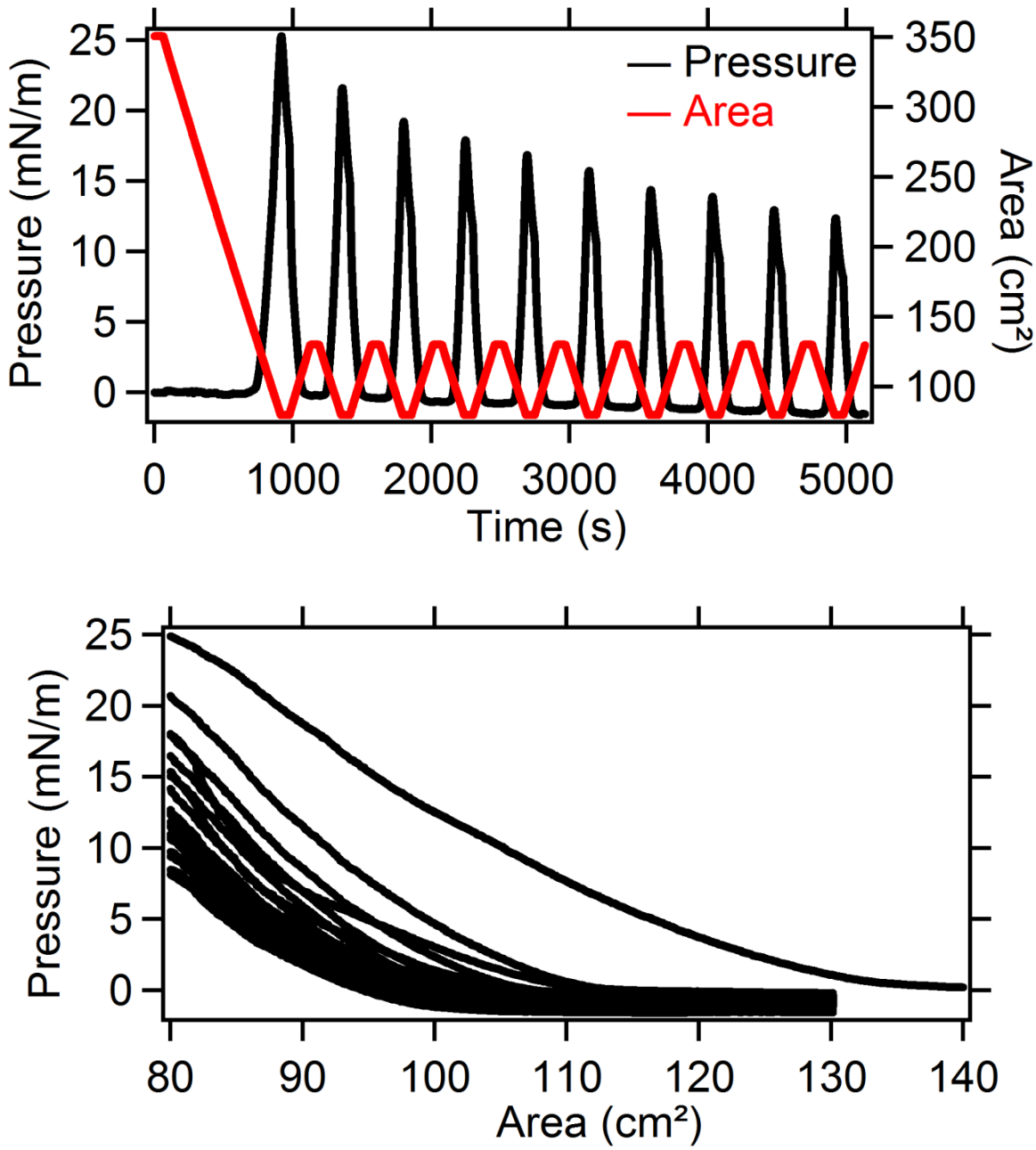

Figure A3: *Stability test of the formed as above thin film after 10 cycles of compression-expansion; after every cycle of compression-decompression the final highest pressure appears to decrease regarding the same differential area (minimum and maximum area value) for every cycle, demonstrating an average 50% decrease of the initial value after completion of the procedure.*

Crystallite Properties

The widths of the diffraction peaks contain information about structural imperfections in the crystal. Here the "width" β of a peak centered at 2θ is taken to be the integral breadth:

$$\beta(2\theta) = \frac{1}{I_{max}(2\theta)} \int_{2\theta-\epsilon}^{2\theta+\epsilon} I(2\theta)\, d(2\theta)$$

where $I(2\theta)$is the radial diffraction pattern and ϵ is chosen to encompass the entire peak. There are two significant factors contributing to this width (after instrument broadening has been accounted for): the finite size of the nano-crystals, and the strain leading to distortions from a perfect crystal structure. The width induced by the former is described by the Scherrer equation[232]

$$\beta_{size}(2\theta) = \frac{K\lambda}{L\cos\theta}$$

where $K = 2\sqrt{\ln 2/\pi} \approx 0.94$ for cubic crystals (which the diffraction suggests PBA is), and L is the average "size" of the nanocrystallite. The width induced by microstrain in the crystal is given by

$$\beta_{strain}(2\theta) = 2\xi \tan\theta$$

where ξ is the integral breadth of the distribution $p(e)$, where $p(e)de$ is the fraction of the crystal with tensile strain between e and $e + de$[233]. The total peak shape is a convolution of the line-shape from both the size and strain effects. Both Lorentzian and Gaussian functions were used to fit the diffraction peaks, and it was found that a Lorentzian line-shape resulted in minimal residuals. In this case, the total integral width is

$$\begin{aligned}\beta(2\theta) &= \beta_{size}(2\theta) + \beta_{strain}(2\theta) \\ &= \frac{K\lambda}{L\cos\theta} + 2\xi\tan\theta\end{aligned}$$

Thus a plot of $\sin\theta/\lambda$ versus $\beta\cos\theta/\lambda$, as suggested by Williamson and Hall[234] and shown in Figure A5, is linear with a slope of 2ξ and an intercept of K/L. In the main text, the convention that the strain is quoted as ξ in percent was followed.

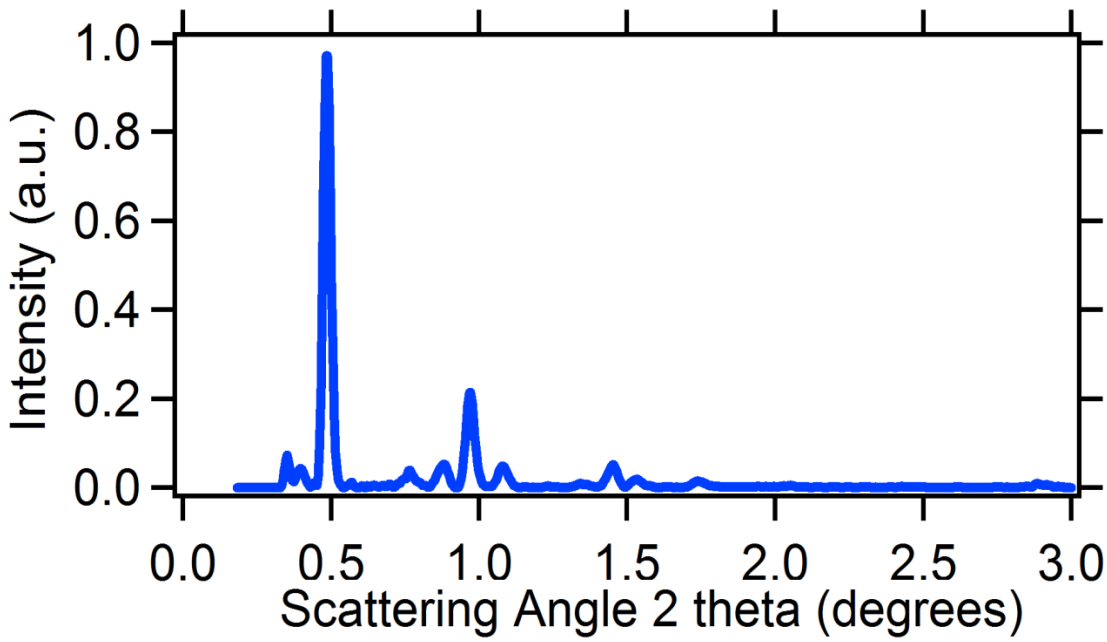

Figure A4*: Radial diffraction pattern of two-dimensional PBA (background contributions from the substrate and inelastic scattering were removed)*

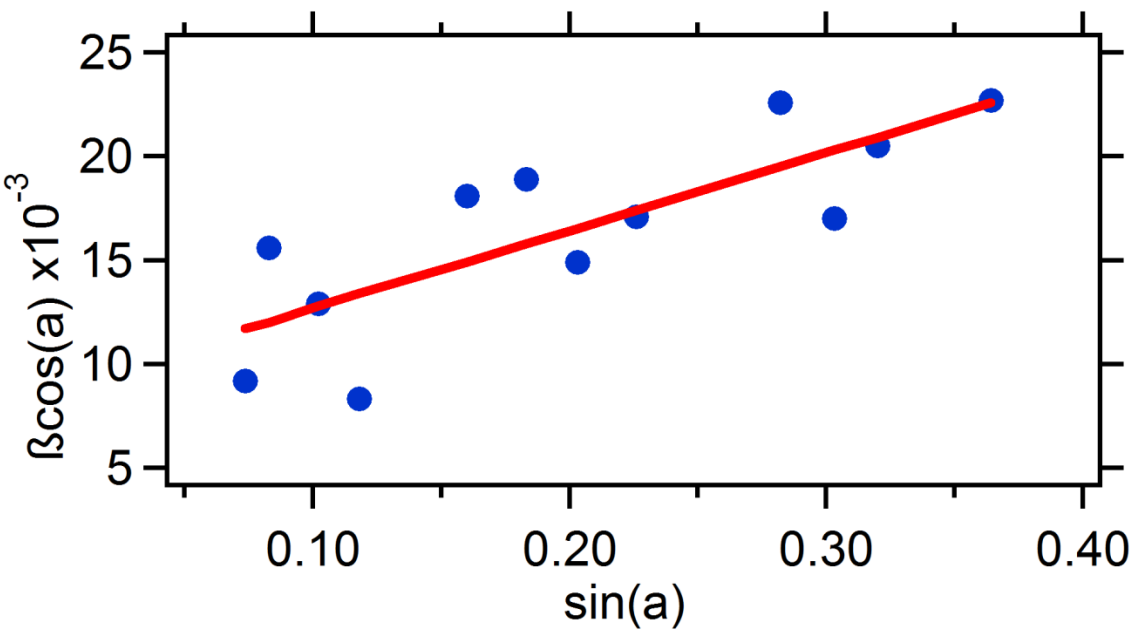

Figure A5*: Williamson-Hall plot of sin(a) versus cos(a) revealing the contribution of the crystallite size and strain to the integral width (ß) of the diffraction peaks where* ***a=ϑ/λ (Å^{-1})***

Part F:

Conclusions-future plans

The major aim of this dissertation was the formation and production of novel nano-structured hybrid materials based on carbon. Using the bottom-up CCVD synthetic method, the control of the products in nanoscale was possible. Using this method, one-dimensional hybrid superconducting and magnetic nanowires and nanorods were successfully developed. Furthermore, graphene oxide was produced beginning for the first time from 'Kish' graphite and monolayers were formed using the Langmuir-Blodgett technique. Finally, Prussian Blue Analogues of reduced dimensionality were produced employing for the first time the 'inverted' Langmuir method.

More specifically, in the first part of this dissertation superconductive tin nanowires were successfully created in the interior of carbon nanotubes using the CCVD method. The role of tin-containing catalysts [metallic tin (Sn), tin oxide (SnO) and tin dioxide (SnO_2)], as well as the effect of the reaction time and temperature during the CCVD in the quality and quantity of the produced nanowires were investigated in details. The final products were characterized by a combination of analytical techniques such as X-Ray Diffraction, Raman Spectroscopy, Differential Thermal and Thermogravimetric Analyses (DTA/TG), TEM and SEM Microscopies and Mössbauer spectroscopy. Electron spectroscopy measurements showed that the produced nanowires covered with nanotubes exhibit a diameter between 20 and 40 nm and length up to 5 μm. In the same images, unreacted catalyst particles (SnO_2) are also observed. The XRD patterns show the characteristic peaks of metallic tin (β-Sn) encapsulated in carbon nanotubes, as well as the reflections of tin dioxide (unreacted catalyst). However, after 90 minutes of acetylene flow the characteristic peaks of tin dioxide in the XRD patterns are almost absent, which leads to the conclusion that all SnO_2 has reacted and lies in the form of metallic tin inside carbon nanotubes. In the case of using SnO as catalyst, the presence of SnO_2 is justified if one takes into account the disproportionation of SnO at temperatures above 500°C which yields equimolar quantities of β-Sn and SnO_2 according to the reaction: $2SnO \rightarrow Sn + SnO_2$. This phenomenon leads to products of carbon nanotubes filled partially with metallic tin compared to the samples produced using SnO_2 as catalyst, where filling is more continuous. This conclusion was in agreement with Mössbauer-effect spectral data, which indicated the existence of two quadruplets corresponding to the SnO_2 and β-Sn for the samples prepared using SnO and SnO_2 as catalysts. Notably, the SnO_2/ β-Sn percent ratio was found to be 0.59 and 1.00 in Sn@CNTs over SnO_2 and SnO respectively, an issue explained by the disproportionation of SnO as mentioned above. Considering the effect of temperature, using SnO_2 as catalyst, the optimal temperature at which tin dioxide peaks are absent seems to be 900°C, while in the case of SnO the same phenomenon is observed at lower temperature (800°C). Concerning the quality of the outer carbon nanotubes surrounding metallic tin nanowires by the use of Raman spectroscopy, the I_D/I_G ratio of all samples was calculated. The ratio ranges between 0.77 and 0.90, which confirms the fine overall quality of the produced CNTs. The TGA analysis indicated that the produced Sn@CNTs were formed at a yield around

11% w/w. Finally, an 80% increase in Vickers hardness of Sn@CNT compared to the pure metallic tin was observed indicating reinforcement of metallic tin due to the presence of carbon nanotubes.

Another goal of this dissertation was the growth of tin nanowires enriched with lead and being encapsulated in carbon nanotubes (SnPb@CNTs) using the CCVD method. Nanowires growth was accomplished on a tin-lead catalytic system, which was stabilized on a sodium chloride substrate and using acetylene gas as precursor carbon source. The effect of the reaction time (different times of acetylene flow) on the quality and quantity of the formed carbon nanotubes was investigated. In order to remove the inactive substrate (NaCl) two procedures were followed: one which included *fast cooling* directly taking the product out of the furnace at 350° and dipping it in a beaker filled with water and one *slow cooling* in room temperature which included afterwards removal of NaCl using sequential washings. As previously mentioned, lead was used due to its higher critical temperature than that of tin and is therefore expected to increase the critical temperature of the alloy. Final products were characterized by X-Ray Diffraction, Raman Spectroscopy, Transmission Electron and Scanning Electron Microscopies, Thermal Analysis (DTA/TGA), Energy Dispersive X-ray Spectroscopy (EDAX), Sn-Mössbauer spectroscopy and SQUID. From the XRD patterns the existence of the characteristic β-Sn, which is encapsulated inside carbon nanotubes as well as the successful NaCl removal after washing is confirmed. The SEM and TEM images showed that the nanotubes exhibit a diameter that ranges from 46.9 to 181 nm and length up to 5μm. As it can be observed from the TEM images, most of carbon nanotubes are fully filled with tin-lead nanowires. There are certain regions though where carbon nanotubes are partially filled. All the observed final edges (tips) of the tin-lead nanowires are totally covered by nanotubes shell, a fact that indicates that nanowires are protected in every spot by atmospheric oxidation and because of this they can stay in the air for a long time. Thermal analysis showed that the produced nanotubes are produced at a yield 9-10%w/w. From the EDAX spectrum it was estimated that the ratio tin to lead is 22:1. Raman shifts confirmed the fine quality of carbon nanotubes as the I_D/I_G ratio for all samples ranges between 0.88 and 0.92. From the I_D/I_G ratios it was observed that the quality of the produced carbon nanotubes is not affected by the type of the cooling process (fast or slow). This led to the conclusion that using less cooling stages (fast cooling), carbon nanotubes of the same quality are formed. From the analysis of the magnetization measurements, it follows that the superconductivity temperature (T_C) is around 7.05 K and the critical magnetic field (HC) is 0.095 T (950 Gauss) that is due to a lead-rich phase. This is significant because now and in order to realize superconducting state, there will no longer be needed to pump above liquid Helium. The Mössbauer spectra indicated the presence of two Sn containing phases, corresponding to β-Sn and SnO_2, as well as a third Sn-containing phase. This fact strongly suggests that there is an unknown Sn-phase, which consists of tin atoms being in contact with lead atoms forming a new layer, a conclusion which was remarkably supported by

STEM-EDX. Additionally, STEM-EDX revealed that the diffraction patterns of the tip crystals fit Pb crystal structure, and also that carbon nanotubes are filled with multi-crystals, composed of SnO_2, Sn and Pb. Finally, it confirmed the distribution of Sn, O and Pb and the existence of a new Sn-dopped Pb phase.

A third part of this dissertation was to produce carbon nanotubes encapsulating manganese-bismuth nanorods, using MnBi alloy impregnated on NaCl as catalyst. The impact of reaction time and temperature was studied using the CCVD method. The final materials were characterized using the X-Ray diffraction (XRD), Raman Spectroscopy, VSM, DTA/TG measurements, SEM and TEM microscopies. Observation of the Raman spectra showed that the ratio I_D/I_G which was calculated for all sample was found to range between 0.91 and 0.98, confirming this way the fine quality of the produced carbon nanotubes. According to XRD patterns, the existence of metallic bismuth and manganese phases, as well as alloy and oxide phases of them, which was expected to be present inside nanotubes, is confirmed. Furthermore, after sodium chloride removal, the characteristic NaCl (which was used as catalyst) peaks are absent. Thermal analysis data exhibited that the produced MnBi nanorods covered by carbon nanotubes gave a yield around 10%w/w. SEM images indicated that the diameter of the nanotubes ranges between 360 and 640 nm. Despite of that there are some nanotubes with a much lower diameter, ranging from 25 to 108 nm. From the TEM images nanowires of diameter between 150 to 485 nm were observed. According to VSM measurements, it was observed that by increasing reaction time, the magnetic signal is enhanced, due to the fact that as the reaction time increases, carbon nanotubes become more filled with the MnBi ferromagnetic alloy.

The next two parts of the dissertation were accomplished in the Center for Free Electron Laser Science (CFEL) facility of Deutsches Elektronen Synchrotron (DESY), Max Plank Institute, Hamburg. Starting from 'Kish'-graphite, graphene oxide was produced using the Staudenmaier oxidation method in order to form 'Kish'-GO flakes of few micrometers that were studied using the Langmuir-Blodgett technique (LB). Injecting different volumes of different initial 'Kish'-GO concentrations, several isotherms (Π-a) were obtained, indicating that the best 'Kish'-GO concentration to give the expected pressure-area dependence and for low injected volumes would be 0.5 mg/ml, at slow injection rate and with the use of an inclined quartz-glass slide, partially submerged in the subphase. All concentrations and injected volumes showed during TEM investigation fine diffraction, proving the crystallinity of 'Kish'-GO, ranging from multi-crystal monolayer (clear ring patterns) to dotted rings. This is indicative of multi-crystaline material that consists of differently oriented crystals, also containing single-crystalline domains (dotted ring patterns taken from the thinner TEM areas, at 0.5 mg/ml). The adequately fine quality of the produced Graphene Oxide rendered it to be a good candidate for potential future

electron diffraction experiments which concern the reduction of GO to graphene as well as IR pump-probe studies.

The final part of the dissertation regarded the development of a Prussian Blue Analogue (PBA) beginning from Potassium Tetra-cyano Platinate (II) hydrate and an aqueous solution of copper chloride as a sub-phase with the first being injected on the second in order to form a PBA 2-D network on the copper chloride-air interface through a double cationic reaction. This set-up was accomplished using the Langmuir-Blodgett method. In this thesis for the first time the use of the 'inverted' LB technique is reported. X-Ray photo-electron spectroscopy results demonstrated that a covalently bonded network was created using an on-surface reaction, and the observed product was indeed PBA as expected. Side products of the reaction were not present on the surface proving that only reacted material forms a floating film. Several injected volumes of different concentrations were investigated, resulting in various isotherms. The favorable tetra-cyanide concentration appeared to be C/8, with C being 15mg/8ml in a water-ethanol solution at 1:3 ratio, while the desired concentration of the sub-phase was chosen to be 0.2g/l. Stability tests were performed using the LB-method which indicated that the formed monolayer was stable enough after compressing and de-compressing several times. Ultraviolet measurements were performed after sequential depositions on a piece of quartz glass with a linear increase of maximum UV-absorption as a function of the thickness to be observed, demonstrating the viability of multilayer deposition. Finally, TEM measurements were performed which showed that the surface would be covered around 30-40% of the formed PBA. What is more, diffraction was obtained showing that the produced material as a monolayer was composed of multi-crystals, awaits though to be further investigated whether it is truly a multi-crystal monolayer or it forms nano-crystals of random dimensions as well. The performed measurements demonstrate though, as proof of principle, that it is possible to synthesize monolayers of PBA at the air-water interface by the 'inverted' LB technique.

As far as Sn@CNTs products are concerned, superconductivity measurements through SQUID should be conducted so as to investigate the optimal conditions of their production (reaction temperature and time). Considering the produced SnPb@CNTs, further studies on lithium batteries are going to be performed, as well as investigation of other tin-lead alloys. Furthermore, more alloys of different percentage of manganese-bismuth are to be explored, aiming at studying the effect of higher than 10% w/w manganese content on the magnetization of the alloys. Additionally, the produced 'Kish'-GO forms a fine candidate for future electron diffraction experiments, which include GO-reduction to graphene, as well as Infra-red pump-probe studies. Finally, the produced PBA requires to be investigated by the use of AFM in order to determine the thickness of the formed monolayer and realize its real 2D character, also using STM as a complementary technique and future electron diffraction study so as to explore potential dynamic phenomena that it might demonstrate.

Part G: Bibliography

[1] D. Gournis, Materials Chemistry-Nanoporous and Phyllomorphous Materials, University Printing Shop, Ioannina (2008)

[2] F. Alikarides, Introduction to Organic Chemistry, available at: http://panacea.med.uoa.gr/topic.aspx?id=928 (2008)

[3] K. Tsipis, P. Palamitzoglou, D. Derpanis & group of chemists, Chemistry Lexicon, Malliaris Education Publications, Thessaloniki (2003)

[4] S. Iijima, "Direct observation of the tetrahedral bonding in graphitized carbon black by high resolution electron microscopy". Journal of Crystal Growth 50 (3): 675 (1980)

[5] E. Diamanti, Novel nanoporous graphene-based materials, characterization and study of properties, Doctoral Thesis, Department of Materials Science and Engineering, University of Ioannina (2014)

[6] A. Andreou, Hybrid derivatives of carbon nanotubes: synthesis-characterization, BSc Thesis, Department of Materials Science and Engineering, University of Ioannina (2012)

[7] E. Mamaki, In situ growth of MnBi nanowires inside carbon nanotubes by the use of Catalytic Chemical Vapor Deposition method, Department of Materials Science and Engineering, University of Ioannina (2012)

[8] E. Latifi, Growth of Sn nanowires enriched with Pb inside Carbon Nanotubes, Department of Materials Science and Engineering, University of Ioannina (2012)

[9] Nanowire (Electronic form) available at: http://en.wikipedia.org/wiki/Nanowire (2012)

[10] X. Wang, Q. Li, J. Xie, Z. Jin, J. Wang, Y. Li, K. Jiang, S. Fan, "Fabrication of Ultralong and Electrically Uniform Single-Walled Carbon Nanotubes on Clean Substrates". Nano Letters 9 (9): 3137–3141 (2009)

[11] E. Babavea, S. I. Bibli, A. Tsantili Kakoulidou, Nanomaterials: Fullerenes and Carbon Nanotubes. Structure, Physical and Chemical Properties-Biological and Healing Applications, Pharmaceutics, vol. 1, No 21, p. 10-21 (2008)

[12] SWeNT, Structure and Applications of Single-Walled Carbon Nanotubes (SWCNTs) Synthesized Using the CoMoCAT® Method, (electronic) available at: http://www.swentnano.com/tech/docs/Spotlight_Article_Sigma_DrResasco.pdf

[13] J. W. Wildoer, L. C. Venema, A. G. Rinzler, R. E. Smalley & C. Dekker, Electronic structure of atomically resolved Carbon nanotubes, Nature, vol. 391, p. 59 (1998)

[14] S. Nitodas, Methods development for the production of Carbon Nanotubes, E&T, vol. 20, September, p. 26 (2006)

[15] G. Rinzler, J. Liu, H. Dai, P. Nikolaev, B. C. Huffman and F. J. Rodriguez-Macias, Appl. Phys. A, 67, p. 29, (1998)

[16] M. Kumar, Carbon Nanotube Synthesis and Growth Mechanism-Carbon Nanotubes - Synthesis, Characterization, Applications, July, pp. 155-156, (2011)

[17] B. Bogdanovic, M. Schwickardi, Appl. Phys. A 72, p. 221 (2001)

[18] Science, Apr 27, vol 292, no. 5517, p. 706 (2001)

[19] I. W. Chiang, B. E. Brinson, R. E. Smalley, J. L. Margrave, and R. H. Hauge, Purification and Characterization of Single-Wall Carbon Nanotubes J. Phys. Chem. B, 105, 1157-1161 (2001)

[20] D. Kastanis, Synthesis and characterization of reinforcing nano-structures and polymer nano-composite materials based on carbon nanotubes, Diploma thesis, University of Patras [21] P.G.Collins, M.S. Arnold and P.Avouris, Science 292 706 (2001)

[21] IBM Researchers Demonstrate New Approach to Carbon Nanotechnology (electronic form) available at: www.azonano.com/news.aspx?newsID=25823

[22] I. Georgiadis, Carbon nanotubes: Synthesis, structure and properties, Diploma thesis (2010)

[23] A. Bezryadin, C.N. Lau, M. Tinkham, Quantum suppression of superconductivity in ultrathin nanowires, Nature, 404, 971 (2000)

[24] G. Ioannatos, Study of carbon nanotubes as hydrogen storage media, Doctoral thesis, Patras (2009)

[25] A. Hirsch, O. Vostrowsky, Functionalization of Carbon Nanotubes, Top Curr Chem 245: 193–237 (2005)

[26] M. S. Dresselhaus, Y. M. Lin, O. Rabin, M. R. Black, S. B. Cronin, G. Dresselhaus, Overview of Bismuth Nanowires for Thermoelectric Applications, p.22

[27] I. Panagiotopoulos, Magnetic Materials, G. A. Pnevmatikos Publications, Ioannina (2010)

[28] J. Bruckbauer, Growth and Properties of Semiconductor Nanowires, St. Petersburg, Russia (2008)

[29] FET (electronic form) available at: http://en.wikipedia.org/wiki/Field-effect_transistor

[30] Nanowire battery (electronic form) available at http://en.wikipedia.org/wiki/Nanowire battery

[31] S. Iijima, Helical microtubules of graphitic carbon, Nature, 354, 56-58 (1991)

[32] V. N. Popov, Materials Science & Engineering Reports, 43, 61 (2004)

[33] M. Terrones, Annual Review of Materials Research, 33, 419 (2003)

[34] R. Andrews, D. Jacques, D. L. Qian, T. Rantell, Accounts of Chemical Research, 35, 1008 (2002)

[35] M. Ouyang, J. L. Huang, C. M. Lieber, Accounts of Chemical Research, 35, 1018 (2002)

[36] P. Avouris, Accounts of Chemical Research, 35, 1026 (2002)

[37] H. J. Dai, Accounts of Chemical Research, 35, 1035 (2002)

[38] O. Zhou, H. Shimoda, B. Gao, S. J. Oh, L. Fleming, G. Z. Yue, Accounts of Chemical Research, 35, 1045 (2002)

[39] R. H. Baughman, A. A. Zakhidov, W. A. de Heer, Carbon Nanotubes – The Route Towards Applications, Science, 297, 787-792 (2002)

[40] C. N. R. Rao, B. C. Satishkumar, A. Govindaraj, M. Nath, Nanotubes, Chemphyschem, 2, 78 (2001)

[41] M. S. Dresselhaus, M. Endo, Carbon Nanotubes, Vol. 80, pp. 11, (2001)

[42] S. Subramoney, Adv. Mater., 10, 1157 (1998)

[43] P. Serp, M. Corrias, P. Kalck, Carbon nanotubes and nanofibers in catalysis, Applied Catalysis a-General, 253, 337 (2003)

[44] G. Mestl, N. I. Maksimova, N. Keller, V. V. Roddatis, R. Schlogl, Angewandte Chemie-International Edition, 40, 2066 (2001)

[45] N. F. Goldshleger, Fullerene Science and Technology, 9, 255 (2001)

[46] M. W. Wang, F. Y. Li, N. C. Peng, New Carbon Materials, 17, 75 (2002)

[47] W. Z. Li, C. H. Liang, J. S. Qiu, W. J. Zhou, H. M. Han, Z. B. Wei, G. Q. Sun, Q. Xin, Carbon nanotubes as support for cathode catalyst of a direct methanol fuel cell, Carbon, 40, 791 (2002)

[48] B. Coq, J. M. Planeix, V. Brotons, Synthesis of carbon nanotubes with Ni/CNTs catalyst - Springer, Applied Catalysis a-General, 173, 175 (1998)

[49] M. Cadek, J. N. Coleman, K. P. Ryan, V. Nicolosi, G. Bister, A. Fonseca, J. B. Nagy, K. Szostak, F. Beguin, W. J. Blau, Reinforcement of Polymers with Carbon Nanotubes: The Role of Nanotube Surface Area, Nano Lett., 4, 353 (2004)

[50] W. De Zhang, L. Shen, I. Y. Phang, T. X. Liu, Carbon Nanotubes Reinforced Nylon-6 Composite Prepared by Simple Melt-Compounding, Macromolecules, 37, 256 (2004)

[51] S. H. Qin, D. Q. Oin, W. T. Ford, D. E. Resasco, J. E. Herrera, Polymer Brushes on Single-walled Carbon Nanotubes by Atom Transfer Radical Polymerization of n-Butyl Methacrylate, J. Am. Chem. Soc., 126, 170 (2004)

[52] A. B. Dalton, S. Collins, J. Razal, E. Munoz, V. H. Ebron, B. G. Kim, J. N. Coleman, J. P. Ferraris, R. H. Baughman, Continuous carbon nanotube composite fibers: properties, potential applications, and problems, J. Mater. Chem., 14, 1 (2004)

[53] X. F. Zhang, T. Liu, T. V. Sreekumar, S. Kumar, V. C. Moore, R. H. Hauge, R. E. Smalley, Poly(vinyl alcohol)/SWNT Composite Film, Nano Lett., 3, 1285 (2003)

[54] A. B. Dalton, S. Collins, E. Munoz, J. M. Razal, V. H. Ebron, J. P. Ferraris, J. N. Coleman, B. G. Kim, R. H. Baughman, Super-tough carbon-nanotube fibres, Nature, 423, 703 (2003)

[55] C. Liu, Y. Y. Fan, M. Liu, H. T. Cong, H. M. Cheng, M. S. Dresselhaus, Hydrogen storage in single-walled carbon nanotubes at room temperature, Science, 286, 1127 (1999)

[56] A. C. Dillon, K. M. Jones, T. A. Bekkedahl, C. H. Kiang, D. S. Bethune, M. J. Heben, Storage of hydrogen in single-walled carbon nanotubes, Nature, 386, 377 (1997)

[57] L. Schlapbach, A. Zuttel, Hydrogen-storage materials for mobile applications, Nature, 414, 353 (2001)

[58] A. D. Lueking, R. T. Yang, N. M. Rodriguez, R. T. K. Baker, Hydrogen Storage in Graphite Nanofibers: Effect of Synthesis Catalyst and Pretreatment Conditions, Langmuir, 20, 714 (2004)

[59] M. Becher, M. Haluska, M. Hirscher, A. Quintel, V. Skakalova, U. Dettlaff-Weglikovska, X. Chen, M. Hulman, Y. Choi, S. Roth, V. Meregalli, M. Parrinello, R. Strobel, L. Jorissen, M. M. Kappes, J. Fink, A. Zuttel, I. Stepanek, P. Bernierg, Hydrogen storage in carbon nanotubes, Comptes Rendus Physique, 4, 1055 (2003)

[60] M. Hirscher, M. Becher, Hydrogen Storage in Carbon Nanotubes, J. Nanosci. Nanotech., 3, 3 (2003)

[61] Z. Q. Yang, Z. L. Xie, Y. S. He, Hydrogen storage in new nanostructured carbon materials, New Carbon Materials, 18, 75 (2003)

[62] P. Sudan, A. Zuttel, P. Mauron, C. Emmenegger, P. Wenger, L. Schlapbach, Physisorption of hydrogen in single-walled carbon nanotubes, Carbon, 41, 2377 (2003)

[63] R. G. Ding, G. Q. Lu, Z. F. Yan, M. A. Wilson, Recent advances in the preparation and utilization of carbon nanotubes for hydrogen storage, J. Nanosci. Nanotech., 1, 7 (2001)

[64] M. Monthioux, Filling single-wall carbon nanotubes, Carbon, 40, 1809 (2002)

[65] S. Iijima, T. Ichihashi, Single-shell carbon nanotubes of 1-nm diameter, Nature, 363, 603 (1993)

[66] D. S. Bethune, C. H. Kiang, M. S. Devries, G. Gorman, R. Savoy, J. Vazquez, R. Beyers, Cobalt-catalysed growth of carbon nanotubes with single-atomic-layer walls, Nature, 363, 605 (1993)

[67] G. L. Che, B. B. Lakshmi, E. R. Fisher, C. R. Martin, Carbon nanotube membranes for electrochemical energy storage and production, Nature, 393, 346 (1998)

[68] Y. N. Xia, P. D. Yang, Y. G. Sun, Y. Y. Wu, B. Mayers, B. Gates, Y. D. Yin, F. Kim, Y. Q. Yan, One-dimensional nanostructures: synthesis, characterization, and applications, Adv. Mater., 15, 353 (2003)

[69] Y. Y. Wu, P. D. Yang, Melting and welding semiconductor nanowires in nanotubes, Adv. Mater., 13, 520 (2001)

[70] A. Loiseau, H. Pascard, Synthesis of long carbon nanotubes filled with Se, S, Sb and Ge by the arc method, Chem. Phys. Lett., 246 (1996)

[71] Y. L. Hsin, K. C. Hwang, F. R. Chen, J. J. Kai, Production and in-situ Metal Filling of Carbon Nanotubes in Water, Adv. Mater., 13, 830 (2001)

[72] P. M. Ajayan, T. W. Ebbesen, T. Ichihashi, S. Iijima, K. Tanigaki, H. Hiura, Opening carbon nanotubes with oxygen and implications for filling, Nature, 362, 522 (1993)

[73] K. Hernadi, A. Fonseca, J. B. Nagy, A. Fudala, D. Bernaerts, I. Kiricsi, Catalytic production of carbon nanofibers over iron carbide doped with Sn^{2+}, Appl. Catalysis a-General, 228, 103 (2002)

[74] W. K. Hsu, M. Terrones, H. Terrones, N. Grobert, A. I. Kirkland, J. P. Hare, K. Prassides, P. D. Townsend, H. W. Kroto, D. R. M. Walton, Electrochemical formation of novel nanowires and their dynamic effects, Chem. Phys. Lett., 284, 177 (1998)

[75] X. P. Gao, Y. Zhang, X. Chen, G. L. Pan, J. Yan, F. Wu, H. T. Yuan, D. Y. Song, Carbon nanotubes filled with metallic nanowires, Carbon, 42, 47 (2004)

[76] J. S. Lee, G. H. Gu, H. Kim, J. S. Suh, I. Han, N. S. Lee, J. M. Kim, G. S. Park, Well-ordered Co nanowire arrays for aligned carbon nanotube arrays, Synthetic Metals, 124, 307 (2001)

[77] P. M. Ajayan, C. Colliex, J. M. Lambert, P. Bernier, L. Barbedette, M. Tence, O. Stephan, Growth of manganese filled carbon nanofibers in the vapor phase, Phys. Rev. Lett., 72, 1722 (1994)

[78] W. Y. Choi, J. W. Kang, H. J. Hwang, Structures of ultrathin copper nanowires encapsulated in carbon nanotubes, Phys. Rev. B, 68 (2003)

[79] R. Che, L. M. Peng, Q. Chen, X. F. Duan, B. S. Zou, Z. N. Gu, Controlled synthesis and phase transformation of ferrous nanowires inside carbon nanotubes, Chem. Phys. Lett., 375, 59 (2003)

[80] Manoj K. Singh, E.Titus, D.S.Misra and F.LeNormand, Ni and Ni/Pt filling in multi walled carbon nanotubes, J. Nanosci. Nanotech., 3, 165 (2003)

[81] G. Y. Zhang, E. G. Wang, Cu-filled carbon nanotubes by simultaneous plasma-assisted copper incorporation, Appl. Phys. Lett., 82, 1926 (2003)

[82] N. Grobert, M. Terrones, A. J. Osborne, H. Terrones, W. K. Hsu, S. Trasobares, Y. Q. Zhu, J. P. Hare, H. W. Kroto, D. R. M. Walton, Thermolysis of C-60 thin films yields Ni-filled tapered nanotubes, Appl. Phys. a-Material Science & Processing, 67, 595 (1998)

[83] F. Okuyama, T. Hayashi, Y. Fujimoto, Formation of carbon nanotubes and their filling with metallic fibers on ion-emitting field anodes , J. Appl. Phys., 84, 1626 (1998)

[84] F. Okuyama, I. Ogasawara, Chromium-containing metallic fibers confined within carbon nanotubes: Possibility of template-mediated crystal growth, Appl. Phys. Lett., 71, 623 (1997)

[85] C. Jo and J. Lee, Magnetism of Fe, Co, and Ni nanowires encapsulated in carbon nanotubes, J. Magn. and Magn. Mater. 320, 3256-3260 (2008)

[86] Z. W. Pan, S. Dai, D. B. Beach, N. D. Evans, D. H. Lowndes, Gallium-mediated growth of multiwall carbon nanotubes, Appl. Phys. Lett., 82, 1947 (2003)

[87] Y. H. Gao, Y. Bando, D. Golberg, Melting and expansion behavior of indium in carbon nanotubes, Appl. Phys. Lett., 81, 4133 (2002)

[88] Y. H. Gao, Y. Bando, Carbon nanothermometer containing gallium, Nature, 415, 599 (2002)

[89] Z. Wang, Z. Zhao and J. Qiu, In situ synthesis of super-long Cu nanowires inside carbon nanotubes with coal as carbon source, Carbon 44, 1845-1869 (2006)

[90] J. Jorge, E. Flahaut, F. Gonzalez-Jimenez, G. Gonzalez, J. Gonzalez, E. Belandria, J. M. Broto and B. Raquet, Preparation and characterization of a-Fe nanowires located inside double wall carbon nanotubes, Chem. Phys. Lett. 457, 347-351 (2008)

[91] Y. Hayashi, T. Fujita, T. Tokunaga, K. Kaneko, T. Butler, N. Rupesinghe, J. D. Carey, S. R. P. Silva and G.A.J. Amaratunga, Encapsulation of Co and Pd multi-metal nanowires inside multi-walled carbon nanotubes by microwave plasma chemical vapor deposition, Diamond & Related Materials 16, 1200-1203 (2007)

[92] H. Yu, J. Peng, M. Zhai, J. Li and G. Wei, Silver nanowires formed within multi-walled carbon nanotubes by radiation-induced reduction of silver ions, Physica E 40, 2694-2697 (2008)

[93] L. Jankovic, D. Gournis, P. N. Trikalitis, I. Arfaoui, T. Cren, P. Rudolf, M.H. Sage, T. T. M. Palstra, B. Kooi, J. D. Hosson, M. A. Karakassides, K. Dimos, A. Moukarika and T. Bakas, Carbon Nanotubes encapsulating Superconducting Single-Crystalline Tin Nanowires, Nano Lett.1132-1134 (2006)

[94] N. Tombros, L. Buit, I. Arfaoui, T. Tsoufis, D. Gournis, P. N. Trikalitis, S. J. van der Molen, P. Rudolf, and B. J. van Wees, Transport in a Single Superconducting Tin Nanowire Encapsulated in a Multiwalled Carbon Nanotube, Nano Lett., Vol. 8, No 9 3060-3064 (2008)

[95] K. Hernadi, A. Fonseca, J.B. Nagy, D. Bernaerts and A.A. Lucas, Fe-catalyzed carbon nanotube formation, Carbon 34(10), 1249-1257 (1996)

[96] R. D. Gupta, G. Schwandt and D. J. Fray, Preparation of tin-filled carbon nanotubes and nanoparticles by molten salt electrolysis, Carbon 70, 142-148, Science Direct (2014)

[97] W. K. Hsu, S. Trasobares, H. Terrones, M. Terrones, N. Grobert, Y. Q. Zhu,W. Z. Li, R. Escudero,J. P. Hare,H. W. Kroto, and D. R. M. Walton, Electrolytic Formation of Carbon-Sheathed Mixed Sn−Pb Nanowires.

[98] Vodolazov, D.Y. Peeters, F.M. Piraux, L. Matefi-Tempfli, S. Michotte, Current-voltage characteristics of quasi-one dimensional superconductors : S-behavior in the constant voltage regime, Phys.ReV. Lett. (2003)

[99] Hsu, Y.J. Lu, S.Y., Vapor−Solid Growth of Sn Nanowires: Growth Mechanism and Superconductivity, J. Phys. Chem. B, 109, 4398 (2005)

[100] Tian, M.L. Wang, J.G. Snyder, J. Kurtz, J. Liu, Y. Schiffer, P. Mallouk, T.E. Chan, M.H. W., Synthesis and characterization of superconducting single-crystal Sn nanowires, Phys. Lett., 83, 1620 (2003)

[101] A. Bezryadin, C. N. Lau, M. Tinkham, Quantum suppression of superconductivity in ultrathin nanowires, Nature, 404, 971 (2000)

[102] A. Hubert and R. Schäfer, Magnetic Domains, Springer-Verlag, Berlin Heidelberg (1998)

[103] D. R. Askeland, Materialwissenschaften, Spektrum, Akad. Verl. (1996)

[104] R. C. O'Handley, Modern magnetic materials: principles and applications, John Wiley & Sons, New York (2000)

[105] D. Jiles, Introduction to Magnetism and Magnetic Materials, Chapman & Hall (1998)

[106] I. Panagiotopoulos, Magnetic Materials, G. A. Pnevmatikos Publications, Ioannina (2010)

[107] J. H. Wijngaard, Magnetic and Magneto-optical Properties of Some Transition Metal Compounds, Rijksuniversiteit Groningen (1991)

[108] J. B. Yang, K. Kamaraju, W. B. Yelon, W. J. James, Q. Cai & A. Bollero, Magnetic properties of the MnBi intermetallic compound. Appl. Phys. Lett. 79, p.1846 (2001)

[109] R. Y. N. Gengler, A modified Langmuir-Schaefer method for the creation of functional thin films, Doctoral Thesis, Zernike Institute for advanced materials, University of Groningen (2010)

[110] K. S. Novoselov et al., Electric field in atomically thin carbon films, Science 306, 666-669 (2004)

[111] P. R. Wallace, The band theory of graphite, Phys. Rev. 71, 622-634 (1947)

[112] C. N. Lau, N. Markovic, M. Bockath, A. Bezryadin, M. Tinkham, Quantum Phase Slips in Superconducting Nanowires, Phys. ReV. Lett. 87, 217003 (2001)

[113] K. S. Novoselov, A. K. Geim, S. V. Morozov, D. Jiang, M. I. Katsnelson, I. V. Grigorieva, S. V. Dubonos, A. A. Firsov, Nature 438, 197-200 (2005)

[114] Y. Zhang, Y. Tan, H. L. Stormer, P. Kim, Experimental Observation of Quantum Hall Effect and Berry's Phase in Graphene, Nature 438, 201-204 (2005)

[115] N. Tombros, C. Jozsa, M. Popinciuc, H. T. Jonkman, B. J. van Wees, Electronic spin transport and spin precession in single graphene layers at room temperature, Nature 448, 571-574 (2007)

[116] K. S. Kim, Y. Zhao, H. Jang, S. Y. Lee, J. M. Kim, K. S. Kim, J. Ahn, P. Kim, J. Choi, B. H. Hong, Large-scale pattern growth of graphene films for stretchable transparent electrodes, Nature 457, 706-710 (2009)

[117] Y. Wang, Y. Huang, Y. Song, X. Zhang, Y. Ma, J. Liang, Y. Chen, Room-Temperature Ferromagnetism of Graphene, Nano Lett. 9, 220-224 (2009)

[118] X. Li, G. Zhang, X. Bai, X. Sun, X. Wang, E. Wang, H. Dai, Highly conducting graphene sheets and Langmuir–Blodgett films, Nat. Nano 3, 538-542 (2008)

[119] C. Gomez-Navarro, R. T. Weitz, A. M. Bittner, M. Scolari, A. Mews, M. Burghard, K. Kern, Electronic transport properties of individual chemically reduced graphene oxide sheets, Nano Lett. 7, 3499-3503 (2007)

[120] H. A. Becerril, J. Mao, Z. Liu, R. M. Stoltenberg, Z. Bao, Y. Chen, Evaluation of solution-processed reduced graphene oxide films as transparent conductors, ACS Nano 2, 463-470 (2008)

[121] C. J. Schafhaeutl, Ueber die Verbindungen des Kohlenstoffes mit Silicium, Eisen und anderen Metallen, welche die verschiedenen Gallungen von Roheisen, Stahl und Schmiedeeisen bilden, J. Prakt. Chem. 21, 129–157 (2010)

[122] H. P.Boehm & E. Stumpp, Citation errors concerning the first report on exfoliated graphite, Carbon 45, 1381-1383 (2007)

[123] B. C. Brodie, Philos. Trans. R. Soc. London 149, 249–259 (1859)

[124] L. Staudenmaier, Ber. Dtsch. Chem. Ges. 31, 1481–1487 (1898)

[125] W. S. Hummers Jr & R. E. Offeman, Preparation of graphitic oxide, J. Am. Chem. Soc. 80, 1339 (1958)

[126] P. V. Lakshminarayanan, H. Toghiani & C. U. Pittman Jr, Nitric acid oxidation of vapor grown Carbon nanofibers, Carbon 42, 2433-2442 (2004)

[127] N. Zhang, L. Y. Wang, H. Liu & Q. K. Cai, Nitric acid oxidation on carbon dispersion and suspension stability, Surface and Interface Analysis 40, 1190-1194 (2008)

[128] U. Hofmann & R. Holst, Ber. Dtsch. Chem. Ges. B 72, 754–771 (1939)

[129] G. Ruess, Monatsh. Chem. 76, 381–417 (1946)

[130] A. Lerf, H. Y. He, M. Forster & J. Klinowski, Structure of graphite oxide revisited, J. Phys. Chem. B 102, 4477-4482 (1998)

[131] N. I. Kovtyukhova, Layer-by-layer assembly of ultrathin composite films from micron-sized graphite oxide sheets and polycations, Chemistry of Materials 11, 771-778 (1999)

[132] A. B. Bourlinos et al, Graphite oxide: Chemical reduction to graphite and surface modification with primary aliphatic amines and amino acids, Langmuir 19, 6050-6055 (2003)

[133] I. Dekany, R. Kruger-Grasser & A. Weiss, Selective liquid sorption properties of hydrophobized graphite oxide nanostructures, Colloid and Polymer Science 276, 570-576 (1998)

[134] P. Liu, K. Gong & P. Xiao, Preparation and characterization of poly (vinyl acetate)-intercalated Graphite oxide, Carbon 37, 2073-2075 (1999)

[135] L. Gross et al, Bond-Order Discrimination by Atomic Force Microscopy, Science 337, 1326-1329 (2012)

[136] D. W. Boukhvalov & M. I. Katsnelson, Chemical functionalization of graphene, J. Phys.-Condensed Matter 21 (2009)

[137] D. R. Dreyer, S. Park, C. W. Bielawski & R. S. Ruoff, The chemistry of graphene oxide, Chem. Soc. Rev. 39, 228-240 (2010)

[138] Y. Chen, X. Zhang, P. Yu & Y. Ma, Stable dispersions of graphene and highly conducting grapheme films: A new approach to creating colloids of graphene monolayers, Chem. Commun., 4527-4529 (2009)

[139] E. Katz & I. Willner, Biomolecule-Functionalized Carbon Nanotubes: Applications in Nanobioelectronics, Chem. Phys. Chem. 5, 1084-1104 (2004)

[140] B. Dai, L. Fu, L. Liao, N. Liu, K. Nan, Y. Chen and Z. Liu, High-Quality Single-Layer Graphene via Reparative Reduction of Graphene Oxide, Nano Res., 4(5): 434–439 (2011)

[141] M. S. Moreno, G. Punte, G. Rigotti, R. C. Mercader, A. D. Weisz, M. A. Blesa, Kinetic study of the disproportionation of tin monoxide, Solid State Ionics, 144, 81 (2001)

[142] S. Stankovich, Synthesis of graphene-based nanosheets via chemical reduction of exfoliated graphite oxide, Carbon 45, 1558-1565 (2007)

[143] G. Eda, G. Fanchini & M. Chhowalla, Large-area ultrathin films of reduced grapheme oxide as a transparent and flexible electronic material, Nature Nanotechnol., 3, 270-274 (2008)

[144] V. C. Tung, M. J. Allen, Y. Yang & R. B. Kaner, High-through-put solution processing of large-scale graphene, Nature Nanotechnol. 4, 25-29 (2009)

[145] A. B. Bourlinos, M. A. Karakassides, D. Gournis, V. Georgakilas & A. Moukarika, A novel route towards iron- and chromium-containing MCM-41 materials through melt-exchange of the template, Chem. Lett. 32, 38-39 (2003)

[146] Y. Si & E. T. Samulski, Synthesis of water soluble graphene, Nano Lett. 8, 1679-1682 (2008)

[147] N. Mohanty, A. Nagaraja, J. Armesto & V. Berry, High-throughput, ultrafast synthesis of

Solution dispersed graphene via a facile hydride chemistry, Small 6, 226-231 (2010)

[148] G. Wang, Facile synthesis and characterization of graphene nano-sheets, J. Phys. Chem. C 112, 8192-8195 (2008)

[149] M. J. McAllister, Single sheet functionalized graphene by oxidation and thermal expansion of graphite, Chem. Mater. 19, 4396-4404 (2007)

[150] H. C. Schniepp, Functionalized single graphene sheets derived from splitting graphite oxide. J. Phys. Chem. B 110, 8535-8539 (2006)

[151] M. Zhou et al, Controlled synthesis of large-area and Patterned electrochemically reduced graphene oxide films, Chem.-Eur. J. 15, 6116-6120 (2009)

[152] R. Y. N. Gengler, D. S. Badali, D. Zhang, K. Dimos, K. Spyrou, D. Gournis and R. J. D. Miller, Revealing the ultrafast process behind the photo-reduction of graphene oxide, Nature Com., 1-5, Macmillan Publishers Limited (2013)

[153] L. J. Cote, R. Cruz-Silva & J. Huang, Flash reduction and patterning of graphite oxide and its polymer composite, J. Am. Chem. Soc. 131, 11027-11032 (2009)

[154] K. Itaya, K. Shibayama, H. Akahoshi, and S. Toshima, Prussian-blue-modified electrodes: An application for a stable electrochromic display device, J. Appl. Phys.53 804 (1982)

[155] K. Itaya, I. Uchida, and V. D. Neff, Electrochemistry of poly-nuclear transition metal cyanides: Prussian blue and its analogues, Acc. Chem. Res. 19, 162 (1986)

[156] A. Gotoh, H. Uchida, M. Ishizaki, T. Satoh, S. Kaga, S. Okamoto, M. Ohta, M. Sakamoto, T. Kawamoto, H. Tanaka, M. Tokumoto, S. Hara, H. Shiozaki, M. Yamada, M. Miyake, and M. Kurihara, Simple synthesis of three primary colour nanoparticle inks of Prussian blue and its analogues, Nanotechnol. 18 345609 (2007)

[157] S. Hara, H. Tanaka, T. Kawamoto, M. Tokumoto, M. Yamada, A. Gotoh, H. Uchida, M. Kurihara, and M. Sakamoto, Electrochromic thin film of Prussian Blue nanoparticles fabricated using wet process, Jpn. J. Appl. Phys. 46 L945 (2007)

[158] X. Zhang, J. Wang, B. Ogorevc, and U. E. Spichiger, Glucose Nanosensor Based on Prussian-Blue Modified Carbon-Fiber Cone Nanoelectrode and an Integrated Reference Electrode, Electroanalysis 11 945 (1999)

[159] F. Ricci, A. Amine, G. Palleschi, and D. Moscone, Prussian Blue based screen printed biosensors with improved characteristics of long-term lifetime and pH stability, Biosens. Bioelectron. 18 165 (2003)

[160] A. A. Karyakin, E. E. Karyakina, and L. Gorton, Amperometric biosensor for glutamate using Prussian Blue based "artificial peroxidase" as a transducer for hydrogen peroxide, Anal. Chem. 72, 1720 (2000)

[161] A. A. Karyakin: Prussian Blue and Its Analogues: Electrochemistry and Analytical Applications, Electroanalysis 13 813 (2001)

[162] R. Y. N. Gengler, L. M. Toma, E. Pardo, F. Lloret, X. Ke, G. Van Tendeloo, D. Gournis and P. Rudolf, Prussian Blue Analogues of Reduced Dimensionality, Small, 8, No. 16, 2532–2540 (2012)

[163] O. Sato, T. Iyoda, A. Fujishima, and K. Hashimoto, Photoinduced Magnetization of a Cobalt-Iron Cyanide, Science 272 704 (1996)

[164] N. Shimamoto, S. Ohkoshi, O. Sato, and K. Hashimoto, Control of Charge-Transfer Induced Spin Transition Temperature on Cobalt-Iron Prussian Blue Analogues, Inorg. Chem. 41 678 (2002)

[165] M. Hanawa, Y. Moritomo, A. Kuriki, J. Tateishi, K. Kato, M. Takata and M. Sakata, Coherent Domain Growth under Photo-Excitation in a Prussian Blue Analogue, J. Phys. Soc. Jpn. 72, 987(2003)

[166] T. Matsuda, J. E. Kim, K. Ohoyama, and Y. Moritomo, Universal thermal response of the Prussian blue lattice, Phys. Rev. B 79 172302 (2009)

[167] Y. Moritomo, F. Nakada, H. Kamioka, J. E. Kim, and M. Takata, Desorption-induced first-order phase transition in a cyano-bridged compound, Appl. Phys. Lett. 92 141907 (2008)

[168] Y. Tokura and N. Nagaosa, Orbital Physics in Transition-Metal Oxides, Science 288 462 (2000)

[169] D.A. Pejakovic, J.L. Manson, J.S. Miller, A.J. Epstein, Photo-induced Magnetism, Dynamics, and Cluster Glass Behavior of a molecule-Based Magnet, Phys. Rev. Lett. Vol 85 No 9, 1994-1997 (2000)

[170] P. Gutlich, G. Yann, T. Woike, Photo-switchable co-ordination compounds, Coordination Chem. Rev. pp839-879 (2001)

[171] J. Brown, Philos. Trans., 33, 17 (1724)

[172] M. B. Robin, P. Day, Adu. Inorg. Chem. Radiochem.,10, 247 (1967)

[173] T. Kawamoto, Y. Asai, S. Abe, Novel Mechanism of Photo-induced Reversible Phase Transitions in Molecule-Based Magnets, Phys. Rev. Lett. Ch86, 348, (2001)

[174] S. Ferlay, T. Mallah, R. Quahes, P. Veillet, M. Verdaguer, A room-temperature organometallic magnet based on Prussian blue, Nature, 378, 701 (1995)

[175] J. M. Manriquez, G. T. Yee, R. S. Mclean, A. J. Epstein, J. S. Miller, A Room Temperature Molecular/Organic-Based Magnet, Science, 252, 1415 (1991)

[176] S. Ohkoshi, T. Iyoda, A. Fujishima, K. Hashimoto, Magnetic Properties of Mixed Ferro-ferrimagnets Composed of Prussian Blue Analogs, Phys. Rev. B, 56, 11642 (1997)

[177] S. Ohkoshi, Y. Abe, A. Fujishima, K. Hashimoto, Design and Preparation of a Novel Magnet Exhibiting Two Compensation Temperatures Based on Molecular Field Theory, Phys. Rev. Lett. 82, 1285 (1999)

[178] W. E. Buschmann, J. Ensling, P. Gütlich, J. S. Miller, Electron Transfer, Linkage Isomerization, Bulk Magnetic Order, and Spin Glass Behavior in the Iron(Hexacyanomanganate(III) Prussian Blue Analog, Chem. Eur. J., 5, 3019 (1999)

[179] F. Gauzzi, B. Verdini, A. Maddalena, G. Principi, X-ray diffraction and mössbauer analyses of SnO disproportionation products, Inorg. Chimica Acta-Articles and Letters, 104, 1 (1985)

[180] S. Ohkoshi, S. Yorozu, O. Sato, T. Iyoda, A. Fujishima, K. Hashimoto, Photoinduced Magnetic Pole Inversion in a Ferro-ferrimagnet: $(Fe^{II}_{0.40}Mn^{II}_{0.60})_{1.5}Cr^{III}(CN)_6$, Appl. Phys. Lett. 70, 1040 (1997)

[181] E. Coronado, M. C. Gimenez-Lopez, G. Levchenko, F. M. Romero, V. Garcia Baonza, A. Milner, M. Paz-Pasternak, Pressure-tuning of Magnetism and Linkage Isomerism in Iron(II) Hexacyanochromate, J. Am. Chem. Soc. 127, 4580 (2005)

[182] S. Margadonna, K. Prassides, A. N. Fitch, Zero Thermal Expansion in a Prussian Blue Analogue, J. Am. Chem. Soc. 126, 15390 (2004)

[183] S. Margadonna, K. Prassides, A. N. Fitch, Large Lattice Responses in a Mixed-Valence Prussian Blue Analogue Owing to Electronic and Spin Transitions Induced by X-ray Irradiation, Angew. Chem. Int. Ed. 43, 6316 (2004)

[184] S. S. Kaye, J. R. Long, Hydrogen Storage in the Dehydrated Prussian Blue Analogues M3[Co(CN)6]2 (M = Mn, Fe, Co, Ni, Cu, Zn), J. Am. Chem. Soc. 127, 6506 (2005)

[185] R. J. Mortimer, Electrochromic materials, Chem. Soc. Rev. 26, 147 (1997)

[186] P. J. Kulezsa, K. Miecznikowski, M. Chojak, M. A. Malik, S. Zamponi, R. Marassi, Electrochromic features of hybrid films composed of polyaniline and metal hexacyanoferrate, Electrochim. Acta 46, 4371 (2001)

[187] M. Kaneko, S. Hara, A. J. Yamada, A photoresponsive graphite electrode coated with prussian blue, Electroanal. Chem. 194, 165 (1985)

[188] R. Koncki, Chemical Sensors and Biosensors Based on Prussian Blues, Critical Rev. Anal. Chem. 32, 79 (2002)

[189] K. Itaya, T. Ataka, S. Tishima, Spectroelectrochemistry and electrochemical preparation method of Prussian blue modified electrodes, J. Am. Chem. Soc. 104, 4767 (1982)

[190] C.A. Lundgren, R. W. Murray, Observations on the composition of Prussian blue films and their electrochemistry, Inorg. Chem. 27, 933 (1988)

[191] H. Fuchs, H. Ohst, W.Prass, Ultrathin Organic Films: Molecular Architectures for Advanced Optical Electronic and Bio-Related Systems, Adv. Mater. 3, No 1, 10-13, VCH Verlagsgesselschaft mbH, W-6940, Weinheim (1991)

[192] K. Itaya and I. Uchida, Electrochemistry of Poly-nuclear Transition Metal Cyanides: Prussian Blue and Its Analogues, Acc. Chem. Res., 19, 162-168 (1986)

[193] T. Yamamoto, Y. Umemura, O.Sato and Y. Einaga, Photoswitchable Magnetic Films: Prussian-Blue intercalated in Langmuir-Blodgett Films consisting of an Amphiphilic Azobenzene and a Clay Mineral, Chem. Mater. Vol. 16, No 17, 1195-1201 (2004)

[194] Y. Unemura, Hybrid Films of a Clay Mineral and an Iron (II) Complex Cation prepared by a combined method of the Langmuir-Blodgett and Self-assembly Techniques, J. Phys. Chem. B, Vol. 106, No 43, 11168, 11171 (2004)

[195] T. Yamamoto, Y. Umemura, O. Sato and Y. Einaga, Observation of the Anisotropic Photoinduced Magnetization Effect in Co-Fe Prussian Blue Thin Films Fabricated by Using Clay Langmuir-Blodgett Films as a Template, J. Am. Chem. Soc., Vol. 127, No 46, 16065-16073 (2005)

[196] Y. Umemura, Y. Einaga, A. Yamagishi, Formation of a stable thin sheet of Prussian Blue in a clay-organic hybrid film, Mater. Lett. 58, 2472-2475 (2004)

[197] G. G. Roberts, Langmuir-Blodgett films, Plenium Press, 444 (1990)

[198] J. D. Swalen, et al, Molecular monolayers and films, A panel report for the Materials Sciences Division of the Department of Energy, Langmuir 3, 932-950 (1987)

[199] M. Breton, Formation and Possible Applications of Polymeric Langmuir-Blodgett Films, A Review, J. Macrom. Sci., Part C 21, 61-87 (1981)

[200] M. C. Petty, Possible applications for Langmuir-Blodgett films, Thin Solid Films 210–211, Part 2, 417-426 (1992)

[201] P. Martin, M. Szablewski, Langmuir-Blodgett Troughs, Operating manual, NIMA Technology, 6th edition (2001)

[202] D. K. Chattoraj & K. S. Birdi, Adsorption and the Gibbs surface excess (1984).

[203] G. L. Gaines, Insoluble monolayers at liquid-gas interfaces, Inter-science Publishers (1966)

[204] R. G. Laughlin, The Aqueous phase behavior of surfactants, Academic Press (1994)

[205] I. Langmuir, The Constitution and Fundamental Properties of Solids and Liquids, J. Am. Chem. Soc. 39, 1848-1906 (1917)

[206] K. Tamura, H. Setsuda, M. Taniguchi, T. Nakamura, A. Yamagishi, A Clay-Metal Complex Ultrathin Film as Prepared by the Langmuir-Blodgett Technique, Chem. Lett., 121-122 (1999)

[207] K. Okamoto, K. Tamura, M. Takahashi, A. Yamagishi, Preparation of a clay-metal complex hybrid film by the Langmuir-Blodgett method and its application as an electrode modifier, Colloids and Surfaces A, 169, 241-249, (2000)

[208] D. K.Chattoraj & K. S. Birdi, Adsorption and the Gibbs surface excess (1984)

[209] E. J. Sonneveld, J.W. Visser: J. Appl. Cryst. 8, 1-7 (1975)

[210] P. G. Gennes, Deposition of Langmuir-Blodgett layers, Colloid & Polymer Sci., 264, 463-465 (1986)

[211] A. Kouloumpis, Master Thesis, Department of Materials Science and Engineering, University of Ioannina (2013)

[212] C. N. R. Rao, G. U. Kulkarni, P. J. Thomas & P. P. Edwards, Metal nanoparticles and their assemblies, Chem. Soc. Rev. 29, 27--35 (2000)

[213] F. Schreiber, Structure and Growth of self-assembling monolayers, Prog. Surf. Sci. 65, 151257 (2000)

[214] D. Anagnostopoulos, D. Gournis, M. A. Karakasides, D. Papagiannis, Materials Characterization Techniques, University Typing Shop, Ioannina (2009).

[215] R. L. Pescok, D. L. Shields, T. Cairns, I. G. McWilliam, Modern Methods in Chemical Analysis, Translation: S. Voliotis, G. A. Pnevmatikos Publications, Athens (1980)

[216] A. Valavanides, Basic Principles of Molecular Spectroscopy and Applications in Organic Chemistry: Infrared Spectroscopy, Nuclear Magnetic Resonance, Ultraviolet and Visible Spectroscopy, Mass Spectroscopy, Raman Spectroscopy, Electronic Paramagnetic Resonance, 2nd Edition, Modern Matters Publications, Non Profit Publishing Company, Athens (2008)

[217] J. R. Ferraro, K. Nakamoto & C. W. Brown, (2003). Introductory Raman spectroscopy, 2nd Edition, Academic Press, California (2003)

[218] D. B. Williams, C. B. Carter, Transmission Electron Microscopy: A Textbook for Materials Science, Springer Science&Business Media, LLC 1996 (2009)

[219] Mössbauer Spectroscopy (electronic form) available at: http://en.wikipedia.org/wiki/M%C3%B6ssbauer_spectroscopy

[220] Superconducting Quantum Interference Device (electronic form) available at: http://en.wikipedia.org/wiki/Superconducting_quantum_interference_device

[221] K.H.J. Buschow and F.R. de Boer, Physics of Magnetism and Magnetic Materials, Kluwer Academic/Plenum Publishers (2003)

[222] L. Michalowsky, Magnettechnik. Fachbuchverlag Leipzig (1993)

[223] J. Schmitt & H. – C. Flemming, FTIR-spectroscopy in microbial and material analysis, International Bio-deterioration &amp, Biodegradation 41, 1-11 (1998)

[224] J. D. Schuttlefield, D. Cox & V. H. Grassian, An investigation of water uptake on clays minerals using ATR-FTIR spectroscopy coupled with quartz crystal microbalance measurements. J. Geophys. Res. 112, D21303 (2007)

[225] Schematic of UV- visible spectrophotometer (electronic form) available at: en.wikipedia.org/wiki/Ultraviolet–visible_spectroscopy

[226] Skoog et al, Principles of Instrumental Analysis, 6th edition, Thomson Brooks/Cole pp.169–173, 349-351 (2007)

[227] X-Photoelectron Spectroscopy (electronic) available at: http://en.wikipedia.org/wiki/X-ray_photoelectron_spectroscopy

[228] Kish graphite (electronic form) available at: https://graphene-supermarket.com/Kish-Graphite

[229] L. J. Cote, F. Kim, and J. Huang, Langmuir-Blodgett Assembly of Graphite Oxide Single Layers, J. Am. Chem. Soc. 131, 1043–1049 (2009)

[230] M. S. Dresselhaus, M. A. Pimenta, P. C. Eklund, G. Dresselhaus, Raman Scattering in Fullerenes and Related Carbon-Based Materials, Springer Series in Materials Science, 42, 314 (2000)

[231] M. Sveningsson, R. E. Morjan, O. A. Nerushev, Y. Sato, J. Backstrom, E. E. B. Campbell, F. Rohmund, Raman spectroscopy and field-emission properties of CVD-grown carbon-nanotube films, Applied Physics a-Materials Science & Processing, 73, 409 (2001)

[232] P. Scherrer, Determination of the size and internal structure of colloidal particles using X-rays, Nachr. Ges. Wiss. Göttingen 26, 98-100 (1918)

[233] A. R. Stokes, A. J. C. Wilson, The diffraction of X rays by distorted crystal aggregates - I, Proc. Phys. Soc. Lond. 56, 174-181 (1944)

[234] G. K. Williamson, W. H. Hall, X-ray line broadening from filed aluminium and wolfram, Acta Metall. 1, 22-31 (1953)

[235] M. S. Dresselhaus, P. C. Eklund, Phonons in Carbon Nanotubes, Advances in Physics 2000, 49, 705

[236] P. C. Eklund, J. M. Holden, R. A. Jishi, Vibrational modes of carbon nanotubes; Spectroscopy and theory, Carbon 1995, 33, 959

[237] W. Z. Li, H. Zhang, C. Y. Wang, Y. Zhang, L. W. Xu, K. Zhu, S. S. Xie, Raman characterization of aligned carbon nanotubes produced by thermal decomposition of hydrocarbon vapor, Appl. Phys. Lett. 1997, 70, 2684

[238] Y. Y. Wu, P. D. Yang, Melting and welding semiconductor nanowires in nanotubes, Advanced Materials 2001, 13, 520

[239] Chem. Mater., 11, 1747-1751 (1999)

[240] Y. J. Hsu, S. Y. J. Lu, Phys. Chem. B, 109, 4398 (2005)

[241] M. L. Tian, J. G. Wang, J. Snyder, J. Kurtz,Y. Liu, P. Schiffer, T. E. Mallouk, M. H. W. Chan, Synthesis and characterization of superconducting single-crystal Sn nanowires, Appl. Phys. Lett., 83, 1620 (2003)

[242] J. E. Han, V. H. Crespi, Discrete transverse superconducting modes in nano-cylinders, Phys. ReV. B, 69, 214526 (2004)

[243] http://www.2spi.com/catalog/new/hopg-kish-graphite.html

Part H: Abstract

Development and study of novel nano-structured hybrid materials based on carbon

Andreas Rossos

Doctoral Dissertation

Department of Materials Science and Engineering, University of Ioannina, 45110 Ioannina, Greece

ABSTRACT

One of the aspects of modern materials science that has been captivating scientific interest in the last decade are low-dimensionality systems, mostly because of their physical, chemical and biological properties which are widely different from their bulk material. By the use of bottom-up synthetic methods, the control of the products in nanoscale is possible, aiming at the same time at producing novel hybrid nano-materials. Towards this aim, the main subject of this dissertation was the design, development, characterization and study of novel low-dimensional hybrid materials based on carbon. Carbon nanotubes encapsulating tin and tin-lead superconducting nanowires as well as magnetic manganese-bismuth nanorods were formed using the conventional catalytic chemical vapor deposition method. The products were examined by the use of a combination of analytical techniques such as XRD, Raman and Mössbauer spectroscopies, DTA/TG, TEM, SEM and SQUID. Additionally, a new graphene oxide form was prepared using for the first time as pristine material 'Kish' graphite and high quality of monolayers were formed using the Langmuir-Blodgett technique. The produced graphene oxide was examined by the use of XRD, Raman and FT-IR spectroscopies while the produced thin films were examined by TEM microscopy. Finally a new low-dimensional Prussian Blue Analogue was produced during a controllable on-surface reaction and the so-called 'inverted' Langmuir-Blodgett method. The success of the reaction was verified by XPS spectroscopy and HRTEM/EDX/SAED results. The obtained final hybrid materials are expected to exhibit a wide range of applications in several fields, such as electronics, gas storage, pharmaceutics, catalysis and nanosensing.

Keywords: nanowires, carbon nanotubes, hybrid materials, graphene oxide, Prussian Blue Analogues, nanorods, superconductivity, magnetic materials.

Ανάπτυξη και μελέτη καινοτόμων νανοδομημένων υβριδικών υλικών με βάση τον άνθρακα

Ανδρέας Ρώσσος

Διδακτορική Διατριβή

Τμήμα Μηχανικών Επιστήμης Υλικών, Πανεπιστήμιο Ιωαννίνων, 45110 Ιωάννινα, Ελλάδα

ΠΕΡΙΛΗΨΗ

Ένας τομέας της επιστήμης των μοντέρνων υλικών που έχει αιχμαλωτίσει το επιστημονικό ενδιαφέρον την τελευταία δεκαετία είναι τα χαμηλοδιάστατα συστήματα, κυρίως εξαιτίας των φυσικών, χημικών και βιολογικών τους ιδιοτήτων, οι οποίες είναι μακράν διαφορετικές από αυτές των αντίστοιχων bulk υλικών. Με τη χρήση 'bottom-up' συνθετικών μεθόδων είναι εφικτός ο έλεγχος των προϊόντων στη νανοκλίμακα, στοχεύοντας ταυτόχρονα στην παραγωγή καινοτόμων υβριδικών νανο-υλικών. Σ' αυτή την κατεύθυνση, το κύριο αντικείμενο της διατριβής αυτής ήταν ο σχεδιασμός, η ανάπτυξη, ο χαρακτηρισμός και η μελέτη καινοτόμων χαμηλοδιάστατων υβριδικών υλικών βασισμένων στον άνθρακα. Νανοσωλήνες άνθρακα με ενσωματωμένα υπεραγώγιμα νανοκαλώδια κασσιτέρου και κασσιτέρου-μολύβδου καθώς και μαγνητικές νανοράβδοι μαγγανίου-βισμουθίου σχηματίστηκαν με χρήση της συμβατικής τεχνικής της καταλυτικής χημικής εναπόθεσης ατμών. Τα προϊόντα χαρακτηρίστηκαν με ένα συνδυασμό αναλυτικών τεχνικών όπως XRD, φασματοσκοπίες Raman και Mössbauer, DTA/TG, TEM, SEM και SQUID. Επιπρόσθετα, παράχθηκε ένας νέος τύπος οξειδίου του γραφενίου χρησιμοποιώντας για πρώτη φορά ως πρώτη ύλη 'Kish' γραφίτη και συντέθηκαν μονομοριακά υμένια υψηλής ποιότητας με τη χρήση της τεχνικής Langmuir-Blodgett. Το παραχθέν οξείδιο του γραφενίου διερευνήθηκε με χρήση XRD, φασματοσκοπίες Raman και FT-IR ενώ τα σχηματισθέντα λεπτά υμένια μελετήθηκαν με μικροσκοπία TEM. Τέλος, ένα νέο χαμηλοδιάστατο Prussian Blue Analogue παράχθηκε μέσω μιας ελεγχόμενης επιφανειακής αντίδρασης και με τη χρήση της επονομαζόμενης 'αντεστραμμένης' τεχνικής Langmuir-Blodgett. Η επιτυχία της αντίδρασης επιβεβαιώθηκε μέσω φασματοσκοπίας XPS και των αποτελεσμάτων HRTEM/EDX/SAED. Τα ληφθέντα τελικά υβριδικά υλικά αναμένεται να παρουσιάζουν ευρύ πεδίο εφαρμογών σε διάφορα πεδία, όπως ηλεκτρονική, αποθήκευση αερίων, φαρμακευτική, κατάλυση και νανο-αισθητήρες.

Λέξεις κλειδιά: nanowires, carbon nanotubes, hybrid materials, graphene oxide, Prussian Blue Analogues, nanorods, superconductivity, magnetic materials.